Electron-electron interactions and optical properties of two-dimensional nanocrystals

Ludmila Szulakowska

Supervisor: Prof. Pawel Hawrylak

Thesis submitted to
the University of Ottawa
in partial fulfilment of the requirements
for the Doctoral Degree in Physics

Department of Physics
Faculty of Sciences
University of Ottawa

To my Mother,

my constant inspiration,

To Bhavaye,

my motivation for the journey.

Abstract

This thesis presents a theory of electron-electron interaction effects and optical properties of nanostructures of two-dimensional (2D) honeycomb crystals - graphene and transition metal dichalcogenides (TMDC). Graphene, a semimetallic hexagonal lattice of carbon atoms can be described by a massless Dirac fermion model, with the conduction band (CB) and valence band (VB) touching in the corners of a hexagonal Brillouin zone, valleys K and $-K$. TMDC crystals sites host either a transition metal atom or a chalcogen dimer, which opens the energy gap and allows for describing their low-energy nature with massive Dirac fermion (mDf) model. The metal atom in TMDC crystals causes strong spin-orbit (SO) coupling, resulting in large SO splitting in bands at both valleys. For TMDCs it is possible to excite carriers in each valley with oppositely circularly polarised light, which offers promising prospects for devices based on electrons valley index, i.e. valleytronic devices. Additionally, the optical response of TMDCs is enhanced by the presence of secondary CB minima, at Q-points.

The dimensionality of 2D crystals can be further reduced to form quantum dots (QDs) - nanostructures confined in all dimensions. This thesis first discusses hexagonal graphene QDs, which exhibit energy gap oscillation as a function of size, due to the edge type: zigzag or armchair. These QDs are divided into concentric rings, analysed with tight-binding (TB) model. An armchair edged QD is built from a zigzag edged QD by adding a 1D Lieb lattice of carbon atoms on its edge. The energy gap is formed differently for both edges: from the outer ring states for zigzag edge and from the 1D Lieb lattice zero-energy states for armchair edge, which causes the energy gap

oscillation with QD size.

The remaining portion of the thesis focuses on TMDC materials. First a TB model is presented for a member of TMDC group, MoS_2, using three d orbitals of Mo atom and three p orbitals of the S_2 dimers. The tunneling matrix elements between nearest-neighbor and next-nearest-neighbour sites are explicitly derived at K and $-K$ to form a six band TB Hamiltonian. Its solutions are fitted to the bands obtained from the density functional theory ab initio calculations to obtain the correct behaviour of bands around $\pm K$ and additional minima at Q-points, which explains the role of d orbitals in TMDCs. Close to $\pm K$ the TB model is reduced to mDf model, which is then studied in response to light, yielding the valley-dependent selection rules for absorption.

The interaction of mDf with light is further studied in the presence of strong external magnetic field, which leads to the formation of Landau levels (LLs), asymmetric between both valleys, and valley Zeeman splitting. These LLs are populated with electrons to form a Hartree-Fock ground state (GS), which can exhibit valley polarisation due to the LL asymmetry. Quasi-electron-hole excitations out of the GS are then formed and their self-energy, vertex corrections and scattering energy is calculated. The effect of electron-electron interactions on valley Zeeman splitting is demonstrated and the Bethe-Salpeter equation is numerically solved to give magnetoexciton spectrum for both valleys. The results include a valley-dependent absorption spectrum for mDf magnetoexcitons that vary with the valley polarisation.

The final part of this thesis discusses the single particle and interacting effects in gated MoS_2 QDs. First, I perform a single electron atomistic calculation for a million-atom computational box with periodic boundary conditions based on a TB model developed from ab initio methods for bulk MoS_2. Electrons are then confined with a parabolic electrostatic potential from top metallic gates. They exhibit twofold degenerate harmonic oscillator energy spectrum with shell spacing ω associated with valleys $\pm K$ as well as a sixfold degenerate energy spectrum derived from the Q-points. The degeneracy of electronic shells is broken due to valley contrasting Berry curvature,

which acts as an effective magnetic field splitting opposite angular momentum states in both valleys. I populate up to five K-derived harmonic oscillator shells with up to six electrons and turn on the electron-electron interactions. The resulting GS phases form two regimes dependent on ω, which are dominated each by a broken-symmetry phase, i.e. valley and spin polarised GS for low ω and valley and spin unpolarised but spin intervalley antiferromagnetic GS for higher ω. This behaviour is explained as an effect of the strong SO splitting, weak intervalley exchange interaction and strong correlations. Means of detecting these effects in experiment based on the spin and valley blockade are proposed. These results advance the understanding of interaction-driven breaking of symmetry for valley systems, crucial for designing of valleytronic devices in the future.

Acknowledgements

I would like to thank prof. Pawel Hawrylak for his wise omnipresent guidance, constant support, and incredible patience throughout my PhD studies. He always offered invaluable insights and motivated me to achieve my goals, for what I am grateful.

I also wish to thank three special figures in my scientific journey: Dr. Alain Delgado Gran, Dr. Amintor Dusko and Dr. Moritz Cygorek. They were always there to answer my never-ending questions and point me in the right direction. I will always cherish all the research as well as life advice I received from you.

I should also like to express my gratitude to all the members of the Quantum Theory Group that I have met on my journey for their eager support and clever advice. I especially thank Dr. Marek Korkusinski for always providing me with precious testcases and for answering his emails late at night. Your most detailed questions to all my presentations kept me sharp. Thank you.

Next, I must thank all my office colleagues, who witnessed my failures and successes, and offered kind words of motivation. You made my studies the most delightful and gratifying experience. Among these, I must say special thanks to Luc Robichaud and Yasser Saleem, who kept following my projects with constant vigour and were always there to discuss the details of my apparently insolvable problems. Also, I would like to thank Eduard Dumitrescu for sharing his computational brilliance.

To my Mom, and Bhavaye, I offer my lifelong gratitude for their love and support. I would have never done this without you. Lastly, I wish to thank my dear brother Jacek and my irreplaceable friends Lena and Thoby, for offering their priceless perspective and endless encouragement throughout this wild endeavour.

Abbreviations

1D	One-dimensional
2D	Two-dimensional
CB	Conduction band
CI	Configuration interaction
DFT	Density functional theory
GQD	Graphene quantum dot
GS	Ground state
HF	Hartree Fock
HO	Harmonic oscillator
LL	Landau level
mDf	Massive Dirac fermion
NN	Nearest neighbor
NNN	Next nearest neighbor
QD	Quantum dot
SO	Spin orbit
TB	Tight binding
TMDC	Transition metal dichalcogenide
VB	Valence band
VZS	Valley Zeeman splitting

Contents

List of Figures

List of Tables

Chapter 1

Introduction

Last decade marks a new era in the physics of nanomaterials, inaugurated by the Nobel prize awarded in 2010 to A. Geim and K. Novoselov for groundbreaking research on graphene, the first two-dimensional (2D) crystal realized in experiment [1–3]. Since then, the physics of low-dimensional materials on a nanoscale has attracted considerable attention due to the promising prospects for tailor-made 2D-based technology. The focus of interest has been a group of materials, called van der Waals (vdW) crystals, built of layers of atoms linked together with weak vdW forces. The atomic planes of vdW materials can be easily peeled off and stacked together again in custom combinations or twisted relative to each other, which enables engineering properties for desired applications [4–8]. This is possible, because vdW crystals host compounds with a variety of properties, from insulators and metals, through semimetals, semiconductors and ferromagnets, to superconductors and topological insulators [5, 9, 10]. Among these, crystals with honeycomb lattice have revealed particularly exotic properties and emerging new phenomena [4, 10–17].

In this thesis I will focus on graphene, a honeycomb one-atom-thick semimetal, and on transition metal dichalcogenides (TMDCs), a group of hexagonal nanocrystals with formula MX_2 (M metal, such as Mo and W, X chalcogen, such as S, Se and Te), which exhibit semiconducting properties [18, 19]. Section 1.1 gives an introduction to these bulk honeycomb 2D crystals, and section 1.2 gives an overview of the applications and properties of graphene and TMDCs quantum dots.

1.1 Hexagonal 2D crystals: graphene and TMDCs.

Graphene crystal lattice is made of carbon atoms arranged in a 2D honeycomb lattice, which stacked and attracted to other graphene layers with vdW forces forms bulk graphite [20]. A 2D hexagonal monolayer contains two inequivalent atomic sites with two carbon atoms in a unit cell and produces a hexagonal Brillouin zone with two inequivalent corners $\boldsymbol{K}$ and $-\boldsymbol{K}$. The extrema of graphene's energy bands are located in these points, where conduction and valence bands touch and make graphene a unique semimetal. The touching energy bands at $\pm\boldsymbol{K}$ are called valleys [3, 21, 22], which are similar to valleys in silicon [3]. This non-conventional band structure was first described by Wallace [23] in 1947. The resulting extraordinary electronic and optical properties include large elasticity, high carrier mobility, high conductivity and almost complete transparency, a set of features unlike any other material previously known [3, 24–27]. These properties can be understood by employing the massless Dirac fermion model, which uses an analogy to relativistic Dirac equation [24, 28]. This shows that graphene is an excellent example of how a material stripped to its 2D form can exhibit properties drastically different from its 3D analogue. Another such example is a TMDC crystal.

TMDCs share the hexagonal shape with graphene, but the atomic composition creates an important distinction. A site of a TMDC hexagonal lattice hosts a transition metal atom with valence d orbitals or a chalcogen dimer with valence p orbitals, with both atoms of the dimer placed out of the metal plane [18,19]. In this way three atomic layers make a monolayer of TMDC crystal, which is a honeycomb structure if viewed from the top . The two sites in a unit cell now have different energies, which breaks the inversion symmetry and opens an energy gap in valleys $\pm\boldsymbol{K}$. Interestingly, the 3D TMDC counterpart actually possesses an indirect energy gap, but as the thickness is reduced to a monolayer, a TMDC crystal becomes a direct gap semiconductor, with the bandgap at $\pm\boldsymbol{K}$ [18, 19, 29]. The direct gap in TMDCs makes it

an optically active material, attractive for optoelectronic applications [30, 31].

However, an even more exciting optical feature of these crystals is a valley-dependent circular dichroism, which means that carriers can be excited in each valley with oppositely circularly polarised light [30, 32–35]. This allows for accessing the valley index with optical measures and creates a possibility of designing valleytronic devices operating on electron's valley *pseudospin* instead of spin [36, 37] - a prospect that has already been explored in silicon [37–39]. Contrary to silicon, the valley-selective optical properties of TMDCs as well as long valley coherence times demonstrated by Jones et al. and Wang et al. [40, 41] offer practical means of valley manipulation for valleytronics. In addition, the heavy metal atoms cause large spin-orbit splitting of the bands at $\pm\boldsymbol{K}$, opposite for each valley, which causes spin-valley locking [35, 36]. This often means translating spin polarisation into valley pseudospin polarisation [35, 36] - an added benefit for valleytronic applications.

Another important aspect of the band structure of TMDCs is the massive Dirac fermion (mDf) description, which applies to the low energy bands at $\boldsymbol{K}$. It involves unique topological properties distinct from standard semiconductors with parabolic bands. The valley pseudospin creates effective topological moments (or orbital magnetic moments) opposite in each valley due to their opposite Berry curvature [42–45], which makes the valleys topologically inequivalent (this is also true for massless Dirac fermions in graphene [46]). This difference leads to the valley spin Hall effect [35, 36], which can be detected in experiment [47, 48]. Topological effects also manifest themselves in the splitting of 2p exciton energies for opposite angular momentum states, unobserved previously in standard semiconductors [44, 49]. This thesis discusses the topological effects in many electron-states in an electrostatic confinement, as described in section 1.2.

It is important to note that there exists another 2D material, which can be described with mDf model, bilayer graphene. It is gapless, like graphene, but the bands are characterised by nonzero effective masses. An energy gap can be opened in bilayer graphene by applying an external electric field. Although this thesis does not

consider bilayer graphene in detail, important analogies exist between gapped bilayer graphene and TMDCs, which I will often use to reveal the physics of mDf.

The rich mDf model however does not capture yet another important feature of TMDC band structure, which has an important effect on its optical properties. It involves the existence of three additional conduction band minima around each valley, at $\boldsymbol{Q}$-points, which cause band nesting [19, 50], and contribute to enhanced optical absorption of TMDCs, e.g. excitons in TMDCs are strongly affected by the presence of $\boldsymbol{Q}$-points [49].

A theory providing explanation to all these features in a consistent manner was needed. Many tight-binding and $\boldsymbol{k} \cdot \boldsymbol{p}$ approaches exist that attempt to reproduce the experimental and ab initio findings [51–56]. Some tend to disregard the complex role of d orbitals in the formation of bands and others lack the simplicity needed in an efficient tool for material property prediction. This thesis focuses on developing a microscopic understanding of the characteristics of the TMDC band structure simultaneously with keeping the model as minimal and intuitive as possible. The approach presented in the thesis allows to build a theory of more complex properties of TMDC, including external magnetic field effects, electrostatic confinement, and electron-electron interactions.

The electron-electron interactions are in fact a vital component of the 2D material theory, as they are pronounced in TMDCs and other 2D materials due to confinement to a single atomic layer. They manifest themselves in large exciton binding energies in TMDCs [57–59], spin or valley polarized broken-symmetry states in TMDCs [14, 60] and strongly correlated systems, e.g. superconducting and Mott-insulating phases in bilayer graphene [16, 17]. This thesis discusses some of the interacting effects in TMDCs that are particularly of interest, including magnetoexcitons - excitons in presence of strong magnetic field, and several electron complexes in confined nanostructures.

In fact, strong external magnetic field amplifies the electron-electron interactions in crystals, which form highly degenerate flat energy bands when exposed to magnetic

field, which are called Landau levels (LLs) [61]. For a standard semiconductor, LLs are equally spaced in energy, but hexagonal crystals exhibit unconventional LL structure. For graphene, the LL spacings decrease with higher LLs as a square root function, which is linked to the massless Dirac fermion nature of electrons in graphene [11, 22]. In TMDCs, the mDf model forms even more complicated structure of LLs, as the 0th LL is located asymmetrically within valleys at the top of the valence band at $\boldsymbol{K}$ and at the bottom of the conduction band at $-\boldsymbol{K}$ [62–66]. Additional strong spin-orbit coupling in TMDCs, opposite for both valleys further increases the LL asymmetry. As a consequence, the first possible LLs in the conduction band are placed at different energies in opposite valleys, causing valley Zeeman splitting [63–65, 67, 68]. These effects enable selective population of TMDC samples with electrons of specific spin and valley pseudospin, to achieve spin and valley polarisation [63–68]. Enhanced interaction effects have been observed in this setting [66,67,69–71], which are a subject of study in this thesis.

1.2 Graphene and TMDC quantum dots.

Quantum dots (QDs) are structures with all dimensions reduced to a nanoscale. The quantum confinement produces discrete energy levels, which bears a resemblence to an atom. This is why QDs are often called artificial atoms [72].

QDs made of conventional 3D materials include self-assembled QDs, i.e. islands formed in epitaxial layers due to the strain produced by mismatch in lattice constants [73, 74], and gated QD, which are electrostatically defined regions that confine electrons. The first demonstration of a single electron manipulation was reported in a GaAs/GaAlAs field-effect transistor, where electrons were localized within a QD-like region by metallic gates [75]. Theoretical predictions for the behaviour of a confined electron in a self-assembled InAs/GaAs QD were confirmed experimentally to be governed by a 2D harmonic oscillator (HO) spectrum with shell spacing ω [74].

Because the energy gap of a QD can be tuned with size, shape, atomic composition and external potentials, they present a variety of applications in optoelectronics, such

as solar cells, photodetectors and lasers [76–81]. The discrete energy levels allow also for manipulation of single electrons, which is used for quantum computing, e.g. in spin-based qubits - quantum computing units [82–93].

However, localizing electrons in a nanoscale region within a macroscopic volume involves interactions with nuclear spins and atomic vibrations, which result in spin decoherence. This is why 2D semiconducting materials offer a possibility of confining electrons in atomically-thin layers, which could potentially decrease decoherence and ensure room-temperature operation [91, 94].

The exploration of 2D QDs started with graphene quantum dots (GQDs), which are small pieces of graphene crystal. GQDs allow to take advantage of graphene's properties, but with an energy gap present, essential for optoelectronics. By tuning the size of the GQD, the bandgap can be continuously tuned within THz to UV range [22,95,96]. There are however more factors determining their properties and the magnitude of the energy gap, namely the shape and type of edge of a QD [12,15,97,98]. Possible edge types in a honeycomb lattice are zigzag and armchair [12, 15, 96]. For hexagonally shaped graphene QDs (GQDs) different edge type induces an oscillation of the energy gap with QD size, which is explained in this thesis.

The analogues of conventional QDs are 2D semiconductor QDs, which exploit the naturally present energy gap for some 2D materials, such as TMDCs or bilayer graphene in external electric field. Due to difficult edge control for nanostructures of TMDC [99–102] (more troublesome than for GQDs [15,103]), a confinement created by gated TMDC QDs is desirable. TMDC gated QDs have been obtained experimentally with lateral metal electrodes [104–106] and gated bilayer graphene QDs have also been realised [107–110]. Coulomb blockade effect has been observed in a transport experiment [104, 111, 112], single electron and hole transfer has been reported [112], as well as optical probing of excitons has been demonstrated in gated TMDC QDs [104,111–113]. Local tuning of confinement and gate tuning of QD molecules have also been shown [104, 114]. Also, recent progress in the manipulation of valley pseudospin includes a demonstration of long valley index lifetimes for holes in QDs [113].

These experimental results have been matched by theoretical efforts to describe the properties of TMDC QDs. The mDf in TMDCs have been proposed for qubit applications [90, 115–122]. Electronic properties of triangular QDs have been studied in Ref. [123]. Three-band tight-binding calculations for various sizes of QD in the presence of magnetic field have been reported by Pavlovic et al. and Chen et al. [124, 125], and other tight-binding studies include Refs. [120, 122, 126]. Effective models have been used for realistic sizes of QDs in Refs. [90, 115, 117–119, 121]. The means of valley control with strain, magnetic field and impurity coupling have been also studied [90, 118, 121, 122]. However, the theory of TMDC QDs presented in this thesis provides the first comprehensive explanation of the role of valleys, topology and the $\boldsymbol{Q}$-points in forming of the single electron QD energy structure.

Furthermore, similarly to atoms, the properties of QDs can change immensely, when additional electrons are placed inside them [12, 74, 127]. Together with enhanced interactions due to the 2D nature, QD of 2D materials offer a unique chance for exploring strong electron-electron interactions. Two electron states in a bilayer graphene QD have been studied theoretically in Refs. [110, 128] and experimental demonstrations of many-body effects in bilayer graphene and TMDC QDs have also been reported [94, 110]. In this thesis, I present a theory of emerging highly tunable interacting system of N electrons in a TMDC QD, which reveals broken-symmetry strongly correlated phases. These results advance our understanding of strongly interacting electrons in valley systems and explain the role of interactions in designing new nanomaterials and valleytronic devices.

1.3 Thesis Contributions.

This thesis includes a tight-binding model for hexagonal graphene quantum dots and bulk MoS_2, as well as a theory of magnetoexcitons of massive Dirac fermions and electron-electron interactions in gated MoS_2 quantum dots. The content of the chapters is based on manuscripts in peer-review journals that have been published or submitted for publication. Below I list all the articles relevant for this thesis:

1. M. Bieniek, M. Korkusiski, L. Szulakowska, P. Potasz, I. Ozfidan, and P. Hawrylak, *Band nesting, massive Dirac fermions, and valley Land and Zeeman effects in transition metal dichalcogenides: A tight-binding model*, Phys. Rev. B, vol. 97, no. 8, p. 085153, 2018.

2. Y. Saleem, L. Najera Baldo, A. Delgado, L. Szulakowska, and P. Hawrylak, *Oscillations of the bandgap with size in armchair and zigzag graphene quantum dots*, J. Phys.: Condens. Matter, vol. 31, no. 30, p. 305503, 2019.

3. L. Szulakowska, M. Bieniek, and P. Hawrylak, *Electronic structure, magnetoexcitons and valley polarized electron gas in 2D crystals*, Solid-State Electronics, vol. 155, pp. 105110, 2019.

4. M. Bieniek, L. Szulakowska, and P. Hawrylak, *Band nesting and exciton spectrum in monolayer MoS_2*, Phys. Rev. B, vol. 101, no. 12, p. 125423, 2020.

5. M. Bieniek, L. Szulakowska, and P. Hawrylak, *Effect of valley, spin, and band nesting on the electronic properties of gated quantum dots in a single layer of transition metal dichalcogenides*, Phys. Rev. B, vol. 101, no. 3, p. 035401, 2020.

6. L. Szulakowska, M. Cygorek, M. Bieniek, and P. Hawrylak, *Valley and spin polarized broken symmetry states of interacting electrons in gated MoS_2 quantum dots*, arXiv:2005.04467 [cond-mat], submitted for publication to Nature Communications, 2020.

For articles 5. and 6., I have conducted all the mentioned calculations and derivations in full, in collaboration with the co-authors as listed. Manuscript 3. is a review article that discusses my results on the magntoexciton spectrum, as well as work by my collaborators within the Quantum Theory Group lead by prof. P. Hawrylak. For articles 1. and 4., I was involved in the analytical aspect of the presented theory. Manuscript 2. includes both my colleagues' DFT results and my tight-binding calculations, in which junior students listed as co-authors were involved.

Chapter 3 and 4 are based on manuscript 2. and 1. respectively. Articles 1, 3 and 4. are relevant for chapter 5 and articles 1., 4., 5. and 6. are relevant for chapter 6.

1.4 Thesis Outline.

This thesis is organised as follows. Methodology is described in chapter 2., which succeeds the introduction in chapter 1. The methods are discussed in three sections, dedicated to single electron picture, the many-body techniques and numerical approaches.

Chapter 3. focuses on the tight-binding study of hexagonal graphene quantum dots (HGQD). By expressing the atomic structure of HGQD in terms of concentric rings, in section 3.1 I show that the energy structure of HGQDs can be understood in terms of analytical solutions of 1D periodic chains coupled together. In order to demonstrate the difference between the energy structure for zigzag-edged and armchair-edged HGQDs, I describe the additon of 1D Lieb lattice in section 3.2 to the zigzag-edged HGQD to form an armchair-edged HGQD in section 3.3.

Chapter 4. presents the tight-binding model for bulk MoS_2. Several contributions to the model are included in sections 4.1-4.3, i.e. the nearest-neighbour, next-nearest-neighbour hopping and the spin-orbit coupling. Section 4.4 describes the massive Dirac fermion (mDf) model for electrons in MoS_2, and the interaction of mDf with light is explained in section 4.5. The theory presented in this chapter is then used in chapter 5. to build on the mDf Hamiltonian and in chapter 6. to highlight the valley and Q-point effects in finite structures.

Chapter 5. includes the theory of magnetoexciton absorption for mDf model. The description starts with a single particle approach in section 5.1, which includes a discussion of a modification of Landau level (LLs) energy spectrum for mDf in comparison to free electron LL spectrum. Section 5.1 also includes a description of the effects of spin-orbit coupling on the spectrum and finally discusses the interaction of mDf in LLs with light. Section 5.2 introduces interaction between mDf in LLs with a detailed description of the Coulomb scattering terms and the exciton Hamil-

tonian, followed by the discussion of the results on valley Zeeman splitting and the magnetoexciton absorption spectrum.

A theory of electronic properties of gated MoS_2 QDs is presented in chapter 6. It is divided in four sections. The first two sections describe the tight-binding model for a QD and the resulting single particle energy spectrum associated with valleys and $Q-$points. Sections 6.3 and 6.4 discuss the interacting effects in MoS_2 QDs, starting with a detailed description of scattering Coulomb matrix elements, which include the distinction between intervalley and intravalley contributions. Section 6.4 discusses the interplay of different single particle and interacting energy scales contributing to valley and spin polarised states for two interacting electrons as well as strongly-correlated broken-symmetry ground states of up to six electrons in gated MoS_2 QDs. Possible verification of the signatures of these states in experiment is also discussed.

Chapter 2

Methodology

This chapter focuses on all methodology used in this thesis. Section 2.1 discusses treatment of a single electron in a solid and it follows with section 2.2, which is dedicated to solving the many-body Hamiltonian for crystals.

2.1 Single particle picture.

Solids contain many atoms closely packed together in a geometrical lattice, building a structure of large complexity. These atoms, containing many electrons, make it impossible to solve exactly for properties of a solid. An approximation is therefore needed. It is useful to start with a single atom solution and then, account for the change in these electronic levels as other atoms are placed close to the original atom. A practical assumption about the wavefunction of a few-atom molecule is to treat it as a linear combination of atomic orbitals (LCAO), which has been described in section 2.1.1. This approximation is then used to form band theory of solids using the tight-binding method, as described in 2.1.2.

2.1.1 Linear combination of atomic orbitals wavefunction.

To solve for electronic states of a molecule, we can use the eigenstates of a single atom potential and account for a modified energy potential of several atoms placed close together, as shown in Fig. 2.1 a)-b). What follows is an example of the approach for

a diatomic molecule. Let us assume that the single atom solutions are:

$$\hat{H}_{at}\phi_n(\boldsymbol{r}) = e_n\phi_n(\boldsymbol{r}), \tag{2.1}$$

where n labels energy levels e_n of an isolated atom with eigenstates ϕ_n, such as $1s, 2s, 2p_x$ etc. (an example of a spectrum shown in Fig. 2.1 a)) and $\hat{H}_{at} = -\frac{\hbar^2}{2m}\nabla^2 + \hat{V}_{at}(\boldsymbol{r})$ is a single atom Hamiltonian. Now, we consider two ideantical atoms a, b placed close together to form a molecular potential shown in Fig. 2.1 b). The Hamiltonian for a single electron in the molecule reads

$$\hat{H} = -\frac{\hbar^2}{2m}\nabla^2 + \hat{V}_a(\boldsymbol{r}) + \hat{V}_b(\boldsymbol{r}), \tag{2.2}$$

where $\hat{V}_{a/b}(\boldsymbol{r}) = \hat{V}_{at}(\boldsymbol{r} - \boldsymbol{R}_{a/b})$ for a potential centred on $\boldsymbol{R}_{a/b}$. To search for the solutions of the Hamiltonian in Eq. 2.2 we assume a trial LCAO wavefunction made of the atomic orbitals n for atom a, identical to orbitals on atom b. I will assume one orbital per atom for simplicity. The LCAO wavefunction in *bracket* notation reads

$$|\psi(\boldsymbol{r})\rangle = c_a\,|\phi_a(\boldsymbol{r})\rangle + c_b\,|\phi_b(\boldsymbol{r})\rangle = \begin{pmatrix} c_a \\ \\ c_b \end{pmatrix}, \tag{2.3}$$

where ϕ_a (ϕ_b) is a single atomic orbital on atom a (b) and c_a (c_b) are coefficients of the LCAO molecular wavefunction on atom a (b) and the LCAO wavefunction is a two component vector in the basis of the atomic orbitals a, b.

We now look for the form of the Hamiltonian in Eq. 2.2 in the basis of the atomic orbitals. Let us consider a diagonal term

$$\begin{aligned} \langle\phi_a|\,\hat{H}\,|\phi_a\rangle &= \langle\phi_a|\left(-\frac{\hbar^2}{2m}\nabla^2 + \hat{V}_a + \hat{V}_b\right)|\phi_a\rangle \\ &= e_a + \langle\phi_a|\,\hat{V}_b\,|\phi_a\rangle = e_a + \delta_a, \end{aligned} \tag{2.4}$$

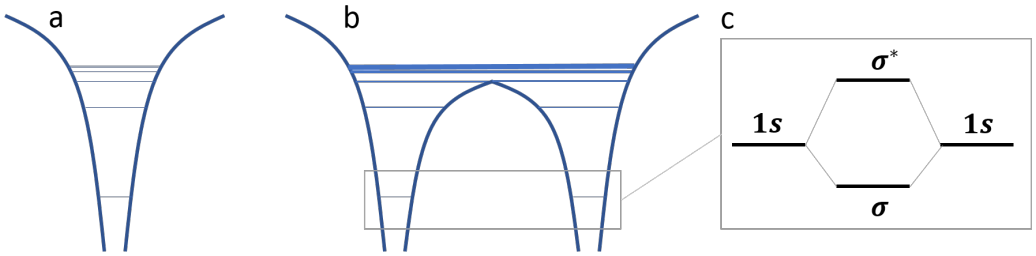

Figure 2.1: a) Potential of a single atom. Horizontal lines denote energy levels. b) Total potential formed by two atoms placed close together. The energy levels of a single atom are modified by the presence of the second potential. c) Close up view of the lowest molecular energy levels . The 1s orbitals from both atoms split and form bonding and antibonding states (σ and σ^* respectively) given by Eq. 2.7 and Eq. 2.8.

where $\hat{V}_b$ shifts the energy of the atom a by δ_a. The off-diagonal term reads

$$\begin{aligned} \langle\phi_a|\,\hat{H}\,|\phi_b\rangle &= \langle\phi_a|\left(-\frac{\hbar^2}{2m}\nabla^2+\hat{V}_a+\hat{V}_b\right)|\phi_b\rangle \\ &= e_b\langle\phi_a|\phi_b\rangle+\langle\phi_a|\,\hat{V}_a\,|\phi_b\rangle = e_b s_{ab}+t_{ab}=\tau, \end{aligned} \tag{2.5}$$

where $s_{ab}=\langle\phi_a|\phi_b\rangle$ is the overlap of the basis atomic wavefunctions and t_{ab} is called a hopping integral. The eigenvalue problem for $\hat{H}$ reads

$$\hat{H}\psi=\begin{pmatrix} e & \tau \\ \tau & e \end{pmatrix}\psi = E\begin{pmatrix} 1 & s_{ab} \\ s_{ab} & 1 \end{pmatrix} = ES\psi, \tag{2.6}$$

where S is the the overlap matrix and $e_a+\delta_a=e_b+\delta_b=e$. The solutions of the generalised eigenvalue problem in Eq. 2.6 are

$$\begin{aligned} E_\sigma &= \frac{e+\tau}{1+s_{ab}}, \\ E_{\sigma^*} &= \frac{e-\tau}{1-s_{ab}}, \end{aligned} \tag{2.7}$$

where E_σ (E_{σ^*}) is the bonding (anti-bonding) energy shown in Fig. 2.1 c). The

corresponding wavefunctions are

$$\begin{aligned}\psi_\sigma &= \frac{1}{\sqrt{2(1+s_{ab})}}\begin{pmatrix}1\\1\end{pmatrix},\\ \psi_{\sigma^*} &= \frac{1}{\sqrt{2(1+s_{ab})}}\begin{pmatrix}1\\-1\end{pmatrix},\end{aligned} \tag{2.8}$$

shown schematically in Fig. 2.1. It is apparent that single atom solutions are different from the two-atom case.

2.1.2 Tight-binding approximation.

The LCAO wavefunction can be used to solve for properties of a variety of materials, made of many atoms. Often, a tight-binding (TB) approximation can be employed. It is well suited to materials with negligible overlap between atoms, so that $S \approx \mathbb{1}$ in Eq. 2.6. This means that electrons are tightly bound to atoms and are less likely to localise in the space between sites than on sites. An example of a TB calculation for a finite crystalline structure has been shown in section 2.1.7 for a graphene quantum dot.

Periodic structures can be treated with the TB model as well. For an infinite crystal, the potential created by many atoms is periodic, $V(\boldsymbol{r}) = V(\boldsymbol{r}+\boldsymbol{R})$, where $\boldsymbol{R}$ defines the periodicity of the lattice. The TB wavefunction for a crystal is written as a LCAO wavefunction and it reads

$$\begin{aligned}\psi_{\boldsymbol{k}} &= \sum_{\boldsymbol{R}} e^{i\boldsymbol{k}\boldsymbol{R}}\phi(\boldsymbol{r}-\boldsymbol{R})\\ &= e^{i\boldsymbol{k}\boldsymbol{r}}\sum_{\boldsymbol{R}} e^{-i\boldsymbol{k}(\boldsymbol{r}-\boldsymbol{R})}\phi(\boldsymbol{r}-\boldsymbol{R})\\ &= e^{i\boldsymbol{k}\boldsymbol{r}}u_{\boldsymbol{k}}(\boldsymbol{r}),\end{aligned} \tag{2.9}$$

where $u_{\boldsymbol{k}}$ is the periodic part of the wavefunction and $\phi(\boldsymbol{r}-\boldsymbol{R})$ is an orbital in unit cel $\boldsymbol{R}$. The TB wavefunction in Eq. 2.9 obeys Bloch's theorem [129], which states

that electron's wavefunctions in a periodic potential can be expressed as a plane wave modulated by a periodic function $u_{\boldsymbol{k}}$. The eigenvalues of a periodic crystal will carry the index $\boldsymbol{k}$, the wavevector, which creates energy bands with dispersion in $\boldsymbol{k}$. An example of a TB treatment for an infinite crystal has been shown in section 2.1.3 for a monolayer graphene.

2.1.3 Example of a tight-binding calculation: bulk graphene.

Graphene is a single layer of carbon atoms arranged in a honeycomb pattern. Each carbon atom has 6 electrons, two of which are $1s$ electrons, strongly confined to the carbon nucleus. They are referred to as core electrons and do not contribute to the properties of graphene as much as valence electrons. Three of these valence electrons occupy $2s$,$2p_x$ and $2p_y$ orbitals, which form hybridised sp^2 bonds, connecting a carbon atom to its three nearest neighbours (NN). These σ bonds are strong and are responsible for unusual mechanical properties of graphene. The last electron occupies a p_z orbital, which extends out of the crystal plane. These electrons from all the carbon atoms form π bonds of highly mobile electrons, which determine the electronic properties of graphene.

I will show here how to build a TB model of monolayer graphene with one valence electron on the p_z orbital of a carbon atom. Graphene lattice is a honeycomb lattice, which is not a Bravais lattice, since two lattice sites need to be translated together to form the structure. Instead, graphene can be treated as two interpenetrating triangular sublattices with one-atom basis, which are Bravais lattices. Both sublattices, shifted with respect to each other by $\boldsymbol{b} = \frac{a}{\sqrt{3}}(0,1)$, are built with vectors:

$$\begin{aligned} \boldsymbol{a_1} &= a(-\frac{1}{2}, \frac{\sqrt{3}}{2}), \\ \boldsymbol{a_2} &= a(\frac{1}{2}, \frac{\sqrt{3}}{2}), \end{aligned} \tag{2.10}$$

where a is the sublattice constant $a = 2.46$Å (all vectors shown in Fig. 2.2). For

integer n & m, vectors $\boldsymbol{R_A}$ & $\boldsymbol{R_B}$ represent lattice sites in sublattices A & B

$$\boldsymbol{R}_A = n\boldsymbol{a_1} + m\boldsymbol{a_2}. \tag{2.11}$$

Vector $\boldsymbol{R}_A$ gives atom positions in sublattice A, while vector $\boldsymbol{R}_B = \boldsymbol{R}_A + \boldsymbol{b} = n\boldsymbol{a_1} + m\boldsymbol{a_2} + \boldsymbol{b}$. gives the positions of atoms in B (Fig. 2.2.).

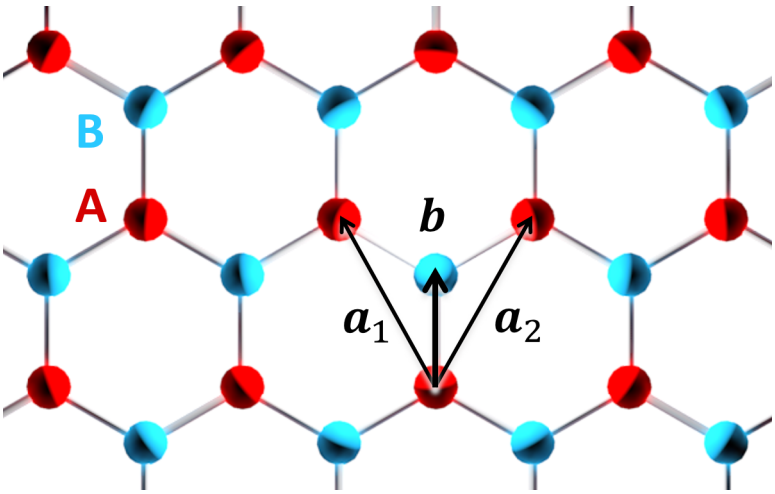

Figure 2.2: Vectors $\boldsymbol{a}_1$, $\boldsymbol{a}_2$ & $\boldsymbol{b}$, building sublattices A & B.

Translational symmetry imposes the commutation of the Hamiltonian with the operator of translation by $\boldsymbol{R}_A$. Thus, the eigenvectors of electrons in sublattices A & B must be the eigenvectors of the translation operator

$$\begin{aligned} \hat{T}_{\boldsymbol{R}_A}\psi_A^{\boldsymbol{k}}(\boldsymbol{r}) &= \psi_A^{\boldsymbol{k}}(\boldsymbol{r} - \boldsymbol{R}_A) \\ \hat{T}_{\boldsymbol{R}_A}\psi_B^{\boldsymbol{k}}(\boldsymbol{r}) &= \psi_B^{\boldsymbol{k}}(\boldsymbol{r} - \boldsymbol{R}_A), \end{aligned} \tag{2.12}$$

where $\boldsymbol{k}$ is wave vector. The wavefunctions must then obey the Bloch theorem, i.e.

$$\begin{aligned} \psi_A^{\boldsymbol{k}}(\boldsymbol{r} - \boldsymbol{R}_A) &= e^{i\boldsymbol{k}\boldsymbol{R}_A}\psi_A^{\boldsymbol{k}}(\boldsymbol{r}), \\ \psi_B^{\boldsymbol{k}}(\boldsymbol{r} - \boldsymbol{R}_A) &= e^{i\boldsymbol{k}\boldsymbol{R}_A}\psi_B^{\boldsymbol{k}}(\boldsymbol{r}). \end{aligned} \tag{2.13}$$

Therefore, we may express the wavefunctions as LCAO Bloch wavefunctions

$$\begin{aligned}\psi_A^{\boldsymbol{k}}(\boldsymbol{r}) &= \frac{1}{\sqrt{N}}\sum_{\boldsymbol{R}_A} e^{i\boldsymbol{k}\boldsymbol{R}_A}\phi^A(\boldsymbol{r}-\boldsymbol{R}_A) = e^{i\boldsymbol{k}\boldsymbol{r}}u_{\boldsymbol{k}}^A(\boldsymbol{r}) \\ \psi_B^{\boldsymbol{k}}(\boldsymbol{r}) &= \frac{1}{\sqrt{N}}\sum_{\boldsymbol{R}_B} e^{i\boldsymbol{k}\boldsymbol{R}_B}\phi^B(\boldsymbol{r}-\boldsymbol{R}_B) = e^{i\boldsymbol{k}\boldsymbol{r}}u_{\boldsymbol{k}}^B(\boldsymbol{r})\end{aligned} \tag{2.14}$$

where $\phi^A(\boldsymbol{r}-\boldsymbol{R}_A)$ is wavefunction of a p_z electron localised on the atom of the cell identified by $\boldsymbol{R}_A$ for sublattice A (and analogously for sublattice B), N is the number of unit cells in the sublattice and $u_{\boldsymbol{k}}^{A/B}(\boldsymbol{r})$ is a periodic function of the Bloch wavefunction. The wavefunction of the whole system is a linear combination of the sublattice wavefunctions

$$\psi^{\boldsymbol{k}}(\boldsymbol{r}) = A_{\boldsymbol{k}}\psi_A^{\boldsymbol{k}}(\boldsymbol{r}) + B_{\boldsymbol{k}}\psi_B^{\boldsymbol{k}}(\boldsymbol{r}), \tag{2.15}$$

where $\psi_A^{\boldsymbol{k}}$ & $\psi_B^{\boldsymbol{k}}$ are given in Eq. 2.14, which gives

$$\psi^{\boldsymbol{k}}(\boldsymbol{r}) = A_{\boldsymbol{k}}\frac{1}{\sqrt{N}}\sum_{\boldsymbol{R}_A} e^{i\boldsymbol{k}\boldsymbol{R}_A}\phi^A(\boldsymbol{r}-\boldsymbol{R}_A) + B_{\boldsymbol{k}}\frac{1}{\sqrt{N}}\sum_{\boldsymbol{R}_B} e^{i\boldsymbol{k}\boldsymbol{R}_B}\phi^B(\boldsymbol{r}-\boldsymbol{R}_B), \tag{2.16}$$

and I will search for a wavefunction solution in a spinor form

$$\psi^{\boldsymbol{k}} = \begin{pmatrix} A_{\boldsymbol{k}} \\ B_{\boldsymbol{k}} \end{pmatrix}. \tag{2.17}$$

The single-particle Hamiltonian reads

$$\hat{H} = \frac{\hat{p}^2}{2m} + \sum_{\boldsymbol{R}_A}[V^A(\boldsymbol{r}-\boldsymbol{R}_A)] + \sum_{\boldsymbol{R}_B}[V^B(\boldsymbol{r}-\boldsymbol{R}_B)], \tag{2.18}$$

where $\frac{\hat{p}^2}{2m}$ is a single electron's kinetic energy, $V^A(\boldsymbol{r}-\boldsymbol{R}_A)$ & $V^B(\boldsymbol{r}-\boldsymbol{R}_B)$ are potentials on the lattice sites given by $\boldsymbol{R}_A$ & $\boldsymbol{R}_B$. The diagonal matrix element of the

Hamiltonian $\hat{H}$ given in Eq. 2.18 in the basis of $\psi_A^{\boldsymbol{k}}(\boldsymbol{r})$ and $\psi_B^{\boldsymbol{k}}(\boldsymbol{r})$ is then

$$\begin{aligned}\left\langle \psi_A^{\boldsymbol{k}} \right| \hat{H} \left| \psi_A^{\boldsymbol{k}} \right\rangle = \left\langle \psi_A^{\boldsymbol{k}} \right| \frac{\hat{p}^2}{2m} + \sum_{\boldsymbol{R}_A} V^A(\boldsymbol{r} - \boldsymbol{R}_A) \left| \psi_A^{\boldsymbol{k}} \right\rangle \\ + \left\langle \psi_A^{\boldsymbol{k}} \right| \sum_{\boldsymbol{R}_B} V^B(\boldsymbol{r} - \boldsymbol{R}_B) \left| \psi_A^{\boldsymbol{k}} \right\rangle\end{aligned} \tag{2.19}$$

and analogously for the $\psi_B^{\boldsymbol{k}}$ diagonal element. The first term in the expression in Eq. 2.19 gives energy of sublattice A E_A, because $\psi_A^{\boldsymbol{k}}$ is an eigenstate of $\frac{\hat{p}^2}{2m} + \sum_{\boldsymbol{R}_A} V^A(\boldsymbol{r} - \boldsymbol{R}_A)$. The last term in Eq. 2.19 describes an electron's hopping from A to A sites. As the NN of A sites are always B sites (as shown in Fig. 2.3), this term accounts for next-nearest neighbour (NNN) and further neighbour hopping and is smaller than NN terms, so I will neglect it for now.

I now calculate the expressions for the off-diagonal terms of the Hamiltonian. The first part is $\left\langle \psi_B^{\boldsymbol{k}} \right| \frac{\hat{p}^2}{2m} + \sum_{\boldsymbol{R}_A} V^A(\boldsymbol{r} - \boldsymbol{R}_A) \left| \psi_A^{\boldsymbol{k}} \right\rangle = E_A \langle \psi_B^{\boldsymbol{k}} | \psi_A^{\boldsymbol{k}} \rangle$, which vanishes if I assume zero overlap. The remaining part is

$$\begin{aligned}&\left\langle \psi_B^{\boldsymbol{k}} \right| \sum_{\boldsymbol{R}'_B} [V^B(\boldsymbol{r} - \boldsymbol{R}'_B)] \left| \psi_A^{\boldsymbol{k}} \right\rangle = \\ &\quad = \frac{1}{N} \cdot \sum_{\boldsymbol{R}_A, \boldsymbol{R}_B} e^{i\boldsymbol{k}(\boldsymbol{R}_A - \boldsymbol{R}_B)} \sum_{\boldsymbol{R}'_B} \left\langle \phi^B(\boldsymbol{r} - \boldsymbol{R}_B) \right| V^B(\boldsymbol{r} - \boldsymbol{R}'_B) \left| \phi^A(\boldsymbol{r} - \boldsymbol{R}_A) \right\rangle \\ &\quad = \frac{1}{N} \cdot \sum_{\boldsymbol{R}_A, \boldsymbol{R}_B} e^{i\boldsymbol{k}(\boldsymbol{R}_A - \boldsymbol{R}_B)} \left\langle \phi^B(\boldsymbol{r} - \boldsymbol{R}_B) \right| V^B(\boldsymbol{r} - \boldsymbol{R}_B) \left| \phi^A(\boldsymbol{r} - \boldsymbol{R}_A) \right\rangle \\ &\quad = \frac{1}{N} \cdot \sum_{<\boldsymbol{R}_A, \boldsymbol{R}_B>} e^{i\boldsymbol{k}(\boldsymbol{R}_A - \boldsymbol{R}_B)} \left\langle \phi^B(\boldsymbol{r} - \boldsymbol{R}_B) \right| V^B(\boldsymbol{r} - \boldsymbol{R}_B) \left| \phi^A(\boldsymbol{r} - \boldsymbol{R}_A) \right\rangle \\ &= \frac{1}{N} \cdot N \cdot t(e^{i\boldsymbol{k}\boldsymbol{R}_{AB_1}} + e^{i\boldsymbol{k}\boldsymbol{R}_{AB_2}} + e^{i\boldsymbol{k}\boldsymbol{R}_{AB_3}}) = t \cdot e^{i\boldsymbol{k}\boldsymbol{b}}(1 + e^{-i\boldsymbol{k}\boldsymbol{a}_1} + e^{-i\boldsymbol{k}\boldsymbol{a}_2}),\end{aligned} \tag{2.20}$$

where the three-body integrals ($\boldsymbol{R}_B \neq \boldsymbol{R}'_B$) were neglected and the last summation is approximately restricted to only the B sites that are NN of sites A. In the expression in Eq. 2.20

$$t = \left\langle \phi^B(\boldsymbol{r} - \boldsymbol{R}_A - \boldsymbol{R}_{AB1}) \right| V^B(\boldsymbol{r} - \boldsymbol{R}_A - \boldsymbol{R}_{AB1}) \left| \phi^A(\boldsymbol{r} - \boldsymbol{R}_A) \right\rangle \tag{2.21}$$

is the NN hopping-term for $\boldsymbol{R}_A - \boldsymbol{R}_B$. In Eq. 2.20 I used

$$\begin{aligned} \boldsymbol{R}_{AB1} &= \boldsymbol{b}, \\ \boldsymbol{R}_{AB2} &= \boldsymbol{b} - \boldsymbol{a}_2, \\ \boldsymbol{R}_{AB3} &= \boldsymbol{b} - \boldsymbol{a}_1, \end{aligned} \tag{2.22}$$

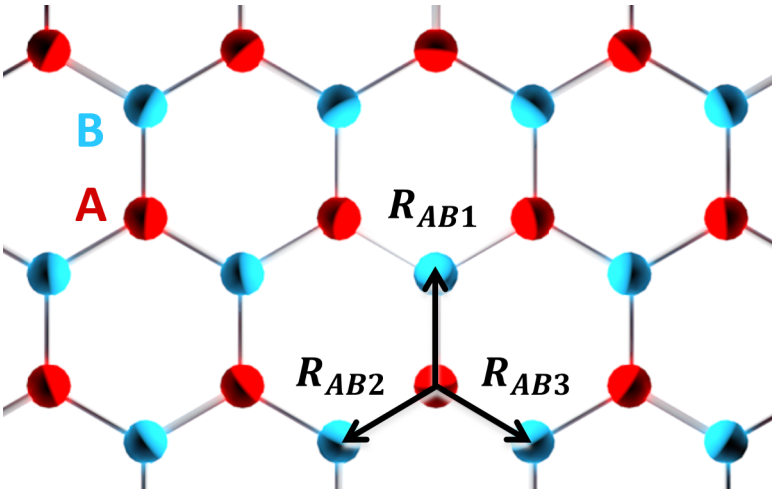

Figure 2.3: Red (blue) atoms depict the sublattice A (B). Three NN vectors R_{ABi} defined in Eq. 2.22 are shown here.

Finally, for $E_A = E_B = 0$, the eigenvalue problem for the system in the matrix form reads

$$\begin{pmatrix} 0 & t \cdot e^{i\boldsymbol{k}\boldsymbol{b}}(1 + e^{-i\boldsymbol{k}\boldsymbol{a}_1} + e^{-i\boldsymbol{k}\boldsymbol{a}_2}) \\ t \cdot e^{-i\boldsymbol{k}\boldsymbol{b}}(1 + e^{i\boldsymbol{k}\boldsymbol{a}_1} + e^{i\boldsymbol{k}\boldsymbol{a}_2}) & 0 \end{pmatrix} \begin{pmatrix} A_{\boldsymbol{k}} \\ B_{\boldsymbol{k}} \end{pmatrix} = E_{\boldsymbol{k}} \begin{pmatrix} A_{\boldsymbol{k}} \\ B_{\boldsymbol{k}} \end{pmatrix}. \tag{2.23}$$

After diagonalising we obtain

$$E_{\boldsymbol{k}}^{\pm} = \pm |t||f(\boldsymbol{k})|, \tag{2.24}$$

where $f(\boldsymbol{k}) = e^{i\boldsymbol{k}\boldsymbol{b}}(1 + e^{-i\boldsymbol{k}\boldsymbol{a}_1} + e^{-i\boldsymbol{k}\boldsymbol{a}_2})$ and

$$|f(\boldsymbol{k})| = \sqrt{3 + 2\cos(\boldsymbol{k}\boldsymbol{a}_1) + 2\cos(\boldsymbol{k}\boldsymbol{a}_2) + 2\cos(\boldsymbol{k}(\boldsymbol{a}_2 - \boldsymbol{a}_1))}. \tag{2.25}$$

The spinor eigenvectors corresponding to $E_{\boldsymbol{k}}^{\pm}$ read

$$\begin{pmatrix} A_{\boldsymbol{k}} \\ B_{\boldsymbol{k}} \end{pmatrix} = \begin{pmatrix} 1 \\ \pm e^{i\theta_{\boldsymbol{k}}} \end{pmatrix} \tag{2.26}$$

The obtained energy dispersion has been shown in Fig. 2.24. In the π band, which we considered, there exists one electron per atom. Because of the possible double occupancy for each orbital π the band is half-filled. As a consequence, the Fermi level is located exactly in the point shared by valence band (VB) and conduction band (CB), for $E = 0$, which are called $\boldsymbol{K}$ & $-\boldsymbol{K}$ and are the corners of graphene's hexagonal Brillouin zone (BZ) (discussed further in section 2.1.4). This makes graphene a semi-metal.

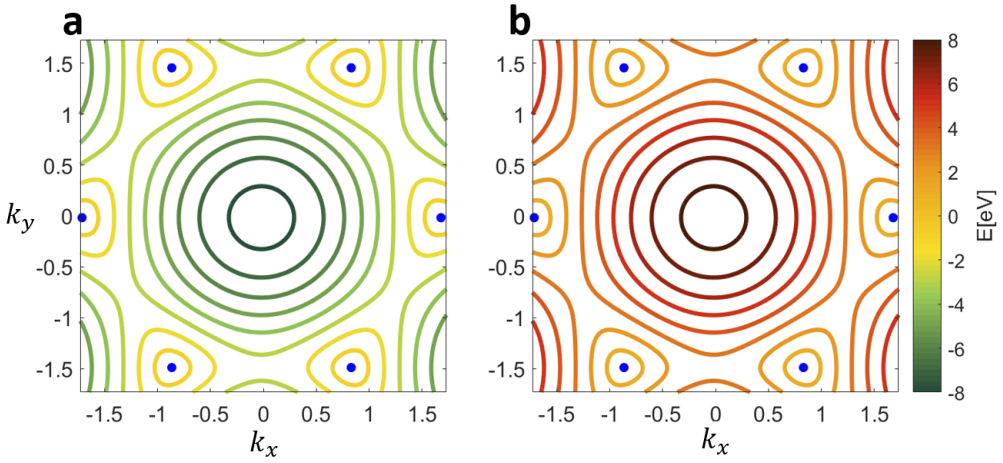

Figure 2.4: Energy dispersion of the π band for graphene in the NN approximation for a) VB and b) CB. Colors encode the energy. Blue dots mark the corners of the BZ $\boldsymbol{K}$ & $-\boldsymbol{K}$. Mirror symmetry of both bands is apparent.

Importantly, the energy dispersion given in Eq. 2.41 is symmetric w.r.t. $E = 0$ plane. This is due to the NN approximation. The NNN hopping introduces an additional term which breakes this symmetry, which is explained in what follows.

Considering NNN means including the last term in the diagonal element of the

Hamiltonian in Eq. 2.19. The term reads

$$\begin{aligned}
&\frac{1}{N}\sum_{\boldsymbol{R}_A,\boldsymbol{R}'_A\neq\boldsymbol{R}_A,\boldsymbol{R}_B} e^{i\boldsymbol{k}(\boldsymbol{R}_A-\boldsymbol{R}'_A)}\left\langle\phi^A(\boldsymbol{r}-\boldsymbol{R}'_A)\right|V^B(\boldsymbol{r}-\boldsymbol{R}_B)\left|\phi^A(\boldsymbol{r}-\boldsymbol{R}_A)\right\rangle \\
&\quad=\frac{1}{N}\cdot\sum_{<<\boldsymbol{R}_A,\boldsymbol{R}'_A>>} e^{i\boldsymbol{k}(\boldsymbol{R}_A-\boldsymbol{R}'_A)}\left\langle\phi^A(\boldsymbol{r}-\boldsymbol{R}'_A)\right|\sum_{\boldsymbol{R}_B}V^B(\boldsymbol{r}-\boldsymbol{R}_B)\left|\phi^A(\boldsymbol{r}-\boldsymbol{R}_A)\right\rangle \\
&\quad=\frac{1}{N}\cdot N\cdot t_2(e^{i\boldsymbol{k}\boldsymbol{R}_{AA_1}}+e^{i\boldsymbol{k}\boldsymbol{R}_{AA_2}}+e^{i\boldsymbol{k}\boldsymbol{R}_{AA_3}}+e^{i\boldsymbol{k}\boldsymbol{R}_{AA_4}}+e^{i\boldsymbol{k}\boldsymbol{R}_{AA_5}}+e^{i\boldsymbol{k}\boldsymbol{R}_{AA_6}}) \\
&\quad=t_2(e^{i\boldsymbol{k}\boldsymbol{a}_2}+e^{i\boldsymbol{k}\boldsymbol{a}_1}+e^{-i\boldsymbol{k}(\boldsymbol{a}_2-\boldsymbol{a}_1)}+e^{-i\boldsymbol{k}\boldsymbol{a}_2}+e^{-i\boldsymbol{k}\boldsymbol{a}_1}+e^{i\boldsymbol{k}(\boldsymbol{a}_2-\boldsymbol{a}_1)}),
\end{aligned}\tag{2.27}$$

and analogously for sublattice B. In the expression in Eq. 2.27 only the NNN terms were included and further neighbours were neglected. In Eq. 2.27

$$t_2=\left\langle\phi^A(\boldsymbol{r}-\boldsymbol{R}_A-\boldsymbol{R}_{AA1})\right|\sum_{\boldsymbol{R}_B}V_B(\boldsymbol{r}-\boldsymbol{R}_B)\left|\phi^A(\boldsymbol{r}-\boldsymbol{R}_A)\right\rangle \tag{2.28}$$

is the NNN hopping integral and the NNN vectors are

$$\begin{aligned}
\boldsymbol{R}_{AA1}&=\boldsymbol{a}_2,\\
\boldsymbol{R}_{AA2}&=\boldsymbol{a}_1,\\
\boldsymbol{R}_{AA3}&=\boldsymbol{a}_1-\boldsymbol{a}_2,\\
\boldsymbol{R}_{AA4}&=-\boldsymbol{a}_2,\\
\boldsymbol{R}_{AA5}&=-\boldsymbol{a}_1,\\
\boldsymbol{R}_{AA6}&=\boldsymbol{a}_2-\boldsymbol{a}_1.
\end{aligned}\tag{2.29}$$

Therefore, the Hamiltonian in the matrix form reads

$$\begin{pmatrix} t_2\cdot g(\boldsymbol{k}) & t\cdot f(\boldsymbol{k}) \\ t^*\cdot f^*(\boldsymbol{k}) & t_2\cdot g(\boldsymbol{k})\end{pmatrix}\begin{pmatrix}A_{\boldsymbol{k}}\\ B_{\boldsymbol{k}}\end{pmatrix}=E_{\boldsymbol{k}}\begin{pmatrix}A_{\boldsymbol{k}}\\ B_{\boldsymbol{k}}\end{pmatrix}. \tag{2.30}$$

where

$$f(\boldsymbol{k})=e^{i\boldsymbol{k}\boldsymbol{b}}(1+e^{-i\boldsymbol{k}\boldsymbol{a}_1}+e^{-i\boldsymbol{k}\boldsymbol{a}_2}), \tag{2.31}$$

$$g(\boldsymbol{k})=2\cos(\boldsymbol{k}\boldsymbol{a}_1)+2\cos(\boldsymbol{k}\boldsymbol{a}_2)+2\cos\Big(\boldsymbol{k}(\boldsymbol{a}_2-\boldsymbol{a}_1)\Big). \tag{2.32}$$

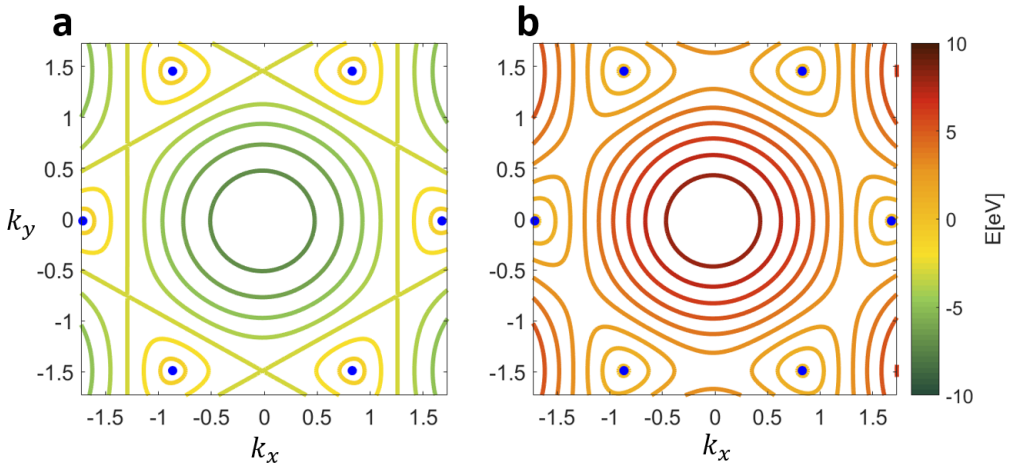

Figure 2.5: Energy dispersion for the NNN approximation for a) VB and b) CB. Colors have the same meaning as in Fig. 2.4 The mirror symmetry of CB and VB has been broken.

After diagonalising we obtain

$$E_{\boldsymbol{k}}^{\pm} = t_2 g(\boldsymbol{k}) \pm t|f(\boldsymbol{k})| = t_2 g(\boldsymbol{k}) \pm t\sqrt{3 + g(\boldsymbol{k})}. \tag{2.33}$$

The energy dispersion has been shown in Fig. 2.5.

2.1.4 Massless Dirac fermions: low energy spectrum of graphene.

In order to describe low energy dispersion for graphene we need to determine the location in the $\boldsymbol{k}$-space where the energy gap closes. These points, $\boldsymbol{K}$ & $-\boldsymbol{K}$ (shown in Fig. 2.6), mark the two nonequivalent corners of the hexagonal Brillouin zone of the honeycomb lattice. Because the gap closes at $\boldsymbol{K}$ & $-\boldsymbol{K}$, we can write

$$\begin{aligned} f(\boldsymbol{K}) &= 1 + e^{-i\boldsymbol{K}\boldsymbol{a}_1} + e^{-i\boldsymbol{K}\boldsymbol{a}_2} = 0, \\ f^*(\boldsymbol{K}) &= 1 + e^{i\boldsymbol{K}\boldsymbol{a}_1} + e^{i\boldsymbol{K}\boldsymbol{a}_2} = 0, \end{aligned} \tag{2.34}$$

which gives

$$\begin{aligned} e^{-i\boldsymbol{K}\boldsymbol{a}_2} &= 1 + e^{-i\boldsymbol{K}\boldsymbol{a}_1}, \\ e^{i\boldsymbol{K}\boldsymbol{a}_1} &= 1 + e^{i\boldsymbol{K}\boldsymbol{a}_2}. \end{aligned} \tag{2.35}$$

Multiplying both equations above by their conjugates we get

$$\begin{aligned} \boldsymbol{K}\boldsymbol{a}_1 &= \pm\frac{2\pi}{3} + 2\pi m, \\ \boldsymbol{K}\boldsymbol{a}_2 &= \mp\frac{2\pi}{3} + 2\pi n. \end{aligned} \tag{2.36}$$

Taking into account the choice of basis vectors given in Eq. 2.10 and solving the equations Eq. 2.36, we obtain

$$\begin{aligned} K_x &= \frac{2\pi}{a}(\pm\frac{2}{3} + (m-n)), \\ K_y &= \frac{2\pi(m+n)}{a\sqrt{3}}. \end{aligned} \tag{2.37}$$

For any (m, n) we get

$$\boldsymbol{K} = (\pm\frac{2}{3}, 0) \qquad \text{or } \boldsymbol{K} = (\pm\frac{1}{3}, \pm\frac{\sqrt{3}}{3}) \tag{2.38}$$

in the units of $2\pi/a$. It is important to state that two of these $\boldsymbol{K}$ points are inequivalent and the rest can be obtained by translating these two points by the reciprocal space vectors $\boldsymbol{G}_1$ & $\boldsymbol{G}_2$ (shown in Fig. 2.6).

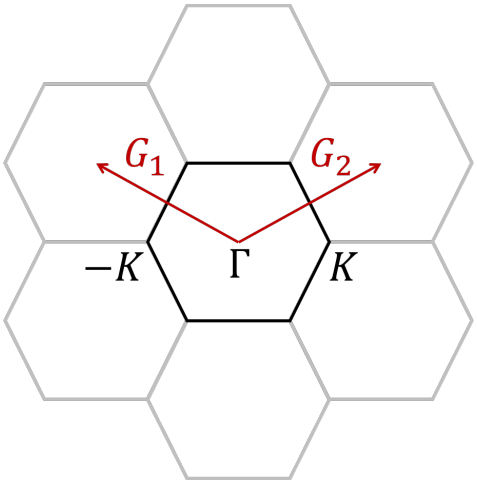

Figure 2.6: 1st BZ for graphene. $\boldsymbol{K}$ and $-\boldsymbol{K}$ mark two inequivalent corners, and Γ is the centre of the BZ. Vectors $\boldsymbol{G}_1$ and $\boldsymbol{G}_2$ are the reciprocal lattice vectors.

Let us now consider the energy dispersion in the proximity of $\boldsymbol{K}$ & $-\boldsymbol{K}$ for small $\boldsymbol{q}$, so that $\boldsymbol{k} = \boldsymbol{K} + \boldsymbol{q}$. We then expand expression in Eq. 2.34 as a Taylor series with

only linear terms. Using Eq. 2.36 we obtain

$$\begin{aligned} f(\boldsymbol{k}) = f(\pm\boldsymbol{K}+\boldsymbol{q}) &= 1 + e^{\mp i\boldsymbol{K}\boldsymbol{a}_1}e^{-i\boldsymbol{q}\boldsymbol{a}_1} + e^{\mp i\boldsymbol{K}\boldsymbol{a}_2}e^{-i\boldsymbol{q}\boldsymbol{a}_2} = \\ &= -i\boldsymbol{q}\boldsymbol{a}_1 e^{\mp i\boldsymbol{K}\boldsymbol{a}_1} - i\boldsymbol{q}\boldsymbol{a}_2 e^{\mp i\boldsymbol{K}\boldsymbol{a}_2} \\ &= \frac{\sqrt{3}}{2}a(\mp q_x + iq_y) \end{aligned} \tag{2.39}$$

and $e^{i\boldsymbol{k}\boldsymbol{b}} = 1$ to the first order in $\boldsymbol{q}$ because $\boldsymbol{K}\cdot\boldsymbol{b} = 0$. Note that for a lattice rotated by 90°, the final expression in Eq. 2.39 would be $f(\boldsymbol{k}) = \frac{\sqrt{3}}{2}a(iq_x \pm q_y)$ due to rotated unit vectors $\boldsymbol{a}_{1/2}$. The linear expansion of the expression given by Eq. 2.32 produces a constant in both diagonal elements, shifting the spectrum only. I therefore neglect them. The expression given by Eq. 2.30 for small $\boldsymbol{q}$ around $\boldsymbol{K}$ point reads

$$|t|\begin{pmatrix} 0 & f_-(\boldsymbol{K}+\boldsymbol{q}) \\ f_-^*(\boldsymbol{K}+\boldsymbol{q}) & 0 \end{pmatrix} = |t|\begin{pmatrix} 0 & \frac{\sqrt{3}}{2}a(q_x - iq_y) \\ \frac{\sqrt{3}}{2}a(q_x + iq_y) & 0 \end{pmatrix} = v_f\boldsymbol{q}\cdot\boldsymbol{\sigma}, \tag{2.40}$$

where $\frac{v_f}{\hbar}$ is Fermi's velocity for graphene and $\boldsymbol{sigma}$ is Pauli matrix vector. Eq. 2.40 has a form of the Dirac equation for massless particles (zero on diagonal), which shows the relativistic nature of the carriers close to $\boldsymbol{K}$ and for low energies. We get the solutions

$$E = \pm|t||f(\boldsymbol{K}+\boldsymbol{q})| = \pm v_f|\boldsymbol{q}|. \tag{2.41}$$

This linear dispersion is characteristic for massless Dirac particles and has been shown in Fig. 2.7. This is the reason the corners of BZ are called the Dirac points and the shape of the energy dispersion - a Dirac cone. This expansion is true only close to the $\boldsymbol{K}$ points and only for low energies. High-energy parts of the bands significantly differ from this behaviour.

2.1.5 Massive Dirac fermions: gapped graphene.

I will now show how to enable gap opening in graphene at $\boldsymbol{K}$. If the atoms on the sublattices A and B have different energies (e.g. from a hBN substrate material), one

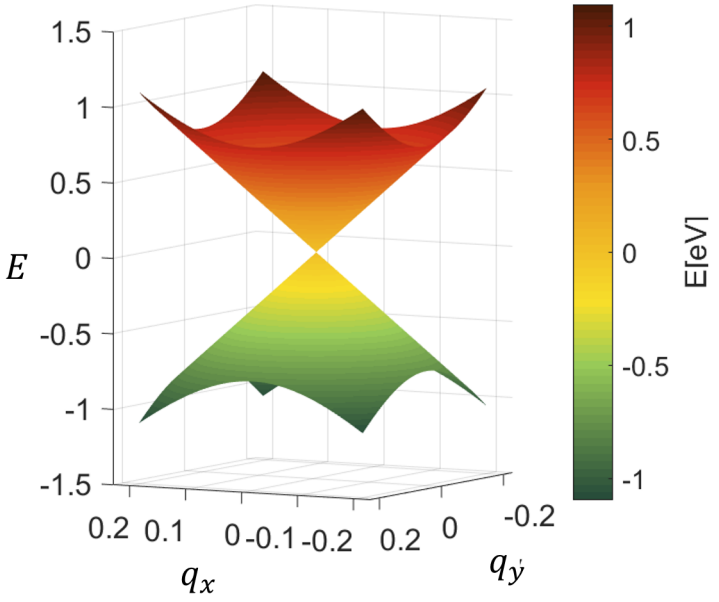

Figure 2.7: Low-energy dispersion given in Eq. 2.41 around the Dirac point $\boldsymbol{K}$.

has to take into account the diagonal energy terms E_A and E_B that are in general different. The gapped graphene NN TB Hamiltonian reads

$$\begin{pmatrix} E_A & t \cdot f(\boldsymbol{k}) \\ t^* \cdot f^*(\boldsymbol{k}) & E_B \end{pmatrix} \begin{pmatrix} A_{\boldsymbol{k}} \\ B_{\boldsymbol{k}} \end{pmatrix} = E_{\boldsymbol{k}} \begin{pmatrix} A_{\boldsymbol{k}} \\ B_{\boldsymbol{k}} \end{pmatrix}. \tag{2.42}$$

After diagonalising we obtain

$$E^{\pm}_{\boldsymbol{k}} = \pm\sqrt{t^2 f^2(\boldsymbol{k}) + \frac{\Delta^2}{4}}, \tag{2.43}$$

where $\Delta = |E_A - E_B|$ is the magnitude of the gap that opens at $\boldsymbol{K}$ (and I choose $(E_A + E_B)/2 = 0$).

The linear expansion of bands near $\boldsymbol{K}$ gives a massive Dirac Hamiltonian with the bands separated by a gap Δ, a mass term which enters expression in Eq. 2.40 on

a diagonal

$$\begin{pmatrix} \frac{\Delta}{2} & t \cdot f_-(\boldsymbol{K}+\boldsymbol{q}) \\ t \cdot f_-^*(\boldsymbol{K}+\boldsymbol{q}) & -\frac{\Delta}{2} \end{pmatrix} = \begin{pmatrix} \frac{\Delta}{2} & \frac{\sqrt{3}}{2}at(q_x - iq_y) \\ \frac{\sqrt{3}}{2}at(q_x + iq_y) & -\frac{\Delta}{2} \end{pmatrix} = v_f \boldsymbol{q} \cdot \boldsymbol{\sigma} + \sigma_z \frac{\Delta}{2}. \tag{2.44}$$

The solutions are now

$$E_{\boldsymbol{q}}^{\pm} = \pm\sqrt{t^2 f^2(\boldsymbol{K}+\boldsymbol{q}) + \frac{\Delta^2}{4}} = \pm\sqrt{v_f^2|\boldsymbol{q}|^2 + \frac{\Delta^2}{4}}, \tag{2.45}$$

where Δ opens the gap, as visible in Fig. 2.8 a).

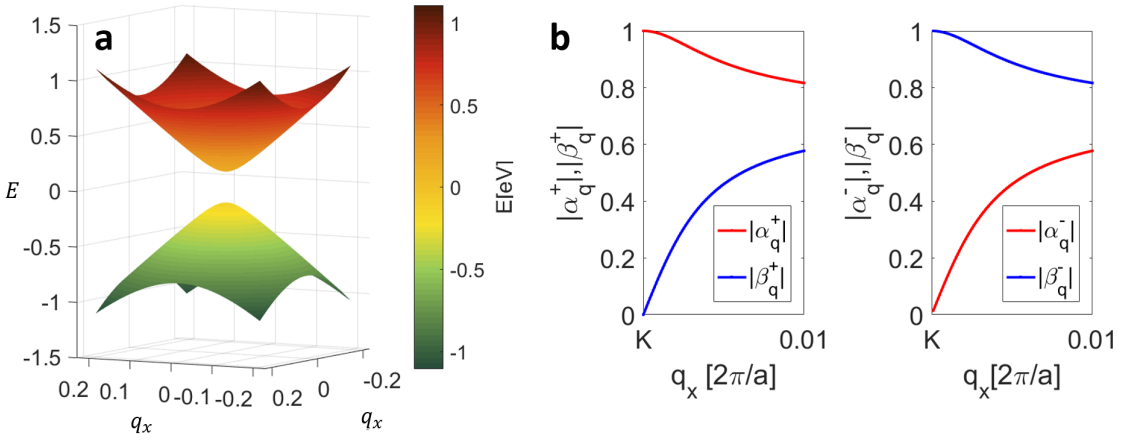

Figure 2.8: a) Low-energy dispersion obtained by linear expansion of the expression in Eq. 2.45 around the Dirac point $\boldsymbol{K}$ for Δ=0.1eV. Energy gap appears. b) Eigenvector components given by Eq. 2.46 for $q_y = 0$.

The eigenvectors of the Hamiltonian in Eq. 2.44 are

$$\left|+_{\boldsymbol{q}}^{\pm\boldsymbol{K}}\right\rangle = \begin{pmatrix} \alpha_{\boldsymbol{q}}^+ \\ \pm\beta_{\boldsymbol{q}}^+ e^{\pm i\theta_{\boldsymbol{q}}} \end{pmatrix}$$
$$\left|-_{\boldsymbol{q}}^{\pm\boldsymbol{K}}\right\rangle = \begin{pmatrix} \alpha_{\boldsymbol{q}}^- \\ \pm\beta_{\boldsymbol{q}}^- e^{\pm i\theta_{\boldsymbol{q}}} \end{pmatrix}, \tag{2.46}$$

where $\pm$ stands for $\boldsymbol{K}$ and $-\boldsymbol{K}$ and where

$$\begin{aligned} \alpha_{\boldsymbol{q}}^{\pm} &= \frac{E_{\boldsymbol{q}}^{\pm} + \frac{\Delta}{2}}{N_{\boldsymbol{q}\pm}}, \\ \beta_{\boldsymbol{q}}^{\pm} &= \frac{v_f|\boldsymbol{q}|}{N_{\boldsymbol{q}\pm}}, \\ N_{\boldsymbol{q}\pm} &= \sqrt{2E_{\boldsymbol{q}}^{\pm}\left(E_{\boldsymbol{q}}^{\pm} + \frac{\Delta}{2}\right)}. \end{aligned} \tag{2.47}$$

The components of the eigenvectors given in Eq. 2.47 were plotted in Fig. 2.8 b).

2.1.6 Second quantisation.

I will now introduce the second quantisation formalism, which focuses on occupation numbers, in anticipation of many-electron systems described in later parts of this thesis. In order to rewrite the TB model introduced in 2.1.3 using the second quantisation, we start with field operators

$$\begin{aligned} \Psi^{\boldsymbol{k}}(\boldsymbol{r}) &= \sum_{\alpha=A,B} c_{\alpha,\boldsymbol{k}}\psi_{\alpha}^{\boldsymbol{k}}(\boldsymbol{r}) \\ \Psi^{\boldsymbol{k}}(\boldsymbol{r})^{\dagger} &= \sum_{\alpha=A,B} c_{\alpha,\boldsymbol{k}}^{\dagger}\psi_{\alpha}^{\boldsymbol{k}*}(\boldsymbol{r}), \end{aligned} \tag{2.48}$$

which describe destroying/ creating an electron on sublattice A or B at position $\boldsymbol{r}$ and at $\boldsymbol{k}$ and $c_{A,\boldsymbol{k}}$ ($c_{B,\boldsymbol{k}}$) and $c_{A,\boldsymbol{k}}^{\dagger}$ ($c_{B,\boldsymbol{k}}^{\dagger}$) are annihilation and creation operators of an electron at $\boldsymbol{k}$ and on sublattice A (B) with fermionic anticommutation relations

$$\begin{aligned} \{c_i, c_j\} &= \{c_i^{\dagger}, c_j^{\dagger}\} = 0 \\ \{c_i, c_j^{\dagger}\} &= \delta_{ij}, \end{aligned} \tag{2.49}$$

where indices i, j include both the $\boldsymbol{k}$ and the sublattice index. The creation and annihilation operators act on vacuum and a filled state respectively to create new

occupation states

$$\begin{aligned} c^{\dagger}_{A,\boldsymbol{k}} \left|0\right\rangle &= \left|\psi^{\boldsymbol{k}}_{A}\right\rangle, \\ c_{A,\boldsymbol{k}} \left|\psi^{\boldsymbol{k}}_{A}\right\rangle &= \left|0\right\rangle. \end{aligned} \tag{2.50}$$

We can use the field operators defined in Eq. 2.48 to obtain the matrix elements of the Hamiltonian in second quantisation

$$\begin{aligned} \int d\boldsymbol{r} \Psi^{\boldsymbol{k}}(\boldsymbol{r})^{\dagger} \hat{H} \Psi^{\boldsymbol{k}}(\boldsymbol{r}) &= \int d\boldsymbol{r} \sum_{\alpha,\beta=A,B} c^{\dagger}_{\alpha,\boldsymbol{k}} \psi^{\boldsymbol{k}}_{\alpha}(\boldsymbol{r})^{*} \hat{H} c_{\beta,\boldsymbol{k}} \psi^{\boldsymbol{k}}_{\beta}(\boldsymbol{r}) \\ &= \sum_{\alpha,\beta=A,B} \left\langle \psi^{\boldsymbol{k}}_{\alpha}(\boldsymbol{r}) \right| \hat{H} \left| \psi^{\boldsymbol{k}}_{\beta}(\boldsymbol{r}) \right\rangle c^{\dagger}_{\alpha,\boldsymbol{k}} c_{\beta,\boldsymbol{k}} \\ &= \sum_{\alpha,\beta=A,B} \hat{H}^{\boldsymbol{k}}_{\alpha,\beta} c^{\dagger}_{\alpha,\boldsymbol{k}} c_{\beta,\boldsymbol{k}}, \end{aligned} \tag{2.51}$$

which rewrites the Hamiltonian in Eq. 2.42 in second quantisation form.

2.1.7 Finite structure tight-binding model: graphene quantum dots.

I will now show the TB model for graphene quantum dots (GQDs), which confine electrons within a small flake of graphene lattice. The Hamiltonian in second quantised form reads

$$\hat{H}_{TB} = \sum_{i,\sigma} \epsilon_{i,\sigma} c^{\dagger}_{i,\sigma} c_{i,\sigma} + \sum_{<i,j>,\sigma} (t_{ij} c^{\dagger}_{i,\sigma} c_{j,\sigma} + h.c.), \tag{2.52}$$

where i, j denote atomic sites within the quantum dot and $c^{\dagger}_{i,\sigma}$ ($c_{i,\sigma}$) creates (annihilates) an electron on a p_z orbital on a site i with spin σ. The second summation in Eq. 2.52 is over the NN pairs of sites and t_{ij} is the hopping integral for the bond between neighbouring i and j sites; $\epsilon_{i,\sigma}$ denotes the onsite energy of atom i and for spin σ. Note that as shown in section 2.1.3, the NN of sites within sublattice A are always in sublattice B, and vice versa.

The Hamiltonian in Eq. 2.52 is represented as a matrix in the basis of N sites within a QD and diagonalised to obtain the single electron energy states. The con-

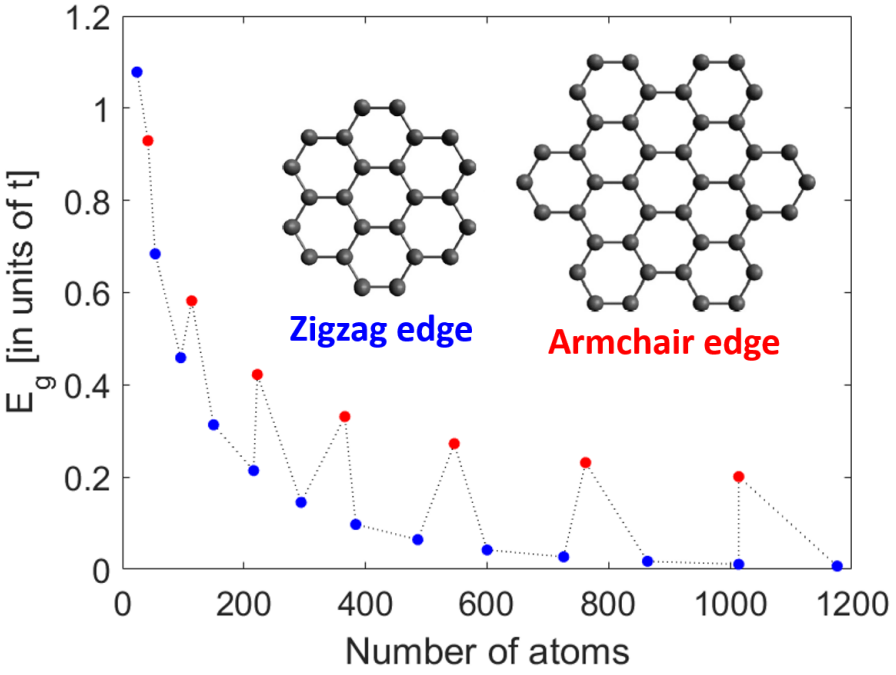

Figure 2.9: Energy gap depdendence on size of graphene quantum dots. Blue (red) points denote energy gap of structures with zigzag (armchair) edge type (smallest examples pictures in insets).

finement opens the gap in the graphene layer, which decreases with size and in a limit of an infinite structure will converge to the gapless spectrum of bulk graphene. The energy gap dependence on the size of the flake is shown in Fig. 2.9 for armchair-edged and zigzag-edged hexagonal GQDs (smallest examples shown in the inset). The energy gap is calculated in the units of the hopping element $t_{ij} = t$ in Eq. 2.52. Despite the same shape of the QDs, different edge termination induces an energy gap oscillation as a function of size.

2.2 Many electron picture.

So far I have considered a single particle (SP) picture, which means that electrons in the system are not interacting and each behaves in the same way. However, electronic, optical or magnetic properties of 2D materials are largely determined by the interactions between the particles in the system, which will be considered in this section.

2.2.1 Many-body Hamiltonian.

The interaction beyond the SP picture is introduced in the N-electron Hamiltonian through the Coulomb potential V_{ee} between all pairs of electrons:

$$\hat{H} = \sum_i \hat{h}_i^{SP} + \frac{1}{2} \sum_{i,j,i\neq j} V_{ee}(\boldsymbol{r}_i - \boldsymbol{r}_j), \tag{2.53}$$

where i, j count electrons and $\hat{h}_i^{SP}$ is a SP Hamiltonian for electron i. The wavefunction of the N-electron system is now an antisymmetrised product of the single electron wavefunctions, described with a Slater determinant (or as I later show, as a combination of Slater determinants)

$$\Psi(\boldsymbol{r}_1, \boldsymbol{r}_2, ...\boldsymbol{r}_N) = \frac{1}{\sqrt{N!}} \begin{vmatrix} \phi_1(\boldsymbol{r}_1) & \phi_2(\boldsymbol{r}_1) & \cdots & \phi_N(\boldsymbol{r}_1) \\ \phi_1(\boldsymbol{r}_2) & \phi_2(\boldsymbol{r}_2) & \cdots & \phi_N(\boldsymbol{r}_2) \\ \vdots & \vdots & \ddots & \vdots \\ \phi_1(\boldsymbol{r}_1) & \phi_2(\boldsymbol{r}_1) & \cdots & \phi_N(\boldsymbol{r}_1) \end{vmatrix}, \tag{2.54}$$

where $\phi(\boldsymbol{r})$ denote orbitals of the SP solution. A single Slater determinant can be written in short as

$$\Psi(\boldsymbol{r}_1, \boldsymbol{r}_2, ...\boldsymbol{r}_N) = \langle \boldsymbol{r} | \phi_1, \phi_2, ...\phi_N \rangle, \tag{2.55}$$

which takes the form of

$$\Psi(\boldsymbol{r}_1, \boldsymbol{r}_2, ...\boldsymbol{r}_N) = \langle \boldsymbol{r} | \, c_1^\dagger c_2^\dagger ... c_N^\dagger \, | 0 \rangle \,, \tag{2.56}$$

in the second quantised notation. The interacting part of the Hamiltonian in Eq. 2.53 expressed in second quantisation reads

$$\hat{H}_{ee} = \frac{1}{2} \sum_{ijkl\sigma,\sigma'} \langle ij | \, V \, | kl \rangle \, c_{i\sigma}^\dagger c_{j\sigma'}^\dagger c_{k\sigma'} c_{l\sigma}, \tag{2.57}$$

where

$$\langle ij | \, V \, | kl \rangle = \int \int d\boldsymbol{r} d\boldsymbol{r}' \phi_{i\sigma}^* \phi_{j\sigma'}^* \frac{e^2}{\kappa \, |\boldsymbol{r} - \boldsymbol{r}'|} \phi_{k\sigma'} \phi_{l\sigma} \tag{2.58}$$

are the two-body Coulomb scattering matrix elements for $V_{ee} = \frac{e^2}{\kappa|\boldsymbol{r}-\boldsymbol{r}'|}$. The matrix elements $\langle ij|\, V\, |kl\rangle$ depend on the specific form of the SP wavefunctions i, j, k, l, which will differ for problems considered in this thesis. The following subsections will introduce different ways to treat $\hat{H}_{ee}$: mean-field approaches within Hartree-Fock (HF) method and density functional theory as well as configuration interaction (CI) method.

2.2.2 Mean-field methods.

The many body Hamiltonian in Eq. 2.53 becomes quickly too complex to solve for a large number of interacting electrons. It is therefore useful to introduce approximations to the form of electron-electron interaction term in Eq. 2.57. Mean-field methods take the interactions into account in a mean-field manner, which involves solving the problem for a single electron (quasiparticle) placed in an effective potential originating from the interactions with all the other electrons [130]. This effective term is calculated using the electron density

$$\rho(\boldsymbol{r}) = \sum_{\lambda<\lambda_F,\sigma} |\psi_{\lambda,\sigma}(\boldsymbol{r})|^2\,, \tag{2.59}$$

where λ runs over occupied SP orbitals $\psi_{\lambda,\sigma}$. We can define a creation operator $b_{\lambda\sigma}$ that creates an electron on a SP mean-field orbital $\left|\psi^{\lambda\sigma}_{SP}\right\rangle = b^\dagger_{\lambda\sigma}\,|0\rangle$, which can be then expanded in terms of the creation operators in the TB basis as

$$\begin{aligned} \left|\psi^{\lambda\sigma}_{SP}\right\rangle = b^\dagger_{\lambda\sigma}\,|0\rangle &= \sum_i A^*_{i\lambda\sigma} c^\dagger_{i\sigma}\,|0\rangle \\ c^\dagger_{i\sigma} &= \sum_\lambda A^*_{i\lambda\sigma} b^\dagger_{\lambda\sigma} \end{aligned} \tag{2.60}$$

The electron density operator in second quantisation becomes

$$\begin{aligned}\hat{\rho} &= \sum_{\lambda<\lambda_F,\sigma} b^\dagger_{\lambda\sigma} b_{\lambda\sigma} \\ &= \sum_{\lambda<\lambda_F,\sigma} \sum_i A^*_{i\lambda\sigma} c^\dagger_{i\sigma} \sum_j A_{\lambda j\sigma} c_{j\sigma} \\ &= \sum_{i,j,\sigma} \Bigg(\sum_{\lambda<\lambda_F} A^*_{i\lambda\sigma} A_{\lambda j\sigma} \Bigg) c^\dagger_{i\sigma} c_{j\sigma} \\ &= \sum_{i,j,\sigma} \rho_{ij\sigma} c^\dagger_{i\sigma} c_{j\sigma},\end{aligned} \tag{2.61}$$

where $\rho_{ij\sigma}$ are matrix elements of the density operator, and λ_F is the index of the highest occupied orbital.

2.2.3 Hartree-Fock approximation.

This section is based on Ref. [130,131]. The HF method involves the following mean-field approximation to the interacting term in Eq. 2.57:

$$\begin{aligned}c^\dagger_{i\sigma} c^\dagger_{j\sigma'} c_{k\sigma'} c_{l\sigma} \approx\ & c^\dagger_{i\sigma} \langle c^\dagger_{j\sigma'} c_{k\sigma'} \rangle c_{l\sigma} + \langle c^\dagger_{i\sigma} c_{l\sigma} \rangle c^\dagger_{j\sigma'} c_{k\sigma'} \\ & - c^\dagger_{i\sigma} c_{k\sigma'} \langle c^\dagger_{j\sigma'} c_{l\sigma} \rangle \delta_{\sigma\sigma'} - \langle c^\dagger_{i\sigma} c_{k\sigma'} \rangle c^\dagger_{j\sigma'} c_{l\sigma} \delta_{\sigma\sigma'} \\ =\ & 2 \Bigg(c^\dagger_{i\sigma} \langle c^\dagger_{j\sigma'} c_{k\sigma'} \rangle c_{l\sigma} - c^\dagger_{i\sigma} c_{k\sigma'} \langle c^\dagger_{j\sigma'} c_{l\sigma} \rangle \delta_{\sigma\sigma'} \Bigg),\end{aligned} \tag{2.62}$$

where $\langle c^\dagger_{j\sigma'} c_{k\sigma'} \rangle = \rho_{jk\sigma'}$ and the expectation values are calculated for the HF GS wavefunction $\langle c^\dagger_{j\sigma'} c_{k\sigma'} \rangle = \langle c^\dagger_{j\sigma'} c_{k\sigma'} \rangle_{HF}$. The assumption of the HF method is that the HF ground state (GS) wavefunction can be described by a single Slater determinant

$$|HF\rangle = \prod_{\lambda<\lambda_F} b^\dagger_{\lambda\uparrow} b^\dagger_{\lambda\downarrow} |0\rangle , \tag{2.63}$$

which involves N electrons placed with opposite spins on lowest $N/2$ levels λ (with no spin splitting of levels).

Following the approximation in Eq. 2.62, the interacting Hamiltonian in Eq. 2.53

becomes the HF Hamiltonian

$$H_{HF} = \sum_{i\sigma} \varepsilon_{i\sigma} c^{\dagger}_{i\sigma} c_{i\sigma} + \sum_{ijkl\sigma\sigma'} \Big(\langle ij| V |kl\rangle - \langle ij| V |lk\rangle \, \delta_{\sigma\sigma'} \Big) \rho_{jk\sigma'} c^{\dagger}_{i\sigma} c_{l\sigma}, \tag{2.64}$$

where the 1/2 from Eq. 2.57 cancels the factor of 2 in Eq. 2.62 and I replaced $k\sigma' \leftrightarrow l\sigma$ in the second term. The matrix elements $\langle ij| V |kl\rangle$ and $\langle ij| V |lk\rangle$ in the second term of Eq. 2.64 are direct and exchange terms respectively. The Hamiltonian in Eq. 2.64 contains the density $\rho_{jk\sigma'}$, which itself is obtained from the eigensolutions of the same Hamiltonian. It therefore needs to be diagonalised in a self-consistent manner. To start, a trial density matrix ρ_{trial} is used, which allows for diagonalising the problem to obtain the eigenvectors, which are then again used to obtain the new density matrix ρ. The solutions eventually converge after several steps.

The search for the GS HF energy in this self-consistent process is possible because of the variational principle. It states that the exact GS energy is always lower or equal to the GS energy obtained from a trial wavefunction:

$$E[\Psi] = \frac{\langle \Psi| \hat{H} |\Psi\rangle}{\langle \Psi| |\Psi\rangle} \geq E_0, \tag{2.65}$$

where the exact GS energy E_0 is reached for the exact GS wavefunction Ψ_0. A converged energy solution will overestimate the true GS energy.

The converged solutions of the HF Hamiltonian in Eq. 2.64 give the quasiparticle states ψ_λ, which include the interactions from the other electrons in the VB in the form of a self energy

$$\Sigma_\lambda = \sum_{\mu} \Big(2 \langle \lambda\mu| V |\mu\lambda\rangle - \langle \lambda\mu| V |\lambda\mu\rangle \Big), \tag{2.66}$$

where the factor of 2 comes from 2 electrons occupying each quasiparticle level in the GS and they both interact through direct term, but only same spin electrons can interact via exchange.

2.2.4 Density functional theory.

I will now describe the density functional theory (DFT) used widely to perform realistic calculations of systems with many electronic degrees of freedom. This section is based on Ref. [132].

DFT uses two Hohenberg-Kohn (HK) theorems. The first HK theorem states that the external potential $V_{ext}(\boldsymbol{r})$ of an electronic system is uniquely determined by the GS density $\rho_0(\boldsymbol{r})$ up to a constant. This implies that the many-body wavefunction and all properties of an interacting system are also fully determined by $\rho_0(\boldsymbol{r})$. It is an important improvement on the assumptions of the many-body problem, because for N electrons the many-body wavefunction $\Psi(\{\boldsymbol{r}_i\})$ is $3N$-dimensional and the density is only 3-dimensional.

The second HK theorem defines an energy functional $E[\rho(\boldsymbol{r})]$ for any external potential $V_{ext}(\boldsymbol{r})$. It states that for any $V_{ext}(\boldsymbol{r})$ the exact GS of the many-body system is determined by the global minimum of the energy functional $E_0[\rho(\boldsymbol{r})] = \min \langle\Psi| H |\Psi\rangle = \min E[\rho(\boldsymbol{r})]$. From the interacting Hamiltonian given in Eq. 2.53 the explicit form of the functional is constructed as

$$E[\rho(\boldsymbol{r})] = \underbrace{T[\rho(\boldsymbol{r})]}_{\substack{\text{Kinetic}\\ \text{energy}}} + \underbrace{\int V_{ext}(\boldsymbol{r})\rho(\boldsymbol{r})d\boldsymbol{r}}_{\substack{\text{External}\\ \text{potential}}} + \underbrace{\frac{1}{2}\int \frac{\rho(\boldsymbol{r})\rho(\boldsymbol{r}')}{|\boldsymbol{r}-\boldsymbol{r}'|}d\boldsymbol{r}d\boldsymbol{r}'}_{\text{Hartree term}} + \underbrace{E_{ncl}[\rho(\boldsymbol{r})]}_{\substack{\text{Nonclassical}\\ \text{interaction}}}. \quad (2.67)$$

Out of the four terms in the functional in Eq. 2.67 only the external potential is system-dependent, while the rest is universal for any system. The external potential is also known exactly and as is the classical Coulomb interaction in the form of a Hartree term $E_H[\rho(\boldsymbol{r})] = \frac{1}{2}\int \frac{\rho(\boldsymbol{r})\rho(\boldsymbol{r}')}{|\boldsymbol{r}-\boldsymbol{r}'|}d\boldsymbol{r}d\boldsymbol{r}'$. The other terms are a priori unknown.

This is where we need the Kohn-Sham (KS) ansatz. It assumes that the GS density of the interacting system $\rho(\boldsymbol{r})$ is equal to the GS density of some fictitious non-interacting system, which could be solved exactly. To solve the fictitious problem an approximate density functional is needed to replace unknown functionals in Eq.

2.67. This allows for constructing the KS functional

$$E_{KS}\left[\rho(\boldsymbol{r})\right] = \underbrace{T_{SP}\left[\rho(\boldsymbol{r})\right]}_{\substack{\text{Kinetic}\\ \text{energy}}} + \underbrace{\int V_{ext}(\boldsymbol{r})\rho(\boldsymbol{r})d\boldsymbol{r}}_{\substack{\text{External}\\ \text{potential}}} + \underbrace{E_H\left[\rho(\boldsymbol{r})\right]}_{\text{Hartree term}} + \underbrace{E_{XC}\left[\rho(\boldsymbol{r})\right]}_{\substack{\text{Exchange-correlation}\\ \text{functional}}}, \tag{2.68}$$

where $E_{XC}\left[\rho(\boldsymbol{r})\right]$ is the exchange correlation (XC) potential, which includes the non-classical interaction: exchange and correlations, as well as the difference $T\left[\rho(\boldsymbol{r})\right] - T_{SP}\left[\rho(\boldsymbol{r})\right]$ between the kinetic energy for the interacting system and the kinetic energy for the fictitious SP system.

The introduction of the KS functional E_{KS} allows now for formulating the problem for the fictitious non-interacting system:

$$\left(-\frac{\hbar^2}{2m}\nabla^2 + V_{KS}(\boldsymbol{r}) \right)\psi^{KS}(\boldsymbol{r}) = \varepsilon^{KS}\psi^{KS}(\boldsymbol{r}), \tag{2.69}$$

where the effective KS potential is the functional derivative of E_{KS} given in Eq. 2.68, $V_{KS}\left[\rho(\boldsymbol{r})\right] = \frac{\delta E_{KS}[\rho(\boldsymbol{r})]}{\delta\rho}$, and it reads

$$V_{KS}\left[\rho(\boldsymbol{r})\right] = V_{ext}(\boldsymbol{r}) + V_H\left[\rho(\boldsymbol{r})\right] + V_{XC}\left[\rho(\boldsymbol{r})\right]. \tag{2.70}$$

The solutions of the fictitious problem in Eq. 2.69 are KS orbitals, similar in nature to the HF orbitals. The KS orbitals allow for the calculation of the density $\rho(\boldsymbol{r}) = \sum_{\lambda}^{occ}\left|\psi_{\lambda}^{KS}\right|^2$, which is then used to calculate the KS potential in Eq. 2.70. The KS equation in 2.69 is solved self-consistently until the solutions converge and yield a GS density $\rho(\boldsymbol{r})$ of the interacting system. Importantly, only the density can be directly taken as a proper solution of the interacting problem, while the KS eigenvalues and KS orbitals do not have a true physical meaning. However the KS eigenvalues are widely used to describe the electronic properties of materials as they often produce results comparable with experiment. Despite this, they should be treated with caution as the energy gaps are often underestimated in the DFT calculations. This is a consequence of the main assumption of DFT: the GS density. It is only the GS

properties that are described well by DFT.

Also, the results of a DFT calculation largely depend on the approximations made to produce the exchange correlation functional $E_{XC}[\rho(\boldsymbol{r})]$. If the exact form of $E_{XC}[\rho(\boldsymbol{r})]$ was known, a DFT calculation would yield the exact GS. Out of all the complex choices for the approximation of E_{XC}, the simplest in form and the most popular ones are functionals constructed within a local density approximation (LDA) and generalised gradient approximation (GGA):

$$\begin{aligned} E_{XC}^{LDA}(\rho(\boldsymbol{r})) &= \int \rho(\boldsymbol{r}')V_{XC}(\rho(\boldsymbol{r}'))\,d\boldsymbol{r}', \\ E_{XC}^{GGA}[\rho(\boldsymbol{r})] &= \int \rho(\boldsymbol{r}')V_{XC}[\rho(\boldsymbol{r}'), \nabla\rho(\boldsymbol{r}')]\,d\boldsymbol{r}', \end{aligned} \tag{2.71}$$

with the GGA approximation depending not only on the density at a point $\boldsymbol{r}$, but also on its gradient at $\boldsymbol{r}$. Other approximations in DFT involve numerical approximations in solving of the KS equation in Eq. 2.69. This requires skill in choice of basis sets, Brillouin k-point meshgrids and convergence criteria for the self-consistent loop procedure, which I will briefly discuss in section 2.2.5.

2.2.5 Example of a DFT calculation: bulk MoS_2.

I will now describe a DFT calculation for bulk monolayer within the TMDC group. The members of TMDCs have a chemical formula of MX_2, where M is a transition metal atom, such as W or Mo and X_2 is a chalcogen dimer, such as S_2, Se_2 or Te_2. Here, I will consider one member of TMDCs - MoS_2.

The crystal structure of MoS_2 looks like a graphene lattice from the top view, but is composed of three layers of atoms, when viewed from the side - the plane of Mo atoms makes up one triangular sublattice and two identical planes of sulphur atoms placed below and above the metal plane build the second sublattice (Fig. 2.10). The analogy with graphene is visible if one consideres a unit cell made of Mo atom (blue) on one site and a S_2 dimer (yellow) on the second site. As these sites hold distinct atoms, the onsite energies on A and B sites will be different, just like in gapped

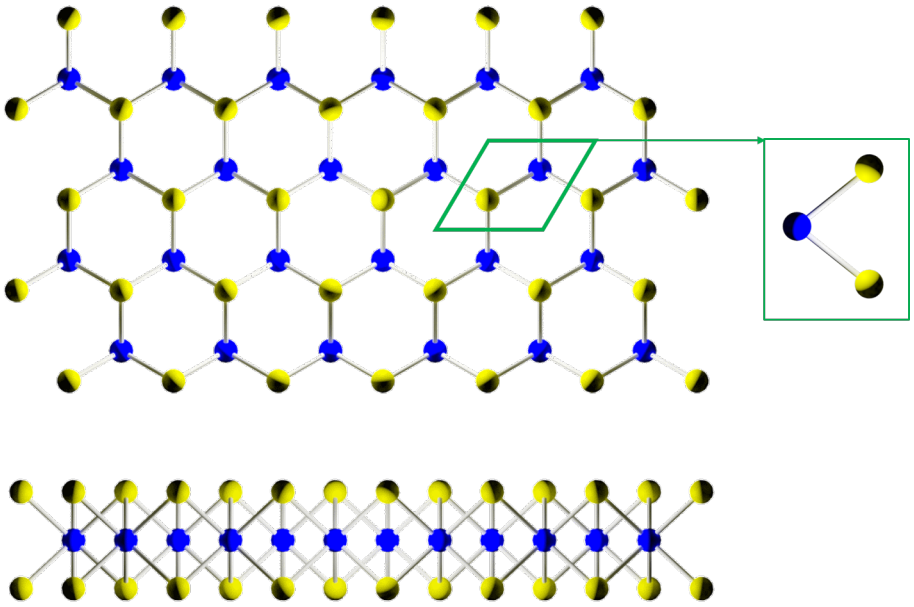

Figure 2.10: Crystal lattice of MoS_2. The top panel shows the view from the top. Blue (yellow) atoms denote Mo and S_2 sites. A green parallelogram marks the unit cell, which contains 3 stoms (right). Bottom panel shows the plane of MoS_2 from the side view.

graphene (section 2.1.5). We should therefore expect MoS_2 to have an energy gap at $\boldsymbol{K}$.

There are many available packages to conduct a DFT calculation, which all use the theory outlined in section 2.2.4, but they differ in practical numerical approaches used in the calculation. I have used the *Abinit* code [133] to obtain the results presented in this section. Below I present a short description of the performed calculation.

Abinit uses a plane wave basis to formulate the KS problem given by Eq. 2.69 and is intended to study 3D periodic systems. However, any low dimensional materials can be studied as well if the supercell approach is taken. To fulfill the periodic boundary condition in 3D, the low dimensional object is repeated in all the "missing" dimensions with sufficient spacing that makes the copies independent. A single copy of the system is called a supercell. This is needed because a linear combination of plane waves poorly describes a localised object, but performs much better if it is periodically repeated. Fig. 2.11 depicts examples of a supercell for a 2D system, 1D system and a 0D system, all build from a square lattice. For a standard 3D system

the supercell is the same as a unit cell of the material.

For calculation of bulk MoS_2, I will use the supercell for a 2D system, shown in Fig. 2.11 a). The supercell will contain two neighbouring sites A and B, just like in graphene, which has been shown for MoS_2 in Fig. 2.10 with a green parallelogram. However, the supercell will now have a length in the z direction, which will be chosen to ensure no tunneling between the planes repeated along z, just like it is pictured in Fig. 2.11 a). The value set in practice was 28.3459 Bohr.

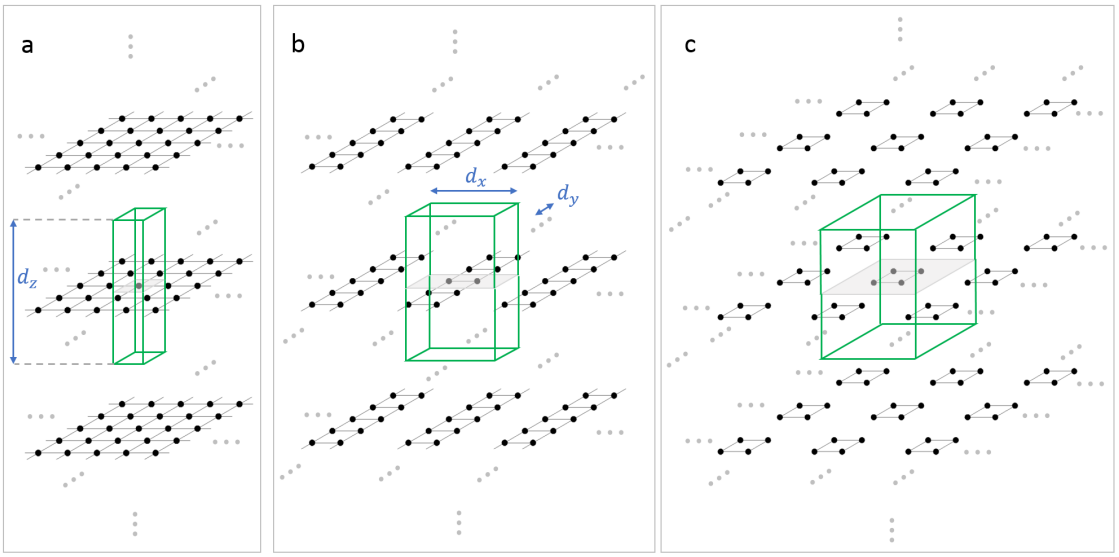

Figure 2.11: DFT supercell for a) 2D, b) 1D and c) 0D systems. Black dots are atoms, green blocks show the 3D supercell and its dimensions are labelled with blue symbols.

I will now explain the choice of the number of plane waves in the basis. According to Bloch's theorem

$$\Psi_{n,\boldsymbol{k}}(\boldsymbol{r}+\boldsymbol{d}_j) = e^{i\boldsymbol{k}\boldsymbol{d}_j}\Psi_{n,\boldsymbol{k}}(\boldsymbol{r}), \tag{2.72}$$

where n labels bands and $\boldsymbol{d}_j$ is the supercell vector, for $j = x, y, z$, as shown in Fig. 2.11. The wavefunction $\Psi_{n,\boldsymbol{k}}$ in Eq. 2.72 reads

$$\Psi_{n,\boldsymbol{k}}(\boldsymbol{r}) = \frac{1}{\sqrt{N\Omega_{SC}}} e^{i\boldsymbol{k}\boldsymbol{r}} u_{n,\boldsymbol{k}}(\boldsymbol{r}), \tag{2.73}$$

where $u_{n,\boldsymbol{k}}$ is the periodic part of the Bloch wavefunction, N is the number of supercells and Ω_{SC} is the volume of the supercell. The function $u_{n,\boldsymbol{k}}$ is expanded in the

basis of plane waves as

$$u_{n,\boldsymbol{k}}(\boldsymbol{r}) = \sum_{\boldsymbol{G}} u_{n,\boldsymbol{k}}(\boldsymbol{G}) e^{i\boldsymbol{G}\boldsymbol{r}}, \tag{2.74}$$

where $\boldsymbol{G}$ are reciprocal superlattice vectors, such that $e^{i\boldsymbol{G}\boldsymbol{d}_j} = 1$, and $u_{n,\boldsymbol{k}}(\boldsymbol{G})$ is the Fourier transform of $u_{n,\boldsymbol{k}}(\boldsymbol{r})$, $u_{n,\boldsymbol{k}}(\boldsymbol{G}) = \frac{1}{\Omega_{SC}} \int_{\Omega_{SC}} e^{-i\boldsymbol{G}\boldsymbol{r}} u_{n,\boldsymbol{k}}(\boldsymbol{r}) d\boldsymbol{r}$. The wavefunction in Eq. 2.73 becomes

$$\Psi_{n,\boldsymbol{k}}(\boldsymbol{r}) = \frac{1}{\sqrt{N\Omega_{SC}}} \sum_{\boldsymbol{G}} u_{n,\boldsymbol{k}}(\boldsymbol{G}) e^{i(\boldsymbol{k}+\boldsymbol{G})\boldsymbol{r}}, \tag{2.75}$$

The energy of the a plane wave in the basis is then $-\frac{\nabla^2}{2} e^{i(\boldsymbol{k}+\boldsymbol{G})\boldsymbol{r}} = \frac{(\boldsymbol{k}+\boldsymbol{G})^2}{2} e^{i(\boldsymbol{k}+\boldsymbol{G})\boldsymbol{r}}$. As the coefficients $u_{n,\boldsymbol{k}}(\boldsymbol{G})$ decrease with kinetic energy $\frac{(\boldsymbol{k}+\boldsymbol{G})^2}{2}$, the set of the plane waves taken in the calculation can be chosen based on a cut-off energy E_{cut}, such that $\frac{(\boldsymbol{k}+\boldsymbol{G})^2}{2} < E_{cut}$. The energy E_{cut} is a parameter of the calculation and needs to be chosen based on the convergence of total energy of the system with varying E_{cut}. The results of such convergence calculation are shown in Fig. 2.12 a). The total energy E_{tot} converges at $E_{cut} = 30$ Ha with 0.00006 Ha≈ 1.7 meV precision sufficient for a calculation of the bulk MoS_2 band structure.

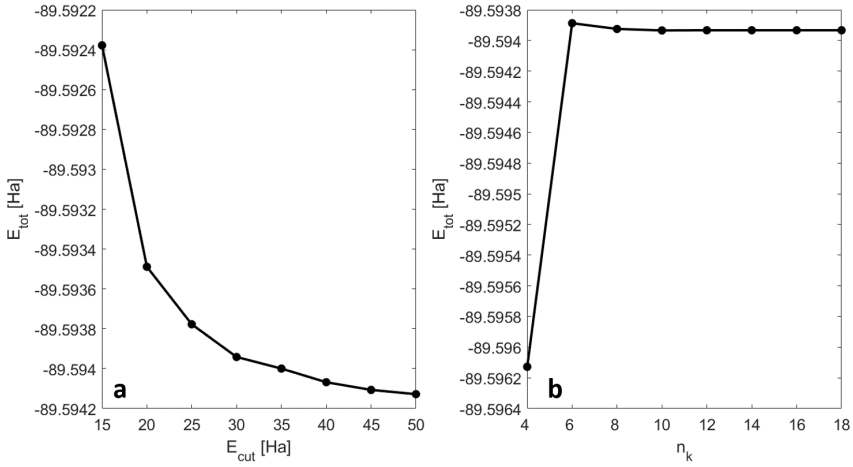

Figure 2.12: Total energy convergence with varying a) E_{cut} and b) $\boldsymbol{k}$-point mesh density.

Another important parameter is linked to calculating all the expectation values in the DFT procedure: the choice of the grid of $\boldsymbol{k}$-points. E.g. the electronic density

(in case of a periodic system) is calculated as

$$\rho(\boldsymbol{r}) = \sum_{\lambda}^{occ} |\psi_\lambda(\boldsymbol{r})|^2 = \sum_{n} \frac{1}{\Omega_{BZ}} \int_{\Omega_{BZ}} f(E_F - E_{n,\boldsymbol{k}}) \, |\psi_{n,\boldsymbol{k}}(\boldsymbol{r})|^2 \, d\boldsymbol{k}, \tag{2.76}$$

where Ω_{BZ} is the volume of the BZ and f is the Fermi distribution. The choice of the mesh of $\boldsymbol{k}$-points in Eq. 2.76 follows the Monkhorst-Pack grid in the I^{st} BZ [134]. An example of a denser and coarser mesh is shown in Fig. 2.13. a). A mesh can also be shifted from the origin (shown in Fig. 2.13. b)) or it can combine both shifted and unshifted meshes (Fig. 2.13. c)). The optimal choices for different lattices are well known [134]. However, the mesh density is always a parameter of the calculation. The denser the mesh, the more costly the calculation becomes. Fig 2.12 b). shows the results of a convergence study with respect to the number of k-points n_k in one direction for an optimal shift $(0, 0, 1/2)$ for a hexagonal lattice. The total energy E_{tot} is well converged already for $n_k = 8$ within 0.00004 Ha$\approx$ 1.1meV.

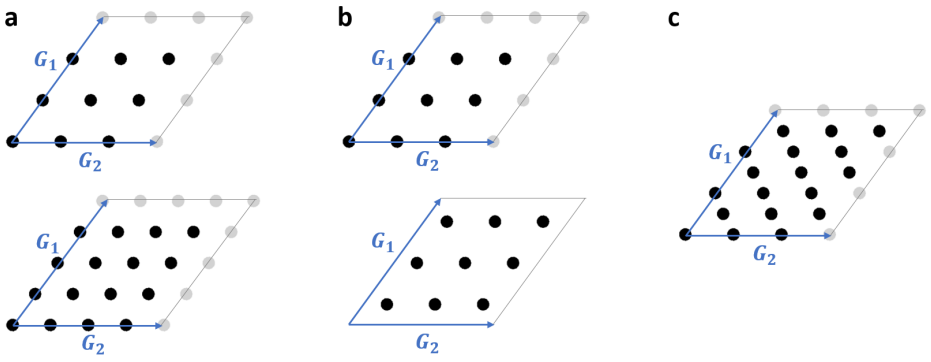

Figure 2.13: Monkhorst-Pack k-point grid for a) varying density, b) different shift and c) for a mixture of shifted and unshifted meshes. $\boldsymbol{G}_i$ are reciprocal lattice vectors.

It is important to also mention a further step of the DFT calculation, which involves optimisation of the supercell shape during the self-consistent procedure. The KS problem for electrons, given by Eq. 2.69, is solved self-consistently, each time for a varied position of ions, to yield the lowest-total-energy arrangement. This procedure needs to be conducted in two steps: first considering a rigid supercell with ions displaced within the cell, and then allowing the supercell to expand and contract to produce an optimal supercell spacing $|d_x|, |d_y|, |d_z|$.

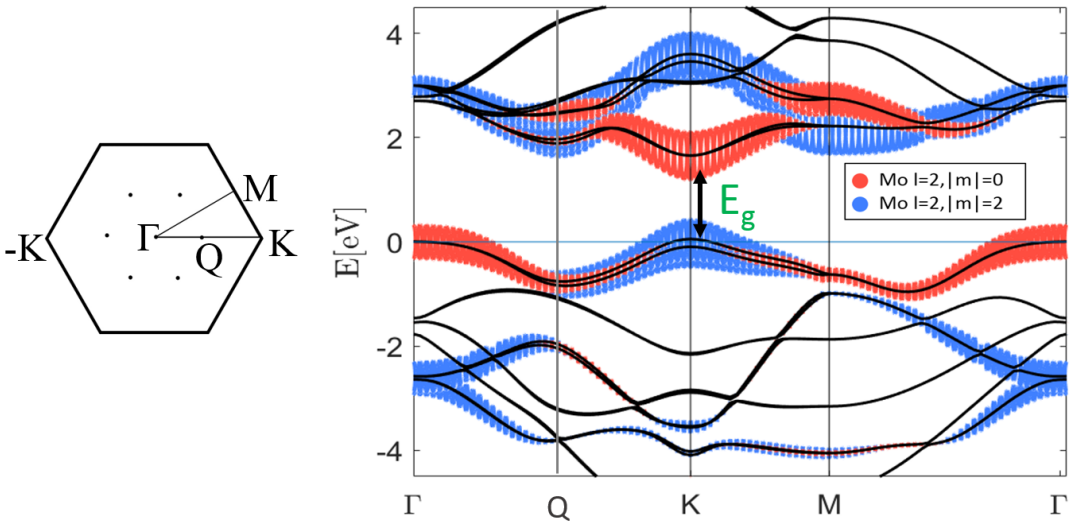

Figure 2.14: DFT band structure of MoS_2. (left) Chosen path in the BZ. (right) Band energies for the path shown on the left. Energies are marked with black lines, while the colorful overlapping patterns depict the orbital content of bands. The thickness of the pattern encodes the amount of orbital content. Colors label Mo orbitals for $m_d = 0$ (red) and $m_d = \pm 2$ (blue). The energy band gap is shown at $\boldsymbol{K}$ with a green symbol.

After this optimisation, the electronic density obtained in the self-consistent calculation is correct and can be used to calculate the band structure, as a last step. This step does not involve any self-consistent procedure, but performs a set of expectation value calculations for a chosen $\boldsymbol{k}$-point path in the BZ. Fig. 2.14. shows the resulting band structure and the path in BZ used to obtain it. Additional run-time parameters allow for extracting the orbital content of the bands, shown in Fig. 2.14 with colors for the Mo atoms. These results were obtained with the following values of the most important parameters mentioned above:

$$\begin{aligned} (|d_x|, |d_y|, |d_z|) &= (5.9077, 5.9077, 28.3459)\text{Bohr}, \\ E_{cut} &= 30.0\text{Ha}, \\ E_{cut}(PAW) &= 55.0\text{Ha}, \\ n_k &= 10, \end{aligned} \tag{2.77}$$

and the XC functional and has been chosen as the Perdew-Burke-Ernzerhof (PBE)

XC functional [135], and the projected augmented wave (PAW) method has been used [136, 137]. It is a standard choice to treat the core electrons on atoms. The simplest method is the norm-conserving method, which "freezes" the core electrons and only does the self-consistent calculation for valence electrons. The PAW method incorporates in it both the valence and the core electrons. It is more costly and requires an additional plane wave parameter, listed here as $E_{cut}(PAW)$, which has been chosen in a similar convergence study as E_{cut}. In the above calculation the spin-orbit (SO) coupling has been enabled, which produced the SO splitting of the bands.

As shown in Fig. 2.14., the direct energy gap E_g for bulk MoS_2 is located at $\boldsymbol{K}$, where the VB is made primarily of $m_d = \pm 2$ orbitals and the CB is made mainly of $m_d = 0$ orbital. This composition is reversed at $\boldsymbol{\Gamma}$. The VB and CB have an additional contribution of the p orbitals from the sulphur dimer. This orbital content motivates the choice of orbitals in the TB presented in section 4.1. The CB includes also an additonal minimum at $\boldsymbol{Q}$, which has a distinct orbital composition from $\boldsymbol{K}$. This shape of the CB around $\boldsymbol{Q}$ and $\boldsymbol{K}$ causes band nesting and the optical effects described also in section 4.1.

2.2.6 Configuration interaction method.

Methods more accurate than the mean-field approach are often needed, e.g. for studies of strongly-correlated systems or describing optical properties and excitations in the system. Configuration interaction (CI) treats the full interacting Hamiltonian, with the interacting part given by Eq. 2.57. We seek for a solution of the form of a linear combination of all possible configurations of N electrons on M SP orbitals (e.g. obtained from TB model). An example of a CI wavefunction for $N = 3$ electrons reads

$$\Psi_{CI}(N=3) = \sum_{pqr} A_{pqr} c_r^\dagger c_q^\dagger c_p^\dagger \left|0\right\rangle = \sum_{pqr} A_{pqr} \left|pqr\right\rangle , \tag{2.78}$$

where $p \neq q \neq r$ label SP states, including spin, and $|pqr\rangle$ is a single configuration of $N = 3$ electrons, which is a short notation for a single Slater determinant given in Eq.

2.54-2.56. Contrary to mean-field methods, which produced single Slater determinant solutions, CI eigenvectors are linear combinations of many Slater determinants. A_{pqr} in Eq. 2.78 needs to be determined through diagonalising the CI Hamiltonian.

The CI basis consists of all possible configurations of N electrons in M SP energy levels. These configurations can be categorised into blocks of different $S_z = (N_\uparrow - N_\downarrow)/2$ for $N_\uparrow$ ($N_\downarrow$) electrons with spin up (down). This allows for splitting the Hamiltonian into blocks to speed up the diagonalisation. The speed-up is needed as the number of configurations in the basis grows quickly with $N = N_\uparrow + N_\downarrow$ and $M = M_\uparrow + M_\downarrow$, as a price for accuracy in CI. The number of configurations can be calculated as

$$N_{conf} = \begin{pmatrix} M_\uparrow \\ N_\uparrow \end{pmatrix} \begin{pmatrix} M_\downarrow \\ N_\downarrow \end{pmatrix} \tag{2.79}$$

and the S_z subblock of the Hamiltonian is a $N_{conf} \times N_{conf}$ matrix.

I will now present examples of calculatng the matrix elements of the CI Hamiltonian, starting with the diagonal matrix element for an example $N = 3$ electron configuration $|a\downarrow b\downarrow c\uparrow\rangle$ (with electron spin explicitly stated), shown in Fig. 2.15 (most left). The SP part of the diagonal CI Hamiltonian matrix element reads

$$\begin{aligned} \langle a\downarrow b\downarrow c\uparrow| \hat{H}_{SP} |a\downarrow b\downarrow c\uparrow\rangle &= \sum_{p\sigma} \varepsilon_p \langle a\downarrow b\downarrow c\uparrow| c^\dagger_{p\sigma} c_{p\sigma} |a\downarrow b\downarrow c\uparrow\rangle \\ &= \sum_{p\sigma} \varepsilon_p \langle 0| c_{a\downarrow} c_{b\downarrow} c_{c\uparrow} c^\dagger_{p\sigma} c_{p\sigma} c^\dagger_{c\uparrow} c^\dagger_{b\downarrow} c^\dagger_{a\downarrow} |0\rangle \\ &= \varepsilon_a + \varepsilon_b + \varepsilon_c. \end{aligned} \tag{2.80}$$

The interacting part of the diagonal matrix element reads

$$\begin{aligned} \langle a\downarrow b\downarrow c\uparrow| \hat{H}_{ee} |a\downarrow b\downarrow c\uparrow\rangle &= \frac{1}{2} \sum_{pqrt\sigma\sigma'} \langle pq| V |rt\rangle \langle abc| c^\dagger_{p\sigma} c^\dagger_{q\sigma'} c_{r\sigma'} c_{t\sigma} |abc\rangle \\ &= \frac{1}{2} \sum_{pqrt\sigma\sigma'} \langle pq| V |rt\rangle \langle 0| c_{a\downarrow} c_{b\downarrow} c_{c\uparrow} c^\dagger_{p\sigma} c^\dagger_{q\sigma'} c_{r\sigma'} c_{t\sigma} c^\dagger_{c\uparrow} c^\dagger_{b\downarrow} c^\dagger_{a\downarrow} |0\rangle \\ &= \langle ab| V |ba\rangle - \langle ab| V |ab\rangle + \langle ac| V |ca\rangle + \langle bc| V |cb\rangle . \end{aligned} \tag{2.81}$$

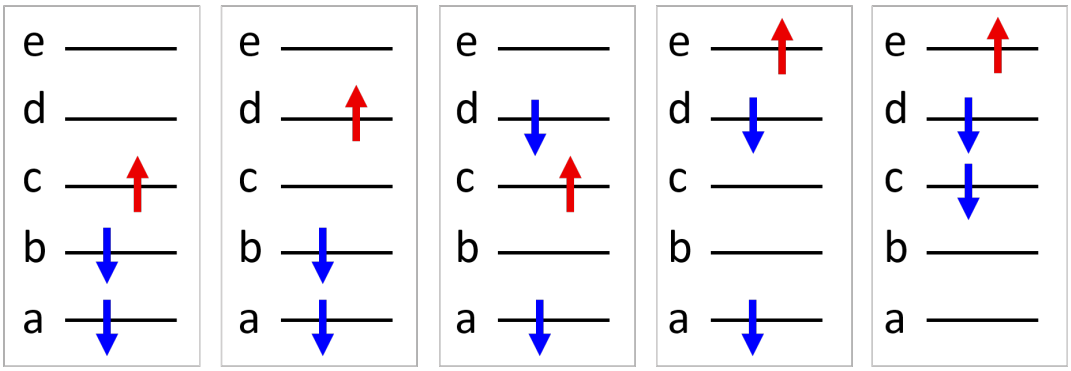

Figure 2.15: Example configurations of 3 electrons. Each panel depicts a single configuration mentioned in this section. Red (blue) arrows depict electrons with spin up (down), and black lines represent spin-degenerate energy levels (labelled with letters a-e).

The interacting term $\hat{H}_{ee}$ also produces off-diagonal elements, but a Coulomb operator cannot mix configurations different by more than two electron occupation, so many off-diagonal terms vanish and the matrix becomes sparse. We can categorise the off-diagonal terms into involving configurations different by 1 or 2 electrons. I will give two examples of both (bold symbols highlight the scattering electrons):

$$\begin{aligned}
\langle a\downarrow b\downarrow \boldsymbol{c}\uparrow|\,\hat{H}_{ee}\,|a\downarrow b\downarrow \boldsymbol{d}\uparrow\rangle &= \frac{1}{2}\sum_{pqrt\sigma\sigma'}\langle pq|\,V\,|rt\rangle\,\langle 0|\,c_{a\downarrow}c_{b\downarrow}\boldsymbol{c_{c\uparrow}}\;\;c^\dagger_{p\sigma}c^\dagger_{q\sigma'}c_{r\sigma'}c_{t\sigma}\boldsymbol{c^\dagger_{d\uparrow}}\;\;c^\dagger_{b\downarrow}c^\dagger_{a\downarrow}\,|0\rangle \\
&= \langle a\boldsymbol{c}|\,V\,|\boldsymbol{d}a\rangle + \langle b\boldsymbol{c}|\,V\,|\boldsymbol{d}b\rangle\,, \\
\langle a\downarrow\boldsymbol{b}\downarrow c\uparrow|\,\hat{H}_{ee}\,|a\downarrow\boldsymbol{d}\downarrow c\uparrow\rangle &= \frac{1}{2}\sum_{pqrt\sigma\sigma'}\langle pq|\,V\,|rt\rangle\,\langle 0|\,c_{a\downarrow}\boldsymbol{c_{b\downarrow}}c_{c\uparrow}c^\dagger_{p\sigma}c^\dagger_{q\sigma'}c_{r\sigma'}c_{t\sigma}c^\dagger_{c\uparrow}\boldsymbol{c^\dagger_{d\downarrow}}c^\dagger_{a\downarrow}\,|0\rangle \\
&= \langle a\boldsymbol{b}|\,V\,|\boldsymbol{d}a\rangle - \langle a\boldsymbol{b}|\,V\,|a\boldsymbol{d}\rangle + \langle c\boldsymbol{b}|\,V\,|\boldsymbol{d}c\rangle\,,
\end{aligned} \tag{2.82}$$

$$\begin{aligned}
\langle a\downarrow\boldsymbol{b}\downarrow\boldsymbol{c}\uparrow|\,\hat{H}_{ee}\,|a\downarrow\boldsymbol{d}\downarrow\boldsymbol{e}\uparrow\rangle &= \frac{1}{2}\sum_{pqrt\sigma\sigma'}\langle pq|\,V\,|rt\rangle\,\langle 0|\,c_{a\downarrow}\boldsymbol{c_{b\downarrow}}\boldsymbol{c_{c\uparrow}}\;\;c^\dagger_{p\sigma}c^\dagger_{q\sigma'}c_{r\sigma'}c_{t\sigma}\boldsymbol{c^\dagger_{e\uparrow}}\;\;\boldsymbol{c^\dagger_{d\downarrow}}c^\dagger_{a\downarrow}\,|0\rangle \\
&= \langle \boldsymbol{cb}|\,V\,|\boldsymbol{de}\rangle\,, \\
\langle \boldsymbol{a}\downarrow\boldsymbol{b}\downarrow c\uparrow|\,\hat{H}_{ee}\,|\boldsymbol{d}\downarrow\boldsymbol{e}\downarrow c\uparrow\rangle &= \frac{1}{2}\sum_{pqrt\sigma\sigma'}\langle pq|\,V\,|rt\rangle\,\langle 0|\,\boldsymbol{c_{a\downarrow}}\boldsymbol{c_{b\downarrow}}c_{c\uparrow}c^\dagger_{p\sigma}c^\dagger_{q\sigma'}c_{r\sigma'}c_{t\sigma}c^\dagger_{c\uparrow}\boldsymbol{c^\dagger_{e\downarrow}}\boldsymbol{c^\dagger_{d\downarrow}}\,|0\rangle \\
&= \langle \boldsymbol{ab}|\,V\,|\boldsymbol{ed}\rangle - \langle \boldsymbol{ab}|\,V\,|\boldsymbol{de}\rangle\,,
\end{aligned} \tag{2.83}$$

where all the configurations involved have been shown in Fig. 2.15 with spin down

(up) electrons marked with blue (red).

2.2.7 Exciton in configuration interaction method.

In order to study optical properties of materials, I will also consider excitations of electrons from a GS of a filled VB, induced by optical fields. Because the VB contains many electrons and the excitations involve only a few particles, I will consider a basis of excitation configurations. An example of a configuration for one excitation in the basis of SP states reads

$$|lm\sigma\rangle = c^{\dagger}_{m\sigma}c_{l\sigma}\,|GS\rangle = c^{\dagger}_{m\sigma}c_{l\sigma}\prod_{pinVB} c^{\dagger}_{p\uparrow}c^{\dagger}_{p\downarrow}\,|0\rangle\,. \tag{2.84}$$

An eigenstate of the CI Hamiltonian for basis of such configurations is a single exciton wavefunction

$$|X\rangle = \sum_{lm\sigma} A_{lm\sigma}\,|lm\sigma\rangle\,, \tag{2.85}$$

where the exciton wavefunction coefficients $A_{lm\sigma}$ are obtained from the eigenvalue problem in the form of a Bethe Salpeter equation [59]

$$\Big(\,(\varepsilon_{m\sigma}+\Sigma_{m\sigma})-(\varepsilon_{l\sigma}+\Sigma_{l\sigma})\,\Big)A_{lm\sigma}+\sum_{ij\sigma'}(V_{ljim}-V_{ljmi})\,A_{ij\sigma'}=EA_{lm\sigma} \tag{2.86}$$

where I will now derive the contributions from self energy Σ and the form of scattering matrix elements V_{ljim}, V_{ljmi}. I will start with the derivation of diagonal matrix elements of the CI Hamiltonian, which is diagonalised to give the solutions of Eq. 2.86. The energies of configurations in this case will be measured with respect to the energy of the GS, which for the example shown in Fig. 2.16 (left) can be calculated

as

$$\begin{aligned} E_{GS} = \langle GS|\, \hat{H}_{CI}\, |GS\rangle &= \sum_{p\sigma} \varepsilon_p \langle 0|\, c_{a\downarrow} c_{b\downarrow} c_{a\uparrow} c_{b\uparrow} c^\dagger_{p\sigma} c_{p\sigma} c^\dagger_{b\uparrow} c^\dagger_{a\uparrow} c^\dagger_{b\downarrow} c^\dagger_{a\downarrow}\, |0\rangle \\ &+ \frac{1}{2} \sum_{pqrt\sigma\sigma'} V_{pqrt} \langle 0|\, c_{a\downarrow} c_{b\downarrow} c_{a\uparrow} c_{b\uparrow} c^\dagger_{p\sigma} c^\dagger_{q\sigma'} c_{r\sigma'} c_{t\sigma} c^\dagger_{b\uparrow} c^\dagger_{a\uparrow} c^\dagger_{b\downarrow} c^\dagger_{a\downarrow}\, |0\rangle \\ &= 2\varepsilon_a + 2\varepsilon_b + \langle aa|\, V\, |aa\rangle + \langle bb|\, V\, |bb\rangle \\ &+ 4 \langle ab|\, V\, |ba\rangle - 2 \langle ab|\, V\, |ab\rangle\,, \end{aligned} \tag{2.87}$$

where $V_{pqrt} = \langle pq|\, V\, |rt\rangle$. An example excitation configuration (shown in Fig. 2.16 in the middle) then has the energy

$$\begin{aligned} E_{|bc\uparrow\rangle} = \langle bc\uparrow|\, \hat{H}_{CI}\, |bc\uparrow\rangle &= \sum_{p\sigma} \varepsilon_p \langle 0|\, c_{a\downarrow} c_{b\downarrow} c_{a\uparrow} c_{c\uparrow} c^\dagger_{p\sigma} c_{p\sigma} c^\dagger_{c\uparrow} c^\dagger_{a\uparrow} c^\dagger_{b\downarrow} c^\dagger_{a\downarrow}\, |0\rangle \\ &+ \frac{1}{2} \sum_{pqrt\sigma\sigma'} V_{pqrt} \langle 0|\, c_{a\downarrow} c_{b\downarrow} c_{a\uparrow} c_{c\uparrow} c^\dagger_{p\sigma} c^\dagger_{q\sigma'} c_{r\sigma'} c_{t\sigma} c^\dagger_{c\uparrow} c^\dagger_{a\uparrow} c^\dagger_{b\downarrow} c^\dagger_{a\downarrow}\, |0\rangle \\ &= 2\varepsilon_a + \varepsilon_b + \varepsilon_c \\ &+ \langle aa|\, V\, |aa\rangle + 2 \langle ab|\, V\, |ba\rangle - \langle ab|\, V\, |ab\rangle \\ &+ 2 \langle ac|\, V\, |ca\rangle - \langle ac|\, V\, |ac\rangle + \langle bc|\, V\, |cb\rangle\,. \end{aligned} \tag{2.88}$$

The energy difference between the GS and configuration $|bc\uparrow\rangle$ then reads

$$\begin{aligned} E_{|bc\uparrow\rangle} - E_{GS} &= - \langle bb|\, V\, |bb\rangle - 2 \langle ab|\, V\, |ba\rangle + \langle ab|\, V\, |ab\rangle \\ &+ 2 \langle ac|\, V\, |ca\rangle - \langle ac|\, V\, |ac\rangle + \langle bc|\, V\, |cb\rangle + \varepsilon_c - \varepsilon_b \\ &= \varepsilon_c - \varepsilon_b + \Sigma_c - \Sigma_b - \Big(\langle bc|\, V\, |cb\rangle - \langle bc|\, V\, |bc\rangle \Big), \\ &= (\varepsilon_c + \Sigma_c) - (\varepsilon_b + \Sigma_b) - V_{vertex}(b, c), \end{aligned} \tag{2.89}$$

where Σ stands for self-energy as in Eq. 2.66 and $V_{vertex} = V_D - V_X$ is a vertex correction, which prevents overcounting while using self energy terms, and it consists of the direct term $V_D = \langle bc|\, V\, |cb\rangle$ and the exchange term $V_X = \langle bc|\, V\, |bc\rangle$. Eq. 2.89 can be regarded as the difference of the interaction of the excited electron and the

left-over hole with the filled VB, corrected by the interaction of the electron with the hole itself. This situation is pictured in Fig. 2.16, using filled (empty) symbols for electrons (holes) with spin up (down) in red (blue), and with the Fermi level marked with a green dashed line. In configuration $|bc\uparrow\rangle$ an electron with spin up has been promoted above the Fermi level and it no longer occupies the level b (only an electron with spin down is still present), which creates a hole below the Fermi level with an opposite spin to the spin of the missing electron (hole spin-down marked with an empty blue arrow). The indices labelling the configurations can be regarded as the indices of levels hosting an electron-hole pair.

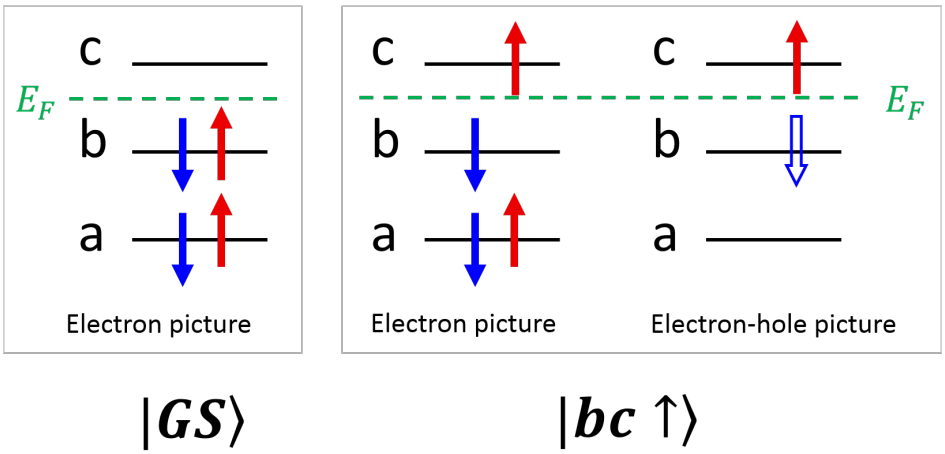

Figure 2.16: (left) GS configuration, with all levels filled with electrons (solid arrows) below the Fermi level E_F. (right) An excitation schematically drawn in the electron and electron-hole picture. In the electron picture, when an electron is promoted above the Fermi energy, an empty level is left behind. The electron-hole picture regards the empty level as a positive charge - a hole (empty arrow), which has an opposite spin to the missing electron.

The matrix element I considered so far in Eq. 2.88 enter the CI Hamiltonian on a diagonal. I will now demonstrate the construction of an off-diagonal matrix element between the excitation configurations. Let us consider a scattering of an arbitrary configuration $|ad\uparrow\rangle$ or $|ad\downarrow\rangle$ into configuration $|bc\uparrow\rangle$ (all shown in Fig. 2.17), given

by

$$\begin{aligned}
\langle bc\uparrow|\,\hat{H}_{ee}\,|ad\uparrow\rangle &= \frac{1}{2}\sum_{pqrt\sigma\sigma'} V_{pqrt}\,\langle GS|\,c^{\dagger}_{b\uparrow}c_{c\uparrow}c^{\dagger}_{p\sigma}c^{\dagger}_{q\sigma'}c_{r\sigma'}c_{t\sigma}c^{\dagger}_{d\uparrow}c_{a\uparrow}\,|GS\rangle \\
&= \langle ac|\,V\,|bd\rangle - \langle ac|\,V\,|db\rangle = V_D - V_X, \\
\langle bc\uparrow|\,\hat{H}_{ee}\,|ad\downarrow\rangle &= \frac{1}{2}\sum_{pqrt\sigma\sigma'} V_{pqrt}\,\langle GS|\,c^{\dagger}_{b\uparrow}c_{c\uparrow}c^{\dagger}_{p\sigma}c^{\dagger}_{q\sigma'}c_{r\sigma'}c_{t\sigma}c^{\dagger}_{d\downarrow}c_{a\downarrow}\,|GS\rangle \\
&= \langle ac|\,V\,|bd\rangle = V_D,
\end{aligned} \tag{2.90}$$

where the positive and negative terms are the direct $V_D = \langle ac|\,V\,|bd\rangle$ and exchange $V_X = \langle ac|\,V\,|db\rangle$ terms respectively. The scattering processes for both cases have been shown in Fig. 2.17 in green arrows, with solid (dashed) lines correspinding to direct V_D (exchange V_X) terms. V_X is only present in the case of the same spin scattering, and the nature of the Coulomb operator $\hat{V}_{ee}$ does not allow for it in case of an opposite spin scattering.

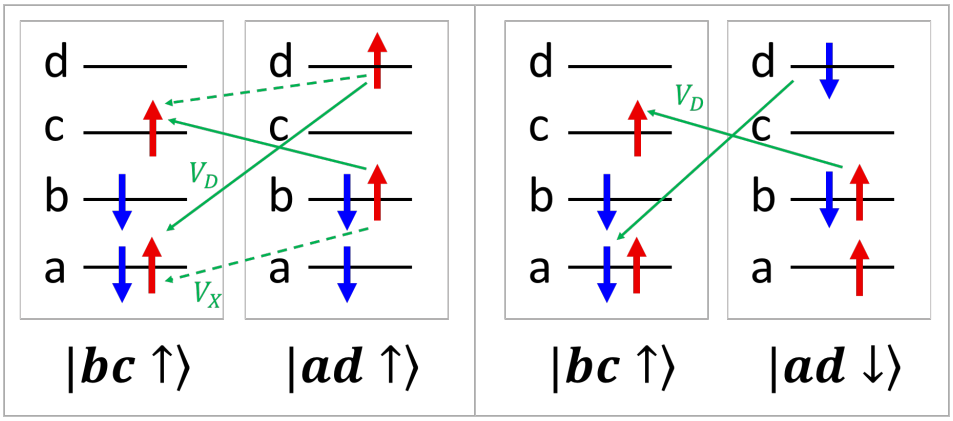

Figure 2.17: Example off-diagonal matrix elements for configurations. (left) Same spin configurations. (right) Opposite spin configurations. When the spin of scattering configurations differs, only the direct element (V_D) is possible. For the same spin configurations also an exchange term is allowed (V_X).

It is important to notice that the SP level indices labelling the configurations do not enter the final matrix elements in the same order as they are written for configurations. This is because the configurations here are labelled with electron and hole indices and the Coulomb scattering matrix elements are defined here solely for electrons. The green arrows in Fig. 2.17 demonstrate this fact by showing that electrons in levels b and d will finally occupy levels a and d.

2.3 Numerical methods.

In this section I will present the numerical methods and reference available software that I have used to obtain the results included in this thesis.

I have written my own *Fortran90* programs that create the TB Hamiltonians described in section 2.1, the HF Hamiltonian given in section 2.2.3 as well as the CI Hamiltonian given in section 2.2.6 and 2.2.7. The most complex CI calculations were done using the *QNano* code developped in the *C++* language at the University of Ottawa [138], which offered better efficiency than my own procedures. My own TB results were used as an input to *QNano*.

For diagonalisation of the Hamiltonian matrices I used several available packages, described in section 2.3.1, which were chosen dependent on the size of the matrices, number of sought eigenvalues and available resources on my own computer, on the Quantum Theory Group cluster at the University of Ottawa and within the Compute Canada clusters.

Often, for time and memory efficiency, I turned to multi-threading options for my calculations. The interfaces that I used have been described in section 2.3.2. Section 2.3.3 includes the description of numerical integration methods needed to solve the many-body Hamiltonians given in 2.2.6 and 2.2.7. The results from a DFT calculation are included only in section 2.2.5 and they have all been performed with *Abinit*.

2.3.1 Matrix diagonalisation.

I will describe here three methods that I used commonly to diagonalise matrices. If the whole eigenvalue spectrum was needed, or in case of small matrices which can be quickly fully diagonalised, I used *LAPACK* routines [139]. It is an open-source *Fortran90* library of routines dedicated to linear algebra, which allows to solve systems of linear equations and eigenvalue problems. It uses Basic Linear Algebra Subprograms (*BLAS*) available in most programming languages.

The most often used *LAPACK* routines are DSYEV and ZHEEV, for a symmetrix matrix of type *double* and hermitian matrix of type *complex double* respectively. These

routines are based on reducing the matrix into a tridiagonal form to perform the QR algorithm [140].

Some of the TB calculations produced Hamiltonian matrices too large for full diagonalisation. I have considered MoS_2 nanoflakes of up to 800×400 (as defined in section 6.1.1), which corresponds to $\approx 1.3 \cdot 10^6$ atoms and results in matrices of up to $3.8 \cdot 10^6$ in dimension. Similarly, the largest CI calculation that I have performed involved all configurations for $N_\uparrow = 3, N_\downarrow = 3$ electrons ($N = 6$ electrons with $S_z = 0$) on $M_\uparrow = 30, M_\downarrow = 30$ states ($M = 60$ states in total), which gives $N_{conf} \approx 1.6 \cdot 10^7$ and a Hamiltonian matrix $N_{conf} \times N_{conf}$ (as defined in section 2.2.6), taking up to $350GB$ of memory.

In case of these large matrices I used two methods: *FEAST* algorithm within the *Math Kernel Library* (*MKL*) by Intel [141] and *Scalable Library for Eigenvalue Problem Computations* (*SLEPc*) routines within the *Portable, Extensible Toolkit for Scientific Computation* (*PETSc*) [142].

The *FEAST* algorithm, as a part of *MKL*, providing efficient math processing routines, is a high performance routine for eigenvalue problems, insipred by the density-matrix representation and contour integration techniques [141]. It takes a sparse matrix as an input and delivers eigenvalues within a chosen energy range. It however requires an initial guess of the number of eigenvalues within that range. I found it useful for finding eigenvalues of the TB Hamiltonian, which can be scaled from small to large systems and makes it easy to provide expectations for the energy spectrum needed to input a guess. It is not well suited for the CI calculations unless a mean-field approach is used to provide a guess of the energy spectrum.

PETSc is a toolkit for creating data structures and scalable scientific computations, which includes *SLEPc*, offering projection-based diagonalisaton techniques, such as Krylov-Schur and Jacobi-Davidson methods [143, 144]. *SLEPc* routines have been implemented within the *QNano* code, which made it easy to use together with the large scale CI calculations done with *QNano* as well. The benefit of *SLEPc* methods for CI is that a variety of input parameters allow to search for eigenvalues within

a desired range of energies as well as to input a number of eigenvalues closest to a chosen energy.

2.3.2 High performance parallel computing.

In interest of time and memory efficiency, I have used two open source parallel computing interfaces, available in many programming languages, *Open Multi Processing* (*OpenMP*) [145] and *Message Passing Interface* (*MPI*) [146]. They allow for exploiting the many nodes and cores available through Compute Canada platform.

OpenMP is a multi-thread method, which uses a parent thread to divide tasks between worker threads. They run their tasks concurrently, thus saving considerable amount of time. *OpenMP* uses multiple threads with shared memory, which means that all the threads access the same variables to read inputs and write outputs, unless they are specified as private for a thread. This requires care when handling variables to avoid overwriting memory and memory access conflicts between threads. I have made use of the *OpenMP* in my own codes in order to enable parallel computing of the scattering Coulomb matrix elements for CI.

The *MPI* protocol creates multiple processes, which do not share memory. The program invoking *MPI* is responsible for distributing the memory between the processes, for combining their results as well as for provoking the communication between processes, when needed. I have used *MPI*, when utilising the *SLEPc* and *FEAST* diagonalisation routines.

Additionally, for evaluation of numerically demanding Coulomb scattering matrix elements implemented in my own *Python* code, I have used the *multiprocessing* package, similar in operation to *OpenMP*.

2.3.3 Numerical integration of scattering Coulomb matrix elements.

I explain here the two approaches I have taken to obtain the scattering Coulomb matrix elements given in Eq. 2.58 for two different projects: magnetoexcitons of

massive Dirac fermions (mDf) described in chapter 5 and many electron properties of MoS_2 parabolic QDs described in chapter 6.

The energy spectrum of mDf in strong magnetic field exhibits the Landau level (LL) structure, which can be expressed as 2D harmonic oscillator (HO) states (as explained in detail in chapter 5.). The HO basis is then used to calculate the scattering Coulomb matrix elements between the electrons in LLs, which can be obtained analytically as [147, 148]

$$\begin{aligned}\langle n_1' m_1', n_2' m_2' | \, V \, | n_2 m_2, n_1 m_1 \rangle = \frac{1}{l} \frac{\delta_{L_L, L_R} (-1)^{n_2'+m_2'+n_2+m_2}}{\sqrt{n_1'! m_1'! n_1! m_1! n_2'! m_2'! n_2! m_2!}} \\ \cdot \sum_{p_1=0}^{\min(n_1, n_1')} p_1! \binom{n_1'}{p_1} \binom{n_1}{p_1} \sum_{p_2=0}^{\min(m_1, m_1')} p_2! \binom{m_1'}{p_2} \binom{m_1}{p_2} \\ \cdot \sum_{p_3=0}^{\min(n_2, n_2')} p_3! \binom{n_1'}{p_3} \binom{n_2}{p_3} \sum_{p_4=0}^{\min(m_2, m_2')} p_4! \binom{m_2'}{p_4} \binom{m_2}{p_4} \\ \left(-\frac{1}{2}\right)^p \Gamma(p + \frac{1}{2}),\end{aligned} \tag{2.91}$$

where $L_R = (m_1 + m_2) - (n_1 + n_2)$ and $L_L = (m_1' + m_2') - (n_1' + n_2')$ are total angular momenta for the electron pair before and after scattering ($L_L = L_R$) , and $p = n_1' + n_2' + m_1 + m_2 - p_1 - p_2 - p_3 - p_4$. The expression in Eq. 2.91 involves multiplications and divisions by large numbers, which leads to accumulation of numerical error. Such expression can only be evaluated using variables with large precision, not available in every programming language. In order to evaluate this expression I have written my own *Python* code using the *mpmath* package, which allows for arbitrarily large precision numbers. Because increasing the precision order increases the computation time, I treated it as a parameter adjusted by comparing the result of a single integral to a result obtained from my own code in another computing software, *Mathematica*. This is because *Mathematica* evaluates expressions based on analytical transformations, which allows for reducing the numerical error. The price for accuracy in *Mathematica* is long computation time, which motivated me to use

a *Python* code with the *multiprocessing* interface and with routinely checks against results from *Mathematica*. It allowed for better efficiency, while keeping the accuracy level on a par with the accuracy in *Mathematica*.

I needed to perform another type of integral to calculate the Coulomb scattering matrix elements for electrons in an MoS_2 parabolic QD. The SP energy levels of an QD are expressed in the site TB basis, so the interaction between the SP states can be expressed using the site basis (as explained in detail in section 6.3). Coulomb scattering matrix elements in the orbital basis are therefore needed:

$$\begin{aligned}\langle ij|\, V\, |kl\rangle &= \int \phi_i^*(\boldsymbol{r})\phi_j^*(\boldsymbol{r}')\frac{e^2}{\kappa\,|\boldsymbol{r}-\boldsymbol{r}'|}\phi_k(\boldsymbol{r}')\phi_l(\boldsymbol{r})d\boldsymbol{r}d\boldsymbol{r}' \\ &= \int \phi_i^*(\widetilde{\boldsymbol{r}})\phi_j^*(\widetilde{\boldsymbol{r}}')\frac{2}{\left|\widetilde{\boldsymbol{r}}-\widetilde{\boldsymbol{r}}'\right|}\phi_k(\widetilde{\boldsymbol{r}}')\phi_l(\widetilde{\boldsymbol{r}})d\widetilde{\boldsymbol{r}}d\widetilde{\boldsymbol{r}}' \quad [Ry]\,,\end{aligned} \tag{2.92}$$

where i, j, k, l label atomic orbitals and $\widetilde{\boldsymbol{r}} = \boldsymbol{r}/a_0$ and a_0 is the Bohr radius. To evaluate this expression I used the Slater-type orbital (STO) form of the wavefunctions $\phi(\boldsymbol{r})$ [149]:

$$\phi_{STO}^{l,m,n}(\boldsymbol{r},\zeta) = Y_l^m(\varphi,\theta)R_n(r,\zeta), \tag{2.93}$$

where $R_n(r,\zeta)$ is the radial part of the wavefunction given by

$$R_n(r,\zeta) = N_{norm}r^{n-1}e^{-\zeta r}, \tag{2.94}$$

where r is in units of Bohr radius a_0, constant ζ depends on the chemical element and $N_{norm} = (2\zeta)^n\sqrt{\frac{2\zeta}{(2n)!}}$ [149]. ζ for Mo and S atoms are $\zeta_{Mo} = 3.111$ and $\zeta_S = 1.827$ [149, 150].

The 6 dimensional integral in Eq. 2.92 is difficult to calculate accurately with a straight-forward implementation. For correct results, an adapted point mesh is needed, which is computationally demanding. To tackle this problem, I have used an existing routine for numerical integration *fgsl_monte_vegas*, which uses the *Vegas* algorithm, implemented within the *GNU Scientific Library* (*GSL*) [151] with a *Fortran90* interface (*FGSL*). This routine performs a multidimensional integral using a

Monte-Carlo method, which involves large number of integrand function calls for randomly chosen points from a defined mesh. The *Vegas* algorithm optimises the choice of the mesh and is based on importance sampling. The points are selected from the probability distribution of the integrand to ensure that the highest concentration of points is located in regions making the largest contribution to the value of the integral. Within the *Vegas* steps, a preliminary result is obtained for a coarse mesh, which allows for producing a histogram of the integrand and redefining a new denser adapted mesh.

Chapter 3

Energy gap of hexagonal graphene quantum dots

In this chapter I will show how the spectrum of hexagonal graphene quantum dots (HGQDs) can be calculated efficiently after decomposing them into 1D rings [152]. Electronic properties of 1D rings can be solved for exactly.

Because of the distinct edge termination of zigzag-edged HGQDs (ZHGQDs) and armchair-edged HGQDs (AHGQDs), the energy gap has different origin for these QDs and it causes the gap oscillation with size shown in Fig. 2.9 [152]. The following sections explain the formation of the energy gap in ZHGQDs and AHGQDs based on the edge termination contribution.

To describe the electronic properties of HGQDs, a NN one-orbital TB model of p_z electrons in carbon atoms in graphene will be used. This model implicitly assumes passivation of p_x, p_y dangling bond orbitals by hydrogen atoms, leaving p_z orbitals unaffected [153]. This choice is justified by the excellent agreement of the TB model with energy gaps obtained within DFT (Fig. 3.1) [152]. The hopping integral t for the NN TB model has been fit by matching the energy gaps obtained within DFT the TB model for benzene (first data point). The rest of the data points has been obtained independently with these two methods and with the use of the previously fitted value of t. The results of both methods agree extremely well, which validates

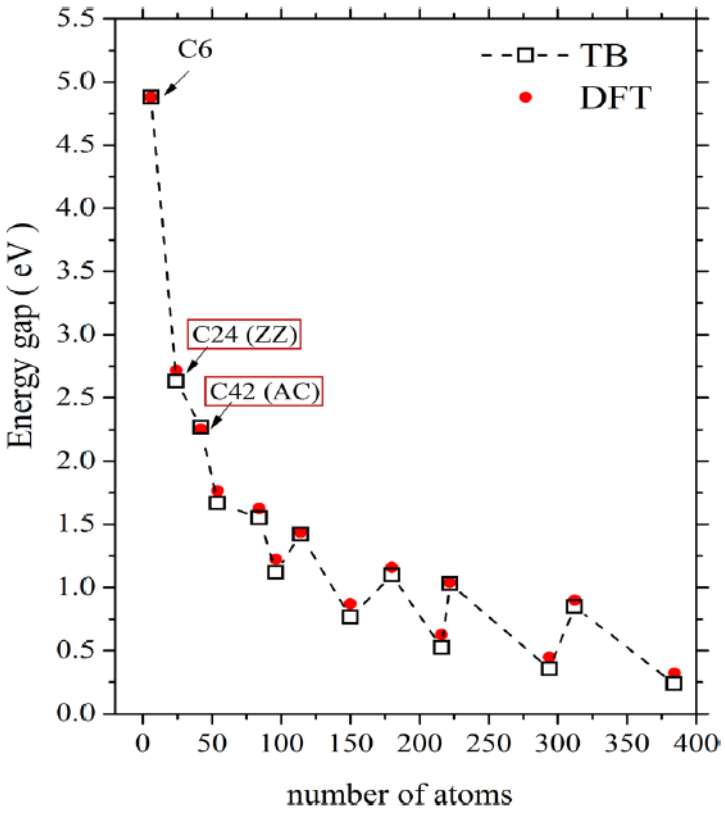

Figure 3.1: Comparison of the energy gap of GQDs obtained from NN TB model and DFT methods. The hopping element t has been fot for the first data point (benzene) and used to obtain remaining TB energy gaps.

the simple NN TB model that excludes the edge passivation.

3.1 Zigzag-edged graphene quantum dot: coronene.

Any ZHGQD can be decomposed into concentric 1D rings of carbon atoms, which are linked together, as shown in Fig. 3.2 a). Fig. 3.2 b) shows how a 24-atom ZHGQD (Z24), called coronene, can be regarded as two concentric rings of 6 and 18 atoms each. Let us call them ring I and ring II, for the inner and outer ring respectively (shown in Fig. 3.2 b)).

The SP TB Hamiltonian for coronene reads

$$\hat{H}_{Z24} = t \sum_{<i,j>\sigma} c^{\dagger}_{i\sigma} c_{j\sigma}, \tag{3.1}$$

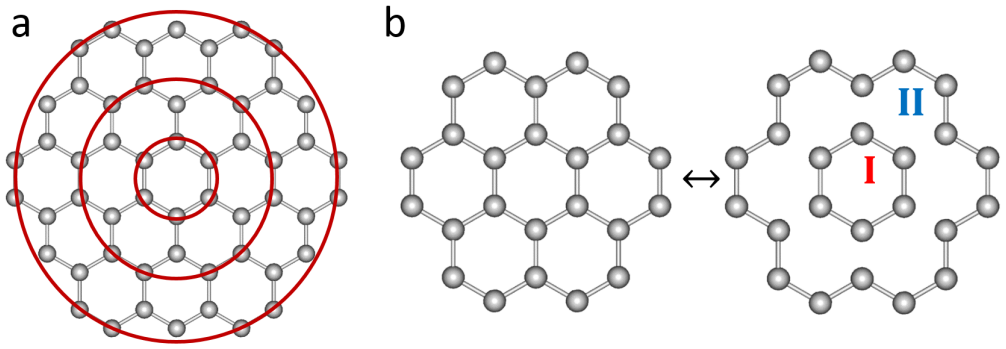

Figure 3.2: a) Decomposition of a HGQD into concentric rings (red). b) Coronene regarded as two concentric rings (I and II).

where i, j labels sites and it can be decomposed into three terms:

$$\hat{H}_{Z24} = \hat{H}_I + \hat{H}_{II} + \tau \hat{V}_{I-II}, \tag{3.2}$$

where $\hat{H}_I$ and $\hat{H}_{II}$ are Hamiltonians for 1D periodic rings of atoms:

$$\begin{aligned} \hat{H}_I &= t \sum_{i=1,\sigma}^{N_I} \left(c_{i\sigma}^{\dagger} c_{i+1\sigma} + h.c. \right), \\ \hat{H}_{II} &= t \sum_{i=1,\sigma}^{N_{II}} \left(c_{i\sigma}^{\dagger} c_{i+1\sigma} + h.c. \right), \end{aligned} \tag{3.3}$$

and $N_I = 6$ ($N_{II} = 18$) for ring I (II), t is the hopping integral and the definition of $\hat{V}_{I-II}$ needs to be determined (the strength of coupling is controlled with τ). The eigensolutions of the Hamiltonians in Eq. 3.3 are Bloch functions

$$\begin{aligned} \Psi_I^k &= \frac{1}{\sqrt{N_I}} \sum_{l=0,\sigma}^{N_I-1} e^{ikal} \psi_l, \\ \Psi_{II}^q &= \frac{1}{\sqrt{N_{II}}} \sum_{m=0,\sigma}^{N_{II}-1} e^{iqam} \psi_m, \end{aligned} \tag{3.4}$$

where ψ_i are p_z orbitals on sites, a is lattice constant and

$$\begin{aligned} k_n &= \frac{2\pi}{N_I a} n = \frac{2\pi}{6a} n, n \in \mathbb{Z}, \\ q_{n'} &= \frac{2\pi}{N_{II} a} n' = \frac{2\pi}{18a} n', n' \in \mathbb{Z}. \end{aligned} \tag{3.5}$$

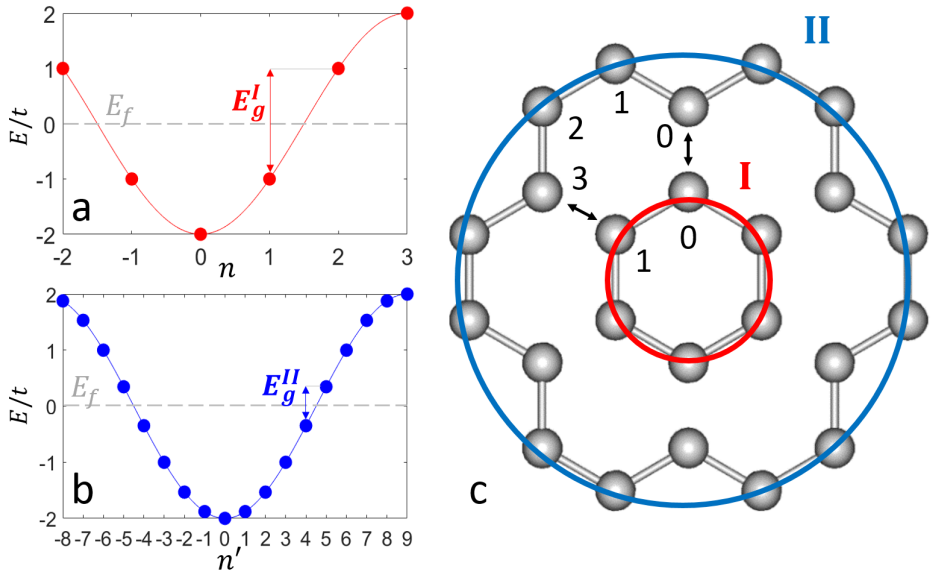

Figure 3.3: Energy spectrum (in the units of t) of ring a) I and b) II. The size of the ring determines the number of states n, n'. Energy gap of each ring E_g^I, E_g^{II} is marked. Fermi level is marked with E_f. c) Coupling rule for both rings (see text for details).

The eigenenergies for ring I and II are analytical:

$$\begin{aligned} E_I(k) &= -2t \cos ka, \\ E_{II}(q) &= -2t \cos qa, \end{aligned} \tag{3.6}$$

which has been shown in Fig. 3.3 a)-b) for both rings. At half filling, the Fermi level E_f is at 0 and the conduction and valence band edge energies are

$$\begin{aligned} E_V^{ring}(N) &= 2t \cos\left(\frac{2\pi}{N} \frac{\frac{N}{2} - 1}{2}\right), \\ E_C^{ring}(N) &= 2t \cos\left(\frac{2\pi}{N} \frac{\frac{N}{2} + 1}{2}\right), \end{aligned} \tag{3.7}$$

for a ring of N sites. For large N the energy gap becomes

$$E_g^{ring} = E_C^{ring} - E_V^{ring} \approx \frac{4t\pi}{N} \sin\left(\pi\left(\frac{1}{2} - \frac{1}{N}\right)\right) \sim \frac{1}{N} \sim \frac{1}{R} \sim \frac{1}{\sqrt{N_{dot}}}, \tag{3.8}$$

where the gap E_g^{ring} is inversely proportional to the radius of the ring R, which depends on the number of atoms enclosed within the dot marked by that ring as $\frac{1}{\sqrt{N_{dot}}}$.

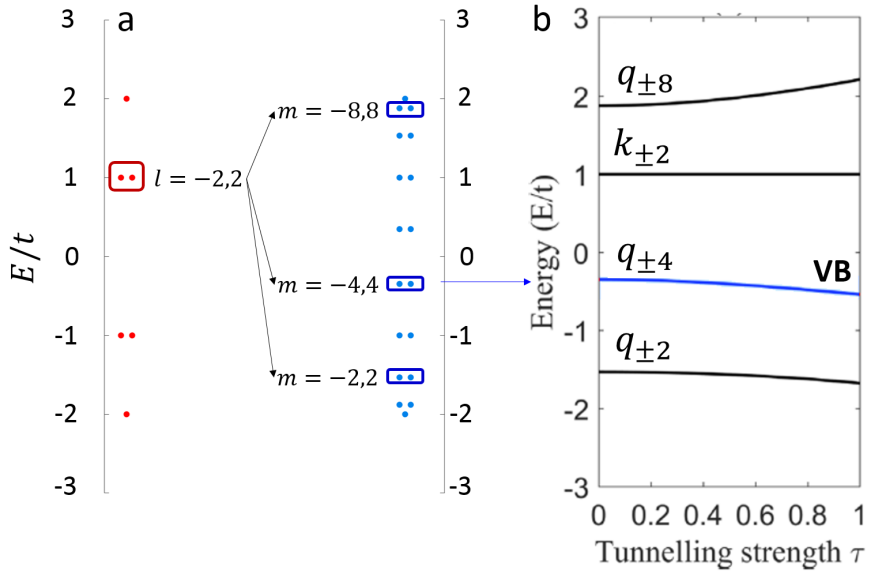

Figure 3.4: a) Levels from both rings (marked with boxes, red and blue for ring I and II) given in Eq. 3.10e couple. b) Resulting energy levels of the coupled block as the tunneling is turned on with τ. Blue energy becomes the VB of Z24.

I will now determine the coupling term $\hat{V}_{I-II}$ using the form of the Bloch wavefunctions given in Eq. 3.4. The coupling becomes

$$\begin{aligned} \left\langle \Psi_I^k \right| \hat{V}_{I-II} \left| \Psi_{II}^q \right\rangle &= -\frac{t}{\sqrt{6 \cdot 18}} \sum_{l=0}^{5} \sum_{m=0}^{17} e^{-ikal} e^{iqam} \left\langle \psi_l \right| \hat{V}_{I-II} \left| \psi_m \right\rangle \\ &= -\frac{t}{\sqrt{6 \cdot 18}} \sum_{l=0}^{5} e^{-i(k-3q)al} = -\frac{t}{\sqrt{3}} \delta_{k,\{3q,3q\pm\frac{2\pi}{a}\}}, \end{aligned} \tag{3.9}$$

where the tunneling matrix element $\left\langle \psi_l \right| \hat{V}_{I-II} \left| \psi_m \right\rangle$ is only nonzero for NN pairs of atoms $(0_I, 0_{II}), (1_I, 3_{II})$, etc. (as shown in Fig. 3.3 c)), so $\left\langle \psi_l \right| \hat{V}_{I-II} \left| \psi_m \right\rangle = \delta_{m,3l}$. The selection rule $k = \{3q, 3q \pm \frac{2\pi}{a}\}$ in Eq. 3.9 enables block diagonal form of the

Z24 Hamiltonian in Eq. 3.1 in the basis of plane waves labelled by k, q, because only some k_n and $q_{n'}$ couple. Using Eq. 3.9, the groups of coupled k_n and $q_{n'}$ (eq. 3.5) are

$$|I, k_{-2}\rangle \rightarrow |II, q_{-8}\rangle, |II, q_{-2}\rangle, |II, q_4\rangle, \tag{3.10a}$$

$$|I, k_{-1}\rangle \rightarrow |II, q_{-7}\rangle, |II, q_{-1}\rangle, |II, q_5\rangle, \tag{3.10b}$$

$$|I, k_0\rangle \rightarrow |II, q_{-6}\rangle, |II, q_0\rangle, |II, q_6\rangle, \tag{3.10c}$$

$$|I, k_1\rangle \rightarrow |II, q_{-5}\rangle, |II, q_1\rangle, |II, q_7\rangle, \tag{3.10d}$$

$$|I, k_2\rangle \rightarrow |II, q_{-4}\rangle, |II, q_2\rangle, |II, q_8\rangle, \tag{3.10e}$$

$$|I, k_3\rangle \rightarrow |II, q_{-3}\rangle, |II, q_3\rangle, |II, q_9\rangle, \tag{3.10f}$$

where the boxed groups produce unique subblocks in the Hamiltonian.

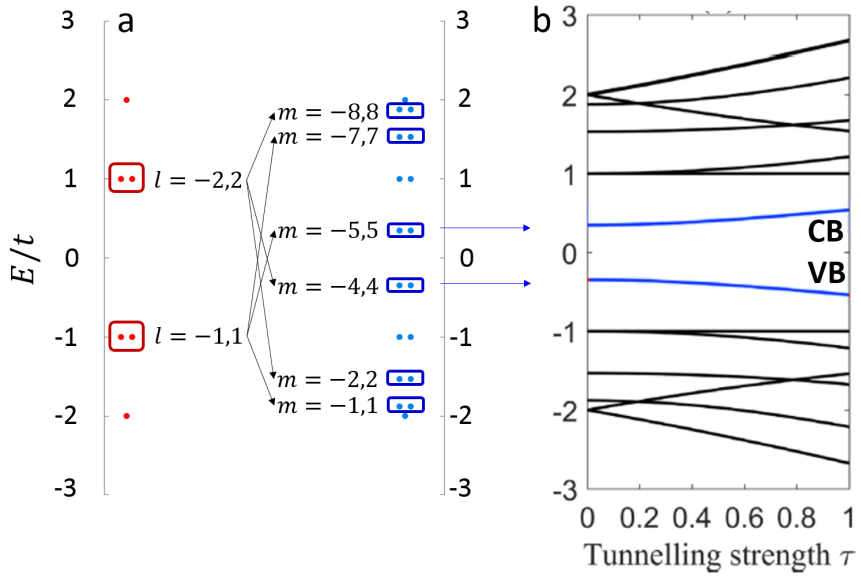

Figure 3.5: a)Energy of states within both rings. Chosen sets of states from both rings couple. b) Resulting energy levels of Z24 as the tunneling is turned on with τ. Blue levels mark VB and CB of Z24.

The eigenvalues of the original 24×24 Hamiltonian can therefore be obtained by diagonalising four 4×4 blocks. Each block includes the diagonal energies $E_I(k)$ and $E_{II}(q)$ and the offdiagonal terms $\langle \Psi_I^k | \hat{V}_{I-II} | \Psi_{II}^q \rangle$, e.g. the block in the basis of states

given in Eq. 3.10e (shown in Fig. 3.4) reads

$$t\begin{pmatrix} 1 & -\frac{\tau}{\sqrt{3}} & -\frac{\tau}{\sqrt{3}} & -\frac{\tau}{\sqrt{3}} \\ -\frac{\tau}{\sqrt{3}} & -0.3472 & 0 & 0 \\ -\frac{\tau}{\sqrt{3}} & 0 & -1.532 & 0 \\ -\frac{\tau}{\sqrt{3}} & 0 & 0 & 1.879 \end{pmatrix}, \tag{3.11}$$

where τ is the coupling strength between the rings. Fig. 3.4 a) and b) shows the evolution of the eigenvalues of the block given in Eq. 3.11 as a function of τ. As the bottom of the CB state of ring I couples to the top of the VB state of ring II, the energies evolve to give a subset of the coronene's energy levels. The level marked in blue in Fig. 3.4 b) originates in the top of the VB of the ring II and becomes the top of the VB of coronene. Fig. 3.5 shows the formation of both the VB and the CB for coronene from states given in Eq. 3.10d and 3.10e.

3.2 1D Lieb lattice.

In order to develop the same approach for an AHGQD, we need to consider the atoms that appear on the edges and surround the inner ZHGQD made of rings I and II. I will consider here the smallest AHGQD, A42. The atoms making the armchair edge are grouped into six three-atom clusters, one of which has been circled with a dashed green ellipse in Fig. 3.6. These clusters make up a periodic lattice with a three-atom basis - the 1D Lieb lattice [154], marked in Fig. 3.6 b) as a green circle, constituting the ring III of A42.

I start with considering a single cluster and its TB solution. Only tunneling between the centre atom and its NN is present, which generates an energy spectrum $E_u = \{-1, 0, 1\}$ in the units of t. The presence of a zero-energy state is typical of a

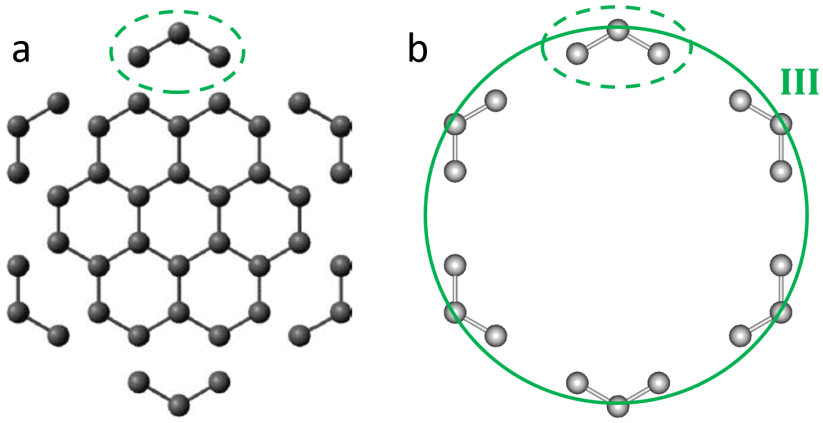

Figure 3.6: 1D Lieb lattice on the edge of an armchair-edged graphene quantum dot. a) Single cluster and b) ring of clusters.

Lieb lattice and plays an important role for this problem. All eigenvectors are:

$$\psi_{u=\pm1} = \frac{1}{\sqrt{2}} \begin{pmatrix} \frac{1}{\sqrt{2}} \\ \pm 1 \\ \frac{1}{\sqrt{2}} \end{pmatrix}, \tag{3.12a}$$

$$\psi_{u=0} = \frac{1}{\sqrt{2}} \begin{pmatrix} -1 \\ 0 \\ 1 \end{pmatrix}. \tag{3.12b}$$

Interestingly, the wavefunction of the state at zero energy given in Eq. 3.12b is localised on the tips of the cluster, i.e. $\psi_{u=0} = \frac{1}{\sqrt{2}}(-\phi_0 + \phi_2)$.

I now consider all clusters made into a periodic 1D lattice. The Bloch wavefunction of ring III reads

$$\Psi^{pu}_{III} = \frac{1}{\sqrt{6}} \sum_{j=0}^{5} e^{ip\cdot 5aj} \psi_{uj}, \tag{3.13}$$

where j labels clusters and the periodicity is present over a $5a$ distance (distance along the lattice bonds), present in the exponential factor. The wavevector in Eq. 3.13 is given by $p = \frac{2\pi}{6\cdot 5a}$.

In order to couple ring III to the inner rings, we need to determine the coupling between them. Let us start with the coupling $\hat{V}_{II-III}$ between the most outer rings

shown in Fig. 3.7 a) (18 ring II states and 6 cluster states):

$$\langle \Psi_{II}^{q} | \hat{V}_{II-III} | \Psi_{III}^{pu} \rangle = \frac{1}{\sqrt{18 \cdot 6}} \sum_{m=0}^{17} \sum_{j=0}^{5} e^{i(5pj-pm)a} \langle \phi_m | \hat{V}_{II-III} | \psi_{uj} \rangle . \tag{3.14}$$

The matrix element $\langle \phi_m | \hat{V}_{II-III} | \psi_{uj} \rangle$ needs to be determined. Tunneling is allowed only between NN as shown in Fig. 3.7 b). The atoms on the tip of the cluster numbered 0 and 2 are coupled to specific atoms on ring II, numbered $3j-1$ and $3j+1$ for a given cluster j. We obtain the tunneling matrix elements

$$\begin{aligned} \langle \phi_m | \hat{V}_{II-III} | \psi_{0,j} \rangle &= -\frac{t}{\sqrt{2}} \left(-\delta_{m,3j-1} + \delta_{m,3j+1} \right), \\ \langle \phi_m | \hat{V}_{II-III} | \psi_{\pm 1,j} \rangle &= -\frac{t}{2} \left(\delta_{m,3j-1} + \delta_{m,3j+1} \right). \end{aligned} \tag{3.15}$$

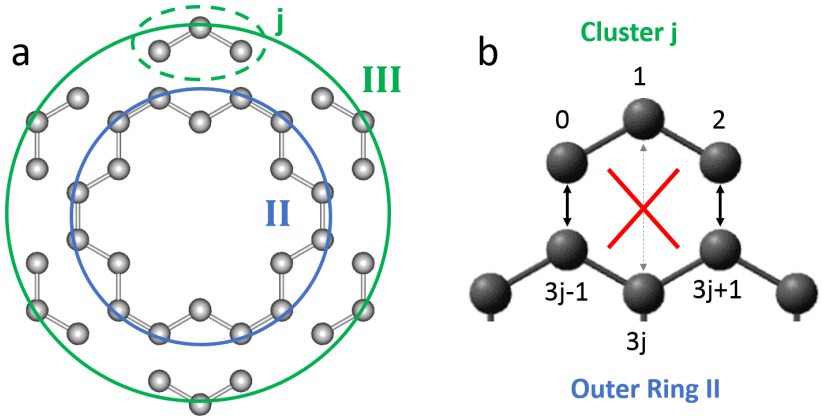

Figure 3.7: a) Ring II and III are coupled. j labels clusters. b) Rule for tunneling between rings II, III. Only the outside atoms of the cluster exhibit tunneling to ring II.

The final matrix elements of $\hat{V}_{II-III}$ are

$$\begin{aligned} \langle \Psi_{II}^{q} | \hat{V}_{II-III} | \Psi_{III}^{p,0} \rangle &= -\frac{t}{\sqrt{6}} \left(e^{-iqa} - e^{iqa} \right) \delta_{5p,\{3q,3q\pm\frac{2\pi}{a}\}} \\ &= \frac{t}{\sqrt{6}} 2i \sin(qa) \delta_{5p,\{3q,3q\pm\frac{2\pi}{a}\}}, \\ \langle \Psi_{II}^{q} | \hat{V}_{II-III} | \Psi_{III}^{p,\pm 1} \rangle &= -\frac{t}{\sqrt{12}} \left(e^{-iqa} + e^{iqa} \right) \delta_{5p,\{3q,3q\pm\frac{2\pi}{a}\}} \\ &= -\frac{t}{\sqrt{12}} 2 \cos(qa) \delta_{5p,\{3q,3q\pm\frac{2\pi}{a}\}}. \end{aligned} \tag{3.16}$$

The sets of coupled states are

$$|II, q_{-8}\rangle, |II, q_{-2}\rangle, |II, q_4\rangle \rightarrow |III, p_{-2}, u = 0, \pm 1\rangle, \tag{3.17a}$$

$$|II, q_{-7}\rangle, |II, q_{-1}\rangle, |II, q_5\rangle \rightarrow |III, p_{-1}, u = 0, \pm 1\rangle, \tag{3.17b}$$

$$|II, q_{-6}\rangle, |II, q_0\rangle, |II, q_6\rangle \rightarrow |III, p_0, u = 0, \pm 1\rangle, \tag{3.17c}$$

$$|II, q_{-5}\rangle, |II, q_1\rangle, |II, q_7\rangle \rightarrow |III, p_1, u = 0, \pm 1\rangle, \tag{3.17d}$$

$$|II, q_{-4}\rangle, |II, q_2\rangle, |II, q_8\rangle \rightarrow |III, p_2, u = 0, \pm 1\rangle, \tag{3.17e}$$

$$|II, q_{-3}\rangle, |II, q_3\rangle, |II, q_9\rangle \rightarrow |III, p_3, u = 0, \pm 1\rangle, \tag{3.17f}$$

where only four blocks are unique again and the block size is now 7×7 (the groups of $q_{n'}$ couple to one more k_n state as given in Eq. 3.10).

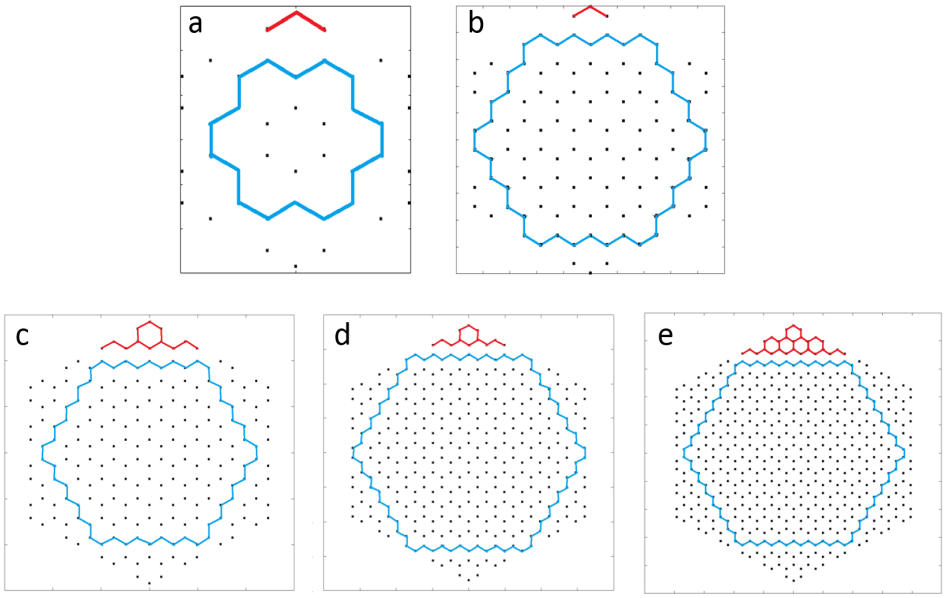

Figure 3.8: Clusters for AHGQDs with increasing size (a-e). Blue lines mark the inner ZHGQDs, and red lines identify clusters.

Before I combine all rings to form an AHGQD in section 3.3, it is important to point out that the 1D Lieb lattice in not unique to the smallest QD example considered here. Larger ZHGQDs are the base to form larger AHGQDs with a 1D Lieb lattice consisting of different clusters, as shown in Fig. 3.8 for several sizes. Blue line marks the inner ZHGQD and red lines highlight the clusters. All these clusters exhibit zero-energy states with the wavefunction localised only on one sublattice, similarly to Eq.

3.12b. The amplitude of the zero-energy states on atoms has been shown for two example clusters in Fig. 3.9 with red circles.

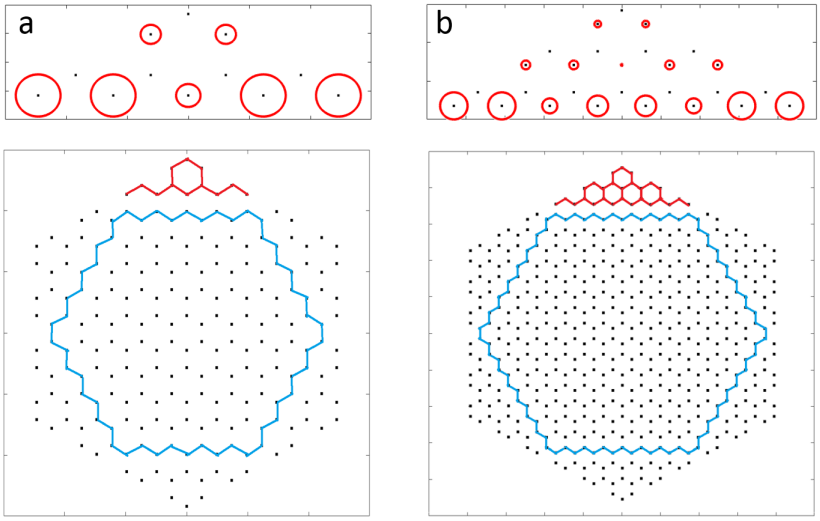

Figure 3.9: Zero-energy state wavefunction amplitude (top) for two (a,b) clusters in AHGQDs (bottom). Size of a circle (top) denotes the magnitude of the wavefunction. Only one sublattice hosts the cluster zero-energy wavefunction.

3.3 Armchair-edged graphene quantum dot: A42.

For ZHGQDs, the energy gap is formed by the states from the outer ring II located on the edge of the QD, as explained in section 3.1. It is important to understand how this picture is changed for AHGQDs, whose edge is built of the 1D Lieb lattice. I will demonstrate this process on the example of A42 shown in Fig. 3.10 (right), which is composed of a smaller ZHGQD (Z24) with the 1D Lieb lattice on the edge (as shown in the left and middle of Fig. 3.10).

We want to add the tunneling from Z24 to ring III, as shown in Fig. 3.11, using the matrix elements derived in Eq. 3.16. Let us start with the eigenstates of the entire coronene QD given as

$$\Omega_\nu = \sum_{k=0}^{5} A_k^\nu \Psi_I^k + \sum_{q=0}^{17} B_q^\nu \Psi_{II}^q, \tag{3.18}$$

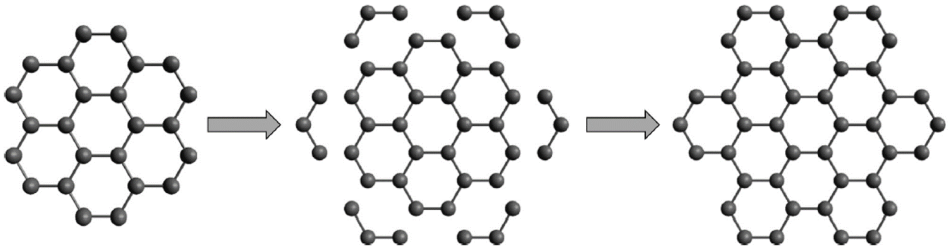

Figure 3.10: Forming of an AHGQD by adding clusters outside of a ZHGQD.

where Ψ_I^k and Ψ_{II}^q are given in Eq. 3.4 and coefficients A_k^ν, B_q^ν are obtained through diagonalising the four 4×4 TB Hamiltonian blocks, like in Eq. 3.11.

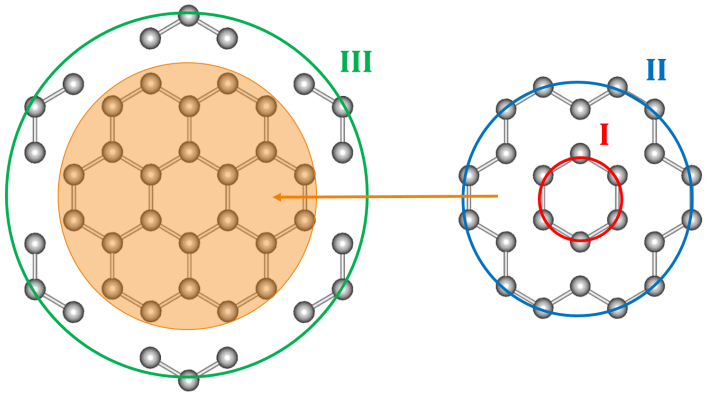

Figure 3.11: Components making the AHGQD are: an inner ZHGQD (yellow, left) made of rings I and II (red and blue on the right), and an outer ring III of clusters (green on the left).

We now couple the eigenstates Ω_ν given in Eq. 3.18 to the states from ring III Ψ_{III}^{pu} given in Eq. 3.13 and obtain

$$\langle \Omega_\nu | \hat{V}_{Z24-III} | \Psi_{III}^{pu} \rangle = \cancel{\sum_{k=0}^{5} A_k^\nu \langle \Psi_I^k | \hat{V}_{Z24-III} | \Psi_{III}^{pu} \rangle} + \sum_{q=0}^{17} B_q^\nu \langle \Psi_{II}^q | \hat{V}_{Z24-III} | \Psi_{III}^{pu} \rangle , \quad (3.19)$$

where the crossed out term vanishes because of no tunneling between the inner ring I and the cluster ring III and $\langle \Psi_{II}^q | \hat{V}_{Z24-III} | \Psi_{III}^{pu} \rangle = \langle \Psi_{II}^q | \hat{V}_{II-III} | \Psi_{III}^{pu} \rangle$ given by Eq. 3.16. The second term in Eq. 3.19 can be evaluated numerically using the numerical form of the eigenvector of the inner Z24 QD.

Fig. 3.12 shows how the energy spectrum of a HGQD evolves as the rings are

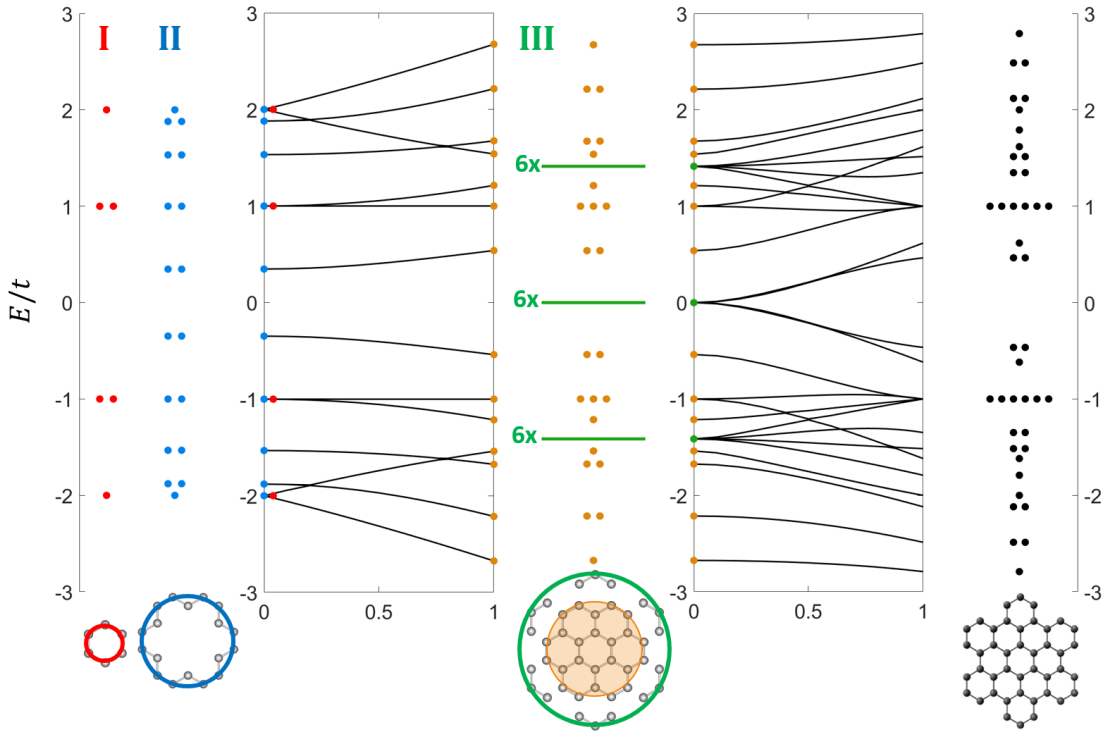

Figure 3.12: Energy spectrum evolution (left to right) from a ZHGQD to an AHGQD. Energy levels of ring I and II (red and blue, far left) evolve when coupled to form ZHGQD energy levels (yellow), and when coupled to the cluster levels (green) they evolve into the AHGQD levels (far right).

coupled together. The left part of Fig. 3.12 (shown in red and blue for ring I and II) contains a summary of the spectrum change shown in Fig. 3.5, due to the coupling of ring I and ring II. In the centre of Fig. 3.12 a complete Z24 QD is shown in orange, and the orange energy levels correspond to eigenvectors Ω_ν given in Eq. 3.18. The green levels which overlap the Z24 spectrum originate in ring III and make up the six-fold degenerate spectrum $E_u = \{-1, 0, 1\}$ of the clusters. The right part of Fig. 3.12 shows how the Z24 energies evolve into the energies of A42 as the tunneling between ring II and ring III is turned on. It is apparent that the energy gap of A42 is formed from the cluster zero-energy state shell of the ring III.

The difference between the mechanisms responsible for forming of the energy gap in ZHGQDs and AHGQDs explains the oscillation in the gap magnitude as a function of GQD size, shown in Fig. 2.9. For ZHGQDs the gap is formed from the states of the outer ring of atoms (ring II for Z24) shown in section 3.1, while for AHGQDs the

gap forms between split zero-energy shell of a 1D Lieb lattice on the edge. This also produces the difference in level degeneracies close to the gap: two-fold for ZHGQDs and a single state followed by a close pair of states for AHGQDs.

An analysis like the one performed in this chapter can be perfomed for any size of a HGQD, using coupled rings of carbon atoms. This method, based on analytical solutions in 1D, could allow for more efficient calculation of the energy spectrum of very large QDs. It could be particularly useful as a first step of many-body calculations based on density matrix renormalisation group (DMRG) techniques [155].

Chapter 4

Tight binding model for monolayer MoS_2

Final chapters of this thesis present studies of valley physics in $MoS_2$2 in the presence of magnetic field and for large finite nanostructures. As magnetic field effects (chapter 5) or large computation boxes (chapter 6) cannot be considered in DFT, a TB model that can efficiently incorporate these effects is needed and will be presented in this chapter. The electronic structure obtained within DFT (section 2.2.5) will serve as guide for the choice of the TB basis, to include the orbitals that mostly build the low-energy bands, as shown in Fig. 2.14. The derivation presented in the following sections is conducted in a similar way to the graphene TB model derivation presented in section 2.1.3., but with a larger basis of d and p orbitals.

4.1 Many-orbital nearest neighbour tight-binding model for MoS_2.

I start with a NN TB model of MoS_2 based on ab initio work described in section 2.2.5. Even though the Mo atoms exhibit strong spin-orbit coupling (SOC) due to presence of heavy metal atoms, I will first consider spinless Hamiltonian for simplicity and return to including the SOC effects at the end of this chapter. The hexagonal

crystal lattice of MoS_2 has been shown in Fig. 2.10.

We start with considering valence orbitals on Mo and S atoms. Motivated by the DFT results for MoS_2 presented in section 2.2.5, we select only the orbitals even with respect to the Mo plane with $l = 2, m_d = 0, \pm 2$ for Mo atom and with $l = 1, m_p = 0, \pm 1$ for the sulphur dimer, with even combinations of the top (T) and bottom (B) atom of the dimer [156]:

$$\begin{aligned} \varphi_{m_p=\pm 1}(\boldsymbol{r}) &= \frac{1}{\sqrt{2}}(\varphi^T_{l=1,m_p=\pm 1}(\boldsymbol{r}) + \varphi^B_{l=1,m_p=\pm 1}(\boldsymbol{r})) \\ \varphi_{m_p=0}(\boldsymbol{r}) &= \frac{1}{\sqrt{2}}(\varphi^T_{l=1,m_p=0}(\boldsymbol{r}) - \varphi^B_{l=1,m_p=0}(\boldsymbol{r})), \end{aligned} \tag{4.1}$$

where the $m_p = 0$ orbital is taken with a minus sign due to the odd nature of the p_z orbital. With these orbitals we construct Bloch wavefunctions for sublattices $(A = Mo, B = S_2)$

$$\Psi^{\boldsymbol{k}}_{A,m_d}(\boldsymbol{r}) = \frac{1}{\sqrt{N_{UC}}} \sum_{\boldsymbol{R}_A} e^{i\boldsymbol{k}\cdot\boldsymbol{R}_A} \varphi_{m_d}(\boldsymbol{r} - \boldsymbol{R}_A), \tag{4.2}$$

$$\Psi^{\boldsymbol{k}}_{B,m_p}(\boldsymbol{r}) = \frac{1}{\sqrt{N_{UC}}} \sum_{\boldsymbol{R}_B} e^{i\boldsymbol{k}\cdot\boldsymbol{R}_B} \varphi_{m_p}(\boldsymbol{r} - \boldsymbol{R}_B). \tag{4.3}$$

We will look for a solution of the form

$$\Psi^{\boldsymbol{k}}_n(\boldsymbol{r}) = \sum_{m_d} A^{\boldsymbol{k},n}_{m_d} \Psi^{\boldsymbol{k}}_{A,m_d}(\boldsymbol{r}) + \sum_{m_p} B^{\boldsymbol{k},n}_{m_p} \Psi^{\boldsymbol{k}}_{B,m_p}(\boldsymbol{r}), \tag{4.4}$$

where n is the band index and $A^{\boldsymbol{k},n}_{m_d}$ and $B^{\boldsymbol{k},n}_{m_p}$ are the coefficients we solve for.

The single electron Hamiltonian reads

$$\hat{H} = \frac{\hat{p}^2}{2m} + \sum_{\boldsymbol{R}_A}[V^A(\boldsymbol{r} - \boldsymbol{R}_A)] + \sum_{\boldsymbol{R}_B}[V^B(\boldsymbol{r} - \boldsymbol{R}_B)], \tag{4.5}$$

where $V^A(\boldsymbol{r})$ is the potential from A atoms (and analogously for B atoms).

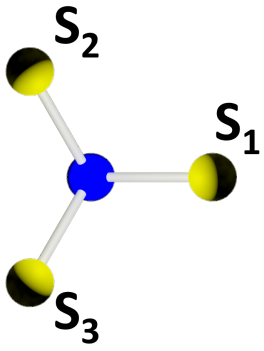

Figure 4.1: Nearest neighbours (yellow) of an Mo atom (blue).

We now construct the off-diagonal elements of Eq. 4.5 in the NN approximation:

$$\begin{aligned}
&\langle \Psi^{\boldsymbol{k}}_{A,m_d} | \, \hat{H} \, | \Psi^{\boldsymbol{k}}_{B,m_p} \rangle \\
&\quad = \frac{1}{N_{UC}} \sum_{<\boldsymbol{R}_A, \boldsymbol{R}_B>} e^{i\boldsymbol{k}(\boldsymbol{R}_B - \boldsymbol{R}_A)} \left\langle \varphi_{m_d}(\boldsymbol{r} - \boldsymbol{R}_A) \right| V^A(\boldsymbol{r} - \boldsymbol{R}_A) \left| \varphi_{m_p}(\boldsymbol{r} - \boldsymbol{R}_B) \right\rangle \\
&\qquad = \sum_{\boldsymbol{\delta}_j} e^{i\boldsymbol{k}\boldsymbol{\delta}_j} \left\langle \varphi_{m_d}(\boldsymbol{r} - \boldsymbol{R}_A) \right| V^A(\boldsymbol{r} - \boldsymbol{R}_A) \left| \varphi_{m_p}(\boldsymbol{r} - \boldsymbol{R}_A - \boldsymbol{\delta}_j) \right\rangle , \quad (4.6)
\end{aligned}$$

where $\boldsymbol{\delta}_j$ are the NN vectors (Fig. 4.1). The NN integral in Eq. 4.6 can be evaluated using the Slater-Koster rules [129]. However we first need to express the orbitals in the angular momentum basis in terms of the spatial orbitals:

$$\begin{aligned}
\varphi_{m_d=0} &= d_{3z^2}, \\
\varphi_{m_d=\pm 2} &= \frac{1}{\sqrt{2}}(d_{x^2-y^2} \pm i d_{xy}), \\
\varphi_{m_p=0} &= \varphi_{p_z}, \\
\varphi_{m_p=\pm 1} &= \frac{1}{\sqrt{2}}(p_x \pm i p_y).
\end{aligned} \quad (4.7)$$

Slater-Koster rules involve directional cosines (L,M,N) (i.e. angles that the bond

makes with all axes) of the nearest neighbour sulphur atoms (as shown in Fig. 4.1)

$$\begin{aligned} S_1: &\quad (L,M,N) = (\frac{d_\parallel}{d}, 0, \pm\frac{d_\perp}{d}), \\ S_2: &\quad (L,M,N) = (-\frac{d_\parallel}{d}, \frac{\sqrt{3}}{2}\frac{d_\parallel}{d}, \pm\frac{d_\perp}{d}), \\ S_3: &\quad (L,M,N) = (-\frac{d_\parallel}{d}, -\frac{\sqrt{3}}{2}\frac{d_\parallel}{d}, \pm\frac{d_\perp}{d}), \end{aligned} \tag{4.8}$$

where $\pm$ in Eq. 4.8 refers to top (bottom) sulphur atoms and $d_\perp$ and $d_\parallel$ are shown in Fig. 4.2. Expressions in Eq. 4.9 list the Slater-Koster matrix elements $V_{pd}(L,M,N)$ for all the orbitals involved [129].

$$\begin{aligned} \langle d_{_{3z^2}}|\, V\, |p_x\rangle &= -\frac{1}{2}L\Big((3N^2-1)V_{dp\sigma} - 2\sqrt{3}N^2V_{dp\pi}\Big), \\ \langle d_{_{3z^2}}|\, V\, |p_y\rangle &= -\frac{1}{2}M\Big((3N^2-1)V_{dp\sigma} - 2\sqrt{3}N^2V_{dp\pi}\Big), \\ \langle d_{_{3z^2}}|\, V\, |p_z\rangle &= -\frac{1}{2}N\Big((3N^2-1)V_{dp\sigma} - 2\sqrt{3}(N^2-1)V_{dp\pi}\Big), \\ \langle d_{_{x^2-y^2}}|\, V\, |p_x\rangle &= -\frac{1}{2}L\Big(\sqrt{3}(L^2-M^2)V_{dp\sigma} + 2(2M^2+N^2)V_{dp\pi}\Big), \\ \langle d_{_{x^2-y^2}}|\, V\, |p_y\rangle &= -\frac{1}{2}M\Big(\sqrt{3}(L^2-M^2)V_{dp\sigma} - 2(2L^2+N^2)V_{dp\pi}\Big), \\ \langle d_{_{x^2-y^2}}|\, V\, |p_z\rangle &= -\frac{1}{2}N(L^2-M^2)(\sqrt{3}V_{dp\sigma} - 2V_{dp\pi}), \\ \langle d_{xy}|\, V\, |p_x\rangle &= -M\Big(L^2(\sqrt{3}V_{dp\sigma} - 2V_{dp\pi}) + V_{dp\pi}\Big), \\ \langle d_{xy}|\, V\, |p_y\rangle &= -L\Big(M^2(\sqrt{3}V_{dp\sigma} - 2V_{dp\pi}) + V_{dp\pi}\Big), \\ \langle d_{xy}|\, V\, |p_z\rangle &= -LMN(\sqrt{3}V_{dp\sigma} - 2V_{dp\pi}). \end{aligned} \tag{4.9}$$

From Eq. 4.8, 4.7 and 4.9 we calculate

$$\begin{aligned} &\langle \varphi_{m_d=0}|\, V\, |\varphi_{m_p=\pm1}\rangle \\ &\quad= \frac{1}{2}\big(\, \langle d_{_{3z^2}}|\, V\, |p_x^T\rangle \pm i\, \langle d_{_{3z^2}}|\, V\, |p_y^T\rangle + \langle d_{_{3z^2}}|\, V\, |p_x^B\rangle \pm \langle d_{_{3z^2}}|\, V\, |p_y^B\rangle\, \big) \\ &\qquad\qquad= -\frac{1}{2}(L \pm iM)\Big(\big(3\frac{d_\perp^2}{d^2} - 1\big)V_{dp\sigma} - 2\sqrt{3}\frac{d_\perp^2}{d^2}V_{dp\pi}\Big), \end{aligned} \tag{4.10}$$

where T (B) subscripts stand for top (bottom) sulphur atoms. By performing anal-

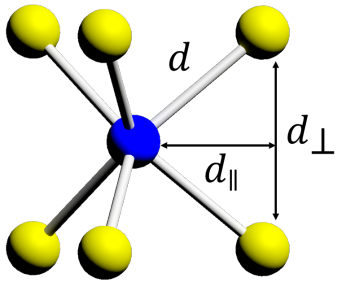

Figure 4.2: Lattice parameters of monolayer MoS_2. The bond length between Mo (blue) and S (yellow) atoms is labelled with d. Parameters $d_\parallel, d_\perp$ are used in Slater Koster rules.

ogous calculation for remaining matrix elements we obtain

$$
\begin{aligned}
\langle\varphi_{m_d=0}|\,V\,|\varphi_{m_p=\pm1}\rangle &= (L\pm iM)V_{m_d=0,m_p=\pm1} = -\frac{1}{2}(L\pm iM)\Big((3\frac{d_\perp^2}{d^2}-1)V_{dp\sigma}-2\sqrt{3}\frac{d_\perp^2}{d^2}V_{dp\pi}\Big),\\
\langle\varphi_{m_d=0}|\,V\,|\varphi_{m_p=0}\rangle &= V_{m_d=0,m_p=0} = -\frac{1}{\sqrt{2}}\frac{d_\perp}{d}\Big((3\frac{d_\perp^2}{d^2}-1)V_{dp\sigma}-2\sqrt{3}(\frac{d_\perp^2}{d^2}-1)V_{dp\pi}\Big),\\
\langle\varphi_{m_d=\pm2}|\,V\,|\varphi_{m_p=\pm1}\rangle &= (L\mp iM)V_{m_d=\pm2,m_p=\pm1} = \frac{1}{\sqrt{2}}(L\mp iM)\Big(\frac{\sqrt{3}}{2}(\frac{d_\perp^2}{d^2}-1)V_{dp\sigma}-(\frac{d_\perp^2}{d^2}+1)V_{dp\pi}\Big),\\
\langle\varphi_{m_d=\pm2}|\,V\,|\varphi_{m_p=\mp1}\rangle &= (L\mp iM)^3V_{m_d=\pm2,m_p=\mp1} = -\frac{1}{\sqrt{2}}(L\mp iM)^3\Big(\frac{\sqrt{3}}{2}V_{dp\sigma}-V_{dp\pi}\Big),\\
\langle\varphi_{m_d=\pm2}|\,V\,|\varphi_{m_p=0}\rangle &= (L\mp iM)^2V_{m_d=\pm2,m_p=0} = -\frac{1}{2}(L\mp iM)^2\frac{d_\perp}{d}\Big(\sqrt{3}V_{dp\sigma}-2V_{dp\pi}\Big).
\end{aligned}
\tag{4.11}
$$

We now insert Eq. 4.11 into the NN hopping matrix element in Eq. 4.6 to obtain

$$
\begin{aligned}
&\langle\Psi^{\boldsymbol{k}}_{A,m_d=0}|\,\hat{H}\,|\Psi^{\boldsymbol{k}}_{B,m_p=1}\rangle\\
&\quad= \sum_{\boldsymbol{\delta}_j} e^{i\boldsymbol{k}\boldsymbol{\delta}_j}\left\langle\varphi_{m_d=0}(\boldsymbol{r}-\boldsymbol{R}_A)\right|V^A(\boldsymbol{r}-\boldsymbol{R}_A)\left|\varphi_{m_p=1}(\boldsymbol{r}-\boldsymbol{R}_A-\boldsymbol{\delta}_j)\right\rangle\\
&\quad= V_{m_d=0,m_p=\pm1}\sum_{\boldsymbol{\delta}_j} e^{i\boldsymbol{k}\boldsymbol{\delta}_j}(L_j\pm iM_j) = V_{m_d=0,m_p=\pm1}\frac{d_\parallel}{d}\sum_{\boldsymbol{\delta}_j} e^{i\boldsymbol{k}\boldsymbol{\delta}_j}e^{\pm i\theta_j}\\
&= V_{m_d=0,m_p=\pm1}\frac{d_\parallel}{d}\Big(e^{ik_xd_\parallel}+e^{-ik_x\frac{d_\parallel}{2}}e^{i\sqrt{3}k_y\frac{d_\parallel}{2}}e^{i\frac{\pm2\pi}{3}}+e^{-ik_x\frac{d_\parallel}{2}}e^{-i\sqrt{3}k_y\frac{d_\parallel}{2}}e^{i\frac{\pm4\pi}{3}}\Big),
\end{aligned}
\tag{4.12}
$$

and analogously for the remaining integrals. In Eq. 4.12 θ_j are phases generated by

tunneling to different nearest neighbours arising from $L_j \pm iM_j$ (Fig. 4.1):

$$\begin{aligned} S_1: &\quad L + iM = e^{i0}\frac{d_\parallel}{d} = \frac{d_\parallel}{d} \\ S_2: &\quad L + iM = e^{i\frac{2\pi}{3}}\frac{d_\parallel}{d} \\ S_3: &\quad L + iM = e^{i\frac{4\pi}{3}}\frac{d_\parallel}{d}. \end{aligned} \tag{4.13}$$

We can evaluate the NN integrals as in Eq. 4.12 at $\boldsymbol{K} = (0, \frac{4\pi}{3\sqrt{3}d_\parallel})$ (here the lattice and Brillouin zone are defined as rotated by 90° w.r.t. graphene lattice in Eq. 2.1.3) to obtain a general expression

$$\langle \Psi^{\boldsymbol{k}=K}_{A,m_d} | \, \hat{H} \, | \Psi^{\boldsymbol{k}=K}_{B,m_p} \rangle = \left(1 + e^{i\left(1-m_d+m_p\right)2\pi/3} + e^{i\left(1-m_d+m_p\right)4\pi/3}\right) V_{m_d,m_p}, \tag{4.14}$$

where V_{m_d,m_p} have been defined in Eq. 4.11. The expression in Eq. 4.14 includes the phases dependent on the angular momentum of the neighbouring orbitals. Analogous phase factors in graphene vanish for p_z orbitals on all sites, which closes the gap. In TMDCs these factors are responsible for removing the degeneracy of d orbitals at $\boldsymbol{K}$, which build VB and CB (in accordance with Fig. 2.14) and therefore must be nonzero. For the nonvanishing tunneling matrix elements in Eq. 4.14, the orbitals satisfy a selection rule $1 + m_d - m_{-p} = 0, \pm 3$. This restricts the pairs of orbitals that build the bands at high symmetry points:

$$\begin{aligned} \boldsymbol{K}: &\left[m_d{=}0, m_p{=}{-1}\right], \left[m_d{=}{+2}, m_p{=}{+1}\right], \left[m_d{=}{-2}, m_p{=}0\right], \\ -\boldsymbol{K}: &\left[m_d{=}0, m_p{=}{+1}\right], \left[m_d{=}{-2}, m_p{=}{-1}\right], \left[m_d{=}{+2}, m_p{=}0\right], \\ \boldsymbol{\Gamma}: &\left[m_d{=}0, m_p{=}0\right], \left[m_d{=}+2, m_p{=}{-1}\right], \left[m_d{=}{-2}, m_p{=}{+1}\right], \end{aligned} \tag{4.15}$$

which makes the Hamiltonian block diagonal at these $\boldsymbol{k}$-points.

We now collect all the NN Hamiltonian matrix elements in the basis of Ψ_{A,m_d} and

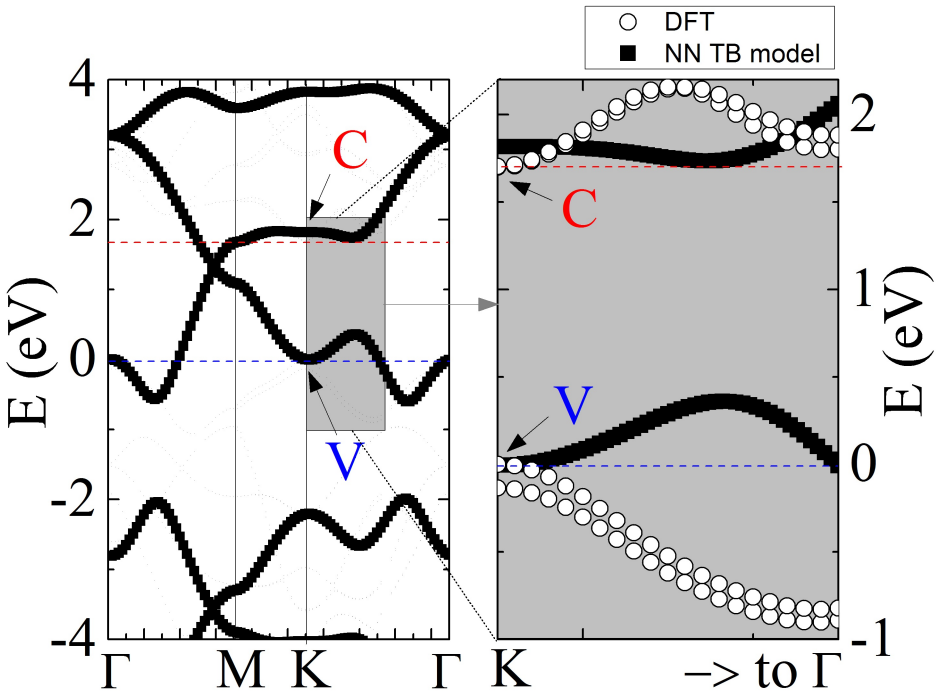

Figure 4.3: (left) TB band structure of MoS_2 obtained by diagonalising the Hamiltonian in Eq. 4.16 with only NN terms included. (right) Comparison of the TB NN band structure (black) to the DFT bands (white). The band masses are incorrect and a closing of the gap around $\boldsymbol{M}$ is visible.

Ψ_{B,m_p}

$$\hat{H}^{NN}(\boldsymbol{k}) = \begin{pmatrix} E_{m_d=-2} & 0 & 0 & V_1 f_{-1}(\boldsymbol{k}) & -V_2 f_0(\boldsymbol{k}) & V_3 f_1(\boldsymbol{k}) \\ & E_{m_d=0} & 0 & -V_4 f_0(\boldsymbol{k}) & -V_5 f_1(\boldsymbol{k}) & -V_4 f_{-1}(\boldsymbol{k}) \\ & & E_{m_d=2} & -V_3 f_1(\boldsymbol{k}) & -V_2 f_{-1}(\boldsymbol{k}) & V_1 f_0(\boldsymbol{k}) \\ & & & E_{m_p=-1} & 0 & 0 \\ & & h.c. & & E_{m_p=0} & 0 \\ & & & & & E_{m_p=1} \end{pmatrix}, \quad (4.16)$$

where V_{1-5} and $f_{0,\pm1}(\boldsymbol{k})$ are

$$
\begin{aligned}
V_1 &= V_{m_d=\pm2,m_p=\pm1}\frac{d_\parallel}{d} = \frac{1}{\sqrt{2}}\left[\frac{\sqrt{3}}{2}\left(\frac{d_\perp^2}{d^2}-1\right)V_{dp\sigma} - \left(\frac{d_\perp^2}{d^2}+1\right)V_{dp\pi}\right]\frac{d_\parallel}{d},\\
V_2 &= V_{m_d=\pm2,m_p=0}\left(\frac{d_\parallel}{d}\right)^2 = \frac{1}{2}\left[\sqrt{3}V_{dp\sigma} - 2V_{dp\pi}\right]\frac{d_\perp}{d}\left(\frac{d_\parallel}{d}\right)^2,\\
V_3 &= V_{m_d=\pm2,m_p=\mp1}\left(\frac{d_\parallel}{d}\right)^3 = \frac{1}{\sqrt{2}}\left[\frac{\sqrt{3}}{2}V_{dp\sigma} - V_{dp\pi}\right]\left(\frac{d_\parallel}{d}\right)^3,\\
V_4 &= V_{m_d=0,m_p=\pm1}\frac{d_\parallel}{d} = \frac{1}{2}\left[\left(3\frac{d_\perp^2}{d^2}-1\right)V_{dp\sigma} - 2\sqrt{3}\frac{d_\perp^2}{d^2}V_{dp\pi}\right]\frac{d_\parallel}{d},\\
V_5 &= V_{m_d=0,m_p=0} = \frac{1}{\sqrt{2}}\left[\left(3\frac{d_\perp^2}{d^2}-1\right)V_{dp\sigma} - 2\sqrt{3}\left(\frac{d_\perp^2}{d^2}-1\right)V_{dp\pi}\right]\frac{d_\perp}{d},
\end{aligned}
\tag{4.17}
$$

$$
\begin{aligned}
f_0(\boldsymbol{k}) &= e^{ik_x} + e^{-ik_x/2}e^{i\sqrt{3}k_y/2}e^{-i2\pi/3} + e^{-ik_x/2}e^{-i\sqrt{3}k_y/2}e^{i2\pi/3},\\
f_{-1}(\boldsymbol{k}) &= e^{ik_x} + e^{-ik_x/2}e^{i\sqrt{3}k_y/2}e^{i2\pi/3} + e^{-ik_x/2}e^{-i\sqrt{3}k_y/2}e^{-i2\pi/3},\\
f_{+1}(\boldsymbol{k}) &= e^{ik_x} + e^{-ik_x/2}e^{i\sqrt{3}k_y/2} + e^{-ik_x/2}e^{-i\sqrt{3}k_y/2}.
\end{aligned}
\tag{4.18}
$$

The Hamiltonian in Eq. 4.16 and expressions in Eq. 4.17 and Eq. 4.18 contain Slater-Koster parameters which can be found if one fits the TB band structure to the band structure obtained within the DFT methods (see section 2.2.4 and 2.2.5). Fig. 4.3 shows such fitting for the NN Hamiltonian done with a genetic algorithm using weights setting the priority of fitting for the VB and CB edges between $\boldsymbol{K}$ and $\boldsymbol{\Gamma}$. It is clear that, even though the simple NN Hamiltonian predicts correct gap at $\boldsymbol{K}$, it results in the gap closing around the $\boldsymbol{M}$-point, incorrect for a semiconductor. This is due to the role of the $m_d = 0$ orbital which builds the CB at $\boldsymbol{K}$ and a VB at $\boldsymbol{\Gamma}$ (Fig. 2.14) [156]. Without any hopping between the d orbitals, which could only come from the NNN terms, the correct orbital composition throughout the BZ can therefore only be achieved if the bands cross. This means that this artifact should be corrected if one included the NNN terms in the TB Hamiltonian in Eq. 4.16, as described in section 4.2.

4.2 Next nearest neighbour tight-binding model for MoS_2.

I will now consider the NNN TB terms, which come from tunnelling between a pair of nearest Mo atoms or between a pair of nearest sulphur dimers (Fig. 4.4). These terms are calculated analogously to NN terms:

$$\langle \Psi^{\boldsymbol{k}}_{A,m_d=0} | \hat{H} | \Psi^{\boldsymbol{k}}_{A,m_d=+2} \rangle = \sum_{\boldsymbol{\gamma}_j} e^{i\boldsymbol{k}\boldsymbol{\gamma}_j} \left\langle \varphi_{m_d=0}(\boldsymbol{r}-\boldsymbol{R}_A) \middle| V^A(\boldsymbol{r}-\boldsymbol{R}_A) \middle| \varphi_{m_d=+2}(\boldsymbol{r}-\boldsymbol{R}_A-\boldsymbol{\gamma}_j) \right\rangle, \tag{4.19}$$

where $\boldsymbol{\gamma}_j$ are the NNN vectors (Fig. 4.4) and the NNN hopping integral requires the Slater-Koster matrix elements [129]:

$$\begin{aligned}
\langle d_{3z^2} | V | d_{3z^2} \rangle &= \left(\frac{1}{2}L^2 + \frac{1}{2}M^2 - N^2\right)^2 V_{dd\sigma} + 3N^2(1-N^2)V_{dd\pi} + \frac{3}{4}(N^2-1)^2 V_{dd\delta}, \\
\langle d_{3z^2} | V | d_{x^2-y^2} \rangle &= \frac{\sqrt{3}}{4}(L^2-M^2)\Big((3N^2-1)V_{dd\sigma} - 4N^2 V_{dd\pi} + (N^2+1)V_{dd\delta}\Big), \\
\langle d_{3z^2} | V | d_{xy} \rangle &= \frac{\sqrt{3}}{2}LM\Big((3N^2-1)V_{dd\sigma} - 4N^2 V_{dd\pi} + (N^2+1)V_{dd\delta}\Big), \\
\langle d_{x^2-y^2} | V | d_{x^2-y^2} \rangle &= \frac{3}{4}(L^2-M^2)^2 V_{dd\sigma} + \Big(L^2+M^2-(L^2-M^2)^2\Big)V_{dd\pi} + \Big(\frac{1}{4}(L^2-M^2)^2 + N^2\Big), \\
\langle d_{x^2-y^2} | V | d_{xy} \rangle &= \frac{1}{2}LM(L^2-M^2)(3V_{dd\sigma} - 4V_{dd\pi} + V_{dd\delta}), \\
\langle d_{xy} | V | d_{xy} \rangle &= 3L^2M^2 V_{dd\sigma} + (L^2+M^2-4L^2M^2)V_{dd\pi} + (L^2M^2+N^2)V_{dd\delta},
\end{aligned} \tag{4.20}$$

$$\begin{aligned}
\langle p_x | V | p_x \rangle &= L^2 V_{pp\sigma} + (1-L^2)V_{pp\pi}, \\
\langle p_x | V | p_y \rangle &= LM(V_{pp\sigma} - V_{pp\pi}), \\
\langle p_x | V | p_z \rangle &= LN(V_{pp\sigma} - V_{pp\pi}) \\
\langle p_y | V | p_y \rangle &= M^2 V_{pp\sigma} + (1-M^2)V_{pp\pi}, \\
\langle p_y | V | p_z \rangle &= MN(V_{pp\sigma} - V_{pp\pi}), \\
\langle p_z | V | p_z \rangle &= N^2 V_{pp\sigma} + (1-N^2)V_{pp\pi}.
\end{aligned} \tag{4.21}$$

Using $N = 0$ and $L^2 + M^2 = 1$ for NNN atoms, and using Eq. 4.7 we get

$$\begin{aligned}
\langle\varphi_{m_d=0}(\boldsymbol{r})|\, V\, |\varphi_{m_d=0}(\boldsymbol{r}+\boldsymbol{\gamma})\rangle &= V^{NNN}_{m_d=0,m_d=0} = \frac{1}{4}V_{dd\sigma} + \frac{3}{4}V_{dd\delta},\\
\langle\varphi_{m_d=\pm2}(\boldsymbol{r})|\, V\, |\varphi_{m_d=\pm2}(\boldsymbol{r}+\boldsymbol{\gamma})\rangle &= V^{NNN}_{m_d=\pm2,m_d=\pm2} = \frac{1}{8}(3V_{dd\sigma} + 4V_{dd\pi} + Vdd\delta),\\
\langle\varphi_{m_d=0}(\boldsymbol{r})|\, V\, |\varphi_{m_d=\pm2}(\boldsymbol{r}+\boldsymbol{\gamma})\rangle &= (L \pm iM)^2 V^{NNN}_{m_d=0,m_d=\pm2} = \frac{\sqrt{3}}{4\sqrt{2}}(L \pm iM)^2(-Vdd\sigma + V_{dd\delta}),\\
\langle\varphi_{m_d=\pm2}(\boldsymbol{r})|\, V\, |\varphi_{m_d=\mp2}(\boldsymbol{r}+\boldsymbol{\gamma})\rangle (L \mp iM)^4 V^{NNN}_{m_d=\pm2,m_d=\mp2} &= (L \mp iM)^4 \frac{1}{8}(3V_{dd\sigma} - 4V_{dd\pi} + V_{dd\delta}).
\end{aligned} \tag{4.22}$$

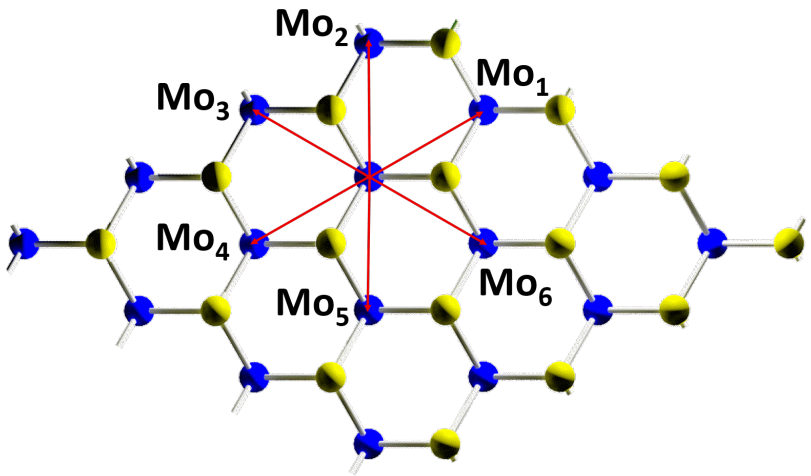

Figure 4.4: Six NNN of an Mo atom are also Mo atoms (blue). The NNN vectors (red) are the same for NNN of an S_2 site (yellow).

To obtain the NNN hopping integrals between sulphur dimers we need to include the hopping between sulphur atoms within the same plane but we neglect the cross terms between the planes:

$$\begin{aligned}
&\langle\varphi_{m_p=0}(\boldsymbol{r})|\, V\, |\varphi_{m_p=0}(\boldsymbol{r}+\boldsymbol{\gamma})\rangle\\
&\qquad = \frac{1}{2}\Big(\langle p_z^T(\boldsymbol{r})|\, V\, |p_z^T(\boldsymbol{r}+\boldsymbol{\gamma})\rangle + \langle p_z^B(\boldsymbol{r})|\, V\, |p_z^B(\boldsymbol{r}+\boldsymbol{\gamma})\rangle\\
&\qquad + \cancel{\langle p_z^T(\boldsymbol{r})|\, V\, |p_z^B(\boldsymbol{r}+\boldsymbol{\gamma})\rangle} + \cancel{\langle p_z^B(\boldsymbol{r})|\, V\, |p_z^T(\boldsymbol{r}+\boldsymbol{\gamma})\rangle}\Big)\\
&\qquad = N^2 V_{pp\sigma} + (1-N^2)V_{pp\pi} = V_{pp\pi},
\end{aligned} \tag{4.23}$$

where we used $N = 0$ for NNN terms. We collect all the NNN hopping integrals:

$$\begin{aligned}
\langle\varphi_{m_p=0}(\boldsymbol{r})|\, V\,|\varphi_{m_p=0}(\boldsymbol{r}+\boldsymbol{\gamma})\rangle &= V^{NNN}_{m_p=0,m_p=0} = V_{pp\pi},\\
\langle\varphi_{m_p=\pm1}(\boldsymbol{r})|\, V\,|\varphi_{m_p=\pm1}(\boldsymbol{r}+\boldsymbol{\gamma})\rangle &= V^{NNN}_{m_p=\pm1,m_p=\pm1} = \frac{1}{2}(V_{pp\sigma}+V_{pp\pi}),\\
\langle\varphi_{m_p=0}(\boldsymbol{r})|\, V\,|\varphi_{m_p=\pm1}(\boldsymbol{r}+\boldsymbol{\gamma})\rangle &= V^{NNN}_{m_p=0,m_p=\pm1} = 0,\\
\langle\varphi_{m_p=-1}(\boldsymbol{r})|\, V\,|\varphi_{m_p=+1}(\boldsymbol{r}+\boldsymbol{\gamma})\rangle &= (L+iM)^2 V^{NNN}_{m_p=-1,m_p=+1} = \frac{1}{2}(L+iM)^2(V_{pp\sigma}-V_{pp\pi}).
\end{aligned} \tag{4.24}$$

We now insert Eq. 4.22 and Eq. 4.24 into Eq. 4.19 to obtain

$$\begin{aligned}
&\langle\Psi^{\boldsymbol{k}}_{A,m_d=0}|\,\hat{H}\,|\Psi^{\boldsymbol{k}}_{A,m_d=+2}\rangle\\
&\quad= \sum_{\boldsymbol{\gamma}_j} e^{i\boldsymbol{k}\boldsymbol{\gamma}_j}\left\langle\varphi_{m_d=0}(\boldsymbol{r}-\boldsymbol{R}_A)\right|V^A(\boldsymbol{r}-\boldsymbol{R}_A)\left|\varphi_{m_d=+2}(\boldsymbol{r}-\boldsymbol{R}_A-\boldsymbol{\gamma}_j)\right\rangle\\
&\quad= V^{NNN}_{m_d=0,m_d=+2}\sum_{\boldsymbol{\gamma}_j} e^{i\boldsymbol{k}\boldsymbol{\gamma}_j}(L_j\pm iM_j)^2 = V^{NNN}_{m_d=0,m_d=+2}\sum_{\boldsymbol{\gamma}_j} e^{i\boldsymbol{k}\boldsymbol{\gamma}_j}e^{2\phi_j}\\
&\qquad= V^{NNN}_{m_d=0,m_d=+2}\Bigg(2\cos\left(3\frac{k_x d_\parallel}{2}+\sqrt{3}\frac{k_y d_\parallel}{2}\right)e^{i\frac{\pi}{3}}\\
&\qquad\quad+2\cos\left(3\frac{k_x d_\parallel}{2}-\sqrt{3}\frac{k_y d_\parallel}{2}\right)e^{-i\frac{\pi}{3}}-2\cos\left(\sqrt{3}k_y d_\parallel\right)\Bigg).
\end{aligned} \tag{4.25}$$

In Eq. 4.25 ϕ_j are phases generated by tunneling to different NNN arising from $L_j \pm iM_j$ (Fig. 4.4):

$$\begin{aligned}
Mo_1:&\quad L+iM = e^{i\frac{\pi}{6}}, &\qquad Mo_4:&\quad L+iM = e^{-i\frac{5\pi}{6}},\\
Mo_2:&\quad L+iM = e^{i\frac{\pi}{2}}, &\qquad Mo_5:&\quad L+iM = e^{-i\frac{\pi}{2}}\\
Mo_3:&\quad L+iM = e^{i\frac{5\pi}{6}}, &\qquad Mo_5:&\quad L+iM = e^{-i\frac{\pi}{6}}.
\end{aligned} \tag{4.26}$$

Parameter	Best fit (in eV)	Parameter	Best fit (in eV)
$E_{m_d=0,\pm2}$	-0.03	$V_{dd\sigma}$	-1.10
$E_{m_p=\pm1}$	-3.36	$V_{dd\pi}$	0.76
$E_{m_p=0}$	-4.78	$V_{dd\delta}$	0.27
$V_{dp\sigma}$	-3.39	$V_{pp\sigma}$	1.19
$V_{dp\pi}$	1.10	$V_{pp\pi}$	-0.83

Table 4.1: Slater-Koster parameters obtained by fitting to DFT band structure.

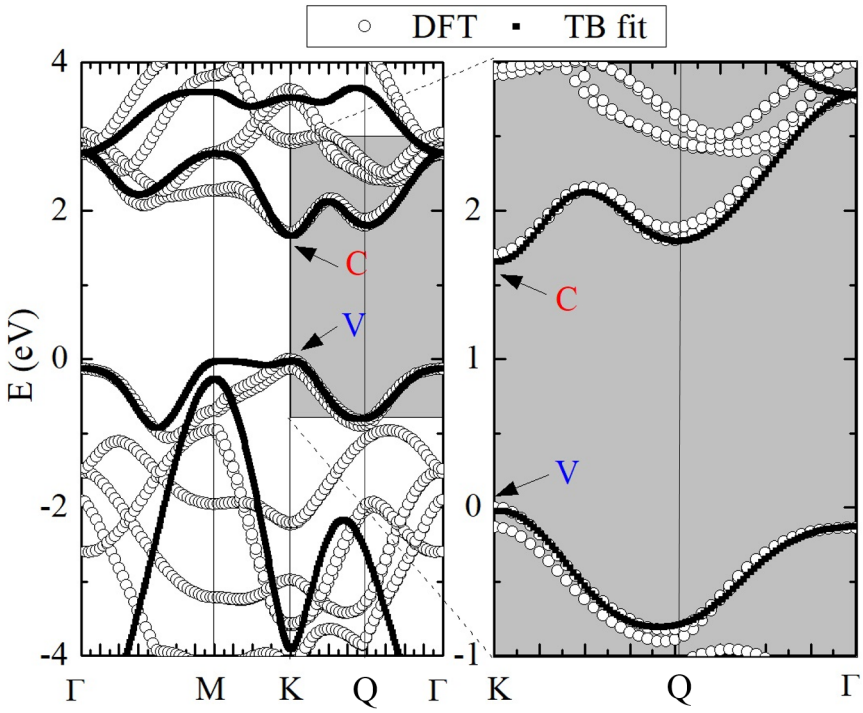

Figure 4.5: (left) TB band structure of MoS_2 obtained by diagonalising the Hamiltonian in Eq. 4.27 with NNN terms included. (right) Comparison between TB (black) and DFT (white) bands. The agreement on the path $\boldsymbol{K} \rightarrow \boldsymbol{\Gamma}$ is excellent.

We now collect all the matrix elements in a NNN Hamiltonian matrix

$$\hat{H}^{NNN}(\boldsymbol{k}) = \begin{pmatrix} E_{m_d=-2} + W_1 g_0(\boldsymbol{k}) & W_3 g_2(\boldsymbol{k}) & W_4 g_4(\boldsymbol{k}) & V_1 f_{-1}(\boldsymbol{k}) & -V_2 f_0(\boldsymbol{k}) & V_3 f_1(\boldsymbol{k}) \\ & E_{m_d=0} + W_2 g_0(\boldsymbol{k}) & W_3 g_2(\boldsymbol{k}) & -V_4 f_0(\boldsymbol{k}) & -V_5 f_1(\boldsymbol{k}) & -V_4 f_{-1}(\boldsymbol{k}) \\ & & E_{m_d=2} + W_1 g_0(\boldsymbol{k}) & -V_3 f_1(\boldsymbol{k}) & -V_2 f_{-1}(\boldsymbol{k}) & V_1 f_0(\boldsymbol{k}) \\ & & & E_{m_p=-1} + W_5 g_0(\boldsymbol{k}) & 0 & W_7 g_2(\boldsymbol{k}) \\ & & h.c. & & E_{m_p=0} + W_6 g_0(\boldsymbol{k}) & 0 \\ & & & & & E_{m_p=1} + W_5 g_0(\boldsymbol{k}) \end{pmatrix}, \quad (4.27)$$

where

$$
\begin{aligned}
W_1 &= V^{NNN}_{m_d=\pm2,m_d=\pm2} = \frac{1}{8}\left(3V_{dd\sigma} + 4V_{dd\pi} + V_{dd\delta}\right), \\
W_2 &= V^{NNN}_{m_d=0,m_d=0} = \frac{1}{4}\left(V_{dd\sigma} + 3V_{dd\delta}\right), \\
W_3 &= V^{NNN}_{m_d=0,m_d=\pm2} = -\frac{\sqrt{3}}{4\sqrt{2}}\left(V_{dd\sigma} - V_{dd\delta}\right), \\
W_4 &= V^{NNN}_{m_d=\pm2,m_d=\mp2} = \frac{1}{8}\left(3V_{dd\sigma} - 4V_{dd\pi} + V_{dd\delta}\right), \\
W_5 &= V^{NNN}_{m_p=\pm1,m_p=\pm1} = \frac{1}{2}\left(V_{pp\sigma} + V_{pp\pi}\right), \\
W_6 &= V^{NNN}_{m_p=0,m_p=0} = V_{pp\pi}, \\
W_7 &= V^{NNN}_{m_p=-1,m_p=+1} = \frac{1}{2}\left(V_{pp\sigma} - V_{pp\pi}\right),
\end{aligned}
\tag{4.28}
$$

and

$$
\begin{aligned}
g_0(\boldsymbol{k}) &= 4\cos\left(3k_x/2\right)\cos\left(\sqrt{3}k_y/2\right) + 2\cos\left(\sqrt{3}k_y\right), \\
g_2(\boldsymbol{k}) &= -2\cos\left(\sqrt{3}k_y\right) + 2\cos\left(3k_x/2 + \sqrt{3}k_y/2\right)e^{i\pi/3} + 2\cos\left(3k_x/2 - \sqrt{3}k_y/2\right)e^{-i\pi/3}, \\
g_4(\boldsymbol{k}) &= 2\cos\left(\sqrt{3}k_y\right) + 2\cos\left(3k_x/2 + \sqrt{3}k_y/2\right)e^{i2\pi/3} + 2\cos\left(3k_x/2 - \sqrt{3}k_y/2\right)e^{-i2\pi/3}.
\end{aligned}
\tag{4.29}
$$

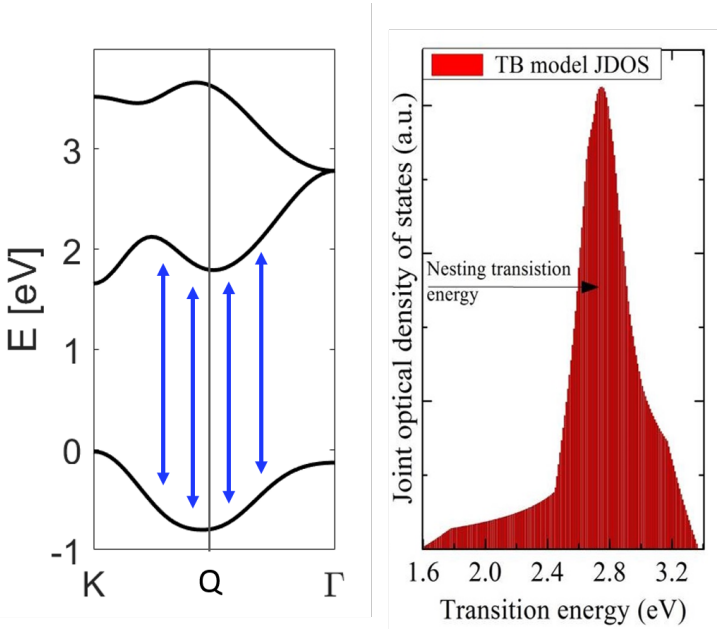

Figure 4.6: (left) The bands around the $\boldsymbol{Q}$-point are approximately parallel, which causes band nesting. The nesting transition energy (blue arrow) around $\boldsymbol{Q}$ is the most common through BZ, which causes the joint optical density of states to peak in the right panel. (right) Joint optical density of states in MoS_2. Peak at ≈ 2.8 eV corresponds to the nesting transition energy in the left panel.

The Hamiltonian in Eq. 4.27 and expressions in Eq. 4.28 contain Slater-Koster parameters which are obtained again by fitting the TB band structure to the band structure obtained within DFT. This is again conducted using a genetic algorithm with a weighted path in the Brillouin zone. The values of parameters obtained through this fitting have been collected in Table 4.1. Fig. 4.5 shows the comparison of TB and DFT bands. We now see that the gap has opened throughout the BZ due to the interaction between d orbitals. There is excellent agreement between the methods for CB and VB around points $\boldsymbol{K}, \boldsymbol{Q}, \boldsymbol{\Gamma}$ [156].

An important feature of these bands is the existence of a secondary CB minimum at $\boldsymbol{Q}$-point, which is built of $m_{_d} = -2$ orbital, contrary to CB minimum at $\boldsymbol{K}$, composed of $m_{_d} = 0$ orbital. Around $\boldsymbol{Q}$ CB and VB are nested, i.e. parallel. This band nesting causes the CB-VB transition energy at $\boldsymbol{Q}$ to be common across a large area in the BZ, which maximises the joint optical density of states (Fig. 4.6) [156].

4.3 Spin orbit-splitting in MoS_2.

So far I have considered a spinless Hamiltonian, but it is important to include the SOC effects due to the presence of heavy atoms. As a consequence of the choice of our basis, the SO term $L \cdot S$ does not couple the states and enters our Hamiltonian only on a diagonal. This can be proven if one considers an explicit form of $L \cdot S$:

$$\begin{aligned} L \cdot S &= \frac{1}{2}\left(L_+ S_- + L_- S_+\right) + L_z S_z, \\ L_z \left|lm\right\rangle &= \hbar m \left|lm\right\rangle, \\ L_\pm \left|lm\right\rangle &= \hbar\sqrt{l(l+1) - m(m\pm 1)}\left|lm \pm 1\right\rangle. \end{aligned} \tag{4.30}$$

Then, I consider possible non-zero off-diagonal matrix elements of $L \cdot S$ for angular momentum eigenstates as

$$\begin{aligned} \langle m_p = 0 \downarrow| \frac{1}{2}\left(L_+ S_- + L_- S_+\right) + L_z S_z \left|m_p = -1 \uparrow\right\rangle &= \frac{\hbar}{2}\sqrt{2}, \\ \langle m_p = 0 \uparrow| \frac{1}{2}\left(L_+ S_- + L_- S_+\right) + L_z S_z \left|m_p = +1 \downarrow\right\rangle &= \frac{\hbar}{2}\sqrt{2}, \end{aligned} \tag{4.31}$$

where all the other elements for m_p vanish and the raising and lowering operators cannot couple states with $\Delta m = 2$, so the matrix elements for m_d also vanish. Using Eq. 4.31, I calculate the couping terms for the elements of the 6-band Hamiltonian basis as

$$\begin{aligned}
&\frac{1}{\sqrt{2}}\Big(\langle m_p = 0 \downarrow|_T - \langle m_p = 0 \downarrow|_B \Big) \frac{1}{2} \left(L_+ S_- + L_- S_+\right) + L_z S_z \cdot \\
&\qquad\qquad \cdot \frac{1}{\sqrt{2}}\Big(|m_p = -1 \uparrow\rangle_T + |m_p = -1 \uparrow\rangle_B \Big) \\
&= \frac{1}{2}\Bigg({}_T\langle m_p = 0 \downarrow| \frac{1}{2} L_+ S_- |m_p = -1 \uparrow\rangle_T - {}_B\langle m_p = 0 \downarrow| \frac{1}{2} L_+ S_- |m_p = -1 \uparrow\rangle_T \\
&+ {}_T\langle m_p = 0 \downarrow| \frac{1}{2} L_+ S_- |m_p = -1 \uparrow\rangle_B - {}_B\langle m_p = 0 \downarrow| \frac{1}{2} L_+ S_- |m_p = -1 \uparrow\rangle_B \Bigg) = 0 \quad (4.32)
\end{aligned}$$

and analogously in the second term in Eq. 4.31. This proves that S_z is still a good quantum number in our basis.

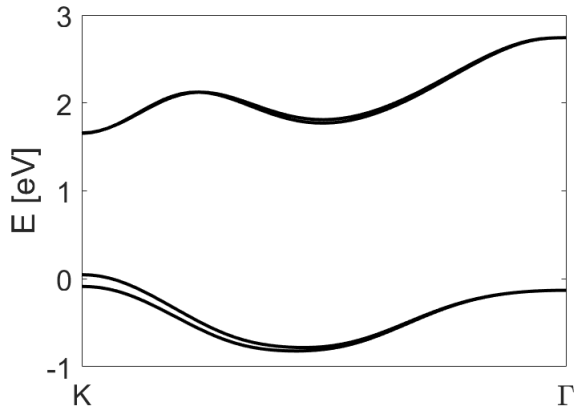

Figure 4.7: VB and CB of MoS_2 with spin-orbit coupling included as in Eq. 4.34. The SO splitting in the CB is not visible on this scale, but the large SO splitting in the VB at $\boldsymbol{K}$ is apparent.

Our spin Hamiltonian reads

$$\hat{H}_{SO}^{NNN}(\boldsymbol{k}) = \hat{H}^{NNN}(\boldsymbol{k}) \otimes \begin{pmatrix} \mathbb{1} & 0 \\ 0 & \mathbb{1} \end{pmatrix} + \begin{pmatrix} \hat{H}_{SO}(\sigma = 1) & 0 \\ 0 & \hat{H}_{SO}(\sigma = -1) \end{pmatrix}, \quad (4.33)$$

where

$$\hat{H}_{SO}(\sigma) = \begin{pmatrix} -\sigma\lambda_{Mo} & & & & & \\ & 0 & & & & \\ & & \sigma\lambda_{Mo} & & & \\ & & & -\sigma\frac{\lambda_{S_2}}{2} & & \\ & & & & 0 & \\ & & & & & \sigma\frac{\lambda_{S_2}}{2} \end{pmatrix} \tag{4.34}$$

and fitting to DFT band structure gives $\lambda_{Mo} = 0.067eV$ and $\lambda_{S_2} = 0.02eV$. Fig. 4.7 shows the band structure of MoS_2 with SO splitting included. The large spin splitting in VB at $\boldsymbol{K}$ $\Delta_{SO}^{VB} = 135meV$ is due to the $m_{_d} = +2$ orbital building the VB. The spin splitting in CB is smaller, $\Delta_{SO}^{CB} = 4meV$, as it is composed of the $m_{_d} = 0$ orbital. It is however still resolvable in an experiment [157].

4.4 Massive Dirac fermion model for MoS_2.

I will now show how the 6×6 NNN Hamiltonian in Eq. 4.27 can be approximated as an effective two-band massive Dirac Hamiltonian at $\boldsymbol{K}$, by analogy to gapped graphene. At $\boldsymbol{K}$ some terms in the NNN Hamiltonian vanish because only 3 pairs of orbitals remain coupled (given in Eq. 4.15)

$$\hat{H}^{NNN}(\boldsymbol{K}) = \begin{pmatrix} E_{m_{_d}=-2} - 3W_1 g_0 & 0 & 0 & 0 & -3V_2 f_0 & 0 \\ & E_{m_{_d}=0} - 3W_2 g_0 & 0 & -3V_4 f_0 & 0 & 0 \\ & & E_{m_{_d}=2} - 3W_1 g_0 & 0 & 0 & 3V_1 f_0 \\ & & & E_{m_{_p}=-1} - 3W_5 g_0 & 0 & 0 \\ & & & & E_{m_{_p}=0} - 3W_6 g_0 & 0 \\ & & & & & E_{m_{_p}=1} - 3W_5 g_0 \end{pmatrix}, \tag{4.35}$$

which is block diagonal if viewed in the basis of the pairs of orbitals

$$\left[m_{_d}{=}0, m_{_p}{=}{-1}\right], \left[m_{_d}{=}2, m_{_p}{=}1\right], \left[m_{_d}{=}{-2}, m_{_p}{=}0\right], \tag{4.36}$$

where the first two pairs build the CB and VB at $\boldsymbol{K}$ and the last pair builds lower and higher bands, so I will disregard it in this model. We can therefore rewrite the original NNN Hamiltonian matrix in Eq. 4.27 as a reduced 4×4 Hamiltonian including only the orbitals building the low-energy bands at $\boldsymbol{K}$

$$\hat{H}^{4\times4}(\boldsymbol{k}) = \begin{pmatrix} E_{m_d=0} + W_2 g_0(\boldsymbol{k}) & W_3 g_2(\boldsymbol{k}) & -V_4 f_0(\boldsymbol{k}) & -V_4 f_{-1}(\boldsymbol{k}) \\ & E_{m_d=2} + W_1 g_0(\boldsymbol{k}) & -V_3 f_1(\boldsymbol{k}) & V_1 f_0(\boldsymbol{k}) \\ & & E_{m_p=-1} + W_5 g_0(\boldsymbol{k}) & W_7 g_2(\boldsymbol{k}) \\ & & & E_{m_p=1} + W_5 g_0(\boldsymbol{k}) \end{pmatrix}. \tag{4.37}$$

Similarly to the way we expanded the off-diagonal expression for the 2×2 Hamiltonian for graphene in Eq. 2.39, we can now expand the $\boldsymbol{k}$-dependent functions as a function of $\boldsymbol{q}$ around $\boldsymbol{K}$ and retain only up to the second order terms in $\boldsymbol{q}$:

$$\begin{aligned} \hat{H}^{4\times4}(\boldsymbol{K}+\boldsymbol{q}) = & \begin{pmatrix} E_{m_d=0} - 3W_2 & 0 & -3V_4 & 0 \\ & E_{m_d=2} - 3W_1 & 0 & 3V_1 \\ & & E_{m_p=-1} - 3W_5 & 0 \\ & & & E_{m_p=1} - 3W_5 \end{pmatrix} + \begin{pmatrix} \frac{9}{4}W_2 & 0 & \frac{3}{4}V_4 & 0 \\ & \frac{9}{4}W_1 & 0 & -\frac{3}{4}V_1 \\ & & \frac{9}{4}W_5 & 0 \\ & & & \frac{9}{4}W_5 \end{pmatrix} |q|^2 d_\parallel \\ & + \begin{pmatrix} 0 & -i\frac{9}{2}W_3 q_- d_\parallel & 0 & -i\frac{3}{2}V_4 q_- d_\parallel \\ & 0 & -i\frac{3}{2}V_3 q_+ d_\parallel & 0 \\ & & 0 & -i\frac{9}{2}W_7 q_- d_\parallel \\ & & & 0 \end{pmatrix} \\ & + \begin{pmatrix} 0 & \frac{9}{8}W_3 q_+^2 d_\parallel^2 & 0 & \frac{3}{8}V_4 q_+^2 d_\parallel^2 \\ & 0 & \frac{3}{8}V_3 q_-^2 d_\parallel^2 & 0 \\ & & 0 & \frac{9}{8}W_7 q_+^2 d_\parallel^2 \\ & & & 0 \end{pmatrix}, \end{aligned} \tag{4.38}$$

where $q_\pm = q_x \pm i q_y$. Since we are interested in an effective two-band Hamiltonian, from each pair of coupled orbitals at $\boldsymbol{K}$ we need to select the states that form the

edges of the bands. We therefore define a new basis

$$\begin{aligned}
\Psi^{+}_{CB} &= \alpha\Psi_{m_d=0} + \beta\Psi_{m_p=-1}, \\
\Psi^{-}_{CB} &= \beta\Psi_{m_d=0} - \alpha\Psi_{m_p=-1}, \\
\Psi^{+}_{VB} &= \mu\Psi_{m_d=2} + \nu\Psi_{m_p=+1}, \\
\Psi^{-}_{VB} &= \nu\Psi_{m_d=2} - \mu\Psi_{m_p=+1}
\end{aligned} \tag{4.39}$$

and rotate Hamiltonian in Eq. 4.38 to this basis, while retaining only the block of Ψ^{+}_{CB} and Ψ^{+}_{VB} (corresponding to the edges of CB and VB):

$$\begin{aligned}
H^{2\times2}(\boldsymbol{K}+\boldsymbol{q}) = &\begin{pmatrix} E^{+}_{CB} + \frac{3}{4}d^2_{\parallel}(3\alpha^2W_2+2\alpha\beta V_4+3\beta^2W_5)|q|^2 & 0 \\ 0 & E^{+}_{VB} + \frac{3}{4}d^2_{\parallel}(3\mu^2W_1+2\mu\nu V_1+3\nu^2W_5)|q|^2 \end{pmatrix} \\
&+ \frac{3}{2}d_{\parallel}(3\alpha\mu W_3 - \beta\mu V_3 + \alpha\nu + 3\beta\nu W_7)\begin{pmatrix} 0 & -iq_- \\ iq_+ & 0 \end{pmatrix} \\
&+ \frac{3}{8}d^2_{\parallel}(3\alpha\mu W_3 + \beta\mu V_3 + \alpha\nu + 3\beta\nu W_7)\begin{pmatrix} 0 & q^2_+ \\ q^2_- & 0 \end{pmatrix},
\end{aligned} \tag{4.40}$$

which has the form of a Hamiltonian given in [158]

$$\begin{aligned}
H_{2\,band}(\boldsymbol{q}) = &at\begin{pmatrix} & \tau q_- \\ \tau q_+ & \end{pmatrix} + \frac{\Delta}{2}\begin{pmatrix} 1 & \\ & -1 \end{pmatrix} \\
&+ \begin{pmatrix} uq^2 & \\ & vq^2 \end{pmatrix} + w\begin{pmatrix} & q^2_+ \\ q^2_- & \end{pmatrix}.
\end{aligned} \tag{4.41}$$

We then fit the eigenvalues of the Hamiltonian in Eq. 4.41 to the *ab initio* TB model given in Eq. 4.1 and obtain the bands shown in Fig. 4.8. For $u = w = 0$ we retrieve the massive Dirac fermion (mDf) Hamiltonian with the best-fit values of its parameters $a = 3.193\mathring{A}$, $t = 1.4677eV$ and $\Delta = 1.6848eV$. The fitted bands have been shown in Fig. 4.8 in red over the TB band structure shown in black.

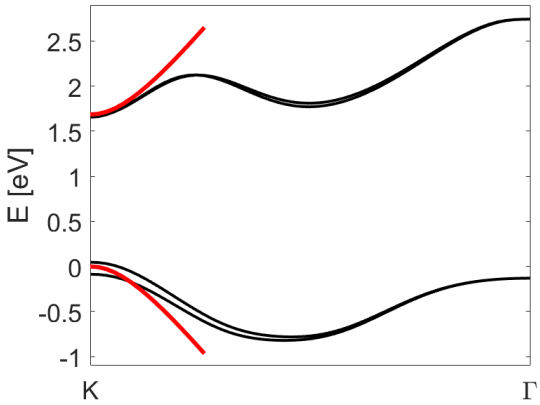

Figure 4.8: Bands obtained through a massive Dirac fermion approximation for MoS_2 at $\boldsymbol{K}$ (red) in comparison to the TB bands for MoS_2 throughout the BZ (black).

4.5 Massive Dirac fermions interacting with light.

I will now derive the optical response of massive Dirac fermions for both valleys when excited with circularly polarised light. From Eq. 2.44 (and from the first term of Eq. 4.41), the unperturbed Hamiltonian for both valleys reads:

$$\hat{H} = \begin{pmatrix} \frac{\Delta}{2} & \frac{v_f}{\hbar}\left(\tau p_x - i p_y\right) \\ \frac{v_f}{\hbar}\left(\tau p_x + i p_y\right) & -\frac{\Delta}{2}, \end{pmatrix} \tag{4.42}$$

where τ is the valley index and $\boldsymbol{p} = \hbar \boldsymbol{q}$. I now take circularly polarised light of the form

$$\begin{aligned} \sigma^{\pm} : \pm\mathcal{E}_x &= \mathcal{E}_0 \sin\omega t, \\ \mathcal{E}_y &= \mathcal{E}_0 \cos\omega t, \end{aligned} \tag{4.43}$$

where $\mathcal{E}_0$ is the strength of the electric field and ω is the frequency of light. We integrate $\boldsymbol{A} = -\int \boldsymbol{\mathcal{E}} dt$ to obtain the vector potential as

$$\begin{aligned} A_x &= \mp\frac{\mathcal{E}_0}{\omega}\cos\omega t, \\ A_y &= -\frac{\mathcal{E}_0}{\omega}\sin\omega t, \end{aligned} \tag{4.44}$$

which can be now inserted in the mDf Hamiltonian at $\boldsymbol{K}$ given in Eq. 4.41 for $u = w = 0$, with a substitution $\boldsymbol{p} \to \boldsymbol{p} - e\boldsymbol{A}$. We obtain

$$\begin{aligned}\hat{H} &= \begin{pmatrix} \frac{\Delta}{2} & \frac{v_f}{\hbar}\Big((p_x - eA_x) - i\,(p_y - eA_y)\Big) \\ \frac{v_f}{\hbar}\Big((p_x - eA_x) + i\,(p_y - eA_y)\Big) & -\frac{\Delta}{2} \end{pmatrix} \\ &= \begin{pmatrix} \frac{\Delta}{2} & \frac{v_f}{\hbar}(p_x - ip_y) \\ \frac{v_f}{\hbar}(p_x + ip_y) & -\frac{\Delta}{2} \end{pmatrix} - g \begin{pmatrix} 0 & \pm e^{\pm i\omega t} \\ \pm e^{\mp i\omega t} & 0 \end{pmatrix} \\ &= \hat{H}_{mDf} + \hat{H}'(\sigma^{\pm}), \end{aligned} \tag{4.45}$$

where $g = \frac{ev_f\mathcal{E}_0}{\hbar\omega}$. The stationary solutions of the unperturbed part $\hat{H}_{mDf}$, $|-_{\boldsymbol{q}}\rangle, |+_{\boldsymbol{q}}\rangle$ have been given in Eq. 2.46. The perturbation for both valleys takes the form:

$$\hat{H}'(\sigma^{\pm}) = -g \begin{pmatrix} 0 & \pm\tau e^{\pm\tau i\omega t} \\ \pm\tau e^{\mp\tau i\omega t} & 0 \end{pmatrix}. \tag{4.46}$$

With the perturbation $\hat{H}'$ added, we seek a time dependent wavefunction of the form

$$|\Psi(t)\rangle = c_-^{\boldsymbol{q}}(t) e^{-\frac{i}{\hbar}E_{\boldsymbol{q}}^- t} |-_{\boldsymbol{q}}\rangle + c_+^{\boldsymbol{q}}(t) e^{-\frac{i}{\hbar}E_{\boldsymbol{q}}^+ t} |+_{\boldsymbol{q}}\rangle, \tag{4.47}$$

where c_- and c_+ are coefficients of the wavefunction components wirtten in the basis of the unperturbed problem with eigenstates $|\pm_{\boldsymbol{q}}\rangle, E_{\boldsymbol{q}}^{\pm}$. We insert the wavefunction in Eq. 4.47 into the time-dependent Schrodinger's equation (TDSE)

$$i\hbar\frac{\partial}{\partial t}\Psi(t) = \left(\hat{H}_{mDf} + \hat{H}'\right)\Psi \tag{4.48}$$

to obtain

$$i\hbar\frac{\partial c_-(t)}{\partial t} e^{-\frac{i}{\hbar}E^- t} |-\rangle + i\hbar\frac{\partial c_+(t)}{\partial t} e^{-\frac{i}{\hbar}E^+ t} |+\rangle = c_-(t) e^{-\frac{i}{\hbar}E^- t}\hat{H}' |-\rangle + c_+(t) e^{-\frac{i}{\hbar}E^+ t}\hat{H}' |+\rangle, \tag{4.49}$$

where the index $\boldsymbol{q}$ has been dropped for simplicity. We then project on $|-\rangle$ and $|+\rangle$

to obtain a system of equations

$$\begin{aligned} i\hbar\dot{c_+}(t) &= c_-(t)H_{+-}e^{\frac{i}{\hbar}\Delta Et} + c_+(t)H_{++}, \\ i\hbar\dot{c_-}(t) &= c_-(t)H_{--} + c_+(t)H_{-+}e^{-\frac{i}{\hbar}\Delta Et}, \end{aligned} \tag{4.50}$$

where $\Delta E = E^+ - E^-$ and H_{+-} etc. denote matrix elements of the perturbation in the basis of the unperturbed states calculated for valley $\boldsymbol{K}$ as

$$\begin{aligned} H_{+-} = \langle + | \hat{H}'(\sigma^+) | - \rangle &= -\frac{gv_f|\boldsymbol{q}|}{N_+N_-}\left(\left(E + \frac{\Delta}{2}\right) e^{i(\omega t+\theta)} + \left(-E + \frac{\Delta}{2}\right) e^{-i(\omega t+\theta)} \right) \\ &= 2g_0\Big(-\frac{\Delta}{2}\cos(\omega t+\theta) - iE\sin(\omega t+\theta)\Big), \\ H_{-+} = \langle - | \hat{H}'(\sigma^+) | - \rangle &= -\frac{gv_f|\boldsymbol{q}|}{N_+N_-}\left(\left(E - \frac{\Delta}{2}\right) e^{i(\omega t-\theta)} + \left(-E - \frac{\Delta}{2}\right) e^{-i(\omega t-\theta)} \right) \\ &= 2g_0\Big(\frac{\Delta}{2}\cos(\omega t-\theta) - iE\sin(\omega t-\theta)\Big) \end{aligned} \tag{4.51}$$

and similarly for other matrix elements. In Eq. 4.51, $g_0 = g\frac{1}{2E}$, $g_\pm = g\frac{v_f|\boldsymbol{q}|}{2E\left(E\pm\frac{\Delta}{2}\right)}$, $E = \left|E^\pm_{\boldsymbol{q}}\right|$ and $\boldsymbol{q} = |\boldsymbol{q}|e^{i\theta}$, where θ is the wavevector's angle. For both valleys we obtain

$$\begin{aligned} \langle + | \hat{H}'(\sigma^\pm) | - \rangle &= -g_0\left(\left(\tau E \pm \frac{\Delta}{2}\right) e^{i(\omega t\pm\theta)} + \left(-\tau E \pm \frac{\Delta}{2}\right) e^{-i(\omega t\pm\theta)} \right) \\ &= 2g_0\Big(\mp\frac{\Delta}{2}\cos(\omega t\pm\theta) - i\tau E\sin(\omega t\pm\theta)\Big), \\ \langle - | \hat{H}'(\sigma^\pm) | - \rangle &= \pm 2g_-\left(E - \frac{\Delta}{2}\right)\cos(\omega t\pm\theta), \\ \langle + | \hat{H}'(\sigma^\pm) | + \rangle &= \mp 2g_+\left(E + \frac{\Delta}{2}\right)\cos(\omega t\pm\theta). \end{aligned} \tag{4.52}$$

We now transform Eq. 4.50 using

$$\begin{aligned} c_+(t) &= e^{-\frac{i}{\hbar}\int_0^t H_{++}(t')dt'}\widetilde{c}_+(t), \\ c_-(t) &= e^{-\frac{i}{\hbar}\int_0^t H_{--}(t')dt'}\widetilde{c}_-(t), \end{aligned} \tag{4.53}$$

and obtain

$$\begin{aligned} i\hbar\dot{\widetilde{c}}_+(t) &= \widetilde{c}_-(t)H_{+-}e^{\frac{i}{\hbar}\int_0^t(\Delta E+H_{++}(t')-H_{--}(t'))dt'}, \\ i\hbar\dot{\widetilde{c}}_-(t) &= \widetilde{c}_+(t)H_{-+}e^{\frac{i}{\hbar}\int_0^t(\Delta E+H_{++}(t')-H_{--}(t'))dt'}. \end{aligned} \tag{4.54}$$

We now use the explicit form of the matrix elements given in Eq. 4.52 and to the first order in the electric field strength $\mathcal{E}_0$ and for $c_-(t=0)=1$ we get

$$\begin{aligned} \sigma^+, \boldsymbol{K}: \quad \dot{\widetilde{c}}_+(t) &= \frac{i}{\hbar}g_0\left(\left(E+\frac{\Delta}{2}\right)e^{i\left(\omega t+\frac{\Delta E}{\hbar}t+\theta\right)}+\cancel{\left(-E+\frac{\Delta}{2}\right)e^{-i\left(\omega t-\frac{\Delta E}{\hbar}t+\theta\right)}}\right), \\ \sigma^-, \boldsymbol{K}: \quad \dot{\widetilde{c}}_+(t) &= \frac{i}{\hbar}g_0\left(\cancel{\left(E-\frac{\Delta}{2}\right)e^{i\left(\omega t+\frac{\Delta E}{\hbar}t-\theta\right)}}+\left(-E-\frac{\Delta}{2}\right)e^{-i\left(\omega t-\frac{\Delta E}{\hbar}t-\theta\right)}\right), \\ \sigma^+, -\boldsymbol{K}: \quad \dot{\widetilde{c}}_+(t) &= \frac{i}{\hbar}g_0\left(\cancel{\left(-E+\frac{\Delta}{2}\right)e^{i\left(\omega t+\frac{\Delta E}{\hbar}t+\theta\right)}}+\left(E+\frac{\Delta}{2}\right)e^{-i\left(\omega t-\frac{\Delta E}{\hbar}t+\theta\right)}\right), \\ \sigma^-, -\boldsymbol{K}: \quad \dot{\widetilde{c}}_+(t) &= \frac{i}{\hbar}g_0\Bigg(\underbrace{\left(-E-\frac{\Delta}{2}\right)e^{i\left(\omega t+\frac{\Delta E}{\hbar}t-\theta\right)}}_{non-resonant}+\underbrace{\cancel{\left(E-\frac{\Delta}{2}\right)e^{-i\left(\omega t-\frac{\Delta E}{\hbar}t-\theta\right)}}}_{resonant}\Bigg), \end{aligned} \tag{4.55}$$

where terms with $\omega - \Delta E/\hbar$ are resonant absorption terms and $\omega + \Delta E/\hbar$ are non-resonant. The crossed out terms in Eq. 4.55 vanish because at $\boldsymbol{K}$ and $-\boldsymbol{K}$, $E = \frac{\Delta}{2}$. We use the rotating wave approximation and keep only the resonant terms to obtain

$$\begin{aligned} \sigma^-, \boldsymbol{K}: \quad \dot{\widetilde{c}}_+(t) &= -\frac{i}{\hbar}g_0\left(E+\frac{\Delta}{2}\right)e^{-i\left(\omega t-\frac{\Delta E}{\hbar}t-\theta\right)}, \\ \sigma^+, -\boldsymbol{K}: \quad \dot{\widetilde{c}}_+(t) &= \frac{i}{\hbar}g_0\left(E+\frac{\Delta}{2}\right)e^{-i\left(\omega t-\frac{\Delta E}{\hbar}t+\theta\right)}. \end{aligned} \tag{4.56}$$

Eq. 4.56 shows that the valleys can be selectively excited using oppositely circularly polarised light, as shown schematically in Fig. 4.9.

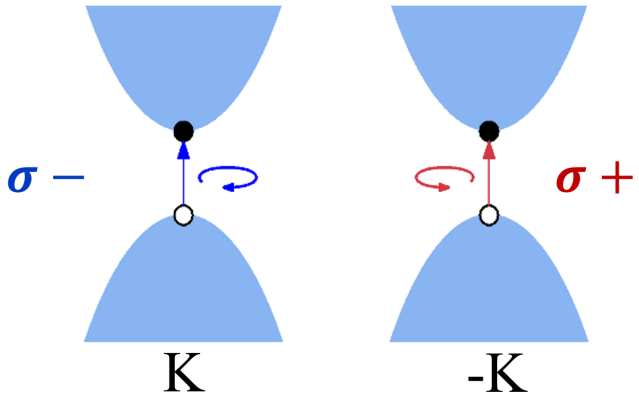

Figure 4.9: Valley-dependent circularly polarised light absorption.

I will now solve Eq. 4.56 to obtain the rate of transition. We calculate

$$\begin{aligned}
\widetilde{c}_+(t) &= -\tau\frac{i}{\hbar}g_0\left(E+\frac{\Delta}{2}\right)e^{i\tau\theta}\int_0^t e^{-i\left(\omega-\frac{\Delta E}{\hbar}\right)t'}dt' \\
&= -\tau\frac{i}{\hbar}g_0\left(E+\frac{\Delta}{2}\right)e^{i\tau\theta}\frac{1}{-\frac{i}{\hbar}w}\left(e^{-\frac{i}{\hbar}wt}-1\right) \\
&= \tau g_0\left(E+\frac{\Delta}{2}\right)\frac{e^{i\tau\theta}}{w}e^{-\frac{i}{\hbar}\frac{w}{2}t}\left(e^{-\frac{i}{\hbar}\frac{w}{2}t}-e^{\frac{i}{\hbar}\frac{w}{2}t}\right) \\
&= \tau g_0\left(E+\frac{\Delta}{2}\right)e^{i\tau\theta}e^{-\frac{i}{\hbar}\frac{w}{2}t}\frac{-2i\sin\frac{w}{2\hbar}t}{\frac{w}{2\hbar}t}\frac{t}{2\hbar} \\
&\quad - i\tau g_0\left(E+\frac{\Delta}{2}\right)e^{i\tau\theta}e^{-\frac{i}{\hbar}\frac{w}{2}t}\frac{\sin\frac{w}{2\hbar}t}{\frac{w}{2\hbar}t}\frac{t}{\hbar}, \qquad (4.57)
\end{aligned}$$

where $w=\omega-\Delta E$. I now calculate the transition rate γ_{fi} as

$$\begin{aligned}
\gamma_{fi} = \frac{|\widetilde{c}_+|^2}{t} &= \frac{1}{t}g_0^2\left(E+\frac{\Delta}{2}\right)^2\left|e^{i\tau\theta-\frac{i}{\hbar}\frac{w}{2}t}\right|^2\frac{\sin^2\frac{w}{2\hbar}t}{\left(\frac{w}{2\hbar}t\right)^2}\left(\frac{t}{\hbar}\right)^2 \\
&= \frac{1}{t}g_0^2\left(E+\frac{\Delta}{2}\right)^2\left|e^{i\tau\theta-\frac{i}{\hbar}\frac{w}{2}t}\right|^2\frac{\pi\delta(w)}{\frac{t}{2\hbar}}\left(\frac{t}{\hbar}\right)^2 \\
&= \frac{1}{t}g_0^2\left(E+\frac{\Delta}{2}\right)^2\left|e^{i\tau\theta-\frac{i}{\hbar}\frac{w}{2}t}\right|^2\frac{2\pi t}{\hbar}\delta(w) \\
&= g^2\frac{\left(E+\frac{\Delta}{2}\right)^2}{4E^2}\frac{2\pi}{\hbar}\delta(\omega-\Delta E), \qquad (4.58)
\end{aligned}$$

where $\frac{\sin^2\frac{xt}{2\hbar}}{\frac{x^2t}{2\hbar}}\to\pi\delta(x)$ as $t\to\infty$, $w=\omega-\Delta E$ and $g=\frac{ev_f\mathcal{E}_0}{\hbar\omega}$. For $\Delta=0$ we retrieve the graphene case. The Eq. 4.58 yields the Fermi Golden rule for mDf, which will be used in chapter 5.

Chapter 5

Magnetoexcitons of massive Dirac fermions

In this chapter I develop a theory of excitons of mDf in the presence of external magnetic field [159]. The SP Hamiltonian used in this chapter is based on the results presented in chapter 4, while the interacting picture solves a single exciton problem using the CI method described in section 2.2.7.

5.1 Non-interacting Massive Dirac fermions in external magnetic field.

Before I study the exciton spectrum of mDf in magnetic field, I will solve this problem for free electrons (section 5.1.1). I will build on this description to treat mDf in sections 5.1.2 and 5.1.3. Section 5.1.4 contains a derivation of the optical selection rules used in the interacting problem.

5.1.1 Free electrons in external magnetic field.

I will first consider a free electron in 2D in the presence of strong external magnetic field and show the emergence of degenerate energy levels, called Landau levels (LL) [160].

I start with a magnetic field in the z direction as $\boldsymbol{B} = (0, 0, B)$. I substitute $\hat{H}(\hat{\boldsymbol{p}}) \rightarrow \hat{H}(\hat{\boldsymbol{\Pi}}) = \hat{H}(\hat{\boldsymbol{p}} + e\hat{\boldsymbol{A}}(\boldsymbol{r}))$ [160] in order to introduce the magnetic field in the free electron Hamiltonian, where $\boldsymbol{A}(\boldsymbol{r})$ is vector potential given by $\nabla \times \boldsymbol{A}(\boldsymbol{r}) = \boldsymbol{B}$. Throughout the thesis I will choose the symmetric gauge, where

$$\begin{aligned} \boldsymbol{A}(\boldsymbol{r}) &= (-\frac{By}{2}, \frac{Bx}{2}, 0). \\ \nabla \times \boldsymbol{A}(\boldsymbol{r}) &= \begin{vmatrix} \frac{\partial}{\partial x} & \frac{\partial}{\partial y} & \frac{\partial}{\partial z} \\ -\frac{By}{2} & \frac{Bx}{2} & 0 \\ \hat{i} & \hat{j} & \hat{k} \end{vmatrix} = \left(\frac{B}{2} + \frac{B}{2}\right)\hat{k} = (0, 0, B). \end{aligned} \tag{5.1}$$

The free electron Hamiltonian in the presence of external magnetic field then reads

$$\hat{H}_B = \frac{1}{2m^*}\hat{\boldsymbol{\Pi}}^2 + g\mu_B B\sigma = \frac{1}{2m^*}\left(\hat{\boldsymbol{p}} + e\hat{\boldsymbol{A}}(\boldsymbol{r})\right)^2 + g\mu_B B\sigma, \tag{5.2}$$

where e is electron charge, g is the Lande factor, $\mu_B = \frac{e\hbar}{2m_e}$ is the Bohr magneton and σ denotes spin. The second term in Eq. 5.2 is the Zeeman term, that splits the energy levels of spin up and spin down and I will neglect it in the following discussion.

Because of the spatial dependence of $\boldsymbol{A}$ in Eq. 5.2, the Hamiltonian $\hat{H}_B$ is no longer translationally invariant $\hat{H}(\hat{\boldsymbol{p}} + e\hat{\boldsymbol{A}}) = \hat{H}(\hat{\boldsymbol{p}}, \hat{\boldsymbol{r}})$.

After introducing $\boldsymbol{A}$ in Eq. 5.2, the components of the new momentum $\boldsymbol{\Pi}$ also no longer commute

$$\begin{aligned} [\Pi_x, \Pi_y] = [p_x + eA_x, p_y + eA_y] &= e\Big([p_x, A_y] - [p_y, A_x] \Big) \\ &= e\Big(\frac{B}{2}[p_x, x] - \frac{B}{2}[p_y, y]\Big) = -i\hbar eB = -i\hbar m^*\omega_c, \end{aligned} \tag{5.3}$$

where $\omega_c = \frac{eB}{m^*}$ is a cyclotron frequency. Now, because the components of momentum $\boldsymbol{\Pi}$ do not commute, the Hamiltonian in Eq. 5.2 cannot be solved separately for x and

y components. I therefore have to introduce ladder operators

$$\begin{aligned} a &= \frac{l_B}{\sqrt{2}\hbar}\left(i\Pi_x + \Pi_y\right), \quad a^\dagger = \frac{l_B}{\sqrt{2}\hbar}\left(-i\Pi_x + \Pi_y\right), \\ \Pi_x &= \frac{1}{i}\frac{\hbar}{\sqrt{2}l_B}\left(a - a^\dagger\right), \quad \Pi_y = \frac{\hbar}{\sqrt{2}l_B}\left(a + a^\dagger\right) \end{aligned} \tag{5.4}$$

where $l_B = \sqrt{\frac{\hbar}{m^*\omega_c}}$ is magnetic length and the commutator of the ladder operators $a, a^\dagger$ is $\left[a, a^\dagger\right] = 1$, as required. The Hamiltonian in Eq. 5.2 written in terms of ladder operators in Eq. 5.4 (without the Zeeman term) reads

$$\begin{aligned} \hat{H}_B = \frac{1}{2m^*}\left(\hat{\Pi}_x^2 + \hat{\Pi}_y^2\right) &= \frac{1}{2m^*}\frac{\hbar^2}{2l_B^2}\Big(- \left(a - a^\dagger\right)^2 + \left(a + a^\dagger\right)^2 \Big) \\ &= \frac{\hbar\omega_c}{2}\left(a^\dagger a + aa^\dagger\right) = \hbar\omega_c\big(a^\dagger a + \frac{1}{2}\big). \end{aligned} \tag{5.5}$$

The Hamiltonian in Eq. 5.5 is in fact a harmonic oscillator (HO) Hamiltonian and the solutions are

$$\begin{aligned} E_n &= \hbar\omega_c\left(n + \frac{1}{2}\right), \\ |n\rangle &= \frac{1}{\sqrt{n!}}\left(a^\dagger\right)^n|0\rangle, \end{aligned} \tag{5.6}$$

where the energy eigenstates $|n\rangle$ are called Landau levels (LL). However, the solutions in Eq. 5.6 are described by one quantum number only. This is not complete, as the Hamiltonian in Eq. 5.2 contains two dimensions. We must therefore search for another pair of operators, which will determine the degeneracy of levels E_n. Let us use $\hat{\widetilde{\boldsymbol{\Pi}}} = \hat{\boldsymbol{p}} - e\hat{\boldsymbol{A}}$ so that we get

$$\begin{aligned} b &= \frac{l_B}{\sqrt{2}\hbar}\left(i\widetilde{\Pi}_x - \widetilde{\Pi}_y\right), \quad b^\dagger = \frac{l_B}{\sqrt{2}\hbar}\left(-i\widetilde{\Pi}_x - \widetilde{\Pi}_y\right), \\ \widetilde{\Pi}_x &= \frac{1}{i}\frac{\hbar}{\sqrt{2}l_B}\left(b - b^\dagger\right), \quad \widetilde{\Pi}_y = \frac{\hbar}{\sqrt{2}l_B}\left(-b - b^\dagger\right) \end{aligned} \tag{5.7}$$

and the commutator of the ladder operators $b, b^\dagger$ is $\left[b, b^\dagger\right] = 1$ and also $[a, b] = \left[a^\dagger, b^\dagger\right] = 0$, as required. This proves that a, b correspond to two independent HO

with eigenstates written in a standard way as

$$\begin{aligned} a\,|n\rangle &= \sqrt{n}\,|n-1\rangle\,, \quad a^\dagger\,|n\rangle = \sqrt{n+1}\,|n+1\rangle\,, \\ b\,|m\rangle &= \sqrt{m}\,|m-1\rangle\,, \quad b^\dagger\,|m\rangle = \sqrt{m+1}\,|m+1\rangle\,. \end{aligned} \tag{5.8}$$

The Hamiltonian in Eq. 5.5 can be also written as

$$\hat{H}_B = \hbar\omega_c\big(a^\dagger a + \frac{1}{2}\big) + 0\cdot\big(b^\dagger b + \frac{1}{2}\big), \tag{5.9}$$

where the additonal HO has a vanishing spacing, which makes the energy levels E_n degenerate. The full 2D HO solutions are

$$\begin{aligned} E_n &= \hbar\omega_c\left(n+\frac{1}{2}\right), \\ |nm\rangle &= \frac{1}{\sqrt{n!m!}}\left(a^\dagger\right)^n\left(b^\dagger\right)^m|00\rangle\,, \end{aligned} \tag{5.10}$$

where m gives the degeneracy of E_n.

In order to discuss this degeneracy, I will turn to a semiclassical interpretation of the cyclotron motion governed by Eq. 5.5. Because the Hamiltonian $\hat{H}_B$ depends only on $\hat{\mathbf{\Pi}}$, but not $\hat{\widetilde{\mathbf{\Pi}}}$, then $\hat{\widetilde{\mathbf{\Pi}}}$ is a constant of motion. Let me express variables x, y in terms of $\mathbf{\Pi}, \widetilde{\mathbf{\Pi}}$. We use

$$\boldsymbol{A} = \frac{B}{2}(-y, x) = \frac{1}{2e}\left(\mathbf{\Pi} - \widetilde{\mathbf{\Pi}}\right) \tag{5.11}$$

to obtain

$$\begin{aligned} y &= \widetilde{\Pi}_x\frac{1}{eB} - \Pi_x\frac{1}{eB} = Y + \eta_y, \\ x &= -\widetilde{\Pi}_y\frac{1}{eB} + \Pi_y\frac{1}{eB} = X + \eta_x, \end{aligned} \tag{5.12}$$

where momentum $\mathbf{\Pi}$ determines the relative cyclotron variable of motion $\boldsymbol{\eta} = \frac{l_B^2}{\hbar}(\Pi_y, -\Pi_x)$ and $\boldsymbol{R} = (X, Y) = \frac{l_B^2}{\hbar}(-\widetilde{\Pi}_y, \widetilde{\Pi}_x)$ is the position of the centre of motion, which is a constant, as one would expect. The electron position is described as $\boldsymbol{r} = \boldsymbol{R} + \boldsymbol{\eta}$, as

shown in Fig. 5.1.

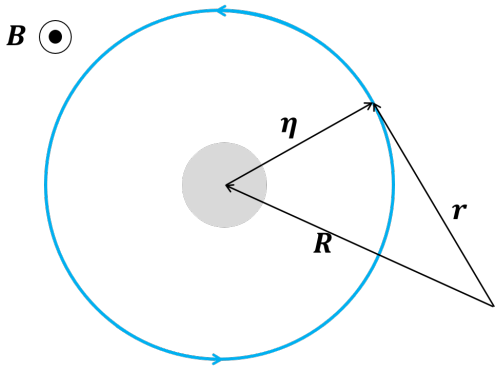

Figure 5.1: Relative cyclotron motion $\boldsymbol{\eta}$ (blue circle) of an electron about the centre $\boldsymbol{R}$ with uncertainty of the position (grey circle).

It is instructive to consider a commutator

$$[X, Y] = \frac{l_B^4}{\hbar^2}\left[-\widetilde{\Pi}_y, \widetilde{\Pi}_x\right] = \frac{l_B^4}{\hbar^2}\frac{\hbar^2}{2l_B^2}\frac{-1}{i}\Big(\left[b, b^\dagger\right] - \left[b^\dagger, b\right]\Big) = il_B^2. \tag{5.13}$$

This means that there is uncertainty regarding the centre postion (X, Y) so the minimal surface it takes is $\Delta X \Delta Y = 2\pi l_B^2$. This allows us to define the number of quantum states per unit area

$$n_B = \frac{1}{\Delta X \Delta Y} = \frac{1}{2\pi l_B^2} = \frac{B}{h/e}, \tag{5.14}$$

which is the magnetic field measured in the units of flux quantum $\frac{h}{e}$. The number of flux quanta n_B penetrating a surface is therefore equal to the degeneracy of a LL. Eq. 5.14 shows that the degeneracy of a LL increases with magnetic field B.

5.1.2 Landau levels for massive Dirac fermions.

I will now describe the LL structure for mDf and highlight the differences from the free electron case given in section 5.1.1.

I start with a mDf Hamiltonian for valley $\boldsymbol{K}$ with vector potential, just as in Eq.

4.45, to obtain

$$\hat{H}^B_{mDf} = \begin{pmatrix} \frac{\Delta}{2} & v_f\Big(-i\partial_x - \partial_y - \frac{eB}{2\hbar}(y+ix)\Big) \\ v_f\Big(-i\partial_x + \partial_y + \frac{eB}{2\hbar}(-y+ix)\Big) & -\frac{\Delta}{2} \end{pmatrix}, \tag{5.15}$$

where $\frac{\boldsymbol{p}}{\hbar} = \boldsymbol{q} = -i\boldsymbol{\partial}$. In order to diagonalise the Hamiltonian in Eq. 5.15 I introduce ladder operators, identical to those given in Eq. 5.4, written explicitly as

$$\begin{aligned} \hat{a} &= \frac{l_B}{\sqrt{2}}\Big(\partial_x - i\partial_y + \frac{1}{2l_B^2}(x-iy)\Big) = \frac{1}{2}\Big(\frac{\zeta}{\sqrt{2}} + \sqrt{2}\partial^*_\zeta\Big), \\ \hat{a}^\dagger &= \frac{l_B}{\sqrt{2}}\Big(-\partial_x - i\partial_y + \frac{1}{2l_B^2}(x+iy)\Big) = \frac{1}{2}\Big(\frac{\zeta^*}{\sqrt{2}} - \sqrt{2}\partial_\zeta\Big), \end{aligned} \tag{5.16}$$

where I introduced dimensionless variables

$$\begin{aligned} \zeta = \frac{x-iy}{l_B}, \quad \zeta^* = \frac{x+iy}{l_B}, \\ \partial_\zeta = l_B(\partial_x + i\partial_y), \quad \partial^*_\zeta = l_B(\partial_x - i\partial_y). \end{aligned} \tag{5.17}$$

The Hamiltonian in Eq. 5.15 can be expressed with the ladder operators given in Eq. 5.16 as

$$\hat{H}^B_{mDf}(\boldsymbol{K}) = \begin{pmatrix} \frac{\Delta}{2} & -iv\hat{a} \\ iv\hat{a}^\dagger & -\frac{\Delta}{2} \end{pmatrix}, \tag{5.18}$$

where $v = \sqrt{2}\frac{v_f}{l_B}$. The Hamiltonian in Eq. 5.18 is written in the basis of CB and VB states at $\boldsymbol{K}$, as explained in section 4.4.

Following the section 5.1.1, we expect a 2D HO wavefunction solution of the Hamiltonian in Eq. 5.18. We postulate a solution of the form

$$\big|\Psi^{\boldsymbol{K}}_B\big\rangle = \begin{pmatrix} \alpha\,|n-1,m\rangle \\ \beta\,|n,m\rangle \end{pmatrix}, \tag{5.19}$$

where $|n,m\rangle$ are LLs for a free electron, given in Eq. 5.10. It is important to emphasize the form of the postulated wavefunction here. The magnetic field modifies its envelope, from the wavefunction in the absence of magnetic field (given by Eq. 2.46)

to the wavefunction in the presence of magnetic field, as:

$$\begin{aligned}\Psi^{\pm}_{\boldsymbol{q}}(\boldsymbol{K}) = \quad & \begin{pmatrix} \alpha^{\pm}_{\boldsymbol{q}} e^{i\boldsymbol{K}\boldsymbol{r}} u^{\boldsymbol{K}}_{C}(\boldsymbol{r}) \\ \beta^{\pm}_{\boldsymbol{q}} e^{i\theta_{\boldsymbol{q}}} e^{i\boldsymbol{K}\boldsymbol{r}} u^{\boldsymbol{K}}_{V}(\boldsymbol{r}) \end{pmatrix} = \begin{pmatrix} C^{\pm}_{\boldsymbol{q}}(\boldsymbol{K}) \\ V^{\pm}_{\boldsymbol{q}}(\boldsymbol{K}) \end{pmatrix} \\ \downarrow B & \\ \Psi^{\pm}_{nm}(\boldsymbol{K}) = & \begin{pmatrix} \alpha^{\pm}_{n} w^{n,m,\boldsymbol{K}}_{C}(\boldsymbol{r}) u^{\boldsymbol{K}}_{C}(\boldsymbol{r}) \\ \beta^{\pm}_{n} w^{n,m,\boldsymbol{K}}_{V}(\boldsymbol{r}) u^{\boldsymbol{K}}_{V}(\boldsymbol{r}) \end{pmatrix} = \begin{pmatrix} C^{\pm}_{nm}(\boldsymbol{K}) \\ V^{\pm}_{nm}(\boldsymbol{K}) \end{pmatrix}, \end{aligned} \tag{5.20}$$

where $\left| w^{n,m,\boldsymbol{K}}_{C} \right\rangle = |n-1,m\rangle$ and $\left| w^{n,m,\boldsymbol{K}}_{V} \right\rangle = |n,m\rangle$ are LL envelopes at $\boldsymbol{K}$ and $u^{\boldsymbol{K}}_{C/V}$ are periodic parts of the wavefunction, and $\pm$ corresponds to positive and negative energy solutions. To solve for α, β and E_n I substitute $\Psi^{\boldsymbol{K}}_{B}$ from Eq. 5.19 in the TISE and obtain

$$\begin{pmatrix} \frac{\Delta}{2} & -iv\hat{a} \\ iv\hat{a}^{\dagger} & -\frac{\Delta}{2} \end{pmatrix} \begin{pmatrix} \alpha\,|n-1,m\rangle \\ \beta\,|n,m\rangle \end{pmatrix} = E^{\pm}_{n} \begin{pmatrix} \alpha\,|n-1,m\rangle \\ \beta\,|n,m\rangle \end{pmatrix}. \tag{5.21}$$

I evaluate

$$\begin{aligned} \frac{\Delta}{2}\alpha\,|n-1\rangle - iv\beta\sqrt{n}\,|n-1\rangle = E\alpha\,|n-1\rangle\,, \\ iv\alpha\sqrt{n}\,|n\rangle - \frac{\Delta}{2}\alpha\,|n\rangle = E\alpha\,|n\rangle\,, \end{aligned} \tag{5.22}$$

where I used $\hat{a}\,|n\rangle = \sqrt{n}\,|n-1\rangle$ and I obtain

$$\begin{pmatrix} \frac{\Delta}{2} & -iv\sqrt{n} \\ iv\sqrt{n} & -\frac{\Delta}{2} \end{pmatrix} \begin{pmatrix} \alpha \\ \beta \end{pmatrix} = E^{\pm}_{n} \begin{pmatrix} \alpha \\ \beta \end{pmatrix}. \tag{5.23}$$

The solutions to Eq. 5.23 are then

$$\begin{aligned} E_n^{\pm} &= \pm\sqrt{v^2 n + \left(\frac{\Delta}{2}\right)^2}, \\ \left|\Psi_{nm}^{\pm}(\boldsymbol{K})\right\rangle &= \begin{pmatrix} \alpha_n^{\pm} \left|n-1, m\right\rangle \\ \beta_n^{\pm} \left|n, m\right\rangle \end{pmatrix} \\ &= \alpha_n^{\pm} \left|n-1, m\right\rangle_{C,\boldsymbol{K}} + \beta_n^{\pm} \left|n, m\right\rangle_{V,\boldsymbol{K}}, \end{aligned} \tag{5.24}$$

where the energies $E_{\pm}^{mDf}$ follow a square root dependence on n for large n, unlike the free electron LL energy levels given in Eq. 5.10, which are linear in n. More importantly, the mDf LL wavefunction for positive and negative energies is a mixture of VB and CB LLs at $\boldsymbol{K}$ with the number of LL different by 1. The coefficients α, β are given by

$$\begin{aligned} \alpha_n^{\pm} &= -\frac{iv\sqrt{n}}{N_n^{\pm}}, \\ \beta_n^{\pm} &= \frac{E_n^{\pm} - \frac{\Delta}{2}}{N_n^{\pm}}, \\ N_n^{\pm} &= \sqrt{2E_n^{\pm}\left(E_n^{\pm} - \frac{\Delta}{2}\right)} \end{aligned} \tag{5.25}$$

and have been plotted in Fig. 5.2 for the lowest LLs for a strong magnetic field of $B = 60T$, close to the highest fields obtained in experiment [161]. For small n it is apparent that the admixture of VB LLs in positive energy solutions and CB LLs in negative energy solutions is low.

In particular, let us consider the wavefunction $|\Psi_{nm}^{\pm}\rangle$ for $n = 0$:

$$\begin{aligned} \left|\Psi_{0,m}^{-}(\boldsymbol{K})\right\rangle &= \begin{pmatrix} 0 \\ \left|0, m\right\rangle \end{pmatrix} = \left|0, m\right\rangle_{V,\boldsymbol{K}} \\ \left|\Psi_{0,m}^{+}(\boldsymbol{K})\right\rangle &= 0, \end{aligned} \tag{5.26}$$

which shows that the zeroth LL is the only level that is not a mixture and is built of the VB states entirely. It is also absent in the positive energies. The missing positive

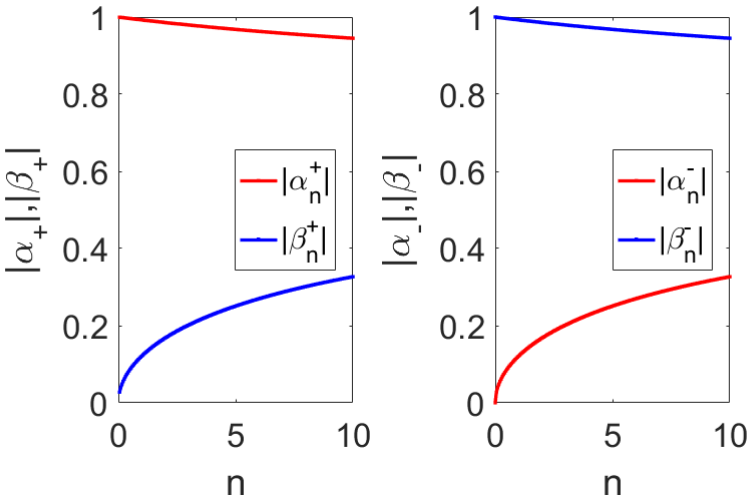

Figure 5.2: Eigenvector components for mDf LLs for (left) positive and (right) negative energies. Red (blue) lines label $\alpha_n, (\beta_n)$ components given by Eq. 5.25.

energy zero LL comes from the $-\boldsymbol{K}$ valley. By substituting the vector potential in Eq. 5.1 into the massive Dirac Hamiltonian around $-\boldsymbol{K}$ given in Eq. 4.42, I obtain the Hamiltonian

$$\hat{H}^B_{mDf}(-\boldsymbol{K}) = \begin{pmatrix} \frac{\Delta}{2} & iv\hat{a}^\dagger \\ -iv\hat{a} & -\frac{\Delta}{2} \end{pmatrix} \tag{5.27}$$

and the solutions are analogously obtained to give

$$\begin{aligned} E_n^\pm &= \pm\sqrt{v^2 n + \left(\frac{\Delta}{2}\right)^2}, \\ \left|\Psi^\pm_{nm}(-\boldsymbol{K})\right\rangle &= \begin{pmatrix} \alpha_n^{\pm *} \left|n, m\right\rangle \\ \beta_n^\pm \left|n-1, m\right\rangle \end{pmatrix} \\ &= \alpha_n^{\pm *} \left|n, m\right\rangle_{C,-\boldsymbol{K}} + \beta_n^\pm \left|n-1, m\right\rangle_{V,-\boldsymbol{K}}, \end{aligned} \tag{5.28}$$

where $\alpha_n^\pm, \beta_n^\pm$ are given with the same expressions as in Eq. 5.25, but $\alpha_n^\pm$ is conjugated. As expected, I obtain the zeroth LL at $-\boldsymbol{K}$ as

$$\begin{aligned} \left|\Psi^-_{0,m}(-\boldsymbol{K})\right\rangle &= 0, \\ \left|\Psi^+_{0,m}(-\boldsymbol{K})\right\rangle &= \begin{pmatrix} \left|0, m\right\rangle \\ 0 \end{pmatrix} = \left|0, m\right\rangle_{C,-\boldsymbol{K}}, \end{aligned} \tag{5.29}$$

which reveals a zeroth LL only for positive energies in valley $-\boldsymbol{K}$.

The LL energy structure for both valleys has been shown in Fig. 5.3, including the asymmetric 0th LL, given by Eq. 5.26 and 5.29. The black lines represent LLs for both valleys, and blue lines show energy dispersion for $B = 0$. Red thick lines denote the 0th LL, with negative energy $E_0^-(\boldsymbol{K}) = -\frac{\Delta}{2}$ at $\boldsymbol{K}$ and positive energy $E_0^+(-\boldsymbol{K}) = \frac{\Delta}{2}$ at $-\boldsymbol{K}$. This places the 0th LL at the top of the VB at $\boldsymbol{K}$ and at the bottom of the CB at $-\boldsymbol{K}$.

It is important to emphasize the emerging asymmetry of the energy structure in both valleys which results in energy splitting between the first available CB state at $\boldsymbol{K}$ and $-\boldsymbol{K}$, called the valley Zeeman splitting (VZS) Δ_{VZ} (shown in green in Fig. 5.3). Δ_{VZ} is given by

$$\Delta_{VZ} = E_1^+(\boldsymbol{K}) - E_0^+(-\boldsymbol{K}) \approx \Delta \left(\frac{v_f}{\Delta}\right)^2 \hbar\omega_c, \tag{5.30}$$

which increases with magnetic field strength B through ω_c. The presence of the splitting Δ_{VZ} enables selective populating of the valleys with charges [63], as will become apparent later in this chapter.

5.1.3 The effect of spin-orbit coupling.

I will now include the SO coupling in the LL spectrum for mDf by accounting for SO splitting in CB and VB at $\boldsymbol{K}$ and $-\boldsymbol{K}$, Δ_{SO}^C and Δ_{SO}^V respectively. The SO mDf

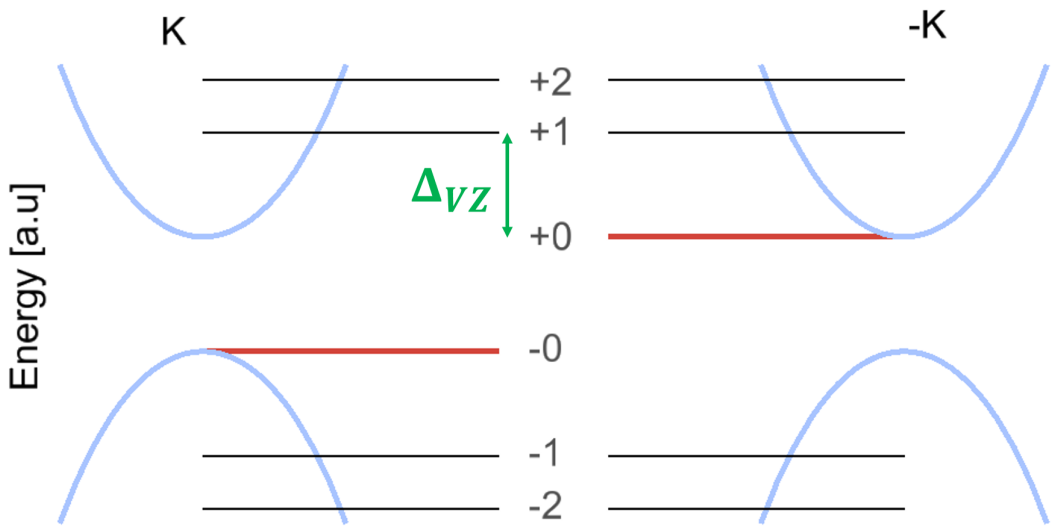

Figure 5.3: Scheamtic asymmetric LL structure for mDf in both valleys (numbers label energy levels). Blue (black and red) lines show energy bands for $B = 0$ ($B > 0$). Red lines denote the 0th LL, which is located at the top of VB (bottom of CB) at $\boldsymbol{K}$ ($-\boldsymbol{K}$). Valley Zeeman splitting Δ_{VZ} originating in the asymmetrical placement of the 0th LL is shown in green.

Hamiltonian for both valleys in the basis $\{CB\downarrow, VB\downarrow, CB\uparrow, VB\uparrow\}$ reads

$$H^B_{SO}(\boldsymbol{K}) = \begin{pmatrix} \frac{\Delta}{2} - \frac{\Delta^C_{SO}}{2} & -iv\hat{a} & 0 & 0 \\ iv\hat{a}^\dagger & -\frac{\Delta}{2} - \frac{\Delta^V_{SO}}{2} & 0 & 0 \\ 0 & 0 & \frac{\Delta}{2} + \frac{\Delta^C_{SO}}{2} & -iv\hat{a} \\ 0 & 0 & iv\hat{a}^\dagger & -\frac{\Delta}{2} + \frac{\Delta^V_{SO}}{2} \end{pmatrix}$$

$$H^B_{SO}(-\boldsymbol{K}) = \begin{pmatrix} \frac{\Delta}{2} + \frac{\Delta^C_{SO}}{2} & iv\hat{a}^\dagger & 0 & 0 \\ -iv\hat{a} & -\frac{\Delta}{2} + \frac{\Delta^V_{SO}}{2} & 0 & 0 \\ 0 & 0 & \frac{\Delta}{2} - \frac{\Delta^C_{SO}}{2} & iv\hat{a}^\dagger \\ 0 & 0 & -iv\hat{a} & -\frac{\Delta}{2} - \frac{\Delta^V_{SO}}{2} \end{pmatrix}, \tag{5.31}$$

where the SO splitting is opposite in both valleys. The solutions for spin s are

$$
\begin{aligned}
E^{\pm}_{ns} &= s\frac{\Delta^C_{SO}+\Delta^V_{SO}}{4} \pm \sqrt{v^2 n + \left(\frac{\Delta + s\frac{\Delta^C_{SO}-\Delta^V_{SO}}{2}}{2}\right)^2} \\
\left|\Psi^{\pm}_{nms}(\boldsymbol{K})\right\rangle &= \begin{pmatrix} \alpha^{\pm}_{n,s}\left|n-1,m\right\rangle \\ \beta^{\pm}_{n,s}\left|n,m\right\rangle \end{pmatrix} \\
\left|\Psi^{\pm}_{nms}(-\boldsymbol{K})\right\rangle &= \begin{pmatrix} \alpha^{\pm^*}_{n,-s}\left|n,m\right\rangle \\ \beta^{\pm}_{n,-s}\left|n-1,m\right\rangle \end{pmatrix}
\end{aligned}
\tag{5.32}
$$

and

$$
\begin{aligned}
\alpha^{\pm}_{n,s} &= -\frac{iv\sqrt{n}}{N^{\pm}_{n,s}}, \\
\beta^{\pm}_{n,s} &= \frac{E^{\pm}_{ns} - \frac{\Delta + s\frac{\Delta^C_{SO}-\Delta^V_{SO}}{2}}{2}}{N^{\pm}_{n,s}}, \\
N^{\pm}_{ns} &= \sqrt{2E^{\pm}_{ns}\left(E^{\pm}_{ns} - \frac{\Delta + s\frac{\Delta^C_{SO}-\Delta^V_{SO}}{2}}{2}\right)}.
\end{aligned}
\tag{5.33}
$$

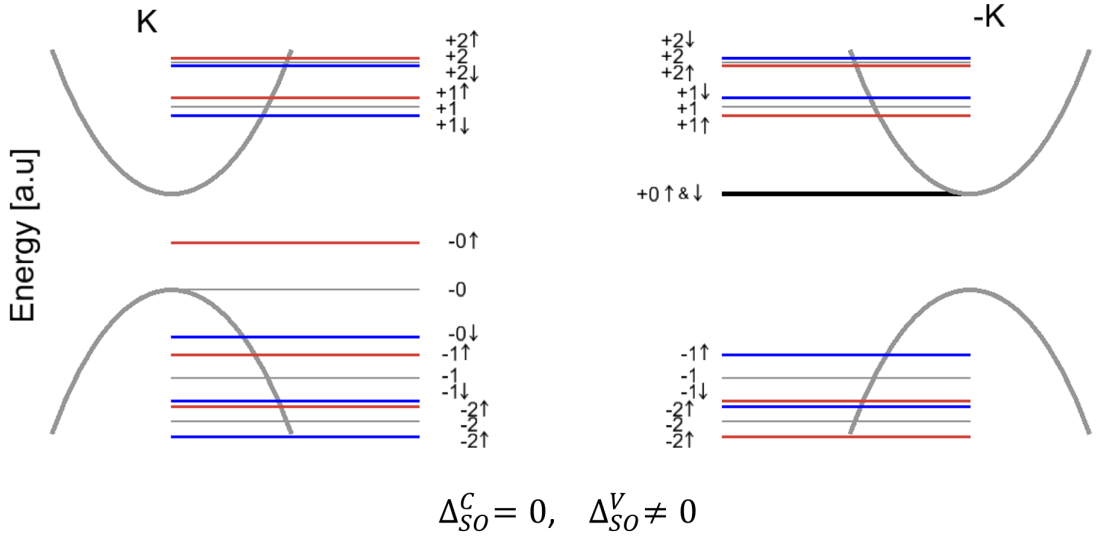

Figure 5.4: Asymmetrical LL structure for mDf with SO splitting $\Delta^V_{SO} > 0, \Delta^C_{SO} = 0$. Red (blue) denotes spin up (down), and grey lines show the LLs for $\Delta^V_{SO} = 0$. Black thick line marks the 0th LL at $-\boldsymbol{K}$, which is not split by $\Delta^V_{SO} > 0$. Other LLs for positive energies are split by $\Delta^V_{SO} > 0$ because of the nature of the mDf LL wavefunction given by Eq. 5.32.

The LL structure with SO splitting has been shown in Fig. 5.4 for $\Delta_{SO}^{C} = 0$ and $\Delta_{SO}^{V} > 0$ (Δ_{SO}^{V} and Δ are not to scale) to emphasise the effect of strong SO splitting for MoS_2 at $\boldsymbol{K}$ and $-\boldsymbol{K}$. Colors show spin-split LLs (red and blue for $\uparrow$ and $\downarrow$), while grey shows the LL with no SO. Strong SO splitting in the VB causes large splitting of LLs for negative energies, but also creates a smaller splitting of positive energy LLs, according to Eq. 5.32. This is a consequence of the mixture of LLs from VB and CB for mDf [156]. The only level, which does not exhibit splitting caused by $\Delta_{SO}^{V} > 0$ is the 0th LL at $-\boldsymbol{K}$, due to the cancellation of the SO term in $E_{0\sigma}^{+}$ in Eq. 5.32. It is apparent that the resulting LL structure is highly assymetric, and additionally, it produces different $\Delta_{VZ}(s)$ for opposite spins s [159].

5.1.4 Coupling to light.

This section describes how mDf in LLs couple to light. I will use the results of section 4.5 to arrive at the transition probability from VB to CB state. We start with the same Hamiltonian of coupling to light $\hat{H}'(\sigma^{\pm})$ as given in Eq. 4.46 and calculate the matrix elements of $\hat{H}'(\sigma^{\pm})$ in the basis of unperturbed LL states given in Eq. 5.24 and 5.28, in a similar fashion to Eq. 4.52. SO splitting does not change the derivation procedure and will be accounted for in the end result. Let us start with the matrix elements of $\hat{H}'(\sigma^{\pm})$ for valley $\boldsymbol{K}$, which read

$$\begin{aligned}
\left\langle \Psi_{nm}^{+}(\boldsymbol{K}) \right| \hat{H}'(\sigma^{+}) \left| \Psi_{n'm'}^{-}(\boldsymbol{K}) \right\rangle &= -g \begin{pmatrix} \alpha_n^{+*} \langle n-1, m|_{C,\boldsymbol{K}} & \beta_n^{+*} \langle n, m|_{V,\boldsymbol{K}} \end{pmatrix} \cdot \\
&\cdot \begin{pmatrix} 0 & e^{i\omega t} \\ e^{-i\omega t} & 0 \end{pmatrix} \begin{pmatrix} \alpha_{n'}^{-} |n'-1, m'\rangle_{C,\boldsymbol{K}} \\ \beta_{n'}^{-} |n', m'\rangle_{V,\boldsymbol{K}} \end{pmatrix} \\
&= -g \Big(e^{-i\omega t} \beta_n^{+*} \alpha_{n'}^{-} {}_{V,\boldsymbol{K}} \langle n, m| \left| n'-1, m' \right\rangle_{C,\boldsymbol{K}} \\
&+ e^{i\omega t} \alpha_n^{+*} \beta_{n'}^{-} {}_{C,\boldsymbol{K}} \langle n-1, m| \left| n', m' \right\rangle_{V,\boldsymbol{K}} \Big),
\end{aligned} \tag{5.34}$$

and analogously for opposite polarisation σ^-. The matrix elements for both $\sigma^\pm$ in valley $\boldsymbol{K}$ read

$$\begin{aligned}\langle +|\,\hat{H}'_{\sigma^+}\,|-\rangle &= -g\Big(e^{-i\omega t}\beta_n^{+^*}\alpha_{n'}^-\langle n,m|n'-1,m'\rangle + e^{i\omega t}\alpha_n^{+^*}\beta_{n'}^-\langle n-1,m|n',m'\rangle\Big)_{CV},\\ \langle +|\,\hat{H}'_{\sigma^-}\,|-\rangle &= g\Big(e^{-i\omega t}\alpha_n^{+^*}\beta_{n'}^-\langle n-1,m|n',m'\rangle + e^{i\omega t}\beta_n^{+^*}\alpha_{n'}^-\langle n,m|n'-1,m'\rangle\Big)_{CV},\end{aligned} \tag{5.35}$$

where $|+\rangle = |\Psi_{nm}^+(\boldsymbol{K})\rangle$ and C, V indices are written as CV for brevity. The reamining matrix elements of $\hat{H}'$ are calculated analogously.

Then, analogously to Eq. 4.47, I can express the time dependent wavefunction as

$$|\Psi(t,\boldsymbol{K})\rangle = c_-^{nm}(t)e^{-\frac{i}{\hbar}E_n^-t}\left|\Psi_{nm}^-(\boldsymbol{K})\right\rangle + c_+^{nm}(t)e^{-\frac{i}{\hbar}E_n^+t}\left|\Psi_{nm}^+(\boldsymbol{K})\right\rangle, \tag{5.36}$$

which is then inserted into the TDSE and the final equations, analogous to Eq. 4.54, read

$$\begin{aligned}i\hbar\dot{\widetilde{c}}_+(t) &= \widetilde{c}_-(t)H_{+-}e^{\frac{i}{\hbar}\int_0^t(\Delta E+H_{++}(t')-H_{--}(t'))dt'},\\ i\hbar\dot{\widetilde{c}}_-(t) &= \widetilde{c}_+(t)H_{-+}e^{\frac{i}{\hbar}\int_0^t(\Delta E+H_{++}(t')-H_{--}(t'))dt'},\end{aligned} \tag{5.37}$$

where $H_{+-} = \langle +|\,\hat{H}'\,|-\rangle$ and we can calculate the analogous expressions for valley $-\boldsymbol{K}$. To the first order in the electric field strength E_0 and for $c_-(t=0)=1$ we get the expressions for both polarisations and both valleys:

$$\begin{aligned}\sigma^+,\boldsymbol{K}: &\quad \dot{\tilde{c}}_+(t) = -\frac{g}{i\hbar}\Big(e^{-i\left(\omega-\frac{\Delta E}{\hbar}\right)t}\beta_n^{+^*}\alpha_{n'}^-\langle n,m|n'-1,m'\rangle + e^{i\left(\omega+\frac{\Delta E}{\hbar}\right)t}\alpha_n^{+^*}\beta_{n'}^-\langle n-1,m|n',m'\rangle\Big)\\ \sigma^-,\boldsymbol{K}: &\quad \dot{\tilde{c}}_+(t) = \frac{g}{i\hbar}\Big(e^{-i\left(\omega-\frac{\Delta E}{\hbar}\right)t}\alpha_n^{+^*}\beta_{n'}^-\langle n-1,m|n',m'\rangle + e^{i\left(\omega+\frac{\Delta E}{\hbar}\right)t}\beta_n^{+^*}\alpha_{n'}^-\langle n,m|n'-1,m'\rangle\Big)\\ \sigma^+,-\boldsymbol{K}: &\quad \dot{\tilde{c}}_+(t) = \frac{g}{i\hbar}\Big(e^{-i\left(\omega-\frac{\Delta E}{\hbar}\right)t}\alpha_n^{+}\beta_{n'}^-\langle n,m|n'-1,m'\rangle + e^{i\left(\omega+\frac{\Delta E}{\hbar}\right)t}\beta_n^{+^*}\alpha_{n'}^{-^*}\langle n-1,m|n',m'\rangle\Big)\\ \sigma^-,-\boldsymbol{K}: &\quad \dot{\tilde{c}}_+(t) = -\frac{g}{i\hbar}\Big(\underbrace{e^{-i\left(\omega-\frac{\Delta E}{\hbar}\right)t}\beta_n^{+^*}\alpha_{n'}^{-^*}\langle n-1,m|n',m'\rangle}_{resonant} + \underbrace{e^{i\left(\omega+\frac{\Delta E}{\hbar}\right)t}\alpha_n^{+}\beta_{n'}^-\langle n,m|n'-1,m'\rangle}_{non-resonant}\Big),\end{aligned} \tag{5.38}$$

where terms with $\omega - \Delta E$ are resonant absorption terms and $\omega + \Delta E$ are non-resonant. We use the rotating wave approximation and keep only the resonant terms

to obtain

$$\sigma^+, \boldsymbol{K}: \quad \dot{\widetilde{c}}_+(t) = \frac{i}{\hbar} g e^{-i\left(\omega - \frac{\Delta E}{\hbar}\right)t} \beta_n^{+*} \alpha_{n'}^- \langle n, m | n' - 1, m' \rangle, \tag{5.39a}$$

$$\sigma^-, \boldsymbol{K}: \quad \dot{\widetilde{c}}_+(t) = -\frac{i}{\hbar} g e^{-i\left(\omega - \frac{\Delta E}{\hbar}\right)t} \alpha_n^{+*} \beta_{n'}^- \langle n-1, m | n', m' \rangle_{CV}, \tag{5.39b}$$

$$\sigma^+, -\boldsymbol{K}: \quad \dot{\widetilde{c}}_+(t) = -\frac{i}{\hbar} g e^{-i\left(\omega - \frac{\Delta E}{\hbar}\right)t} \alpha_n^{+} \beta_{n'}^- \langle n, m | n' - 1, m' \rangle_{CV}, \tag{5.39c}$$

$$\sigma^-, -\boldsymbol{K}: \quad \dot{\widetilde{c}}_+(t) = \frac{i}{\hbar} g e^{-i\left(\omega - \frac{\Delta E}{\hbar}\right)t} \beta_n^{+*} \alpha_{n'}^{-*} \langle n-1, m | n', m' \rangle, , \tag{5.39d}$$

similarly to Eq. 4.56. We obtain one dominant transition (boxed) and one much weaker. This is because the terms with a prefactor α_n^-, β_n^+ in Eq. 5.39a and Eq. 5.39d are much smaller for low n than the ones with β_n^-, α_n^+ in Eq. 5.39b and Eq. 5.39c, because $\alpha_n^-, \beta_n^+ \ll \beta_n^-, \alpha_n^+$ for low n, as shown in Fig. 5.2. Later on I will focus only on the dominant transitions. In order to determine the allowed transitions, we notice that for the expressions in Eq. 5.39a-5.39d to be non-zero, we require that

$$\sigma^+, \boldsymbol{K}: \quad n' - 1 = n, \quad m = m' \quad \rightarrow \quad \Delta n = -1, \quad \Delta m = 0 \tag{5.40a}$$

$$\sigma^-, \boldsymbol{K}: \quad n' = n - 1, \quad m = m' \quad \rightarrow \quad \Delta n = +1, \quad \Delta m = 0 \tag{5.40b}$$

$$\sigma^+, -\boldsymbol{K}: \quad n' - 1 = n, \quad m = m' \quad \rightarrow \quad \Delta n = -1, \quad \Delta m = 0, \tag{5.40c}$$

$$\sigma^-, -\boldsymbol{K}: \quad n' = n - 1, \quad m = m' \quad \rightarrow \quad \Delta n = +1, \quad \Delta m = 0, \tag{5.40d}$$

so the dominant (boxed) LL absorption selection rules are in short $\Delta n = \pm 1, \Delta m = 0$ for $\pm\boldsymbol{K}$ [62], which has been pictured in Fig. 5.5 by red solid (dashed) arrows for σ^- (σ^+) polarisation. The selection rules corresponding to weaker transitions have been marked with grey arrows. The arrows link only the LLs allowed by Eq. 5.40 and by the assumption of a filled VB and empty CB.

We can now obtain the transition rate for the dominant absorption (boxed in Eq. 5.39b and Eq. 5.39c) from Fermi Golden rule, analogously to Eq. 4.58. It reads

$$\Delta n = \pm 1, \pm\boldsymbol{K}: \quad \gamma_{fi} = \frac{\left|\widetilde{c}_+\right|^2}{t} = g^2 \left|\alpha_n^+ \beta_{n'}^-\right|^2 \frac{2\pi}{\hbar} \delta(\hbar\omega - \Delta E), \tag{5.41}$$

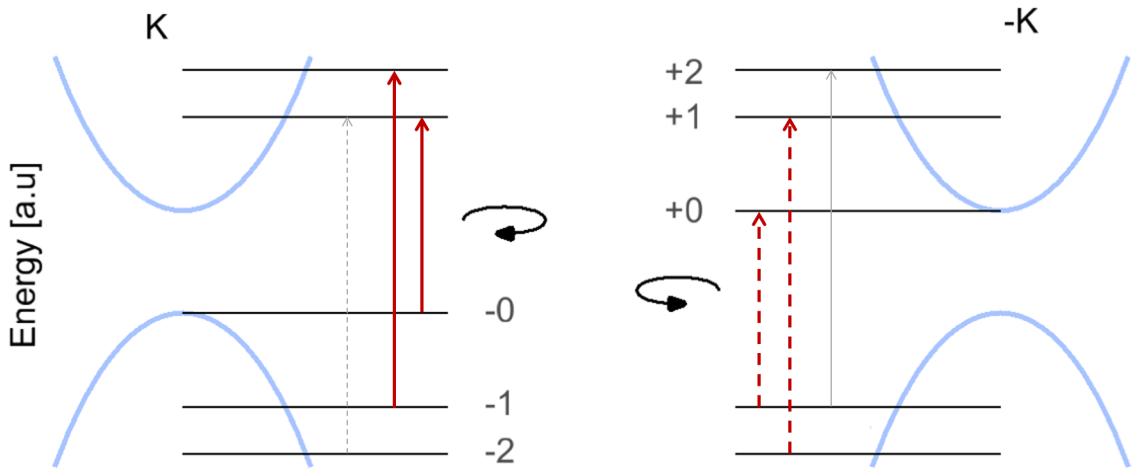

Figure 5.5: Schematical representation of the optical selection rules for mdF LLs. Thick red (thin grey) lines mark the dominant (weak) transitions allowed by Eq. 5.40. The dominant selection rules at $\pm\boldsymbol{K}$ are $\Delta n = \pm 1, \Delta m = 0$ for $\sigma^{\mp}$ (shown with solid and dashed lines respectively) and opposite polarisation for the weak transitions.

where

$$W_{+n,-n'} = g^2 \left|\alpha_n^+ \beta_{n'}^-\right| \tag{5.42}$$

is the dipole moment used in later sections, corresponding to σ^- (σ^+) polarisation at $\boldsymbol{K}$ ($-\boldsymbol{K}$).

5.2 Interacting massive Dirac fermions.

This section describes the interaction of mDf in LLs and derives a magnetoexciton spectrum for mDf. I first discuss the form of scattering Coulomb matrix elements in section 5.2.1 and consider valley polarisation due to the asymmetric LL structure in section 5.2.2. Detailed expressions for the interacting Hamiltonian matrix elements needed to solve the exciton problem are derived in section 5.2.3. My results on the effect of interactions on VZS is discussed in section 5.2.4 and the magnetoexciton absorption spectrum results are presented in section 5.2.5.

5.2.1 Scattering Coulomb matrix elements.

I begin by considering the interaction of mDf in LLs, which are described by a wavefunction in Eq. 5.20. To explain the form of scattering Coulomb matrix elements I will use the envelope function approximation, which separates two scales of the wavefucntion. The envelope of the wavefunction is assumed to be constant on the scale of one unit cell, that is the scale of the oscillation of the periodic part u. For mDf LLs, the C and V parts of the spinor wavefunction are given by Eq. 5.20. Let us consider a Coulomb matrix element betwen different spinor components at $\boldsymbol{K}$, e.g.

$$\begin{aligned}\left\langle V^{\pm}_{n_1,m_1}\boldsymbol{K}, C^{\pm}_{n_2,m_2}\boldsymbol{K}\right| V \left|C^{\pm}_{n_3,m_3}\boldsymbol{K}, V^{\pm}_{n_4,m_4}\boldsymbol{K}\right\rangle &= \iint d\overline{\boldsymbol{r}}d\overline{\boldsymbol{r}}' V^{\pm^*}_{n_1m_1}(\boldsymbol{r}) C^{\pm^*}_{n_2m_2}(\boldsymbol{r}')\cdot \\ &\cdot \frac{e^2}{4\pi\varepsilon_r\varepsilon_0}\frac{1}{|\overline{\boldsymbol{r}}-\overline{\boldsymbol{r}}'|} C^{\pm}_{n_3m_3}(\boldsymbol{r}')V^{\pm}_{n_4m_4}(\boldsymbol{r}) \\ \sim \frac{e^2}{4\pi\varepsilon_r\varepsilon_0}\iint d\overline{\boldsymbol{r}}d\overline{\boldsymbol{r}}' w_V^{n_1,m_1,\boldsymbol{K}^*}(\boldsymbol{r}) u_V^{\boldsymbol{K}^*}(\boldsymbol{r}) w_C^{n_2,m_2,\boldsymbol{K}^*}(\boldsymbol{r}') u_C^{\boldsymbol{K}^*}(\boldsymbol{r}')\cdot \\ &\cdot \frac{1}{|\overline{\boldsymbol{r}}-\overline{\boldsymbol{r}}'|} w_C^{n_3,m_3,\boldsymbol{K}}(\boldsymbol{r}') u_C^{\boldsymbol{K}}(\boldsymbol{r}') w_V^{n_4,m_4,\boldsymbol{K}}(\boldsymbol{r}) u_V^{\boldsymbol{K}}(\boldsymbol{r}) \quad (5.43)\end{aligned}$$

where I separated $\overline{\boldsymbol{r}} = (\boldsymbol{r}, z)$ and I dropped the α, β factors in front which are independent of $\boldsymbol{r}$ (they will be explicitly accounted for in the expressions for CI Hamiltonian matrix elements in section 5.2.3).

I now distinguish between two length scales: within and outside of a single unit cell of the crystal. I replace an integral $\int d\overline{\boldsymbol{r}}$ in Eq. 5.43 by a summation over unit cells and an integral over a single unit cell $\sum_{\boldsymbol{R}}\int_{UC} d\widetilde{\boldsymbol{r}}$, where $\boldsymbol{R}$ labels unit cells. Assuming that the LL envelopes and the Coulomb potential changes slowly on the scale of a unit cell, I can integrate out the unit cell space and again replace $\sum_{\boldsymbol{R}} \approx \Omega\int d\boldsymbol{R}$, to obtain

$$\begin{aligned}&\left\langle V^{\pm}_{n_1,m_1}\boldsymbol{K}, C^{\pm}_{n_2,m_2}\boldsymbol{K}\right| V \left|C^{\pm}_{n_3,m_3}\boldsymbol{K}, V^{\pm}_{n_4,m_4}\boldsymbol{K}\right\rangle \sim \left\langle u_V^{\boldsymbol{K}}\right| \left\langle u_C^{\boldsymbol{K}}|u_C^{\boldsymbol{K}}\right\rangle \left|u_V^{\boldsymbol{K}}\right\rangle \cdot \\ &\cdot \frac{e^2}{4\pi\varepsilon_r\varepsilon_0}\iint d\boldsymbol{R}d\boldsymbol{R}' w_V^{n_1,m_1,\boldsymbol{K}^*}(\boldsymbol{R}) w_C^{n_2,m_2,\boldsymbol{K}^*}(\boldsymbol{R}')\frac{1}{|\boldsymbol{R}-\boldsymbol{R}'|} w_C^{n_3,m_3,\boldsymbol{K}}(\boldsymbol{R}') w_V^{n_4,m_4,\boldsymbol{K}}(\boldsymbol{R}) \\ &= V_{VCCV}\left\langle n_1,m_1;n_2,m_2\right| V \left|n_3,m_3;n_4,m_4\right\rangle, \quad (5.44)\end{aligned}$$

where

$$\begin{aligned}\langle u_V^{\boldsymbol{K}}|u_V^{\boldsymbol{K}}\rangle &= \int_{UC} d\widetilde{\boldsymbol{r}} u_V^{\boldsymbol{K}^*}(\widetilde{\boldsymbol{r}}) u_V^{\boldsymbol{K}}(\widetilde{\boldsymbol{r}}) = 1,\\ \langle u_C^{\boldsymbol{K}}|u_C^{\boldsymbol{K}}\rangle &= \int_{UC} d\widetilde{\boldsymbol{r}} u_C^{\boldsymbol{K}^*}(\widetilde{\boldsymbol{r}}) u_C^{\boldsymbol{K}}(\widetilde{\boldsymbol{r}}) = 1\end{aligned} \tag{5.45}$$

and

$$V_{VCCV} = \left\langle u_V^{\boldsymbol{K}}\right| \langle u_C^{\boldsymbol{K}}|u_C^{\boldsymbol{K}}\rangle \left|u_V^{\boldsymbol{K}}\right\rangle = \langle u_V^{\boldsymbol{K}}|u_V^{\boldsymbol{K}}\rangle\langle u_C^{\boldsymbol{K}}|u_C^{\boldsymbol{K}}\rangle = 1. \tag{5.46}$$

The components $V/C_{n_i,m_i}$ decide on the nature of the matrix element and on the products $\langle u_V^{\boldsymbol{K}}|u_V^{\boldsymbol{K}}\rangle$, which in case of a matrix element $VCVC$ are

$$V_{VCVC} = \left\langle u_V^{\boldsymbol{K}}\right| \langle u_C^{\boldsymbol{K}}|u_V^{\boldsymbol{K}}\rangle \left|u_C^{\boldsymbol{K}}\right\rangle = \langle u_V^{\boldsymbol{K}}|u_C^{\boldsymbol{K}}\rangle\langle u_C^{\boldsymbol{K}}|u_V^{\boldsymbol{K}}\rangle \approx 0. \tag{5.47}$$

Analogously the other possible factors are

$$\begin{aligned}V_{VCCV} = V_{CVVC} = V_{VVVV} = V_{CCCC} = 1,\\ V_{VCVC} = V_{CVCV} \approx 0.\end{aligned} \tag{5.48}$$

However, because we made a significant approximation by separating the length scales in Eq. 5.44, the relations in Eq. 5.46 and Eq. 5.47 do not hold exactly, which is why a sign $\approx$ is placed in Eq. 5.48. In practice, I will consider two cases: $V_{VCVC} = V_{CVCV} = 0$ and $V_{VCVC} = V_{CVCV} = 0.1$.

The matrix elements in Eq. 5.44 involve also the Coulomb scattering matrix elements between LL states, which can be obtained using an analytical formula, given in Eq. 2.91. The computational details of evaluation of these matrix elements have been described in the same section, 2.3.3.

Additionally, I have to consider the overall strength of the matrix element in Eq. 5.44. The expression in Eq. 2.91 is given in the units of Rydberg Ry, and it consists of a unitless magnetic length $l_B = la_B$. I need to account for the effective units Ry^*, a_B, which can be obtained by extracting the effective mass m^* from the energy bands, given by solutions of the Hamiltonian in Eq. 4.27. I obtain $m^* = 0.34m_0$, where m_0

is the free electron mass. For a dielectric constant $\varepsilon_r = 2.5$ [162], this gives

$$\begin{aligned} Ry^* &= \frac{\hbar^2}{2m^* a_B^2} = \frac{e^2}{2 \cdot 4\pi\varepsilon_r\varepsilon_0 a_B}, \\ a_B &= \frac{4\pi\varepsilon_r\varepsilon_0\hbar^2}{e^2 m^*} = \frac{\varepsilon_r m_0}{m^*} a_0 = 3.9\mathring{A}, \\ Ry^* &= \frac{Ry \cdot m^*}{\varepsilon_r^2 m_0} = 740meV, \\ V_{Ry} &= Ry^* \frac{1}{l} = Ry^* \frac{a_B}{l_B} = 2.88eV \cdot \sqrt{B}. \end{aligned} \tag{5.49}$$

The scattering Coulomb matrix elements described in this section make up the CI Hamiltonian matrix elements derived in section 5.2.3.

5.2.2 Valley polarisation.

I will now populate the negative energy LLs derived in section 5.1.2 with N electrons, to form a HF GS

$$|GS\rangle = \prod_{\lambda<\lambda_f} \left(c^-_{\lambda,K}\right)^\dagger \prod_{\lambda<\lambda_f} \left(c^-_{\lambda,-K}\right)^\dagger |0\rangle\,, \tag{5.50}$$

where $\lambda = (n, m, s)$ corresponds to a collective LL index and the superscript $-$ stands for LLs for negative energy (in the VB). A schematic picture of the HF GS has been shown in Fig. 5.6. Due to large SO splitting in the VB, the VB LLs are split into red (spin up) and blue (spin down).

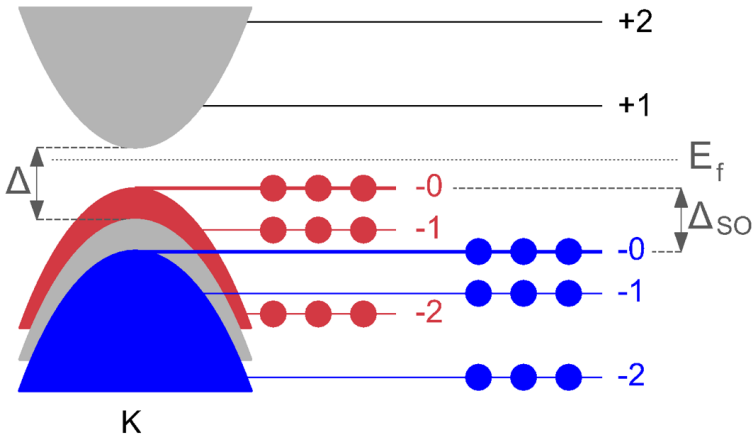

Figure 5.6: HF GS for mDf. Red (blue) dots depict electrons with spin up (down) populating levels below the Fermi level E_f. Spin splitting in the VB and the energy gap are labelled with Δ_{SO} and Δ respectively.

The HF GS involves many filled LLs, so to reach convergence of absorption spectra in section 5.2.5, I will use a fixed number of electrons N and an energy cut-off E_c in the VB, which restricts the number of filled LLs counted from the top of the VB and allows for finite number of available SP states in my computations. This procedure of choosing N and E_c is shown in Fig. 5.7 (left) for mDf LLs.

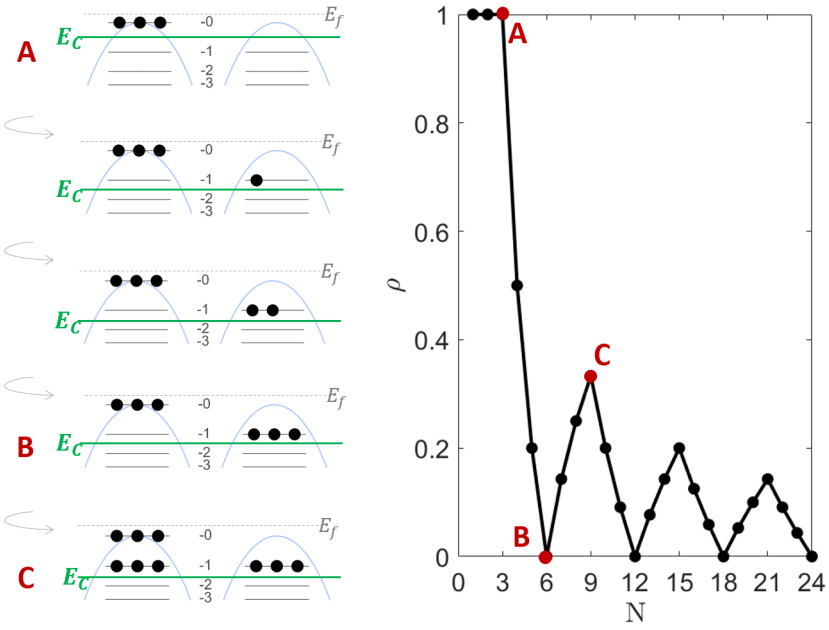

Figure 5.7: (left) Choice of E_C, which determines the number of electron N in the VB for a fixed degeneracy of a LL $M = 3$. Cases A and C contain more electrons at $\boldsymbol{K}$ than $-\boldsymbol{K}$, which causes a valley polarisation ρ. (right) ρ for mDf LLs oscillates as a function of N. Cases A-C are marked with red dots.

The mDf LL energy structure, asymmteric in opposite valleys, creates a possibility of filling the levels with unequal number of electrons in opposite valleys as E_c increases. This produces a finite valley polarisation

$$\rho = \frac{N_K - N_{-K}}{N}, \tag{5.51}$$

where N_K and N_{-K} counts the electrons in each valley. The choice of N, E_c and strength of magnetic field B determines the value of ρ, which has been plotted in Fig. 5.7 (right) for the degeneracy of a LL $M = 3$. For case A, $E_c < E_0^-$, and for cases B and C $E_c < E_1^-$. As N grows, ρ oscillates between 0 (unpolarised) and a finite value,

which is maximised for $\rho(N \leq M) = 1$. This is due to the unpaired states within the 0th LL, which bring smaller contribution to ρ as N increases.

5.2.3 Single magneto-exciton Hamiltonian.

With the GS defined, I will now create excitations from this GS, as shown in Fig. 5.8, where filled (empty) circles represent an electron (hole). Due to large SO splitting in the VB, the energies of transitions A and B will be significantly different. I now express the magnetoexciton wavefunction as a linear combination of all possible single excitations as

$$|X, k\rangle = \sum_{ab} A_{ab,k} \, |ab, k\rangle \, , \tag{5.52}$$

according to the definition in Eq. 2.85, where $k = \pm \boldsymbol{K}$ labels valleys and $|ab, k\rangle$ is a mDf LL excitation configuration for valley k, given as

$$|ab, k\rangle = \left|\Psi_b^+(k)\right\rangle \left|\Psi_a^-(k)\right\rangle , \tag{5.53}$$

and the collective index $a = (n, m, s)$ carries LL indices n, m and spin s and $\left|\Psi_b^+(k)\right\rangle$, $|\Psi_a^-(k)\rangle$ have been defined in Eq. 5.32. In analogy to Eq. 2.86, the wavefunction coefficients $A_{ab,k}$ are obtained by solving the Bethe Salpeter equation (BSE)

$$\Big(\left(\varepsilon_{bk}^+ + \Sigma_{bk}^+\right) - \left(\varepsilon_{ak}^- + \Sigma_{ak}^-\right) - V_{vertex}(a, b, k) \Big) A_{ab,k} + \sum_{ij} \left(V_{ajib} - V_{ajbi}\right) A_{ij,k} = E A_{ab,k}. \tag{5.54}$$

I will now construct the CI Hamiltonian in the basis of configurations $|ab, k\rangle$, which needs to be diagonalised to solve Eq. 5.54. I will use the definitions introduced in section 2.2.7. I start with a diagonal element, as in Eq. 2.89, which for mDf in LLs reads

$$\langle ab, k| \, \hat{H}_{CI} \, |ab, k\rangle = \left(\varepsilon_{bk}^+ + \Sigma_{bk}^+\right) - \left(\varepsilon_{ak}^- + \Sigma_{ak}^-\right) - V_{vertex}(a, b, k), \tag{5.55}$$

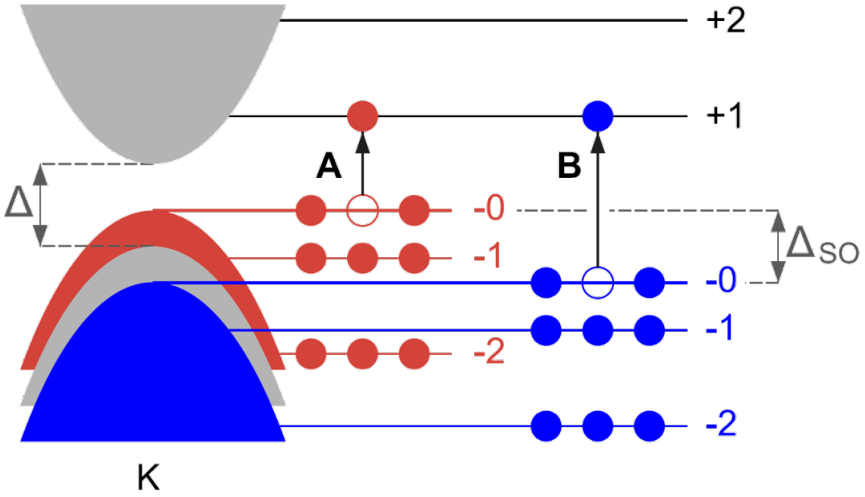

Figure 5.8: Single electron-hole excitations between mDf LLs. Red (blue) filled dots depict electrons with spin up (down), empty dots denote holes (missing electrons). Black arrows mark electrons promoted to the CB. Excitations different in energy have been labelled with A and B. Spin splitting in the VB and the energy gap are labelled with Δ_{SO} and Δ respectively.

where

$$\begin{aligned}
\Sigma^{-}_{ak} &= -\sum_{\lambda<\lambda_f} \left\langle \Psi^{-}_{a}(k)\Psi^{-}_{\lambda}(k)\right| V \left|\Psi^{-}_{a}(k)\Psi^{-}_{\lambda}(k)\right\rangle, \\
\Sigma^{+}_{bk} &= -\sum_{\lambda<\lambda_f} \left\langle \Psi^{+}_{b}(k)\Psi^{-}_{\lambda}(k)\right| V \left|\Psi^{+}_{b}(k)\Psi^{-}_{\lambda}(k)\right\rangle, \\
V_{vertex}(a,b,k) &= \left\langle \Psi^{-}_{a}(k)\Psi^{+}_{b}(k)\right| V \left|\Psi^{+}_{b}(k)\Psi^{-}_{a}(k)\right\rangle \\
&\quad - \left\langle \Psi^{-}_{a}(k)\Psi^{+}_{b}(k)\right| V \left|\Psi^{-}_{a}(k)\Psi^{+}_{b}(k)\right\rangle,
\end{aligned} \tag{5.56}$$

where to simulate a neutral system I am accounting for the uniform positive background charge, which produces contributions exactly cancelling the direct terms of self energies Σ, leaving solely the exchange terms [162].

Let us examine the self energies Σ more closely. The general expression for $\Sigma^{-}_{ak}, \Sigma^{+}_{bk}$

at $\boldsymbol{K}$ is

$$\begin{aligned}\Sigma^{+}_{nm} = &- \left|\alpha^{+}_{n}\right|^2 \sum_{n'm'} \Bigg(\left|\alpha^{-}_{n'}\right|^2 \langle n-1,m;n'-1,m'|\, V\, |n-1,m;n'-1,m'\rangle_{CCCC} \\ &\qquad + \left|\beta^{-}_{n'}\right|^2 \langle n-1,m;n',m'|\, V\, |n-1,m;n',m'\rangle_{CVCV} \Bigg) \\ &- \left|\beta^{+}_{n}\right|^2 \sum_{n'm'} \Bigg(\left|\alpha^{-}_{n'}\right|^2 \langle n,m;n'-1,m'|\, V\, |n,m;n'-1,m'\rangle_{VCVC} \\ &\qquad + \left|\beta^{-}_{n'}\right|^2 \langle n,m;n',m'|\, V\, |n,m;n',m'\rangle_{VVVV} \Bigg) \\ &- \alpha^{+^*}_{n}\beta^{+}_{n} \sum_{n'm'} \beta^{-^*}_{n'}\alpha^{-}_{n'} \langle n-1,m;n',m'|\, V\, |n,m;n'-1,m'\rangle_{CVVC} \\ &- \beta^{+^*}_{n}\alpha^{+}_{n} \sum_{n'm'} \alpha^{-^*}_{n'}\beta^{-}_{n'} \langle n,m;n'-1,m'|\, V\, |n-1,m;n',m'\rangle_{VCCV}\end{aligned} \tag{5.57}$$

and

$$\begin{aligned}\Sigma^{-}_{nm} = &- \left|\alpha^{-}_{n}\right|^2 \sum_{n'm'} \Bigg(\left|\alpha^{-}_{n'}\right|^2 \langle n-1,m;n'-1,m'|\, |n-1,m;n'-1,m'\rangle_{CCCC} \\ &\qquad + \left|\beta^{-}_{n'}\right|^2 \langle n-1,m;n',m'|\, V\, |n-1,m;n',m'\rangle_{CVCV} \Bigg) \\ &- \left|\beta^{-}_{n}\right|^2 \sum_{n'm'} \Bigg(\left|\alpha^{-}_{n'}\right|^2 \langle n,m;n'-1,m'|\, V\, |n,m;n'-1,m'\rangle_{VCVC} \\ &\qquad + \left|\beta^{-}_{n'}\right|^2 \langle n,m;n',m'|\, V\, |n,m;n',m'\rangle_{VVVV} \Bigg) \\ &- \alpha^{-^*}_{n}\beta^{-}_{n} \sum_{n'm'} \beta^{-^*}_{n'}\alpha^{-}_{n'} \langle n-1,m;n',m'|\, V\, |n,m;n'-1,m'\rangle_{CVVC} \\ &- \beta^{-^*}_{n}\alpha^{-}_{n} \sum_{n'm'} \alpha^{-^*}_{n'}\beta^{-}_{n'} \langle n,m;n'-1,m'|\, V\, |n-1,m;n',m'\rangle_{VCCV}\,,\end{aligned} \tag{5.58}$$

and $a = (n,m), b = (n,m), \lambda = (n',m')$ and we neglect spin here for clarity.

I now calculate the self energy contribution to an electron-hole pair in lowest

possible LLs at $\boldsymbol{K}$ as

$$\begin{aligned}
\delta\Sigma_{10}(m) = \Sigma^{+}_{1m} - \Sigma^{-}_{0m} \\
&= -\left|\alpha_1^+\right|^2 \sum_{m'} \Bigg(\left|\alpha_1^-\right|^2 \langle 0,m;0,m'|\, V\, |0,m;0,m'\rangle_{CCCC} \\
&\quad + \langle 0,m;0,m'|\, V\, |0,m;0,m'\rangle_{CVCV} + \left|\beta_1^-\right|^2 \langle 0,m;1,m'|\, V\, |0,m;1,m'\rangle_{CVCV} \Bigg) \\
&- \left|\beta_1^+\right|^2 \sum_{m'} \Bigg(\left|\beta_1^-\right|^2 \langle 1,m;0,m'|\, V\, |1,m;0,m'\rangle_{VVVV} + \left|\beta_1^-\right|^2 \langle 1,m;1,m'|\, V\, |1,m;1,m'\rangle_{VVVV} \Bigg) \\
&\quad - 2Re\Bigg(\alpha_1^{+^*} \beta_1^+ \beta_1^{-^*} \alpha_1^- \sum_{m'} \langle 0,m;1,m'|\, V\, |1,m;0,m'\rangle_{CVVC} \Bigg) \\
&+ \left|\alpha_1^-\right|^2 \sum_{m'} \langle 0,m;0,m'|\, V\, |0,m;0,m'\rangle_{VCVC} + \sum_{m'} \langle 0,m;0,m'|\, V\, |0,m;0,m'\rangle_{VVVV} \\
&\quad \approx \left(V_{VVVV} - \left|\alpha_1^+\right|^2 V_{CVCV}\right) \cdot \\
&\quad \cdot \sum_{m'} \Bigg(\langle 0,m;0,m'|\, V\, |0,m;0,m'\rangle + \left|\beta_1^-\right|^2 \langle 0,m;1,m'|\, V\, |0,m;1,m'\rangle \Bigg), \qquad (5.59)
\end{aligned}$$

where I used $\left|\beta_0^-\right|^2 = \left|\beta_0^+\right|^2 = 1$ and assumed $\left|\alpha_n^-\right|^2 \approx 0$ and $\left|\beta_n^+\right|^2 \approx 0$ for low n and the amplitudes of the Coulomb matrix elements (e.g. V_{VVVV}) have been factored out in front of the expression in Eq. 5.59, and their values are given in Eq. 5.48. The resulting value of the electron-hole pair self energy $\delta\Sigma_{10}(m)$ has been plotted in Fig. 5.9 for $B = 60T$. The values of $\delta\Sigma_{10}(m)$ for large m decrease due to finite size effects, which appear for this infinite lattice model when the CI basis needs to be truncated to a finite number of LLS. Therefore, for modelling a bulk system, I need to remove this artefact and in the following sections I will consider an unchanging $\delta\Sigma_{10}(m = 0)$.

An analogous expression to Eq. 5.59 can be found for $-\boldsymbol{K}$ and, for both valleys, the electron-hole self energies $\delta\Sigma$ read

$$\begin{aligned}
\delta\Sigma_{10}(m,\boldsymbol{K}) &\approx \left(V_{VVVV} - \left|\alpha_1^+\right|^2 V_{CVCV}\right) \cdot \\
&\quad \cdot \sum_{m'} \Bigg(\langle 0,m;0,m'|\, V\, |0,m;0,m'\rangle + \left|\beta_1^-\right|^2 \langle 0,m;1,m'|\, V\, |0,m;1,m'\rangle \Bigg) \\
\delta\Sigma_{01}(m,-\boldsymbol{K}) &\approx \left(\left|\beta_1^-\right|^2 V_{VVVV} - V_{CVCV} \right) \left|\beta_1^-\right|^2 \sum_{m'} \langle 0,m;0,m'|\, V\, |0,m;0,m'\rangle ,
\end{aligned} \qquad (5.60)$$

which shows that $\delta\Sigma_{10}(m,\boldsymbol{K}) > \delta\Sigma_{01}(m,-\boldsymbol{K})$ because $\left|\beta_1^-\right|^2 < 1$. This is due to the

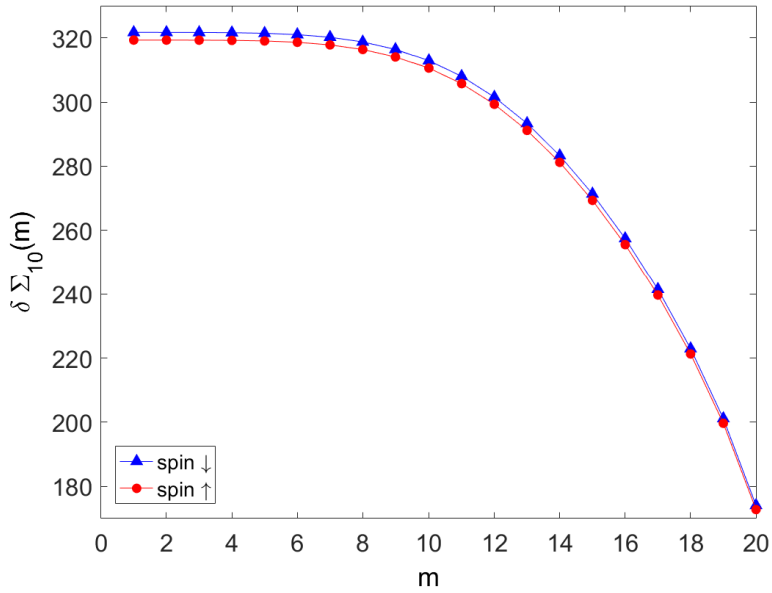

Figure 5.9: Self energy of an electron in a massive Dirac fermion Landau level. Changing values of Σ for growing m appear due to a finite size effect due to the truncation of the CI basis.

assymetrically filled VB, with the 0th LL in the VB located at $\boldsymbol{K}$.

I now evaluate the remaining terms of the CI Hamiltonian. The vertex correction terms for both valleys read

$$\begin{aligned} V_{vertex}(n_1,m_1,n_2,m_2,\boldsymbol{K}) \approx \left|\alpha^+_{n_2}\right|^2\left|\beta^-_{n_1}\right|^2 \Big(&\langle n_2-1,m_2;n_1,m_1|\,V\,|n_1,m_1;n_2-1,m_2\rangle_{CVVC} \\ &- \langle n_2-1,m_2;n_1,m_1|\,V\,|n_2-1,m_2;n_1,m_1\rangle_{CVCV} \Big) \\ V_{vertex}(n_1,m_1,n_2,m_2,-\boldsymbol{K}) \approx \left|\alpha^+_{n_2}\right|^2\left|\beta^-_{n_1}\right|^2 \Big(&\langle n_2,m_2;n_1-1,m_1|\,V\,|n_1-1,m_1;n_2,m_2\rangle_{VCCV} \\ &- \langle n_2,m_2;n_1-1,m_1|\,V\,|n_2,m_2;n_1-1,m_1\rangle_{VCVC} \Big), \end{aligned} \tag{5.61}$$

where I assumed $|\alpha^-_n|^2 \approx 0$ and $|\beta^+_n|^2 \approx 0$. I need also to evaluate the off-diagonal terms using Eq. 2.90, and for two different configurations I obtain

$$\begin{aligned} \langle bc,k'|\,\hat{H}_{CI}\,|ad,k\rangle = &\left\langle \Psi^-_a(k)\Psi^+_c(k')\right|V\left|\Psi^-_b(k')\Psi^+_d(k)\right\rangle \\ &- \delta_{ss'}\left\langle \Psi^-_a(k)\Psi^+_c(k')\right|V\left|\Psi^+_d(k)\Psi^-_b(k')\right\rangle. \end{aligned} \tag{5.62}$$

where the attractive term $\langle \Psi_a^-(k)\Psi_c^+(k')|\, V\, |\Psi_d^+(k)\Psi_b^-(k')\rangle$ is "direct" w.r.t. band indices but "exchange" w.r.t. k indices and the repulsive term $\langle \Psi_a^-(k)\Psi_c^+(k')|\, V\, |\Psi_b^-(k')\Psi_d^+(k)\rangle$ has opposite features. The off-diagonal terms for both valleys read

$$\begin{aligned}
\langle bc, \boldsymbol{K}|\, \hat{H}_{CI}\, |ad, \boldsymbol{K}\rangle \approx & \beta^{-^*}_{n_1 s}\alpha^{+^*}_{n_2' s'}\beta^-_{n_1' s'}\alpha^+_{n_2 s}\Big(\langle n_1, m_1; n_2' - 1, m_2'|\, V\, |n_1', m_1'; n_2 - 1, m_2\rangle_{VCVC} \\
& - \delta_{ss'}\, \langle n_1, m_1; n_2' - 1, m_2'|\, V\, |n_2 - 1, m_2; n_1', m_1'\rangle_{VCCV}\Big), \\
\langle bc, -\boldsymbol{K}|\, \hat{H}_{CI}\, |ad, -\boldsymbol{K}\rangle \approx & \beta^{-^*}_{n_1 s}\alpha^{+^*}_{n_2' s'}\beta^-_{n_1' s'}\alpha^+_{n_2 s}\Big(\langle n_1 - 1, m_1; n_2', m_2'|\, V\, |n_1' - 1, m_1'; n_2, m_2\rangle_{VCVC} \\
& - \delta_{ss'}\, \langle n_1 - 1, m_1; n_2', m_2'|\, V\, |n_2, m_2; n_1' - 1, m_1'\rangle_{VCCV}\Big),
\end{aligned} \tag{5.63}$$

where $a = (n_1, m_1, s), b = (n_1', m_1', s'), c = (n_2', m_2', s'), d = (n_2, m_2, s)$ and I also assumed $|\alpha_n^-|^2 \approx 0$ and $|\beta_n^+|^2 \approx 0$.

The last remaining matrix element of the CI Hamiltonian is an intervalley off-diagonal element, i.e. for excitations in two different valleys ($k \neq k'$ in Eq. 5.62). Using Eq. 5.44, I calculate the biggest contribution to this matrix element, assuming again $|\alpha_n^-|^2 \approx 0$ and $|\beta_n^+|^2 \approx 0$, which reads

$$\begin{aligned}
\langle bc, -\boldsymbol{K}|\, \hat{H}_{CI}\, |ad, \boldsymbol{K}\rangle \approx & \left\langle V_a^-\boldsymbol{K}, C_c^+ - \boldsymbol{K}\right|\, V\, \left|V_b^- - \boldsymbol{K}, C_d^+\boldsymbol{K}\right\rangle \\
& - \delta_{ss'}\left\langle V_a^-\boldsymbol{K}, C_c^+ - \boldsymbol{K}\right|\, V\, \left|C_d^+\boldsymbol{K}, V_b^- - \boldsymbol{K}\right\rangle \\
= & \left\langle u_V^{\boldsymbol{K}}\right|\langle u_C^{-\boldsymbol{K}}|u_V^{-\boldsymbol{K}}\rangle\left|u_C^{\boldsymbol{K}}\right\rangle \beta^{-^*}_{n_1 s}\alpha^{+^*}_{n_2' s'}\beta^-_{n_1' s'}\alpha^+_{n_2 s}\, \langle n_1, m_1; n_2', m_2'|\, V\, |n_1', m_1'; n_2, m_2\rangle \\
- \delta_{ss'}\left\langle u_V^{\boldsymbol{K}}\right|\langle u_C^{-\boldsymbol{K}}|u_C^{\boldsymbol{K}}\rangle\left|u_V^{-\boldsymbol{K}}\right\rangle & \beta^{-^*}_{n_1 s}\alpha^{+^*}_{n_2' s'}\beta^-_{n_1' s'}\alpha^+_{n_2 s}\, \langle n_1, m_1; n_2', m_2'|\, V\, |n_2, m_2; n_1', m_1'\rangle \\
= & V^{\boldsymbol{K}-\boldsymbol{K}-\boldsymbol{K}\boldsymbol{K}}_{VCVC}\beta^{-^*}_{n_1 s}\alpha^{+^*}_{n_2' s'}\beta^-_{n_1' s'}\alpha^+_{n_2 s}\, \langle n_1, m_1; n_2', m_2'|\, V\, |n_1', m_1'; n_2, m_2\rangle \\
- \delta_{ss'}V^{\boldsymbol{K}-\boldsymbol{K}\boldsymbol{K}-\boldsymbol{K}}_{VCCV} & \beta^{-^*}_{n_1 s}\alpha^{+^*}_{n_2' s'}\beta^-_{n_1' s'}\alpha^+_{n_2 s}\, \langle n_1, m_1; n_2', m_2'|\, V\, |n_2, m_2; n_1', m_1'\rangle
\end{aligned} \tag{5.64}$$

where $a = (n_1, m_1, s), b = (n_1', m_1', s'), c = (n_2', m_2', s'), d = (n_2, m_2, s)$. The factors $V^{\boldsymbol{K}-\boldsymbol{K}-\boldsymbol{K}\boldsymbol{K}}_{VCVC}$ and $V^{\boldsymbol{K}-\boldsymbol{K}\boldsymbol{K}-\boldsymbol{K}}_{VCCV}$ in Eq. 5.64 never involve the same periodic functions u, because the matrix element is either "direct" in band index and "exchange" in valley index or "exchange" in band index and "direct" in valley index. This makes these elements close to 0, which will introduce negligible splittings in the Bethe-Salpeter solutions [49]. I will therefore neglect the intervalley scattering in my calculations of the magneto-exciton spectrum.

5.2.4 Renormalisation of valley Zeeman splitting with interactions.

Section 5.2.3 discusses all contributions to the interacting Hamiltonian for a magnetoexciton. Here I show the effect of the self energy on VZS given by Eq. 5.30 and shown in Fig. 5.3. Using Eq. 5.57 for valley $\boldsymbol{K}$ and analogously for $-\boldsymbol{K}$, the renormalised VZS with self energy contribution becomes

$$\Delta^{\Sigma}_{VZ}(m) = \Delta_{VZ} + \Sigma^{+}_{1m}(\boldsymbol{K}) - \Sigma^{+}_{0m}(-\boldsymbol{K}). \tag{5.65}$$

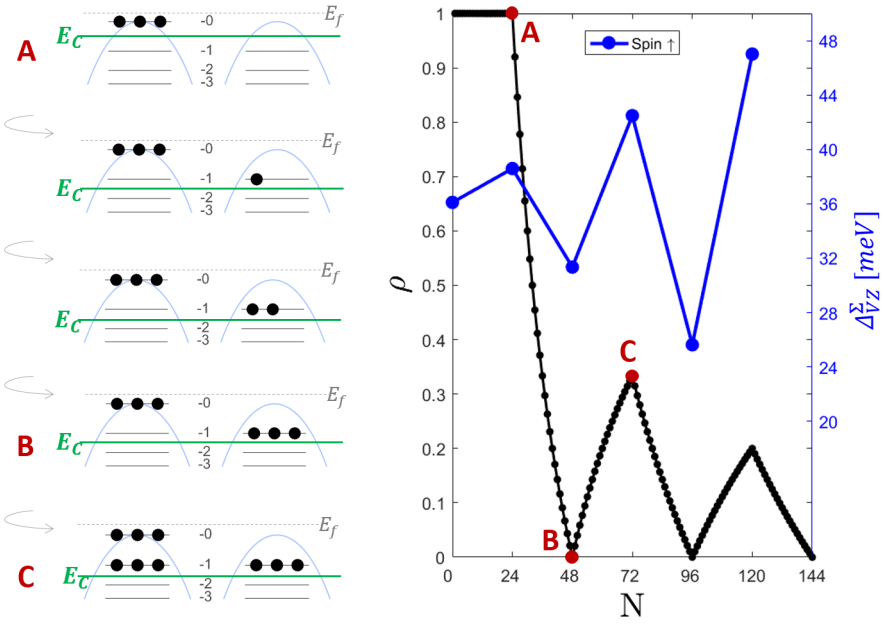

Figure 5.10: (left) Choice of N determines the valley polarisation ρ. Cases A and C exhibit $\rho > 0$. (right) VZS Δ_{VZ} renormalised by interactions as a function of N shown together with $\rho(N)$. The oscillations of Δ_{VZ} follow the oscillations of ρ.

I have computed $\Delta^{\Sigma}_{VZ}(m = 0)$ renormalised by interactions for three lowest CB LL in both valleys, which has been shown in Fig. 5.10 for $B = 60T$ and for $M = 24$ (Fig. 5.10 left shows only 3 particles in a LL for clarity). It shows oscillatory behaviour, which mimics the valley polarisation ρ. In an unpolarized case the VZS renormalised by interactions decreases with the number of particles N and it increases when polarisation is present [159].

5.2.5 Magnetoexciton absorption spectrum.

After solving the BSE given in Eq. 5.54 we obtain the magnetoexciton wavefunctions $|X,k\rangle_\mu$ given by Eq. 5.52 and energies E^k_μ. We can calculate the magnetoexciton absorption spectrum from Fermi's golden rule as [148]

$$A(\omega,k)=\sum_\mu \left|\langle X,k|_\mu \hat{P}^\dagger |GS\rangle\right|^2 \delta(\hbar\omega - E^k_\mu), \tag{5.66}$$

where the GS has been defined in Eq. 5.50 and E^k_μ are measured from the GS. In Eq. 5.66 $\hat{P}^\dagger$ is the interband polarisation operator corresponding to photon absorption given by

$$\hat{P}^\dagger=\sum_{ab} d_{ab}\left(c^+_b\right)^\dagger c^-_a, \tag{5.67}$$

where d_{ab} is the dipole moment given by

$$d_{ab}=W_{nn'}=g^2\left|\alpha^{+*}_n \beta^-_{n'}\right|, \tag{5.68}$$

where $W_{nn'}$ has been derived in Eq. 5.42. To compute the absorption spectrum in Eq. 5.66 I have used the selection rules $\Delta m=0, \Delta n=\pm 1$ for valleys $\pm\boldsymbol{K}$, derived in Eq. 5.40 and shown in Fig. 5.5 with red arrows.

Fig. 5.11 shows the absorption spectrum $A(\omega,\boldsymbol{K})$ for $N_{LL}=1$ LL in VB and CB, with $V_{VCCV}=1$ and V_{CVCV}=0. Panels a-d show how different contributions to the CI Hamiltonian affect the spectrum. The axis is measured in a SP gap with no SO, but the exciton lines include SO (shown in red and blue for exciton A and B). I start with SP energies, which gives many degenerate exciton lines at energy differences calculated from Eq. 5.32. Inclusion of the self energy contributions given by Eq. 5.57 and Eq. 5.58 shifts the spectrum for all lines, which remain degenerate. This is because I implemented the correction of finite-size effects by using $\Sigma(m=0)$ for all m states. The vertex correction given in Eq. 5.61 is different for all m, which splits the exciton lines. Finally, I include the off-diagonal terms of the Hamiltonian, which is responsible for scattering of configurations. This changes the composition of

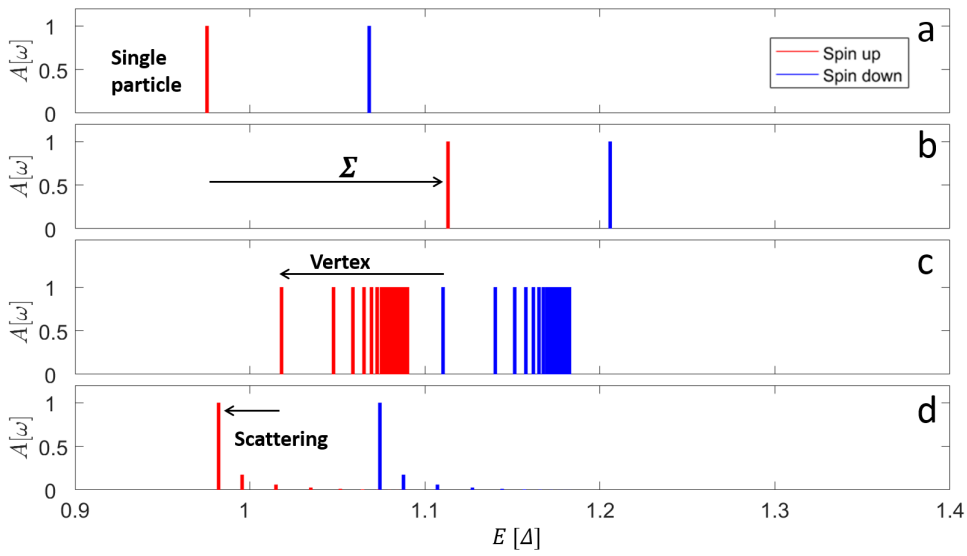

Figure 5.11: Magnetoexciton absorption spectrum for mDf for $N_{LL} = 1$, $M = 24$ and $B = 60$ T. Colors denote spins. a) With no interactions all exciton lines are equal to the SP energy of an electron-hole pair. b) Self-energy contribution shifts all exciton lines to higher energies. c) Vertex correction is different for each excitation, which splits the lines. Off-diagonal terms in the Hamiltonian produce varied oscillator strength and one dominant peak for each spin remains. All contributions to the exciton energy cancel almost exactly.

each exciton state and is responsible for the fading of the oscillator strength of the exciton lines. The blue shifts from self energy are almost exactly cancelled by the red shifts from vertex correction and scattering of configurations, so the final peaks are slightly blue-shifted w.r.t. the SP energies [159].

A similar case is showed in Fig. 5.12 for $N_{LL} = 3$ LLs in CB and VB. However, the resulting absorption peaks are shifted more towards higher energies as all the contributions do not fully cancel. A single exciton line for each spin remains dominant even for more LLs included in the CI basis. The difference in oscillator strength for absorption peaks on panel a-c is due to the varying transition probability $W_{nn'}$.

Fig. 5.13 shows the position of the dominant absorption peak for both spins for up to $N_{LL} = 7$ LLs and $M = 5$ included in the calculations. Each panel includes one more LL than the previous panel. A converging tendency of the exciton energies is visible when it reaches $\approx 130meV$ above the SP gap marked with a green line on all panels.

Fig. 5.14 shows the exciton A (lower energy) dominant absorption peak energy

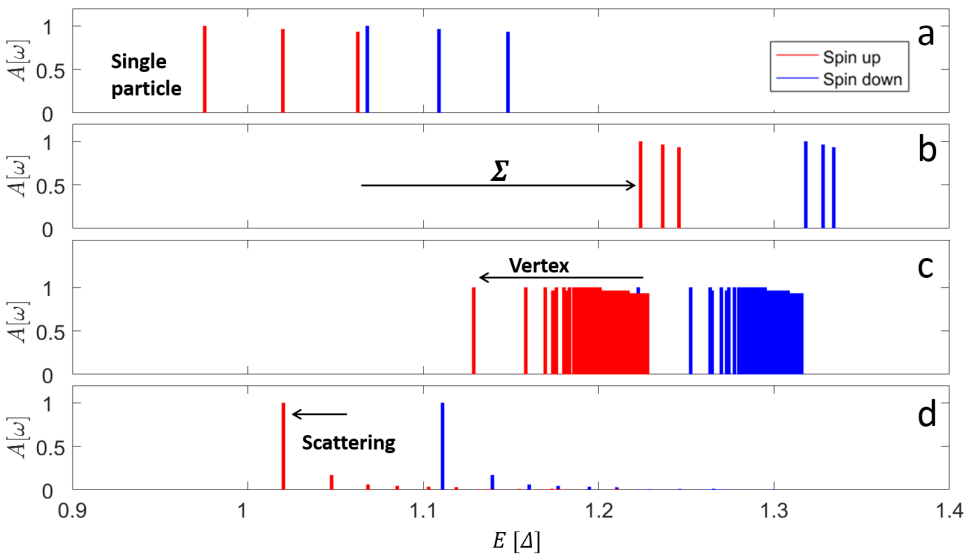

Figure 5.12: Magnetoexciton absorption spectrum for mDf for $N_{LL} = 3$, $M = 24$ and $B = 60$ T. Panels a-d shows the same contributions as Fig. 5.11. The final absorption peaks are blue-shifted w.r.t. SP energy gap.

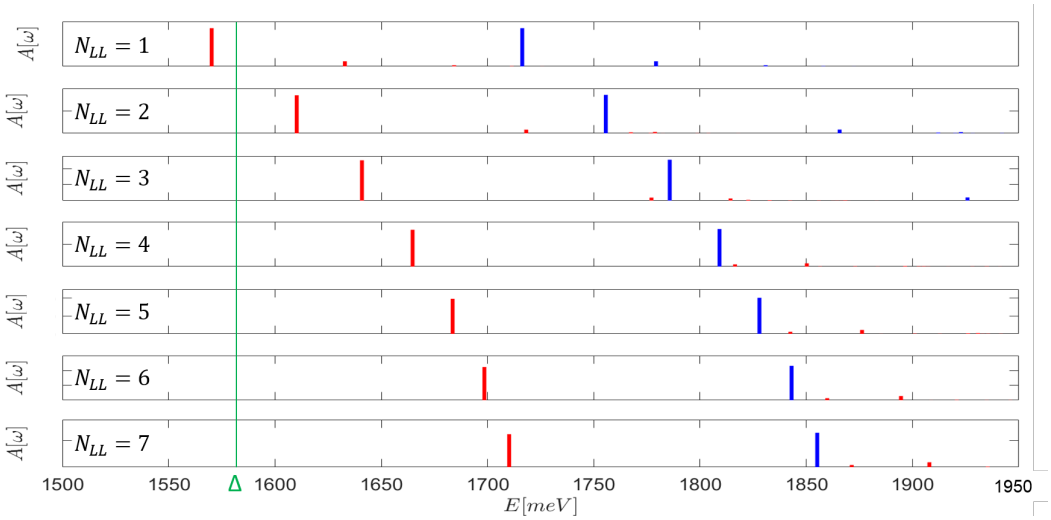

Figure 5.13: Final magnetoexciton absorption peaks for mDf for $N_{LL} = 1 \rightarrow 7$, $M = 5$ and $B = 60$ T. The absorption peaks move to higher energies as N_{LL} grows. A converging tendency is visible for high N_{LL}.

for both valleys as a function of the valley polarisation ρ defined in Eq. 5.6. As more LLs are filled with electrons, the absorption peaks shift towards higher energies. For all N it is clearly visible that the exciton peak at $\boldsymbol{K}$ remains at higher energy than the exciton absorption peak at $-\boldsymbol{K}$. This can be attributed to higher self-energy contribution to the exciton energy at $\boldsymbol{K}$, as demonstrated in Eq. 5.59 for low n. This is a consequence of the assymetrical LL structure in both valleys.

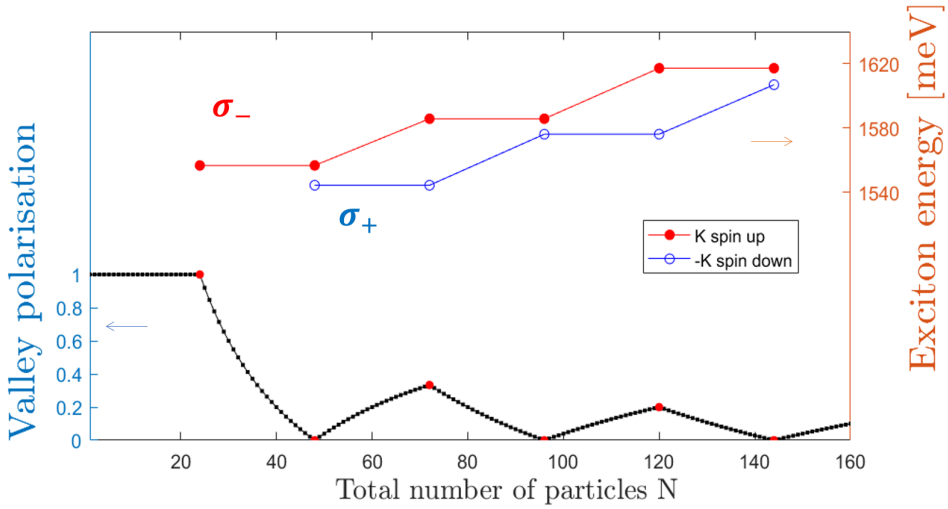

Figure 5.14: Magnetoexciton absorption spectrum for exciton A for $N_{LL} = 1 \to 3$, $M = 24$ and $B = 60$ T for both valleys. The exciton energy follows the valley polarisation and remains smaller in valley $-\boldsymbol{K}$ than in valley $\boldsymbol{K}$, as N is increased. Colors label spins and valleys for exciton A.

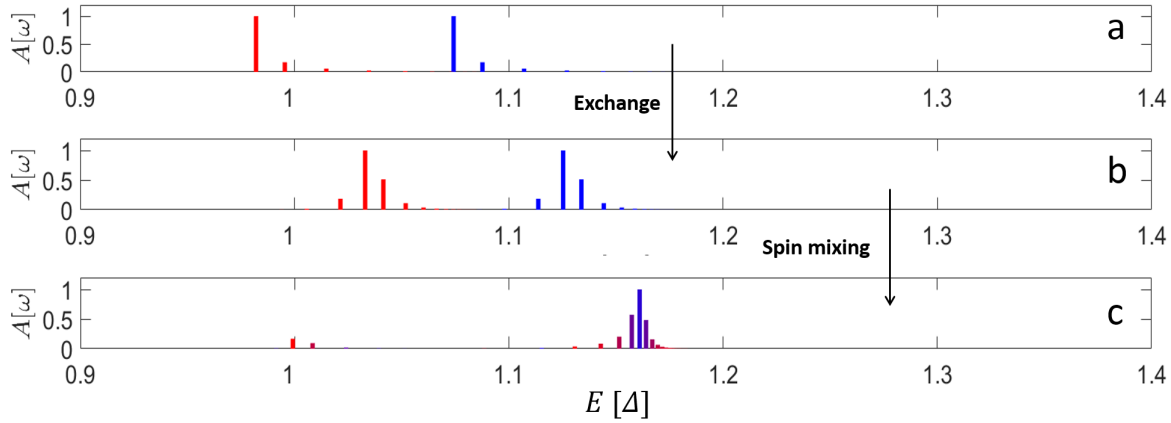

Figure 5.15: a) Magnetoexciton absorption spectrum for N_{LL}, $M = 24$ and $B = 60$ T. b) Effect of the exchange term in vertex correction ($V_{CVCV} = 0.1$). Second exciton line for each spin dominates and peaks move to higher energies. c) The effect of spin mixing on the absorption spectrum. The peak at higher energy dominates and is visible at $\approx 1.15\Delta$.

I now allow for nonzero $V_{CVCV} = 0.1$ and spin mixing of configurations. Fig. 5.15 shows the resulting absorption spectrum in subsequent steps. Panel b shows the exciton lines in case of nonzero exchange between the electron and a hole, given in Eq. 5.61 by the term with V_{CVCV} contribution. This causes the second exciton line to acquire oscillator strength, as the whole spectrum shift to higher energies at the same time. Panel c shows the effect of the scattering of different spin configurations as

dictated by Eq. 5.63. Both spin contributions have been pictured with continuously varying color from red (spin up mostly) to blue (spin down mostly) and purple denotes equal spin contributions. The emerging peak has a mixed spin composition with more spin down contribution and appears at much higher energy than the SP gap. Weak residual spin up peak is still visible at energies slightly higher than the SP gap.

Chapter 6

Electron-electron interactions in parabolic gated MoS_2 quantum dots

This chapter presents a theory of SP and many-body properties of parabolic MoS_2 QDs [163, 164]. Section 6.1 contains the TB model of a finite MoS_2 structure and is followed by the results on the SP energy structure of a parabolic QD in section 6.2. I discuss the details of the electron-electron interactions in MoS_2 QDs in section 6.3 and give prediction of broken-symmetry many-body states in these nanostructures in section 6.4.

6.1 Tight-binding model for MoS_2 quantum dots.

In this section I derive the TB model of a MoS_2 finite structure and of an electrostatically defined parabolic MoS_2 QD. I will first consider a rectangular piece of MoS_2 in section 6.1.1, which will serve as a computational box for an atomistic problem of a single electron in a parabolic QD in section 6.1.2. Section 6.1.3 discusses the same problem in the Bloch basis, which provides information on valley effects in QDs.

6.1.1 Nanostructures of MoS_2 in the basis of atomic orbitals.

I first consider a rectangular piece of MoS_2 shown in Fig. 6.1. The unit cell contains four lattice sites (marked with a green rectangle) and is repeated by a multiple of the supercell vectors $\boldsymbol{d}_1$ and $\boldsymbol{d}_2$ (shown in Fig. 6.1) to make an entire structure. I will identify structures of different sizes by numbers $N \times M$ of the repetitions of the unit cell.

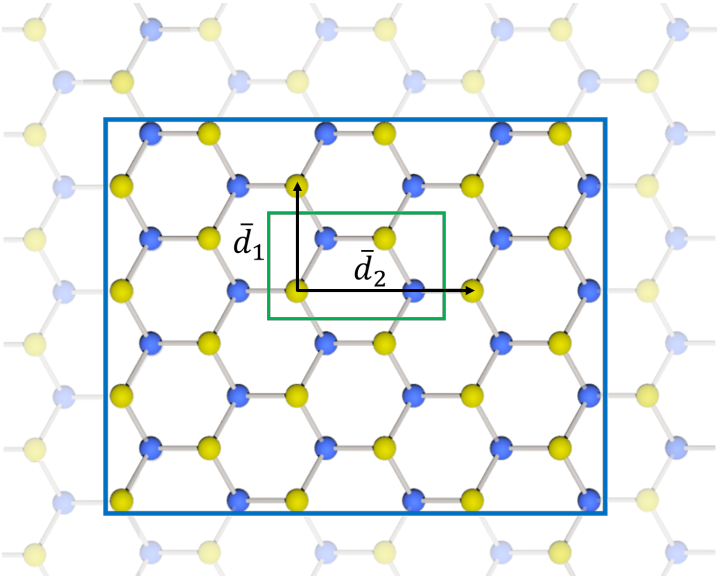

Figure 6.1: Rectangular piece (supercell) of MoS_2.Green box marks the unit cell of a rectangular structure with 4 sites. Vectors d_i define the repetition of the unit cell to form supercell contained in the blue box.

I will use the 6-band TB model derived in section 4.1 but, because I want to study finite structures, k will generally not be a good quantum number, so I will write the TB Hamiltonian in the basis of all the A & B ($A = Mo, B = S_2$) sites within the

rectangle

$$\begin{aligned}\hat{H}_{QD}^{TB} = &\sum_i \sum_{\alpha=\{m_d=0,\pm2\}} \mathcal{E}_\alpha^A c_{i,A,\alpha}^\dagger c_{i,A,\alpha} + \sum_i \sum_{\beta=\{m_p=0,\pm1\}} \mathcal{E}_\beta^B c_{i,B,\beta}^\dagger c_{i,B,\beta} \\ &+ \sum_{<i,j>} \sum_{\alpha=\{m_d=0,\pm2\}} \sum_{\beta=\{m_p=0,\pm1\}} \left(T_{ij,\alpha\beta} c_{i,A,\alpha}^\dagger c_{j,B,\beta} + h.c. \right) \\ &+ \sum_{<<i,j>>} \sum_{\alpha,\alpha'=\{m_d=0,\pm2\}} \left(U_{ij,\alpha\alpha'}^A c_{i,A,\alpha}^\dagger c_{j,A,\alpha'} + h.c. \right) \\ &+ \sum_{<<i,j>>} \sum_{\beta,\beta'=\{m_p=0,\pm1\}} \left(U_{ij,\beta\beta'}^B c_{i,B,\beta}^\dagger c_{j,B,\beta'} + h.c. \right),\end{aligned} \tag{6.1}$$

where T is a 3×3 NN hopping integral matrix in the basis of orbitals equal to $T_{ij,\alpha,\beta} = \langle \varphi_\alpha(\boldsymbol{r}) | \, V \, | \varphi_\beta(\boldsymbol{r} + \boldsymbol{\delta}_j) \rangle$ defined in Eq. 4.11 and $U^{A/B}$ is a 3×3 NNN hopping integral matrix in the basis of orbitals equal to $U_{ij,\alpha,\alpha'}^A = \langle \varphi_\alpha(\boldsymbol{r}) | \, V \, | \varphi_{\alpha'}(\boldsymbol{r} + \boldsymbol{\gamma}_j) \rangle$ defined in Eq. 4.22 and 4.24 and $\mathcal{E}_{\alpha/\beta}^{A/B}$ is a 3×3 diagonal matrix of onsite energies for orbitals and A & B denote sublattices. Note that the pairs of NN and NNN atoms could obey periodic boundary conditions (PBC) or not - I will begin by selecting pairs of neighbours without PBC.

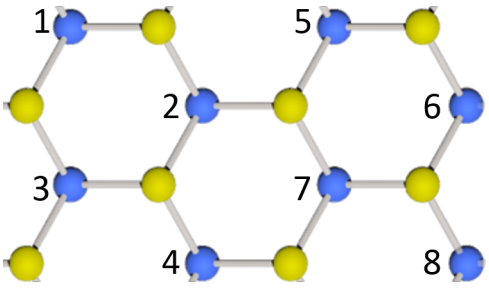

Figure 6.2: Rectangular MoS_2 2×2 computation box. Numbers label the atoms within sublattice A.

It is useful to represent the Hamiltonian in Eq. 6.1 for the smallest meaningful case of 2×2 supercells without PBC (pictured in Fig. 6.2) in a matrix form in the

basis of atoms $\{1A, 2A, 3A, ..., 1B, 2B, 3B, ...\}$

$$\hat{H}_{QD}^{TB} = \begin{pmatrix} \begin{pmatrix} \mathcal{E}^A & U^A & U^A & & & & & \\ & \mathcal{E}^A & U^A & U^A & U^A & & U^A & \\ & & \mathcal{E}^A & U^A & & & & \\ & & & \mathcal{E}^A & & & U^A & \\ & & & & \mathcal{E}^A & U^A & U^A & \\ & & & & & \mathcal{E}^A & U^A & U^A \\ & & & & & & \mathcal{E}^A & U^A \\ & & & & & & & \mathcal{E}^A \end{pmatrix} & \begin{pmatrix} T & T & & & & & & \\ T & & T & & & T & & \\ & T & T & T & & & & \\ & & T & & & & & T \\ & & & & T & T & & \\ & & & & T & & T & \\ & & & & & T & T & T \\ & & & & & & & T \end{pmatrix} \\ \begin{pmatrix} \mathcal{E}^B & U^B & U^B & & & U^B & & \\ & \mathcal{E}^B & U^B & U^B & & & & \\ & & \mathcal{E}^B & U^B & & U^B & & U^B \\ & & & \mathcal{E}^B & & & & \\ & & & & \mathcal{E}^B & U^B & U^B & \\ & & & & & \mathcal{E}^B & U^B & U^B \\ & & & & & & \mathcal{E}^B & U^B \\ & & & & & & & \mathcal{E}^B \end{pmatrix} & \end{pmatrix}, \tag{6.2}$$

where each T is understood as a 3×3 matrix in the basis of orbitals $T_{ij,\alpha,\beta} = T_{\alpha,\beta}(\theta_{ij})$, dependent on angle θ_{ij}, originating in directional cosines defined in Eq. 4.13, and each $U^{A/B}$ is understood as a 3×3 matrix in the basis of orbitals $U^A_{ij,\alpha,\alpha'} = U^A_{\alpha,\alpha'}(\phi_{ij})$, dependent on angle ϕ_{ij}, originating in directional cosines defined in Eq. 4.26. Explicit forms of the elements in Eq. 6.2 read

$$\mathcal{E}^A = \begin{pmatrix} E_{m_d=-2} & & \\ & E_{m_d=0} & \\ & & E_{m_d=+2} \end{pmatrix} \quad \mathcal{E}^B = \begin{pmatrix} E_{m_p=-1} & & \\ & E_{m_p=0} & \\ & & E_{m_p=+1} \end{pmatrix} \tag{6.3}$$

$$T(\theta) = \begin{pmatrix} V_1 e^{i\theta} & -V_2 e^{2i\theta} & -V_3 e^{3i\theta} \\ -V_4 e^{-i\theta} & -V_5 & -V_4 e^{i\theta} \\ -V_3 e^{-3i\theta} & -V_2 e^{-2i\theta} & V_1 e^{-i\theta} \end{pmatrix} \tag{6.4}$$

$$U^A(\phi) = \begin{pmatrix} W_1 & W_3 e^{2i\phi} & W_4 e^{4i\phi} \\ W_3 e^{-2i\phi} & W_2 & W_3 e^{2i\phi} \\ W_4 e^{-4i\phi} & W_3 e^{-2i\phi} & W_1 \end{pmatrix} \quad U^B(\phi) = \begin{pmatrix} W_5 & 0 & W_7 e^{2i\phi} \\ 0 & W_6 & 0 \\ W_7 e^{-2i\phi} & 0 & W_5 \end{pmatrix}, \tag{6.5}$$

where V_{1-5} and W_{1-7} have been defined in Eq. 4.17 and 4.28.

The dimension of the Hamiltonian matrix in Eq. 6.2 is $N_{dim}(N \times M) = 3 \cdot 2 \cdot 2 \cdot$

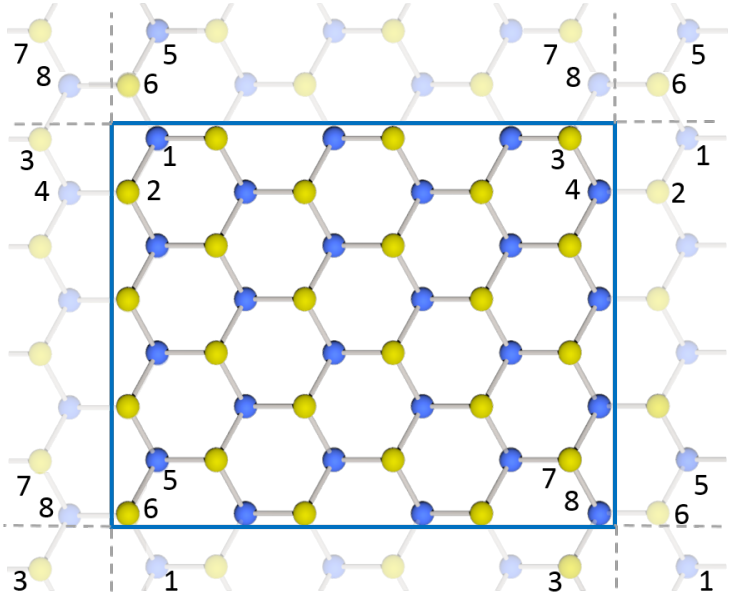

Figure 6.3: Periodic boundary conditions in a rectangular piece of MoS_2. Numbers label some edge atoms to demonstrate the process of finding NN within the copies of a supercell repeated in space.

$(N \cdot M)$, which for the case of a 2×2 structure is $N_{dim}(2 \times 2) = 48$.

Now, if I consider the PBC, I must fill in additional matrix elements in the matrix in Eq. 6.2 corresponding to neighbours linked across the edges of the structure, as shown in Fig. 6.3 for a bigger structure. Some edge atoms have been numbered to depict how the structure is repeated in space to enable PBC.

The Hamiltonian matrix in Eq. 6.1 is diagonalised for a $N \times M$ structure with or without PBC to obtain the eigenvalues and eigenvectors. Details on the diagonalisation routines have been included in section 2.3.1.

Fig. 6.4 shows the energy spectrum of a 6×6 structure with and without PBC for comparison. It is visible how a gap opens in the structure treated with PBC. This is due to elimination of edge effects, which is demonstrated in Fig. 6.5. The orientation of the lattice in Fig. 6.5 is the same as in Fig 6.3, so right (left) edge is built of Mo (S) atoms. Fig. 6.5 shows the wavefunction amplitude of states 288-291, which appear in the gap in case without PBC. The wavefunction is strongly localised on Mo atoms on the box edges. Therefore, studying the structures with PBC enables me to remove the edge effects, which will prove useful in case of electrostatically confined QD.

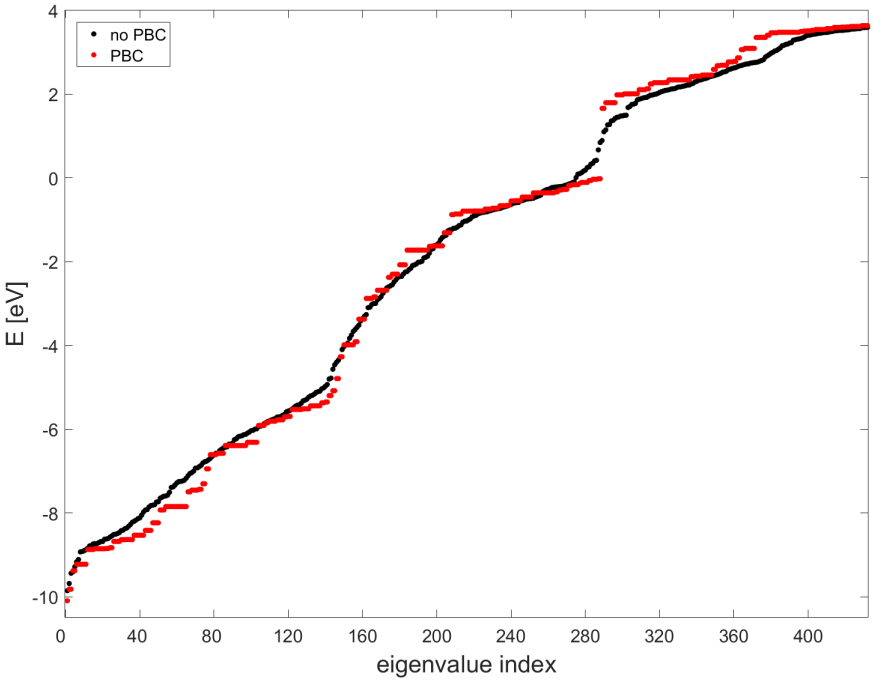

Figure 6.4: Comparison of the energy spectrum of a 6×6 MoS_2 QD with (red) and without PBC (black). A gap opens at $\approx 0 - 2$ eV.

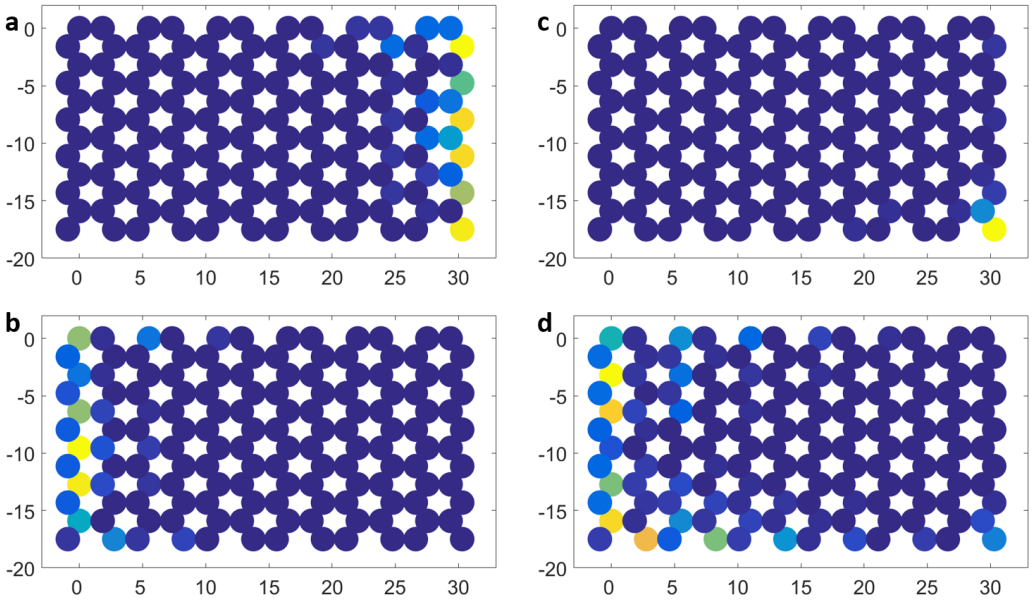

Figure 6.5: Wavefunction amplitude for states 288-291 for a 6×6 MoS_2 piece without PBC. They are edge states, which can be eliminated if PBC is employed. Bright color denote higher amplitude.

6.1.2 Electrostatically defined MoS_2 quantum dots.

This section includes description of the QDs that are defined electrostatically within a nanostructure of MoS_2. Contrary to graphene, MoS_2 is a semiconductor, which

makes it possible to trap charges within potential wells in its plane. We want to do so to enable manipulation of single charges within a QD for e.g. quantum computing applications. It is done by adding an external parabolic potential (shown in Fig. 6.6) to the Hamiltonian describing a piece of MoS_2 given in Eq. 6.1. The parabolic form of the potential is used because any smooth potential profile can be described by a parabola at low energies, and a single practical parameter ω (shell spacing) can be used to describe the eigenstates of a parabolic well. The external potential can be generated by metallic gates placed on top of the nanostructure. The gates introduce a perpendicular electric field to the MoS_2 layer, which modifies the onsite energies on atomic sites. Such metallic gates are typically located far above and below the plane of MoS_2, which keeps the potential difference between the top and bottom edge of the crystal very small, so the assumption made in our TB model in section 4.1 on the even nature of contributing orbitals still holds (I estimate the effect of odd admixture to the wavefunction below 1%).

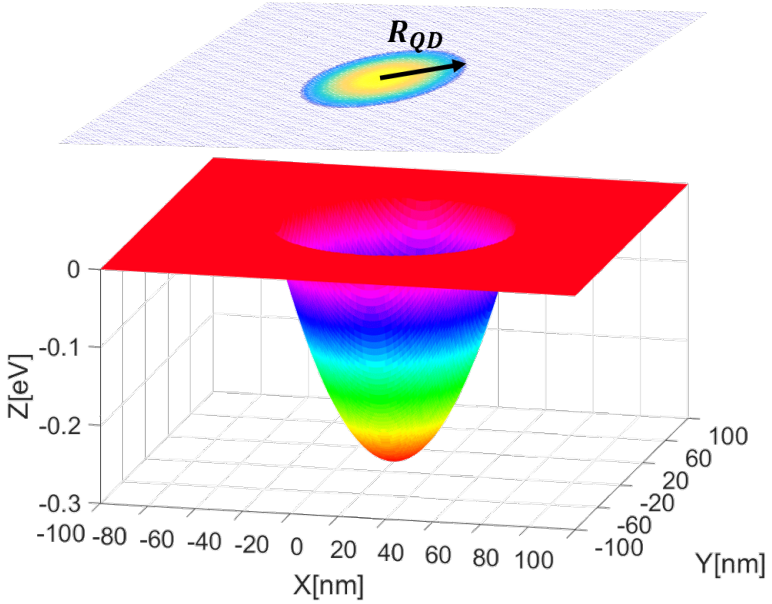

Figure 6.6: External confining parabolic potential well with radius $R_{QD} = 40nm$ and $V_{max} = 300$ meV.

The Hamiltonian of an electrostatically confined parabolic QD with radius R_{QD} is given by

$$\hat{H}_{para} = \hat{H}_{QD}^{TB} + \sum_{i\alpha} V_i c_{i\alpha}^{\dagger} c_{i\alpha}, \tag{6.6}$$

where V_i is the external potential on an atomic site generated by metallic gates given by

$$V_i = V(\boldsymbol{r}_i) = \begin{cases} \frac{1}{2}\widetilde{\omega}^2 \boldsymbol{r}_i^2 - V_{max}, & |\boldsymbol{r}_i| \leqslant R_{QD}, \\ 0, & |\boldsymbol{r}_i| > R_{QD}, \end{cases} \tag{6.7}$$

where $\widetilde{\omega} = \sqrt{2|V_{max}|/R_{QD}^2}$ is the corresponding harmonic oscillator level spacing defined by the depth of the confining potential V_{max}. In Eq. 6.7, i runs over all the A and B sites of the $N \times M$ computational box of the MoS_2. While choosing R_{QD} we keep the size of the computational box sufficiently big so that the confined states are not affected by the edges. To avoid clouding the energy spectrum with edge states while analysing the confined states, we use PBC. As we are interested in additional electrons trapped in the potential well I will focus on the lowest states within the CB. These states should not be associated with the edges and therefore should not depend on the choice of the boundary conditions. Fig. 6.7 shows the energy spectrum of the same computation box 24×16 with a confined QD of the same radius $R_{QD} = 2$nm in two cases: with and without PBC. For such small dot we obtain only two confined energy shells (highlighted in boxes), which remain at the same energy in both cases. This proves that we can study those confined states with PBC, which eliminates the effect of the edges of computation box for boxes sufficiently larger than R_{QD}.

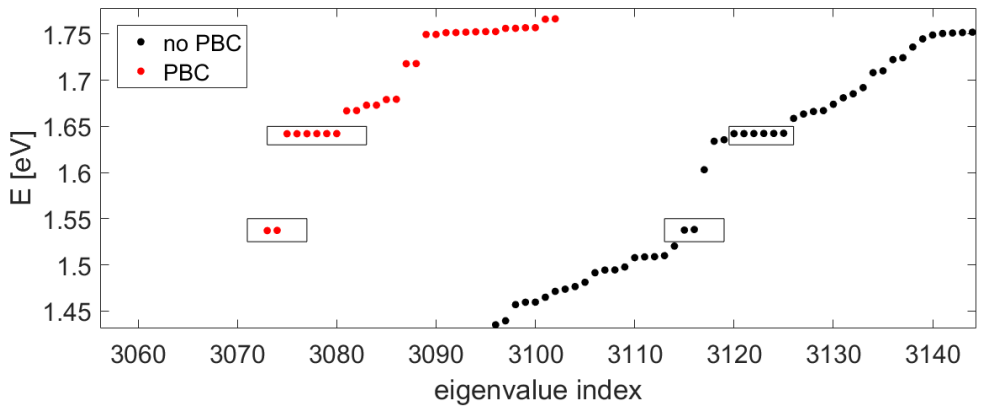

Figure 6.7: Comparison of the energy specturm of a 24×16 computation box with a confined QD of $R_{QD} = 2$nm with (red) and without PBC (black). Boxed levels are the same for both cases and are therefore confined inside the QD.

6.1.3 MoS_2 quantum dots in the basis of Bloch states.

Below I will show how to obtain the energies of MoS_2 confined QD in the basis of Bloch states instead of atomic sites to gain the important information about the origin of levels in $\boldsymbol{k}$-space. I will consider different shapes of the computational box: rectangular (as shown in Fig. 6.1) and romboidal (Fig. 6.8), with PBC in each case. Each computational box is composed of $N \times M$ unit supercells, as before. We will now label the unit supercells as $\boldsymbol{R}_{ij} = \boldsymbol{(i,j)} = (i-1)\boldsymbol{d}_1 + (j-1)\boldsymbol{d}_2$, where $\boldsymbol{d}_1$ and $\boldsymbol{d}_2$ are the supercell vectors for a chosen shape of a computational box.

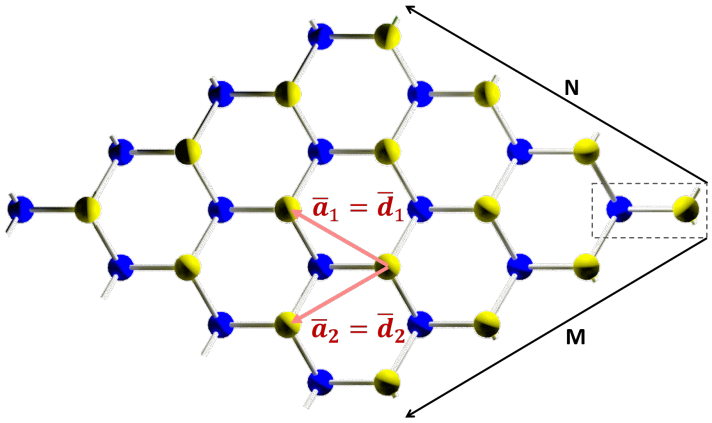

Figure 6.8: $N \times M$ romboidal computation box. Unit cell is shown in a dashed box. Unit vectors of a hexagonal lattice $\boldsymbol{a}_i$ are the same as the supercell vectors $\boldsymbol{d}_i$.

I will use the Fourier transform of the operators in the site basis $c_{ijA/B}(c^\dagger_{ijA/B})$ to obtain the operators in the Bloch basis $a_{pqA/B}(a^\dagger_{pqA/B})$:

$$
\begin{aligned}
a^\dagger_{pq,A/B} &= \frac{1}{\sqrt{NM}} \sum_{ij=1,N,M} e^{-i\boldsymbol{k}_{pq}\boldsymbol{(i,j)}} c^\dagger_{ij,A/B}, \\
a_{pq,A/B} &= \frac{1}{\sqrt{NM}} \sum_{ij=1,N,M} e^{i\boldsymbol{k}_{pq}\boldsymbol{(i,j)}} c_{ij,A/B}, \\
c^\dagger_{ij,A/B} &= \frac{1}{\sqrt{NM}} \sum_{pq=1,N,M} e^{i\boldsymbol{k}_{pq}\boldsymbol{(i,j)}} a^\dagger_{pq,A/B}, \\
c_{ij,A/B} &= \frac{1}{\sqrt{NM}} \sum_{pq=1,N,M} e^{-i\boldsymbol{k}_{pq}\boldsymbol{(i,j)}} a_{pq,A/B}, \\
\boldsymbol{k}_{pq} &= p\frac{\boldsymbol{v}_1}{N} + q\frac{\boldsymbol{v}_2}{M}, \quad p = 0, ..., N-1, \quad q = 0, ..., M-1,
\end{aligned}
\tag{6.8}
$$

where $\boldsymbol{v}_1$ and $\boldsymbol{v}_2$ are reciprocal supercell vectors, obtained from supercell vectors $\boldsymbol{d}_1$

and $\boldsymbol{d}_2$, which are equal to hexagonal lattice unit vectors $\boldsymbol{a}_1$ and $\boldsymbol{a}_2$ for a romboidal box and are distinct for a rectangular box:

$$\begin{aligned} \boldsymbol{d}_1^{romb} &= \boldsymbol{a}_1 = d_\parallel\sqrt{3}(-\frac{\sqrt{3}}{2}, \frac{1}{2}), & \boldsymbol{d}_1^{rect} &= d_\parallel\sqrt{3}(0,1), \\ \boldsymbol{d}_2^{romb} &= \boldsymbol{a}_2 = d_\parallel\sqrt{3}(-\frac{\sqrt{3}}{2}, -\frac{1}{2}), & \boldsymbol{d}_2^{rect} &= d_\parallel\sqrt{3}\big(\sqrt{3}, 0\big), \end{aligned} \tag{6.9}$$

as shown in Fig. 6.8 for a rhombus and in Fig. 6.1 for a rectangle. Then the reciprocal supercell vectors read

$$\begin{aligned} \boldsymbol{v}_1^{romb} &= \boldsymbol{G}_1 = \frac{2\pi}{d_\parallel\sqrt{3}}\left(-\frac{1}{\sqrt{3}}, 1\right), & \boldsymbol{v}_1^{rect} &= \frac{2\pi}{d_\parallel\sqrt{3}}(0,1), \\ \boldsymbol{v}_2^{romb} &= \boldsymbol{G}_2 = \frac{2\pi}{d_\parallel\sqrt{3}}\left(-\frac{1}{\sqrt{3}}, -1\right), & \boldsymbol{v}_2^{rect} &= \frac{2\pi}{d_\parallel\sqrt{3}}\left(\frac{2}{\sqrt{3}}, 0\right), \end{aligned} \tag{6.10}$$

where $\boldsymbol{G}_1$ and $\boldsymbol{G}_2$ are reciprocal lattice vectors of the hexagonal lattice. The resulting mesh of $\boldsymbol{k}_{pq}$ has been shown in detail in Fig. 6.9 with black dots for both shapes of computation boxes. High symmetry points and the contours of the reciprocal lattice have been marked.

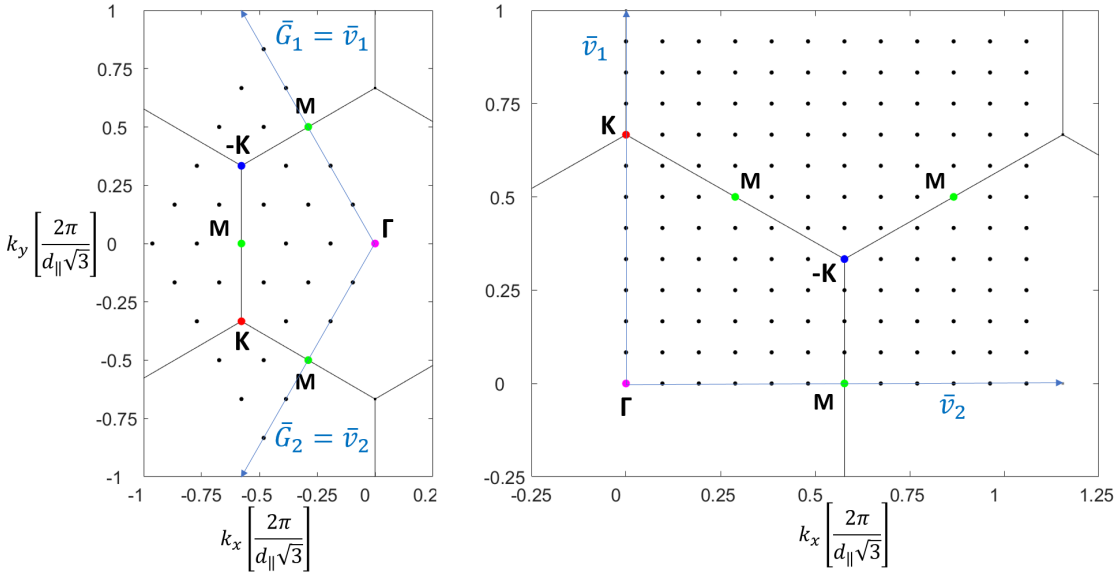

Figure 6.9: $\boldsymbol{k}$-point meshes for a (left) romboidal and (right) rectangular computation boxes (6×6 and 12×12 respectively). Black lines give BZ edges. High symmetry points are labelled with colorful dots. Reciprocal supercell vectors $\boldsymbol{v}$ are shown (they are the same as reciprocal lattice vectors $\boldsymbol{G}$ for a rhombus piece).

I will now transform the QD Hamiltonian given by Eq. 6.1 into the Bloch state

basis in parts $\hat{H}_{QD}^{TB} = \hat{H}_{QD}^{onsite} + \hat{H}_{QD}^{NN} + \hat{H}_{QD}^{NNN}$. Using Eq. 6.8, the onsite terms of the QD Hamiltonian given by Eq. 6.1 can be expressed as

$$\begin{aligned}\hat{H}_{QD}^{onsite} &= \sum_{ij} \sum_{\alpha=\{m_d=0,\pm2\}} \mathcal{E}_\alpha^A c_{ij,A,\alpha}^\dagger c_{ij,A,\alpha} + \sum_{ij} \sum_{\beta=\{m_d=0,\pm2\}} \mathcal{E}_\beta^B c_{ij,B,\beta}^\dagger c_{ij,B,\beta} \\ &= \frac{1}{NM} \sum_{pq,rs} \sum_{ij} e^{i(\boldsymbol{k}_{pq}-\boldsymbol{k}_{rs})\boldsymbol{R}_{ij}} \sum_{\alpha=\{m_d=0,\pm2\}} \left(\mathcal{E}_\alpha^A a_{pq,A,\alpha}^\dagger a_{rs,A,\alpha} + \mathcal{E}_\beta^B a_{pq,B,\beta}^\dagger a_{rs,B,\beta} \right) \\ &= \sum_{pq} \sum_{\alpha=\{m_d=0,\pm2\}} \left(\mathcal{E}_\alpha^A a_{pq,A,\alpha}^\dagger a_{pq,A,\alpha} + \mathcal{E}_\beta^B a_{pq,B,\beta}^\dagger a_{pq,B,\beta} \right),\end{aligned} \tag{6.11}$$

because $\sum_{ij} e^{i(\boldsymbol{k}_{pq}-\boldsymbol{k}_{rs})\boldsymbol{R}_{ij}} = NM\delta_{pr,qs}$ for a periodic system. The NN terms are expressed analogously as

$$\begin{aligned}\hat{H}_{QD}^{NN} &= \sum_{\substack{ij \\ \alpha=\{m_d=0,\pm2\} \\ \beta=\{m_p=0,\pm1\}}} \left(T_{\alpha\beta}(\theta_1) c_{ij,A,\alpha}^\dagger c_{ij,B,\beta} + T_{\alpha\beta}(\theta_2) c_{ij,A,\alpha}^\dagger c_{i+1j,B,\beta} + T_{\alpha\beta}(\theta_3) c_{ij,A,\alpha}^\dagger c_{ij+1,B,\beta} + h.c. \right) \\ &= \sum_{pq} \sum_{\substack{\alpha=\{m_d=0,\pm2\} \\ \beta=\{m_p=0,\pm1\}}} e^{-i\boldsymbol{k}_{pq}\boldsymbol{b}} \left(T_{\alpha\beta}(\theta_1) + T_{\alpha\beta}(\theta_2) e^{i\boldsymbol{k}_{pq}\boldsymbol{a}_2} + T_{\alpha\beta}(\theta_3) e^{i\boldsymbol{k}_{pq}\boldsymbol{a}_1} + h.c. \right) a_{pq,A,\alpha}^\dagger a_{pq,B,\beta} \\ &= \sum_{pq} \sum_{\substack{\alpha=\{m_d=0,\pm2\} \\ \beta=\{m_p=0,\pm1\}}} f_{MoS_2}^{\alpha\beta}(\boldsymbol{k}_{pq})) a_{pq,A,\alpha}^\dagger a_{pq,B,\beta}\end{aligned} \tag{6.12}$$

and the NNN terms for sublattice A are expressed as

$$\begin{aligned}\hat{H}_{QD}^{NNN} &= \sum_{ij} \sum_{\alpha,\alpha'=\{m_d=0,\pm2\}} \Big(U_{\alpha\alpha'}^A(\phi_1) c_{ij,A,\alpha}^\dagger c_{ij-1,A,\alpha'} + U_{\alpha\alpha'}^A(\phi_2) c_{ij,A,\alpha}^\dagger c_{i+1,j-1,A,\alpha'} \\ &\quad + U_{\alpha\alpha'}^A(\phi_3) c_{ij,A,\alpha}^\dagger c_{i+1j,A,\alpha'} + U_{\alpha\alpha'}^A(\phi_4) c_{ij,A,\alpha}^\dagger c_{ij+1,A,\alpha'} \\ &\quad + U_{\alpha\alpha'}^A(\phi_5) c_{ij,A,\alpha}^\dagger c_{i-1,j+1,A,\alpha'} + U_{\alpha\alpha'}^A(\phi_6) c_{ij,A,\alpha}^\dagger c_{i-1j,A,\alpha'} + h.c. \Big) \\ &= \sum_{pq} \sum_{\alpha,\alpha'=\{m_d=0,\pm2\}} \Big(U_{\alpha\alpha'}^A(\phi_1) e^{-i\boldsymbol{k}_{pq}\boldsymbol{a}_1} + U_{\alpha\alpha'}^A(\phi_2) e^{-i\boldsymbol{k}_{pq}(\boldsymbol{a}_2-\boldsymbol{a}_1)} + U_{\alpha\alpha'}^A(\phi_3) e^{i\boldsymbol{k}_{pq}\boldsymbol{a}_2} \\ &\quad + U_{\alpha\alpha'}^A(\phi_4) e^{i\boldsymbol{k}_{pq}\boldsymbol{a}_1} + U_{\alpha\alpha'}^A(\phi_5) e^{-i\boldsymbol{k}_{pq}(\boldsymbol{a}_1-\boldsymbol{a}_2)} + U_{\alpha\alpha'}^A(\phi_6) e^{-i\boldsymbol{k}_{pq}\boldsymbol{a}_2} + h.c. \Big) a_{pq,A,\alpha}^\dagger a_{pq,A,\alpha'} \\ &= \sum_{pq} \sum_{\alpha,\alpha'=\{m_d=0,\pm2\}} g_{MoS_2}^{\alpha\alpha'}(\boldsymbol{k}_{pq}) a_{pq,A,\alpha}^\dagger a_{pq,A,\alpha'}\end{aligned} \tag{6.13}$$

and analogously for sublattice B. Phases θ and ϕ in expressions in Eq. 6.11,6.12 and 6.13 correspond to NN and NNN phases given in Eq. 4.13 and 4.26.

It is apparent that $\hat{H}_{QD}^{TB}$ is block-diagonal in $\boldsymbol{k}$-states, where the blocks are in the basis of sublattices A and B. However, when the external confining potential is added, the problem is not periodic in space any more. Therefore the $\boldsymbol{k}$-blocks are mixed.

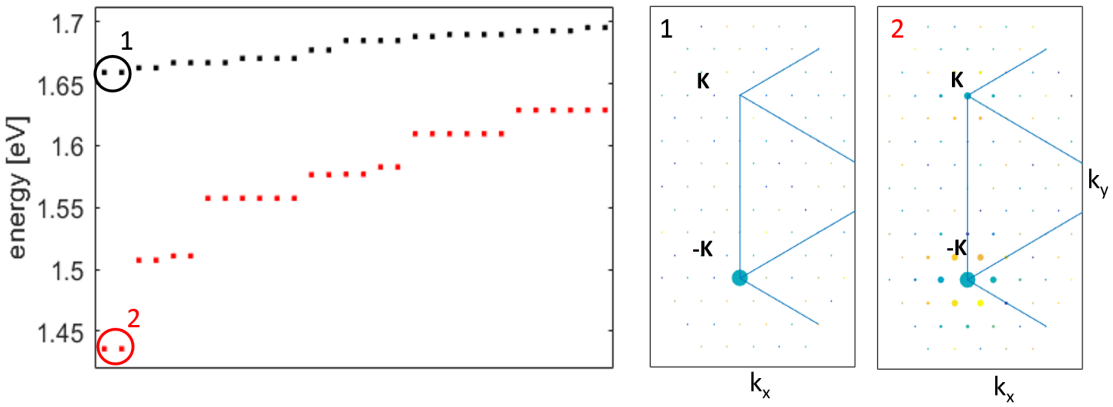

Figure 6.10: (left) Energy levels of QD states with (red) and without (black) the confining potential for a rhombus box. (right) $\boldsymbol{k}$-point distribution of the wavefunction for states #1 (#2) (encoded in colorful dot sizes) has been shown for both cases in panel 1 (2). Without the confining potential the state is localised at $-\boldsymbol{K}$, and with the confining potential it spreads to surrounding $\boldsymbol{k}$-points. Small valley mixing is visible.

The full form of the Hamiltonian with the confining term given in Eq. 6.6 expressed in the Bloch state basis reads

$$\begin{aligned}\hat{H}_{para} &= \hat{H}^{TB}_{QD} + \sum_{ij\alpha} V_{ijA} c^{\dagger}_{ij,A,\alpha} c_{ij,A\alpha} + \sum_{ij\beta} V_{ijB} c^{\dagger}_{ij,B,\beta} c_{ij,B\beta} \\ &= \hat{H}^{TB}_{QD} + \sum_{\substack{ij \\ pq,rs}} e^{i(\boldsymbol{k}_{pq}-\boldsymbol{k}_{rs})\boldsymbol{R}_{ij}} \left(\sum_{\alpha} V_{ijA} a^{\dagger}_{pq,A,\alpha} a_{rs,A,\alpha} + \sum_{\beta} V_{ijB} e^{i(\boldsymbol{k}_{pq}-\boldsymbol{k}_{rs})\boldsymbol{b}} a^{\dagger}_{pq,B,\beta} a_{rs,B,\beta} \right), \end{aligned} \quad (6.14)$$

which is not diagonal in $\boldsymbol{k}$-basis. In order to diagonalise Hamiltonian given in Eq. 6.14, I use the mesh of $\boldsymbol{k}$-points given by PBC for a chosen shape and size of a box (Fig. 6.9). Solutions of the Hamiltonian in Eq. 6.14 are naturally the same as in section 6.1.2 but this time the eigenvectors carry the information about the $\boldsymbol{k}$-point distribution. An example of such eigenvector has been shown in Fig. 6.10. The energy levels are obtained for a 12×12 computation box with and without a confining potential (shown in red and black respectively). The panels 1 and 2 show the $\boldsymbol{k}$-point distribution of the eigenvector of state 1153 in both cases (size of a dot encodes the amplitude for a given $\boldsymbol{k}$-point). Without the confining potential the whole wavefunction is located in the $\boldsymbol{K}$-point, and when the potential is added, the state spreads to surrounding $\boldsymbol{k}$-points. Very slight mixing of both valleys is also visible.

6.2 Single particle energy spectrum.

In this section I will present the results I have obtained on the SP properties of MoS_2 QDs. The energy structure for QDs with radii $R_{QD} = 12, 15, 18, 20$ nm and $V_{max} = 300$ meV have been shown in Fig. 6.11. The computations were performed on a 160×220 box with PBC and no SO splitting. As the radius R_{QD} grows, more states are confined within the dot, and the spacing between states decreases.

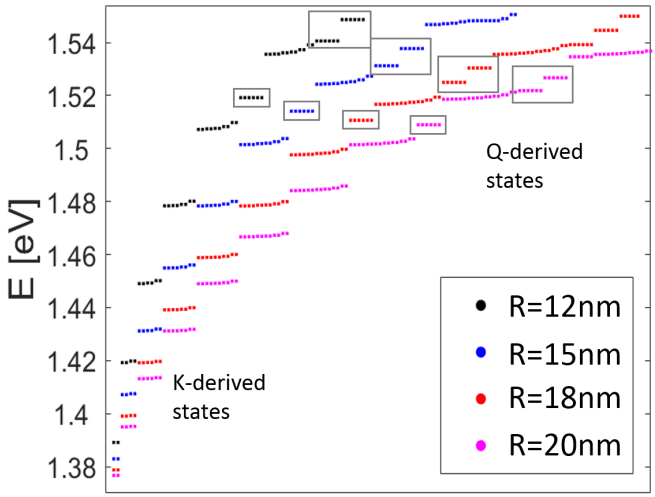

Figure 6.11: Energy levels of MoS_2 QDs with $R_{QD} = 12, 15, 18, 20$ nm (colors). Lower ladder of states can be attributed to valleys $\pm\boldsymbol{K}$, while higher levels originate in $\boldsymbol{Q}$-points. For growing R_{QD} level spacing decreases.

In the low-energy spectrum in Fig. 6.11 states originating in valleys $\pm\boldsymbol{K}$ are visible. They have been described in section 6.2.1. At higher energies a ladder of states associated with the $\boldsymbol{Q}$-points appears, which I described in section 6.2.2. The effects of SO coupling in MoS_2 have been neglected in section 6.2.1 and 6.2.2 and are discussed finally in section 6.2.3.

6.2.1 Spectrum associated with valleys K and $-K$.

I will now discuss the low-energy levels associated with the $\boldsymbol{K}$ valleys.

The levels form groups of almost-degenerate shells, spaced equally by ω, as shown schematically in green in Fig. 6.12 (left). It resembles a HO spectrum consisting of electronic shells, but in case of the QD, the spectrum degeneracy is doubled w.r.t. the

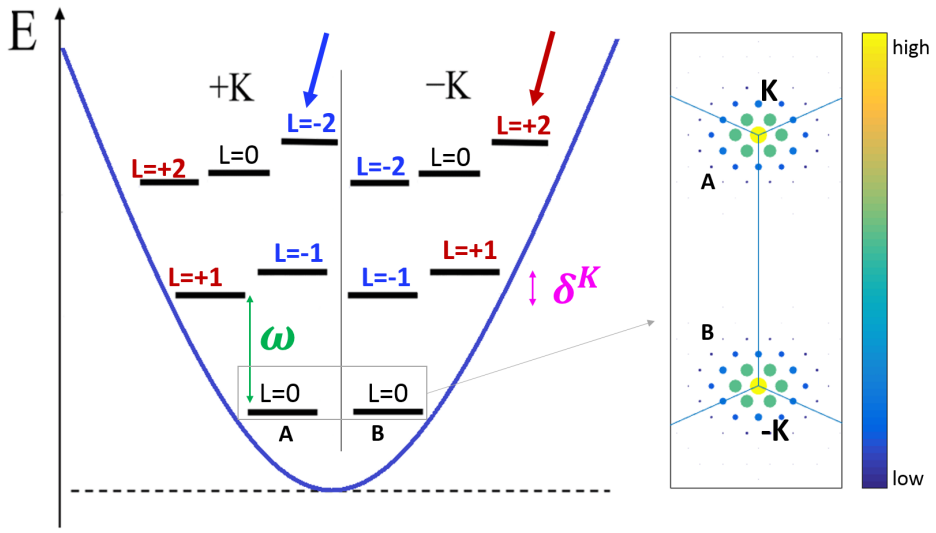

Figure 6.12: (left) QD energy levels associated with valleys $\pm\boldsymbol{K}$. For each valley almost-degenerate levels are grouped, so shells are formed. ω is a shell spacing (not to scale) and L is angular momentum. Shells are split by δ^K, which appears because $\pm\boldsymbol{K}$ are topologically inequivalent. Levels order according to L oppositely in both valleys. (right) $\boldsymbol{k}$-point distribution for the wavefunction of two lowest levels A and B. They are associated with the $\pm\boldsymbol{K}$ valleys.

HO spectrum. This is a consequence of two valleys $\pm\boldsymbol{K}$, as shown in the right panel of Fig. 6.12 [163]. It pictures the Fourier composition of the two lowest states plotted against the hexagonal BZ, and this information has been obtained by diagonalising the Hamiltonian in the Bloch basis using Eq. 6.14. The wavefunction amplitude has been encoded with the size of a dot and its color at the same time. The eigenvector is localised mainly at $\boldsymbol{K}$ and $-\boldsymbol{K}$ and their surrounding points. Levels A and B can be classified as localised around $\boldsymbol{K}$ and $-\boldsymbol{K}$ respectively, which will be proven with SO coupling included in section 6.2.3.

In analogy to standard HO, the shells from both valleys can be labelled by 2D HO quantum numbers (n, m) (along $x \pm iy$ directions), or equivalently by the shell number $I = n+m$ and shell angular momentum $L = n-m$. The values of L have been marked in Fig. 6.12 for all levels. They have been assgned to numerical eigenstates based on the charge density and degeneracy resembling the 2D HO solutions, as discussed in detail in section 6.3.

A further modification of the HO spectrum for MoS_2 QDs involves intra-shell

splitting δ^K (shown in pink in Fig. 6.12 left, not to scale), which depends on L, and the splitting is opposite in opposite valleys, as shown in Fig. 6.12 with red and blue labels. The thick red and blue arrows emphasize this difference for the $|L| = 2$ states in the $I = 2$ shell. This effect is similar to the degeneracy lifting in standard HO by an external magnetic field [165] and appears also in excitons in MoS_2 [44, 163]. This effect resembles a conventional orbital Zeeman effect, which arises due to magnetic field coupling to the angular momentum of atomic orbitals [44]. In consequence, $2p$ atomic states with opposite m_l quantum number are split. A parabolic MoS_2 QD is an artificial atom, with discrete energy levels that are angular momentum eigenstates, and they are associated with either of the two valleys $\boldsymbol{K}$ and $-\boldsymbol{K}$ in momentum space. At the same time, the mDf nature of an MoS_2 crystal produces a non-zero Berry curvature, opposite for opposite valleys, which is an analogue of a magnetic field vector acting on finite angular momentum states, with opposite directions in opposite valleys [44–46]. Berry curvature couples to the angular momentum of quantum dot states from each valley, just as a magnetic field does in real space in case of atomic orbitals. As a result, the degeneracy of p-shell states in an MoS_2 QD is broken, similar to a Landé splitting in an atom [44]. I call the intra-shell splitting δ a "topological" splitting. The magnitude of splitting δ^K is analysed together with splittings in the $\boldsymbol{Q}$-derived spectrum in section 6.2.2.

6.2.2 Spectrum associated with the Q-points.

I now turn to the description of the states visible at higher energy in Fig. 6.11.

The shells are six-fold degenerate, as shown in Fig. 6.13 (left), which has its origin in the 6 inequivalent $\boldsymbol{Q}$-points [163], three per valley, as shown in the inset at the bottom of Fig. 6.13 with red blue and green points. These colors correspond to the energy levels in Fig. 6.13 (left). This ladder of states can be attributed to the $\boldsymbol{Q}$-points, because of the Fourier composition of the levels, which has been pictured in Fig. 6.13 (right) for the two lowest energy groups of states A and B (groupped with solid and dashed lined polygons respectively). The size and colors of the dots encode

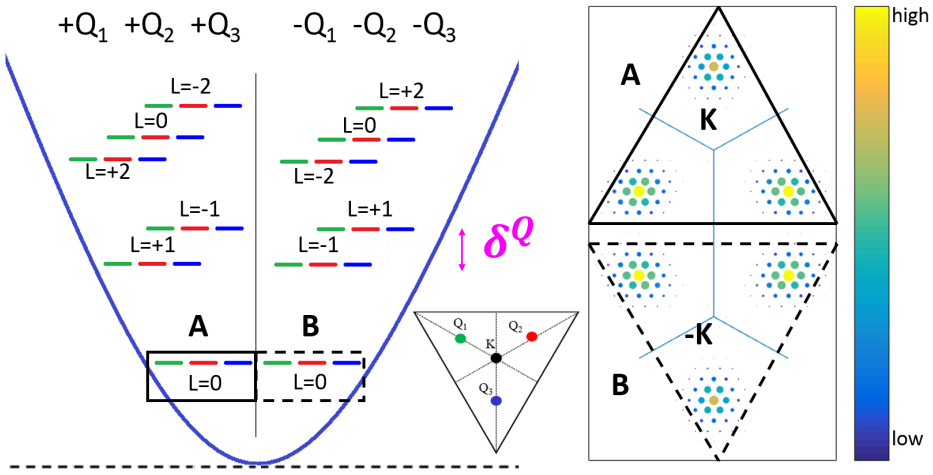

Figure 6.13: (left) QD energy levels associated with $\boldsymbol{Q}$-points (not to scale). For each valley there are three $\boldsymbol{Q}$-points (red, blue and green in inset and corresponding energy levels), which produce threefold degenerate spectrum for each valley. Topological splitting δ^Q is larger than δ^K. (right) $\boldsymbol{k}$-point distribution for lowest 6 states (groups A and B) shows localisation at $\boldsymbol{Q}$-points.

the probability density at these points.

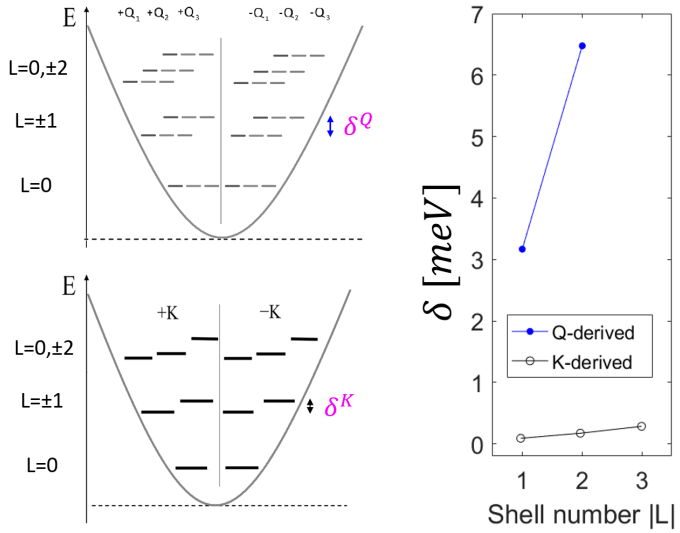

Figure 6.14: (left) Topological splitting δ for $\boldsymbol{K}$-derived and $\boldsymbol{Q}$-derived states (identified on the bottom and top of left panel, not to scale). (right) Magnitude of δ^K and δ^Q shown for different shells with black empty and blue solid dots. δ^Q is an order of magnitude larger than Δ^K and reaches up to 6.5 meV.

The $\boldsymbol{Q}$-derived ladder of states also exhibits topological splitting δ^Q, opposite for states around opposite valleys, as shown schematically in Fig. 6.13. The topological

splitting for both ladder of states, δ^K and δ^Q, have been schematically marked again in Fig. 6.14 (left) with pink symbols. Fig. 6.14 (right) plots the magnitude of δ^K and δ^Q for $R_{QD} = 30$ nm as a function of the maximum angular momentum in a shell $|L|$. It is clear that δ^Q is an order of magnitude larger than δ^K for the lowest energy shells, and it reaches up to $\delta^Q \approx 6.5$ meV for the second $I = 1$ shell.

6.2.3 Spin-orbit splitting vs shell spacing.

I now include the SO coupling, as in Eq. 4.34, which results in a SO splitting Δ_{SO} in the QD energy levels. Fig. 6.15 shows schematically how Δ_{SO} modifies the QD energy structure, by illustrating the effect on the lowest shells of both ladders, $\boldsymbol{K}$-derived and $\boldsymbol{Q}$-derived (as shown in the left panel of Fig. 6.15). Spin spliting for both ladders, Δ_{SO}^K and Δ_{SO}^Q, are opposite around opposite valleys (red and blue arrows denote spin up and down). These spin states have been classified by examining the Fourier spectrum of the lowest four states (marked by green box), which has been shown in Fig. 6.15 (right) for all four states (arrows link the Fourier spectrum to the energy level). The localisation of a state in a given valley together with the spin quantum number produce the spin arrangement of states pictured in Fig. 6.15 (middle).

The relative arrangement of spin states between the $\boldsymbol{K}$-derived and $\boldsymbol{Q}$-derived ladder depends on the bulk properties of the material. As shown in Fig. 6.16 (right), MoS_2 exhibits the same spin bands at the bottom of the CB at $\boldsymbol{K}$ and $\boldsymbol{Q}$, which is reflected in the QD energy structure in Fig. 6.16 (left). For a similar TMDC QD, consisting of a different metal, e.g. for WS_2, the spin of the bottom of the CB at $\boldsymbol{K}$ and $\boldsymbol{Q}$ are opposite, which would reverse the spin states in one ladder of QD states. This fact can be used to engineer the desired energy structure for custom spintronic devices.

I now discuss the relevant energy scales ω and Δ_{SO} (marked again in Fig. 6.17 right) as a function of R_{QD}. Fig. 6.17 (left) shows ω decreasing as $\sim 1/r_{QD}$, while the middle panel plots Δ_{SO} increasing as $\sim -1/R_{QD}$. Grey horizontal line in Fig. 6.16 (middle) marks the limiting value of SO splitting for bulk.

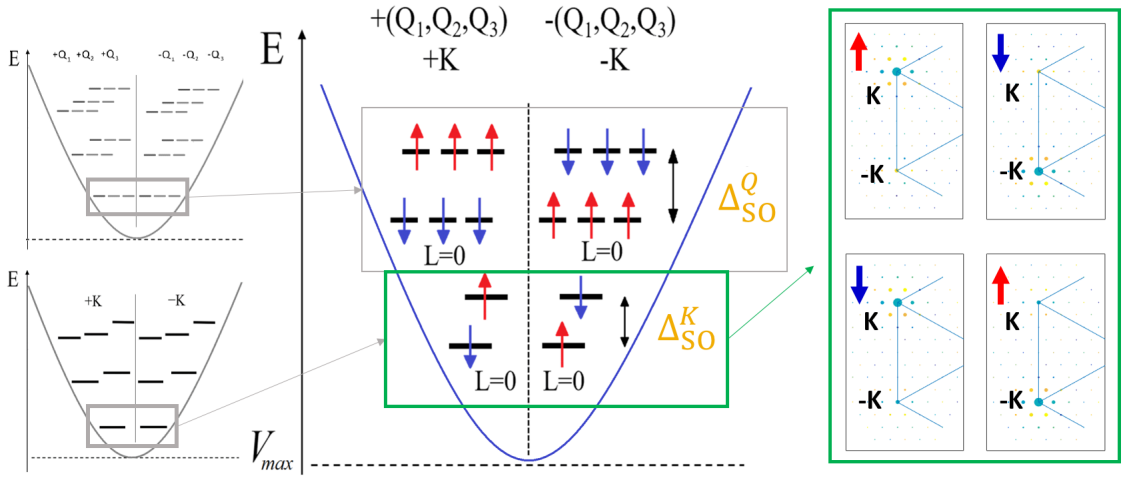

Figure 6.15: The effect of Δ_{SO} on SP energy levels of an MoS_2 QD. The SO splitting of lowest shell (left) is shown in the middle (not to scale). Spin up and down are denoted with red and blue arrows respectively. Δ_{SO}^{K} and Δ_{SO}^{Q} are opposite in opposite valleys. and the same within a valley. (right) Fourier distribution of the $\boldsymbol{K}$-derived $L = 0$ shell (marked with green box). Each level is clearly linked to valley and spin, which allows for distinction.

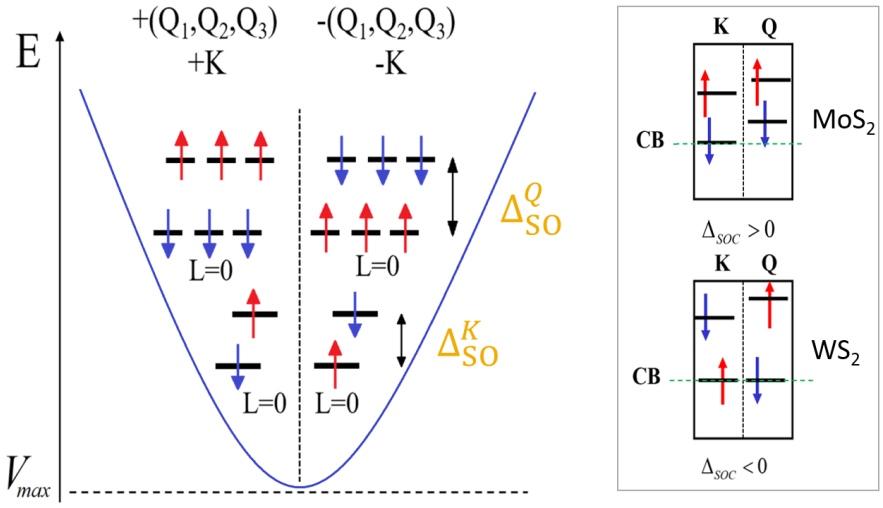

Figure 6.16: Demonstration of possible spin arrangement in different TMDC materials. (left) Spin levels for an MoS_2 QD. (right) Two possible spin band arrangements for bulk MoS_2 and WS_2 at $\boldsymbol{K}$ and at $\boldsymbol{Q}$. Spins are aligned (anti-aligned) for MoS_2 (WS_2).

The values spanned by ω and Δ_{SO} shown in Fig. 6.17 create a possibility for the forming of two regimes: $\omega > \Delta_{SO}$ and $\omega < \Delta_{SO}$, as pictured schematically in Fig. 6.18. Red and blue colors denote energy levels of opposite spin. In situation a),

$\omega > \Delta_{SO}$, the levels are grouped within a shell, and filling of the first shell requires 4 electrons (in a non-interacting picture). In case b), $\omega < \Delta_{SO}$, the levels of the same spin group together within a valley, with opposite spins at lower energy in opposite valleys, and the filling of the lowest energy incomplete shell requires just 2 electrons.

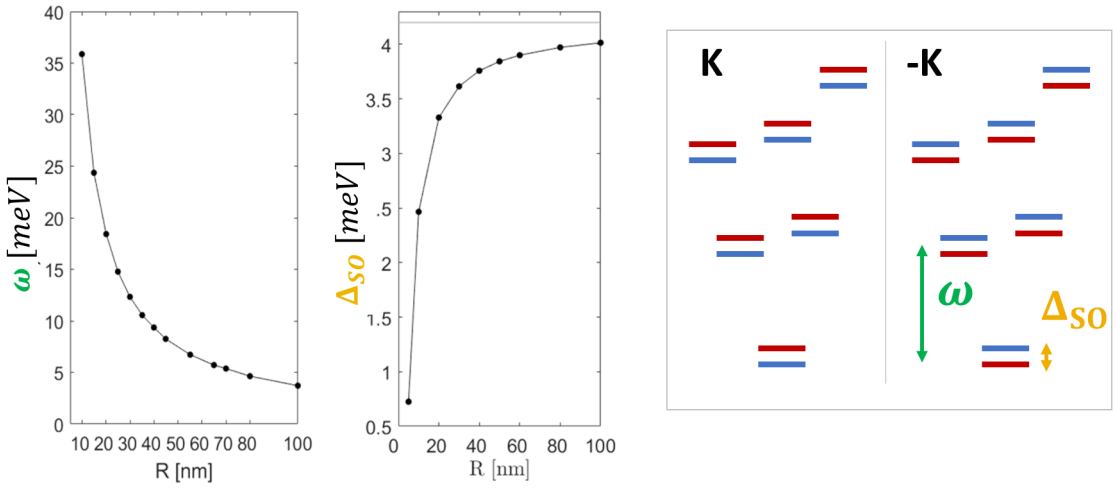

Figure 6.17: (left) Δ_{SO} grows and ω decreases as a function of R_{QD}. (right) Δ_{SO} and ω identified within a QD energy structure for $\Delta_{SO} < \omega$ (spins showed in red and blue).

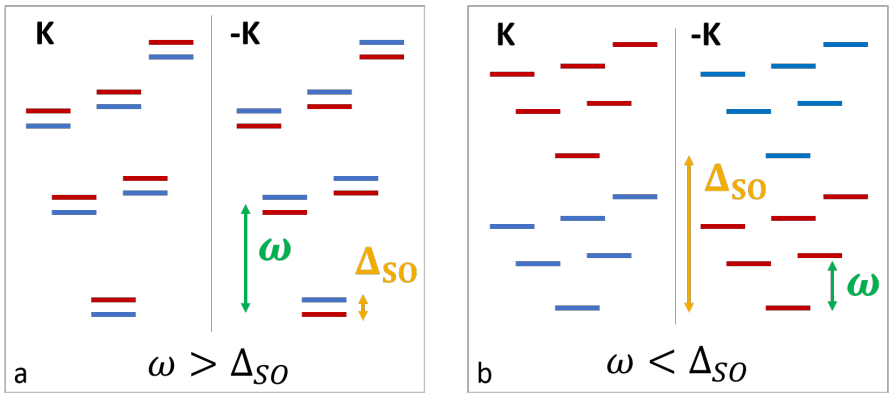

Figure 6.18: Order of energy levels for $\Delta_{SO} < \omega$ (left) and $\Delta_{SO} > \omega$ (right).

In fact, Fig. 6.18 b) shows $\omega < \Delta_{SO}/3$, but for slightly higher ω within the same regime a peculiar energy structure is possible, where shells intertwine. By varying ω and Δ_{SO} different scenarios can be realised, when lower incomplete shells "pass" above the higher shells. Such "passings" happen at $\omega < \Delta_{SO}$, $\omega < \Delta_{SO}/2$, $\omega < \Delta_{SO}/3$, etc.

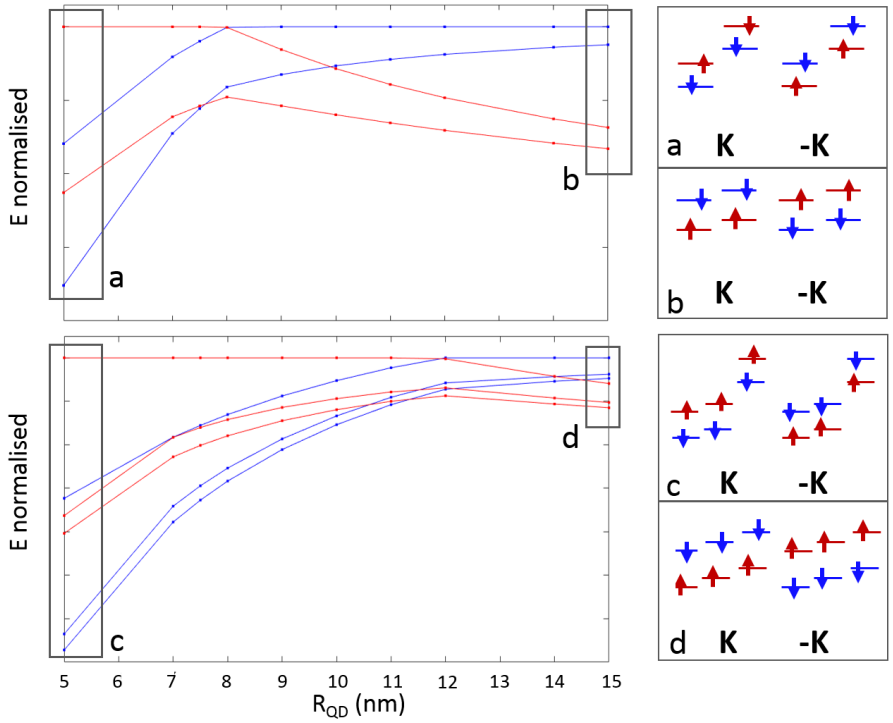

Figure 6.19: Energy level ordering (normalised) for spin states within (top) $I = 1$ and (bottom) $I = 2$ shell for varying R_{QD}. Black boxes a-d gather levels that are schematically pictured in a-d panels. Colors denote spins. The variable ordering is a result of the interplay of Δ_{SO} and δ, and it reaches a "final" arrangement for large R_{QD} (b,d).

The value of Δ_{SO} affects also higher shells, which are split by larger δ (as shown in Fig. 6.14). Because of the interplay of δ and Δ_{SO} for different dot sizes, the order of levels within a shell changes as R_{QD} increases. This process is described by Fig. 6.19 for $I = 1, 2$ $\boldsymbol{K}$-derived shells (shown in top and bottom). Left panels of Fig. 6.19 show normalised energy of levels within a shell, and colors depict spin states. Initial and starting level arrangement have been labelled with a and b (c and d) for $I = 1$ ($I = 2$) shell. These arrangements have been schematically shown in the right panels a-d to illustrate the transition. For larger dots (small ω) $\delta \ll \Delta_{SO}$ which results in a spin arrangement similar to that in Fig. 6.15 shown for the first $I = 0$ shell. Such process is true for all shells, but the transition to the final arrangement (as in b and d in Fig. 6.19) happens at larger R_{QD} for higher shells (e.g. at ≈ 10 nm for $I = 1$ and at ≈ 15 nm for $I = 2$).

6.3 Scattering Coulomb matrix elements.

In order to study the many-electron properties of MoS_2 QDs I first have to obtain the Coulomb scattering matrix elements between electrons in SP QD states. By diagonalising the Hamiltonian in Eq. 6.14, I obtain the eigenvectors for these states in the atomic site basis or in the Bloch state basis. The Bloch state representation allows me to categorise the SP QD states as belonging to specific valleys, while the atomistic basis enables me to explicitly calculate the value of the Coulomb integrals.

The Coulomb matrix elements in the SP QD basis read

$$\langle pq|\, V\, |st\rangle = \iint d\boldsymbol{r} d\boldsymbol{r}' \psi_p^*(\boldsymbol{r})\psi_q^*(\boldsymbol{r}')V(\boldsymbol{r},\boldsymbol{r}')\psi_s(\boldsymbol{r}')\psi_t(\boldsymbol{r}), \tag{6.15}$$

where each QD TB eigenvector for state $p = (\pm\boldsymbol{K}, n, m, \sigma)$ (σ labels spin) is given in the atomic basis as

$$\psi_p(\boldsymbol{r}) = \sum_i \sum_{\nu=A,B} \sum_{\alpha_\nu=\left\{\substack{m_d=0,\pm2\\ m_p=0,\pm1}\right\}} A^p_{i,\nu,\alpha_\nu}\phi_{i,\nu,\alpha_\nu}(\boldsymbol{r}), \tag{6.16}$$

where the amplitudes A^p_{i,ν,α_ν} are obtained by diagonalising the TB Hamiltonian in Eq. 6.14. In Eq. 6.16 all indices have the same meaning as in Eq. 6.1 and ν labels sublattices. The functions $\phi_{i,\nu,\alpha_\nu}(\boldsymbol{r}) = \phi_{\alpha_\nu}(\boldsymbol{r} - \boldsymbol{R}_{i,\nu})$ in Eq. 6.16 are atomic orbital functions on site $\boldsymbol{R}_{i,\nu}$.

Examples of distribution of $\left|A^p_{i,\nu,\alpha_\nu}\right|$ for $p = \left\{(0,0,\downarrow),(0,1,\downarrow),(1,0,\downarrow)\right\}$ (all at $\boldsymbol{K}$) have been shown in Fig. 6.20 for $R_{QD} = 10$ nm and a 160×220 box. The plots show only fragments of the box, red circle marks the QD boundary and bright colors denote higher amplitude. The $(0,0)$ state has a clear s-type nature, while the $(0,1),(1,0)$ states resemble p-type orbitals, as expected for a HO ladder of states. There is no visible difference in $\left|A^p_{i,\nu,\alpha_\nu}\right|$ between the valleys $\pm\boldsymbol{K}$. However, there is a slight difference in $\left|A^p_{i,\nu,\alpha_\nu}\right|$ for both p-type states in the very centre of the dot, which will affect the strength of interaction of electrons in these states, due to the different wavefunction overlap.

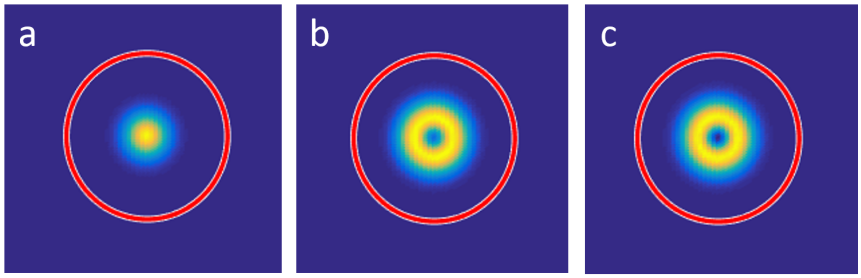

Figure 6.20: Absolute value of the wavefunction for SP QD states for $R_{QD} = 10$ nm for a) $(0, 0, \downarrow)$ s-type level, b) $(0, 1, \downarrow)$ p-type and c) $(1, 0, \downarrow)$ p-type levels. Red cirlce marks the boundary of the dot (only fragments of the computation box are showed). There is a slight difference between the amplitude of b) and c) in the centre.

Fig. 6.21 shows the phase $\theta^p_{i,\nu,\alpha_\nu}$ of $A^p_{i,\nu,\alpha_\nu} = \left|A^p_{i,\nu,\alpha_\nu}\right| e^{i\theta^p_{i,\nu,\alpha_\nu}}$ for the same QD $R_{QD} = 10$ nm and for the four lowest energy states for both valleys, i.e. $(0, 0, \downarrow), (0, 0, \uparrow), (0, 1, \downarrow), (1, 0, \downarrow)$ (and opposite spin for valley $-\boldsymbol{K}$). Fig. 6.21 a-d (e-h) show the phase for valley $\boldsymbol{K}$ ($-\boldsymbol{K}$). Red circle marks the boundary of a QD, and the values of the phase outside of this boundary constitute a numerical error, as the problem is diagonalised for the entire computational box (only fragments of the box are shown here). The values of the phase remain uniform for the s-type states in a,b,e,f, but exhibit a cyclic behaviour for other plots, which corresponds to p-type states. The phase winds 3 times for a 2π rotation around the QD (the pattern follows for higher shells, which wind 6 times, etc.), which appears to mimic the crystal symmetry. There is a difference in phase distribution in the s-type states for opposite valleys, as well as the phase cycles oppositely in opposite valleys for the p-type states, i.e. the phase grows clockwise in Fig. 6.21 c and h, and increases counterclockwise in Fig. 6.21 d and g. This enables classification of states according to L, as shown in Fig. 6.12. Additionally, all plots in Fig. 6.21 exhibit rapid phase oscillations on the scale of a unit cell, which is manifested in striped features in all plots.

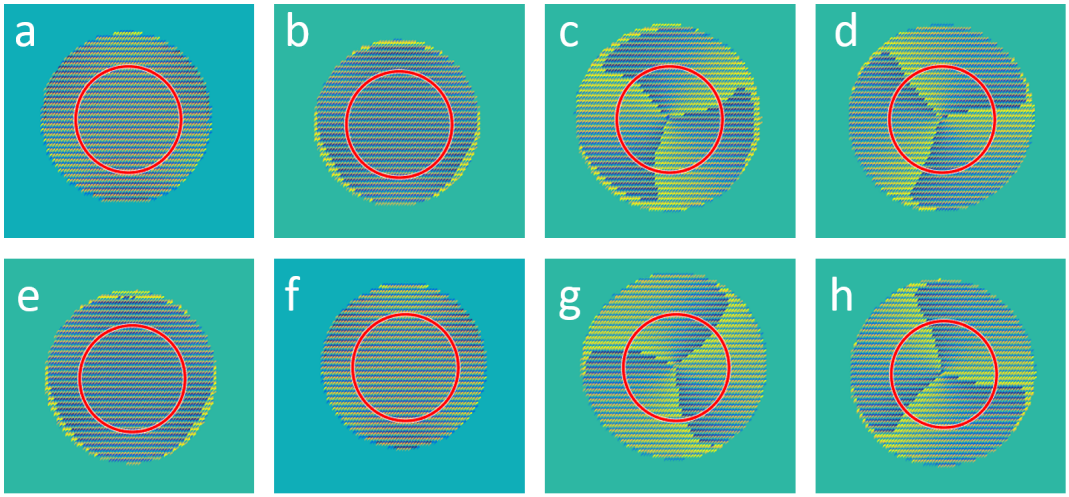

Figure 6.21: Phase of the wavefunction (shown with colors) for SP QD states for $R_{QD} = 10$ nm for a) $(0, 0, \downarrow)$ s-type, b) $(0, 0, \uparrow)$ s-type levels, c) $(0, 1, \downarrow)$ p-type and d) $(1, 0, \downarrow)$ p-type levels for $\boldsymbol{K}$ (and e-h for $-\boldsymbol{K}$ with opposite spins). Red circle marks the boundary of the dot (only fragments of the computation box are showed). Values of the phase outside of the dot constitute numerical error. a,b,e,f show no angular phase modulation on the scale of the dot and c,h (d,g) show clockwise (anticlockwise) angular phase modulation. The opposite direction of rotation enables classification of states with opposite L. Threefold winding is attributed to the symmetry of the crystal. Stripped pattern in all subplots originates in rapid oscillations in periodic part of the wavefunction $u(\boldsymbol{r})$ (see discussion in section 6.3.3).

I now return to the Coulomb integral definition. Using Eq. 6.16, Eq. 6.15 becomes

$$\begin{aligned}\langle pq|\, V\, |st\rangle = &\sum_{\substack{ijkl\\ \mu\nu\xi\varrho}} \sum_{\alpha,\beta\gamma\delta=\substack{\{m_d=0,\pm2\}\\ \{m_p=0,\pm1\}}} A^{p^*}_{i,\mu,\alpha_\mu} A^{q^*}_{j,\nu,\beta_\nu} A^{s}_{k,\xi,\gamma_\xi} A^{t}_{l,\varrho,\delta_\varrho} \cdot \\ &\cdot \iint d\boldsymbol{r} d\boldsymbol{r}'\, \phi^*_{i,\mu,\alpha_\mu}(\boldsymbol{r}) \phi^*_{j,\nu,\beta_\nu}(\boldsymbol{r}') V(\boldsymbol{r},\boldsymbol{r}') \phi_{k,\xi,\gamma_\xi}(\boldsymbol{r}') \phi_{l,\varrho,\delta_\varrho}(\boldsymbol{r}) \\ = &\sum_{\substack{ijkl\\ \mu\nu\xi\varrho}} \sum_{\alpha,\beta\gamma\delta=\substack{\{m_d=0,\pm2\}\\ \{m_p=0,\pm1\}}} A^{p^*}_{i,\mu,\alpha_\mu} A^{q^*}_{j,\nu,\beta_\nu} A^{s}_{k,\xi,\gamma_\xi} A^{t}_{l,\varrho,\delta_\varrho} \langle i\mu\alpha_\mu; j\nu\beta_\nu|\, V\, |k\xi\gamma_\xi; l\varrho\delta_\varrho\rangle\,, \quad (6.17)\end{aligned}$$

where $ijkl$ run over unit cells, $\mu\nu\xi\varrho$ denote sublattices and $\alpha\beta\gamma\delta$ stand for orbitals.

$V(\boldsymbol{r},\boldsymbol{r}')$ in Eq. 6.15 is the Coulomb interaction $V(\boldsymbol{r},\boldsymbol{r}') = \frac{e^2}{4\pi\epsilon_r\epsilon_0|\boldsymbol{r}-\boldsymbol{r}'|}$ with static screening ϵ_r or with Keldysh screening, which are compared in section 6.3.1. The integrals $\langle i\mu\alpha_\mu; j\nu\beta_\nu|\, V\, |k\xi\gamma_\xi; l\varrho\delta_\varrho\rangle$ in Eq. 6.17 have been given in section 6.3.2. The resulting Coulomb matrix elements $\langle pq|\, V\, |st\rangle$ for SP QD states have been discussed in section 6.3.3.

6.3.1 Static screening vs Keldysh screening.

To describe the electron-electron interaction potential I start with the Coulomb potential screened everywhere by a dielectric constant ϵ_r, which reads

$$V_C^{3D}(\boldsymbol{r}-\boldsymbol{r}') = \frac{1}{\epsilon_r}\frac{e^2}{4\pi\epsilon_0}\frac{1}{\sqrt{(\boldsymbol{\rho}-\boldsymbol{\rho}')^2+(z-z')^2}}, \tag{6.18}$$

where I separated a 3D vector $\boldsymbol{r}$ into the radial and z component as $\boldsymbol{r} = (\boldsymbol{\rho}, z)$. Eq. 6.18 can be written in terms of a 2D Fourier transform as [166]

$$V_C^{3D}(\boldsymbol{r}-\boldsymbol{r}') = \frac{1}{\epsilon_r}\frac{e^2}{4\pi\epsilon_0}\frac{1}{(2\pi)^2}\int_{-\infty}^{\infty}\frac{2\pi}{|\boldsymbol{k}|}\cdot e^{-|z-z'||\boldsymbol{k}|}e^{i\boldsymbol{k}(\boldsymbol{\rho}-\boldsymbol{\rho}')}d^2\boldsymbol{k}. \tag{6.19}$$

To study 2D another model of screening is relevant, Keldysh screening. It accounts for the effect of the reduced dimension on interactions. To obtain the Keldysh screening form [167, 168], Eq. 6.18 needs to be modified by the 2D polarisability α, which defines the screening length $r_0 = 2\pi\alpha$ [162, 166]. Eq. 6.18 becomes

$$V_K^{3D}(\boldsymbol{r}-\boldsymbol{r}') = \frac{1}{\epsilon^*}\frac{e^2}{4\pi\epsilon_0}\frac{1}{(2\pi)^2}\int_{-\infty}^{\infty}\frac{2\pi}{|\boldsymbol{k}|}\cdot\frac{1}{1+2\pi\alpha\,|\boldsymbol{k}|}e^{-|z-z'||\boldsymbol{k}|}e^{i\boldsymbol{k}(\boldsymbol{\rho}-\boldsymbol{\rho}')}d^2\boldsymbol{k}, \tag{6.20}$$

where $\alpha = 2.2\mathring{A}$ and I used ϵ^* instead of ϵ_r to include the screening by the materials surrounding the MoS_2 plane. I use $\epsilon^* = \frac{\epsilon_1+\epsilon_3}{2}$, where $\epsilon_1 = 1.0$ and $\epsilon_3 = 4.0$ are the dielectric constants of the material layers below and above MoS_2, taken here as SiO_2 and vacuum respectively [162]. In section 6.3.3 I compare results obtained with $\epsilon_r = \epsilon^* = 2.5$.

For two electrons in the MoS_2 plane Eq. 6.20 can be written in real space, when $z = z'$. It reads [166]

$$\begin{aligned} V_{K0}^{3D}(\boldsymbol{\rho}-\boldsymbol{\rho}', z=z') &= \frac{1}{\epsilon^*}\frac{e^2}{4\pi\epsilon_0}\frac{1}{(2\pi)^2}\int_{-\infty}^{\infty}\frac{2\pi}{|\boldsymbol{k}|}\cdot\frac{1}{1+2\pi\alpha\,|\boldsymbol{k}|}e^{i\boldsymbol{k}(\boldsymbol{\rho}-\boldsymbol{\rho}')}d^2\boldsymbol{k} \\ &= \frac{1}{4\epsilon^*\alpha}\frac{e^2}{4\pi\epsilon_0}\left(H_0\big(\frac{|\boldsymbol{\rho}-\boldsymbol{\rho}'|}{2\pi\alpha}\big) - Y_0\big(\frac{|\boldsymbol{\rho}-\boldsymbol{\rho}'|}{2\pi\alpha}\big)\right), \end{aligned} \tag{6.21}$$

where H_0, Y_0 are Struve and Bessel functions respectively [166].

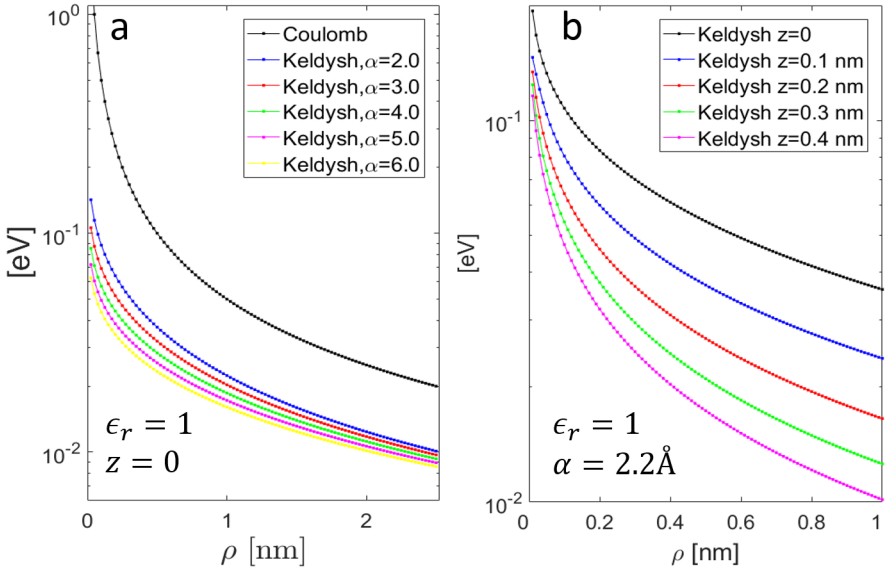

Figure 6.22: a) Coulomb potential with static screening (black) vs. Keldysh screening (couloured) for $z = 0$ and $\epsilon_r = 1$ and varied α (Eq. 6.18 and Eq. 6.21). b) Keldysh screening for varied z and $\alpha = 2.2\mathring{A}$.

Fig. 6.22 (left) shows the Coulomb potential function with Keldysh screening in Eq. 6.21 compared to static screening from Eq. 6.18 for varying α and $\epsilon_r = \epsilon^* = 1$. As expected, Keldysh screening lowers the value of the potential very strongly at small ρ and less drastically for large ρ. Larger α produces stronger screening. Fig. 6.22 (right) shows the comparison of approximate expression in Eq. 6.21 and the full Keldysh potential in Eq. 6.20 for increasing z, which creates larger discrepancy.

6.3.2 Long and short-range contributions to Coulomb integrals.

Here I describe the contribution of $\langle i\mu\alpha_\mu; j\nu\beta_\nu | V | k\xi\gamma_\xi; l\varrho\delta_\varrho \rangle$ to Eq. 6.17.

I find that the main contribution to the value of $\langle pq | V | st \rangle$ comes from the long range part, which involves sites far away from each other. This part has been treated classically as $\langle i\mu\alpha_\mu; j\nu\beta_\nu | V | j\nu\gamma_\nu; i\mu\delta_\mu \rangle = \frac{e^2}{4\pi\epsilon_r\epsilon_0 |\boldsymbol{R}_{i\mu} - \boldsymbol{R}_{j\nu}|}$. Because the Mo and S dimer sites are located at $z = 0$, for Keldysh screening I used Eq. 6.21.

For small $|\boldsymbol{r} - \boldsymbol{r}'|$, I obtain accurate values of integrals $\langle i\mu\alpha_\mu; j\nu\beta_\nu | V | k\xi\gamma_\xi; l\varrho\delta_\varrho \rangle$, using the Vegas algorithm within the GSL library, as described in section 2.3.3. Onsite

as well as the biggest NN and NNN integrals have been listed in Table 6.1. Numbers in Table 6.1 correspond to the atoms labels in Fig. 6.23 as well as orbitals, i.e. $d0$ is $m_d = 0$ etc. Columns V_C, V_{K0}, V_K correspond to Eq. 6.18,6.21 and 6.20.

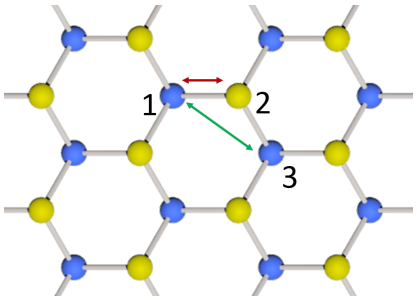

Figure 6.23: MoS_2 atomic sites included in the evaluation of Coulomb integrals. Numbers label atoms identified in integrals in Table 6.1. Red (green) arrows mark NN (NNN) integrals (rows 7,8 in the Table).

Integral $\langle i\alpha; j\beta \vert V \vert k\gamma; l\delta\rangle$	static V_C [eV]	Keldysh $z=0$ V_{K0} [eV]	Keldysh V_K [eV]
$\langle 1,d0;1,d0 \vert V \vert 1,d0;1,d0\rangle$	7.32	2.16	1.05
$\langle 1,d2;1,d2 \vert V \vert 1,d2;1,d2\rangle$	7.11	1.90	1.10
$\langle 1,d0;1,d2 \vert V \vert 1,d2;1,d0\rangle$	6.55	1.98	1.05
$\langle 2,p0;2,p0 \vert V \vert 2,p0;2,p0\rangle$	4.54	2.36	0.92
$\langle 2,p1;2,p1 \vert V \vert 2,p1;2,p1\rangle$	3.60	1.79	0.80
$\langle 2,p1;2,p0 \vert V \vert 2,p0;2,p1\rangle$	3.74	2.01	0.85
$\langle 1,d0;2,p0 \vert V \vert 2,p0;1,d0\rangle$	2.67	1.47	0.79
$\langle 1,d0;3,d0 \vert V \vert 3,d0;1,d0\rangle$	1.78	1.00	0.69

Table 6.1: Selected coulomb integrals in atomistic basis. Columns V_C, V_{K0}, V_K correspond to Eq. 6.18,6.21 and 6.20 and numbers in column "Integral" have been marked in Fig. 6.23.

The onsite terms alone account for only $\approx 1\%$ of the value of $\langle pq \vert V \vert st\rangle$. I have checked that including all the NN and NNN integrals possible (not all are listed here) does not change the value of $\langle pq \vert V \vert st\rangle$ by more than 0.5% or the values of energy differences between the CI eigenvalues by more than 3%. This is true both for static and Keldysh screening. Therefore, I neglect all these NN and NNN terms.

6.3.3 Intervalley vs intravalley exchange interaction.

I discuss here the scattering Coulomb matrix elements $\langle pq \vert V \vert st\rangle$ between QD $\boldsymbol{K}$-derived electron states, as defined in Eq. 6.17. Fig. 6.24 shows the values of chosen

matrix elements, which read

$$\begin{aligned} V_1 &= \langle \boldsymbol{K},0,0,\downarrow;-\boldsymbol{K},0,0,\uparrow|V|-\boldsymbol{K},0,0,\uparrow;\boldsymbol{K},0,0,\downarrow\rangle \\ V_2 &= \langle \boldsymbol{K},0,0,\downarrow;\boldsymbol{K},0,0,\uparrow|V|\boldsymbol{K},0,0,\uparrow;\boldsymbol{K},0,0,\downarrow\rangle \\ &= \langle \boldsymbol{K},0,0,\downarrow;-\boldsymbol{K},0,0,\downarrow|V|-\boldsymbol{K},0,0,\downarrow;\boldsymbol{K},0,0,\downarrow\rangle \\ V_3 &= \langle \boldsymbol{K},0,0,\uparrow;-\boldsymbol{K},0,0,\downarrow|V|-\boldsymbol{K},0,0,\downarrow;\boldsymbol{K},0,0,\uparrow\rangle \\ V_4 &= \langle \boldsymbol{K},0,0,\downarrow;\boldsymbol{K},0,1,\downarrow|V|\boldsymbol{K},0,1,\downarrow;\boldsymbol{K},0,0,\downarrow\rangle \end{aligned} \tag{6.22}$$

and

$$\begin{aligned} V_5 &= \langle \boldsymbol{K},0,0,\downarrow;\boldsymbol{K},0,1,\downarrow|V|\boldsymbol{K},0,0,\downarrow;\boldsymbol{K},0,1,\downarrow\rangle \\ V_6 &= \langle \boldsymbol{K},0,0,\downarrow;-\boldsymbol{K},0,0,\downarrow|V|\boldsymbol{K},0,0,\downarrow;-\boldsymbol{K},0,0,\downarrow\rangle\,, \end{aligned} \tag{6.23}$$

where Eq. 6.22 list direct matrix elements V_d and Eq. 6.23 lists exchange matrix elements V_x.

Fig. 6.24 shows the ω dependence of all elements given in Eq. 6.22 and Eq. 6.23 with static ("st") and Keldysh ("K") screening shown with a solid and dashed line respectively. All V_d with static screening follow the $\sim\sqrt{\omega}$ dependence, as for a standard QD [73]. As does the intravalley exchange element V_5 with static screening, as expected in an standard HO [73]. The intervalley exchange V_6, however, is an order magnitude smaller that V_5 and departs from the square root behaviour. All Keldysh elements exhibit some deviation from $\sim\sqrt{\omega}$ dependence. In particular, the intervalley exchange element V_6 with Keldysh screening stands out, as two orders of magnitude smaller than its intravalley analogue, and significantly deviating from $\sqrt{\omega}$.

These large differences between the matrix elements within and between the opposite valleys are crucial for observing the broken symmetry many-electron states discussed in section 6.4.4 [164].

In order to better understand the role of valleys in the observed Coulomb matrix elements, I will consider the SP QD states within the envelope function approximation. The SP QD wavefunction can be regarded as a product of a periodic part of a

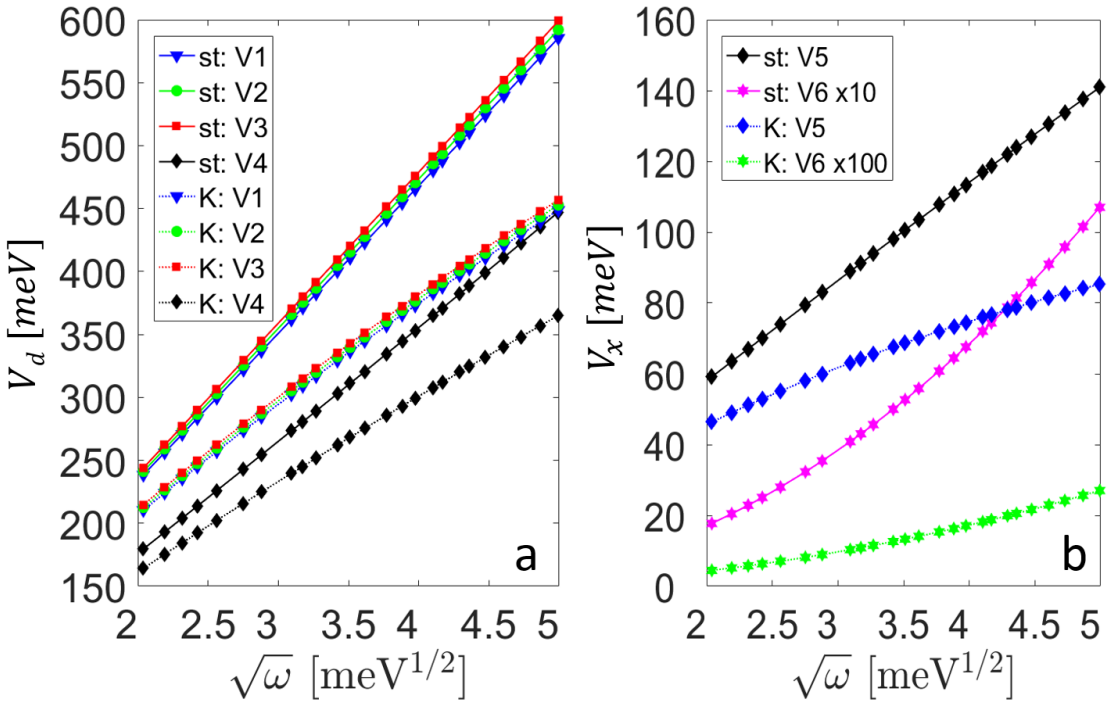

Figure 6.24: Direct and exchange Coulomb integrals for QD states given by Eq. 6.22 (left) and 6.23 (right) with static ("st") and Keldysh ("K") screening. Statically screened elements V_d and V_5 follow $\sim \sqrt{\omega}$. Others depart from this behaviour. Intervalley V_x are one (two) orders magnitude smaller than the intravalley V_x for static (Keldysh) screening (V_5 is intravalley, V_6 is intervalley).

Bloch function $u_{\boldsymbol{k}}(\boldsymbol{r})$ (manifesting itself in the fast phase oscillations on the scale of a unit cell in Fig. 6.21) and an envelope, resembling the atomic orbitals, as in Fig. 6.20. If I include the strong association with a particular valley $\pm\boldsymbol{K}$, the wavefunction reads

$$\psi_p(\boldsymbol{r}) = \psi_{\pm\boldsymbol{K},n,m,\sigma}(\boldsymbol{r}) \approx w_{\pm\boldsymbol{K},n,m,\sigma}(\boldsymbol{\rho}) u_{\pm\boldsymbol{K}}(\boldsymbol{r})\chi(\sigma) = w_p(\boldsymbol{\rho}) u_{\pm\boldsymbol{K}}(\boldsymbol{r})\chi(\sigma), \qquad (6.24)$$

where $w_{\pm\boldsymbol{K}n,m,\sigma}(\boldsymbol{\rho})$ is a 2D HO envelope and χ is the spin part of the wavefunction.

I can now express the integral in Eq. 6.15 as

$$\begin{aligned}\langle pq|\, V\, |st\rangle &= \iint d\boldsymbol{r}d\boldsymbol{r}'\psi_p^*(\boldsymbol{r})\psi_q^*(\boldsymbol{r}')V(\boldsymbol{r},\boldsymbol{r}')\psi_s(\boldsymbol{r}')\psi_t(\boldsymbol{r}) \\ &= \langle\chi_p|\chi_t\rangle\langle\chi_q|\chi_s\rangle \iint d\boldsymbol{r}d\boldsymbol{r}'w_p(\boldsymbol{\rho})u_{\boldsymbol{K}_p}(\boldsymbol{r})w_q(\boldsymbol{\rho}')u_{\boldsymbol{K}_q}(\boldsymbol{r}')\cdot \\ &\qquad \cdot V(\boldsymbol{r}-\boldsymbol{r}')w_s(\boldsymbol{\rho}')u_{\boldsymbol{K}_s}(\boldsymbol{r}')w_t(\boldsymbol{\rho})u_{\boldsymbol{K}_t}(\boldsymbol{r}). \quad (6.25)\end{aligned}$$

I now separate the two length scales, analogously to section 5.2.1: within and outside of a unit cell. This allows me to replace an integral $\int d\boldsymbol{r}$ in Eq. 6.25 by a summation over unit cells and an integral over a single unit cell $\sum_{\boldsymbol{R}}\int_{UC} d\widetilde{\boldsymbol{r}}$ ($\boldsymbol{R}$ labels unit cells). Fig. 6.20 shows that the envelope functions w change slowly on the scale of a single unit cell. Assuming that the Coulomb potential behaves similarly, I can integrate out the unit cell space and finally replace $\sum_{\boldsymbol{R}} \approx \Omega \int d\boldsymbol{R}$, which gives

$$\begin{aligned}\langle pq|\, V\, |st\rangle &= \langle\chi_p|\chi_t\rangle\langle\chi_q|\chi_s\rangle\langle u_{\boldsymbol{K}_p}|u_{\boldsymbol{K}_t}\rangle\langle u_{\boldsymbol{K}_q}|u_{\boldsymbol{K}_s}\rangle\cdot \\ &\qquad \cdot \Omega^2 \iint d\boldsymbol{R}d\boldsymbol{R}'w_p(\boldsymbol{P})w_q(\boldsymbol{P}')V(\boldsymbol{R}-\boldsymbol{R}')w_s(\boldsymbol{P}')w_t(\boldsymbol{P}), \quad (6.26)\end{aligned}$$

where $\boldsymbol{R} = (\boldsymbol{P}, Z)$ and $\langle u_{\boldsymbol{K}_p}|u_{\boldsymbol{K}_t}\rangle = \int_{UC} d\widetilde{\boldsymbol{r}}u^*_{\boldsymbol{K}_p}(\widetilde{\boldsymbol{r}})u_{\boldsymbol{K}_t}(\widetilde{\boldsymbol{r}})$. Eq. 6.26 clearly shows that the valley index plays a similar role for the Coulomb integral as spin, which is reflected in the term *valley pseudospin*. The magnitude of the element in Eq. 6.26 depends on the envelope functions, but the whole integral can vanish if $\boldsymbol{K}_p \neq \boldsymbol{K}_t$ or $\boldsymbol{K}_q \neq \boldsymbol{K}_s$. This means that the exchange elements are non-zero only for the same valley (parallel valley pseudospin), i.e. only in the intravalley case.

However, unlike for spin, the vanishing of $\langle pq|\, V\, |st\rangle$ holds only approximately for valley pseudospin, because $\boldsymbol{K}$ is not a good quantum number (states are localised around $\pm\boldsymbol{K}$, but not at $\boldsymbol{K}$ exactly, and other $\boldsymbol{k}$-points participate). This approximate vanishing of the intervalley pseudospin exchange elements explains the small numerical values presented in Fig. 6.24.

6.4 Many electron properties.

This section presents the results of CI calculations for MoS_2 QD for up to $N = 6$ electrons and up to $M = 60$ states included in a CI calculation. I first present a thorough analysis of the $N = 2$ electron behaviour for increasing number of shells populated by electrons, which has been described in sections 6.4.1, 6.4.2 and 6.4.3. Section 6.4.4 discusses the broken symmetry many-electron states for $N \geq 2$.

6.4.1 Two electrons on the first harmonic oscillator shell.

I start with $N = 2$ interacting electrons in the first $(0, 0)$ shell with $\Delta_{SO} = 0$. The solutions of this problem for a standard parabolic QD can be obtained exactly for a given confinement [73]. It yields a spin singlet GS, because there is only one possible level $(0, 0)$ in a standard QD, and due to Pauli exclusion principle the spins of electrons antialign. In an MoS_2 QD however, there are two spin-degenerate $(0, 0)$ levels due to the double valley degeneracy. Therefore, the $N = 2$ properties can be understood in terms of spin singlet and triplets, similarly to the physics of half-filled p-type shell of a self-assembled QD [73]. The GS is a three-fold degenerate spin triplet

$$\begin{aligned} \left|T^s_+\right\rangle &= |\uparrow\rangle\,|\uparrow\rangle\,, \\ |T^s_0\rangle &= \frac{1}{\sqrt{2}}\left(|\uparrow\rangle\,|\downarrow\rangle + |\downarrow\rangle\,|\uparrow\rangle\right), \\ \left|T^s_-\right\rangle &= |\downarrow\rangle\,|\downarrow\rangle\,, \end{aligned} \tag{6.27}$$

which has been shown in Fig. 6.25 in the bottom panel for $\omega = 36$ meV. The three-fold degenerate GS energy has been marked with a red dot in Fig. 6.25 (left). Because the two levels are also labelled by the valley pseudospin, the spin triplet in Eq. 6.27 is at the same time a valley singlet

$$|S^v\rangle = \frac{1}{\sqrt{2}}\left(|\boldsymbol{K}\rangle\,|-\boldsymbol{K}\rangle - |-\boldsymbol{K}\rangle\,|\boldsymbol{K}\rangle\right). \tag{6.28}$$

The labels $|S^v\rangle\,|T^s\rangle$ in Eq. 6.27 and Eq. 6.28 have been marked in Fig. 6.25 (left) with a red box.

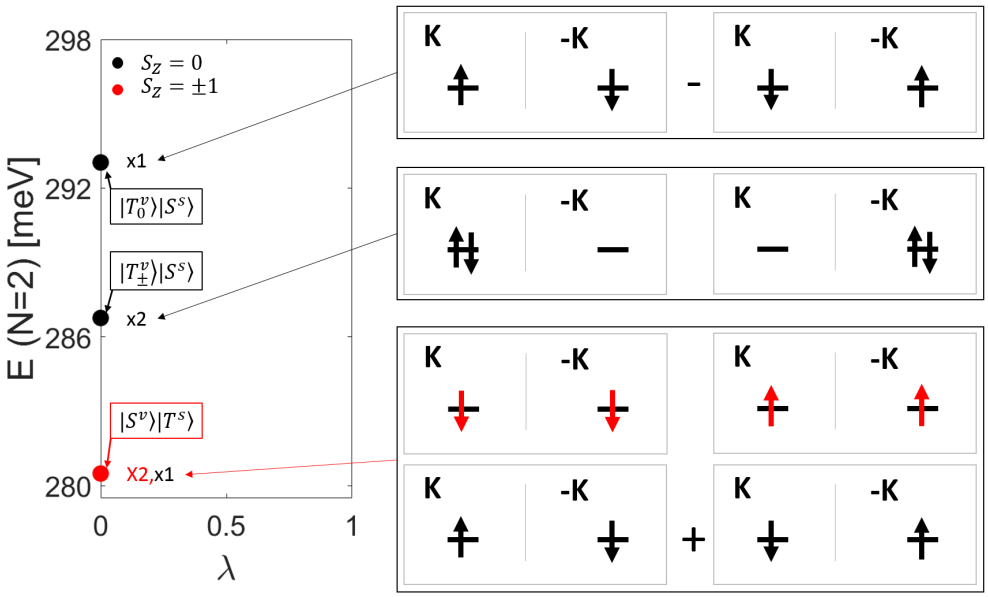

Figure 6.25: (left) Solutions of $N = 2$ interacting electrons in the first $I = 0$ shell of an Mo_2 QD with SO strength $\chi = 0$ ($\Delta_{SO} \to \chi\Delta_{SO}$). The GS is a spin triplet $|T^s\rangle$ and valley singlet $|S^v\rangle$. Excited stated are labelled analogously. (right) Eigenvectors building states in the left. Spins are shown with arrows, colors label S_z eigenstates.

The spin nature of the GS is clear when we consider its energy

$$E_{T^s} = 2e_{00} + V_D^0(\boldsymbol{K}, -\boldsymbol{K}) - V_X^0(\boldsymbol{K}, -\boldsymbol{K}), \tag{6.29}$$

where e_{00} is the SP energy of the (0,0) shell with $\Delta_{SO} = 0$ and $V_D^0(\boldsymbol{K}, -\boldsymbol{K})$ and $V_X^0(\boldsymbol{K}, -\boldsymbol{K})$ are direct and exchange intervalley Coulomb matrix element respectively. It is expected that the triplet has the lower energy due to $-V_X^0$ contribution. The excited state are therefore spin singlets

$$|S^s\rangle = \frac{1}{\sqrt{2}}\left(|\uparrow\rangle\,|\downarrow\rangle - |\downarrow\rangle\,|\uparrow\rangle\right), \tag{6.30}$$

which are also valley triplets at the same time

$$\begin{aligned}\left|T^v_-\right\rangle &= |\boldsymbol{K}\rangle\,|\boldsymbol{K}\rangle\,,\\ |T^v_0\rangle &= \frac{1}{\sqrt{2}}\left(|\boldsymbol{K}\rangle\,|-\boldsymbol{K}\rangle + |-\boldsymbol{K}\rangle\,|\boldsymbol{K}\rangle\right),\\ \left|T^v_+\right\rangle &= |-\boldsymbol{K}\rangle\,|-\boldsymbol{K}\rangle\,,\end{aligned} \tag{6.31}$$

which gives the character of all the excited states for $N = 2$ electrons, as shown in Fig. 6.25 (left) with black boxes. It is now apparent that the V_X^0 contribution that decreased the energy of $|S^v\rangle\,|T^s\rangle$, causes the energy of $|T^v_0\rangle\,|S^s\rangle$ to increase, while the states $\left|T^v_\pm\right\rangle\,|S^s\rangle$ are not affected by the exchange V_X^0.

The energy structure shown in Fig. 6.25 agrees with experimental results obtained by Kurzmann et al. [110] for bilayer graphene QDs, which is also a valley system, but with negligible Δ_{SO}.

6.4.2 Effect of spin orbit coupling.

I now include the spin orbit splitting $\Delta_{SO} \approx 4$ meV for CB of MoS_2, which has been discussed in section 4.3. For other TMDC materials the CB SO splitting can reach up to $\Delta_{SO} \approx 30$ meV, which would emphasise the effects described here even more.

Nonzero Δ_{SO}, which I turn on with a parameter $\chi = 0 \to 1$, causes the spin down (up) state to decrease its energy in valley $\boldsymbol{K}$ ($-\boldsymbol{K}$), as discussed in section 6.2.3. As a consequence, the spin triplets $|T^s\rangle$ and singlets $|S^s\rangle$ mix, which breaks the degeneracy of the $|S^v\rangle\,|T^s\rangle$ GS, as shown in Fig. 6.26 (left) for increasing strength of SO coupling χ. The right top panel of Fig. 6.26 shows the spin degenerate $(0,0)$ shell for $\chi = 0$, and the bottom panel depicts the formation of a spin-valley unpolarised GS at $\chi = 1$, which is a mixutre of $|T^s\rangle$ and $|S^s\rangle$. This mixture can be expressed as

$$|S^{sv}\rangle = \frac{1}{\sqrt{2}}\left(|\boldsymbol{K}\downarrow\rangle\,|-\boldsymbol{K}\uparrow\rangle - |-\boldsymbol{K}\uparrow\rangle\,|\boldsymbol{K}\downarrow\rangle\right), \tag{6.32}$$

which reflects the spin-valley locking, i.e. strong linking of the spin to valley due to large Δ_{SO}.

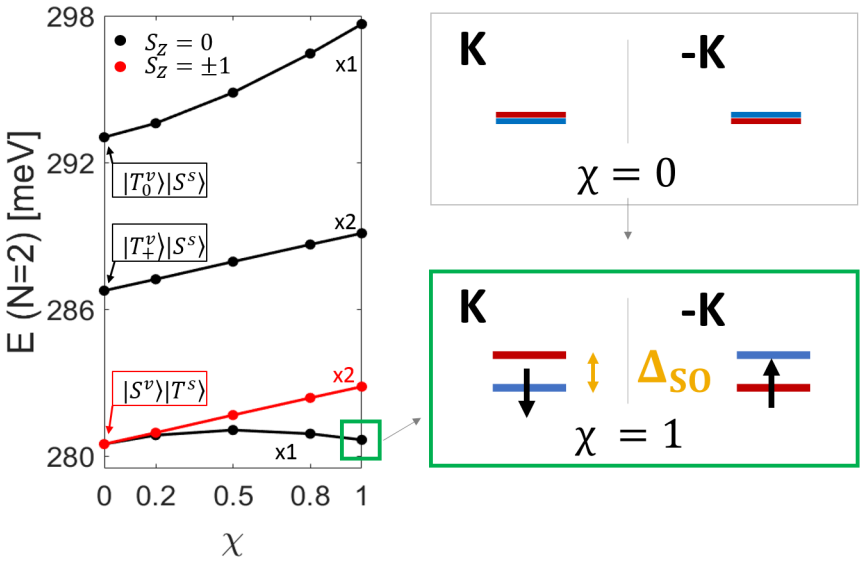

Figure 6.26: (left) Solutions of $N = 2$ interacting electrons in the first $I = 0$ shell of an Mo_2 QD with varied SO strength χ ($\Delta_{SO} \to \chi\Delta_{SO}$). The GS becomes a mix of spin triplet $|T^s\rangle$ and spin singlet $|S^s\rangle$, shown with a green box. (right,top) Energy levels for $\chi = 0$. (right,bottom) GS for $\chi = 1$ is spin and valley unpolarised.

The unpolarised nature of the GS for $\Delta_{SO} \neq 0$ arises because of the competition of Δ_{SO} with $V_X^0(\boldsymbol{K}, -\boldsymbol{K})$. With the weak intervalley exchange (as discussed in section 6.3.3), the SO splitting dominates $\Delta_{SO} \gg V_X^0(\boldsymbol{K}, -\boldsymbol{K})$, and causes the unpolarised configuration shown with a green box in Fig. 6.26 to become the GS [164].

6.4.3 Two electrons on two harmonic oscillator shells.

I now allow the population of higher HO oscillator shells for $N = 2$ electrons. More configurations are now possible, in addition to the ones shown in Fig. 6.25.

Fig. 6.27 shows two of the configurations discussed previously in sections 6.4.1 and 6.4.2, labelled as A and B respectively, as well as two new configurations of $N = 2$ electrons with parallel spins and within the same valley, labelled as C and D. Configuration A involves direct interaction V_D^0 within the $(0, 0)$ shell and the intervalley exchange interaction $V_X^0(\boldsymbol{K}, -\boldsymbol{K})$ and for $\Delta_{SO} = 0$ it was forming the GS of $N = 2$ electrons in one shell only (see section 6.4.3). The energy of configuration B includes the direct interaction V_D^0 only and B is the GS of $N = 2$ in only one shell with the presence of Δ_{SO} (see section 6.4.2).

Configurations C and D involve direct interaction $V_D^{\pm 1}$ and, importantly, the intravalley exchange interaction $V_X^{\pm 1}(\boldsymbol{K}, \boldsymbol{K})$. The right panel of Fig. 6.27 shows the energies of all the configurations A-D as a function of the strength of interactions η, when I switch on the interactions gradually $\eta = 0 \to 1$. A and B, initially the lower energy configurations, move to higher energies as $\eta \approx 0.5$, and the valley and spin-polarised configurations C and D reach the lowest energies.

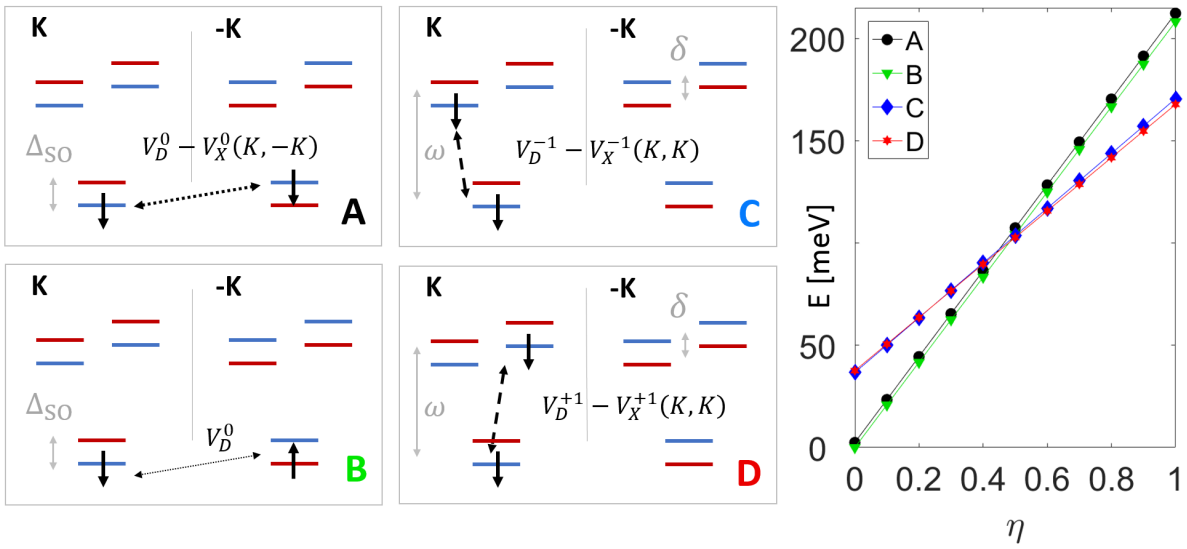

Figure 6.27: (left) Four relevant $N = 2$-electron configurations. A and B (C and D) are valley unpolarised (polarised), B (A,C,D) is spin unpolarised (polarised). $\Delta_{SO}, \omega, \delta$ (V_D, V_X) mark relevant SP (interaction) energies. (right) Energies of configurations A-D for varied strength of interactions η. For non-interacting case $\eta = 0$ B is the GS (valley-spin unpolarised), and for interacting case $\eta = 1$ D is the GS (valley-spin polarised).

I will now analyse all the contributing factors carefully, in order to understand the effect pictured in Fig. 6.27 (right). Let me start with listing all allowed configurations, assuming the fermionic antisymmetric total wavefunction of $N = 2$ electrons:

$$|S^e\rangle\,|T^v\rangle\,|T^s\rangle \tag{6.33a}$$

$$|S^e\rangle\,|S^v\rangle\,|S^s\rangle \tag{6.33b}$$

$$|T^e\rangle\,|S^v\rangle\,|T^s\rangle \tag{6.33c}$$

$$|T^e\rangle\,|T^v\rangle\,|S^s\rangle\,, \tag{6.33d}$$

where $|S^e\rangle$ and $|T^e\rangle$ are antisymmetric (singlet-like) and symmetric (triplet-like) combinations of the two envelope functions respectively. Considering relevant energy scales will allow me to understand which of Eq. 6.33 forms the GS. The determining factors are:

1. **Coulomb repulsion** V_D. The SP energy ω competes with the Coulomb interaction V_D, which is dependent on $\sim \sqrt{\omega}$, so at high ω occupation of lower shells is preferable (T^e_-) and at low ω population of higher shells (S^e or T^e_0) gives lower energy. These regimes correspond to shell spacings lower and higher than a critical spacing $\widetilde{\omega}_C \approx 0.785$ [73].

   Let us determine which of these regimes is relevant for MoS_2 QDs. The experimentally achievable QD sizes and potential strengths of $R_{QD} \approx 10 - 100$ nm and $V_{max} \approx 100 - 500$ meV produce $\omega \approx 5 - 35$ meV, which gives $\widetilde{\omega} = \frac{\omega}{Ry^*} \approx 0.007 - 0.05$, using $Ry^* = 740$ meV (given in Eq. 5.49). Therefore the MoS_2 QDs lie in the strongly interacting regime, where occupation of higher shells is energetically favourable. The configuration energies for A-D in Fig. 6.27 follow this argument.

2. **Exchange interaction** V_X. Exchange interaction causes spatially antisymmetric wavefunctions to lower their energies below the symmetric ones, which points to the $|S^e\rangle$ nature of the GS wavefunction (given in Eq. 6.33a and b). Because of the dominance of the intravalley exchange over the intervalley exchange $V_X^{\pm}(\boldsymbol{K}, \boldsymbol{K}) \gg V_X^0(\boldsymbol{K}, -\boldsymbol{K})$, valley-polarised configurations, like C and D in Fig. 6.27, are energetically favourable.

3. **SO splitting** Δ_{SO}. Large Δ_{SO} induces spin-valley locking and mixing of spin singlets and triplets $|S^s\rangle, |T^s\rangle$. This is why it is useful to introduce explicitly

these mixtures, which reflect the spin-valley locking. They read

$$\begin{aligned}
\left|T_{-}^{sv}\right\rangle &= \left|T_{-}^{v}\right\rangle \left|T_{-}^{s}\right\rangle = |\boldsymbol{K}\downarrow\rangle\,|\boldsymbol{K}\downarrow\rangle\,, \\
\left|T_{+}^{sv}\right\rangle &= \left|T_{+}^{v}\right\rangle \left|T_{+}^{s}\right\rangle = |-\boldsymbol{K}\uparrow\rangle\,|-\boldsymbol{K}\uparrow\rangle\,, \\
|T_{0}^{sv}\rangle &= \frac{1}{\sqrt{2}}\left(|T_{0}^{v}\rangle\,|T_{0}^{s}\rangle - |S^{v}\rangle\,|S^{s}\rangle\right), \\
&= \frac{1}{\sqrt{2}}\left(|\boldsymbol{K}\downarrow\rangle\,|-\boldsymbol{K}\uparrow\rangle + |-\boldsymbol{K}\uparrow\rangle\,|\boldsymbol{K}\downarrow\rangle\right), \\
|S^{sv}\rangle &= \frac{1}{\sqrt{2}}\left(|S^{v}\rangle\,|T_{0}^{s}\rangle - |T_{0}^{v}\rangle\,|S^{s}\rangle\right), \\
&= \frac{1}{\sqrt{2}}\left(|\boldsymbol{K}\downarrow\rangle\,|-\boldsymbol{K}\uparrow\rangle - |-\boldsymbol{K}\uparrow\rangle\,|\boldsymbol{K}\downarrow\rangle\right).
\end{aligned} \tag{6.34}$$

Out of the states given by Eq. 6.34, only the triplets $|T^{sv}\rangle$ allow for decreasing the energy due to the strong intravalley exchange $V_X^{\pm}(\boldsymbol{K},\boldsymbol{K})$, because they impose the antisymmetric envelope part $|S^{e}\rangle$.

The remaining $|S^{sv}\rangle$ only takes part in forming the GS for a single shell $(0,0)$, with the triplet-like envelope part $\left|T_{-}^{e}\right\rangle$, i.e. in the case described in section 6.4.2 and written explicitly in Eq. 6.32. It is also the GS configuration shown in a green box in Fig. 6.26 as well as the configuration B in Fig. 6.27.

Importantly, for more shells, $|T^{sv}\rangle$ is always the GS. Out of these triplet states, the GS can prove fully spin-valley polarised (SVP) $\left|T_{\pm}^{sv}\right\rangle$ or intervalley antiferromagnetic (IVAF) $|T_{0}^{sv}\rangle$ [164], as discussed in section 6.4.4. The labels SVP and IVAF are used for more electrons to reflect the same underlying physics, even if the strongly correlated states have much more complex form than described here for $N = 2$ electrons.

4. **Topological splitting** δ. The topological splitting δ creates a difference between C and D configurations in Fig. 6.27, which would be degenerate in energy for a standard 2D HO. The SP energy for C and D is $\omega \mp \frac{\delta}{2}$ respectively, which is higher for D. However, due to smaller wavefunction overlap of the electrons in $(0,0),(1,0)$ states than the electrons in $(0,0),(0,1)$ states, the direct interaction is smaller for the higher $L = +1$ state, $V_D^{+1} < V_D^{-1}$. At

the same time, the exchange included in configuration D is larger than for C, $V_X^{+1}(\boldsymbol{K},\boldsymbol{K}) > V_X^{-1}(\boldsymbol{K},\boldsymbol{K})$. These interaction contributions compensate the SP energy gain and lower the energy of D below C. Hence, D-type configurations always form the GS, also for higher shells. This means populating the highest L states within a shell for valley $\boldsymbol{K}$ (and the time-reversed degenerate in energy partner configuration involves the lowest L states at $-\boldsymbol{K}$).

6.4.4 Broken-symmetry many-electron states in a quantum dot.

I have so far analysed the GS and excited states of $N = 2$ electrons in up to $I_{max} = 2$ HO shells. I now turn to the results of my CI calculations for up to $N = 6$ electrons and with up to $M = 60$ SP states (up to $I_{max} = 5$ HO shells).

All my numerical results show spin-valley locking for the GS wavefunctions. This means that all spin down (up) electrons occupy valley $\boldsymbol{K}$ ($-\boldsymbol{K}$), regardless of the total S_z of the many-electron state. I always observe $N_\downarrow = N_{\boldsymbol{K}}$ and $N_\uparrow = N_{-\boldsymbol{K}}$ for the GS. I therefore introduce one quantum number

$$\widetilde{V} = \frac{N_{-\boldsymbol{K}} - N_{\boldsymbol{K}}}{N} = S_z \frac{2}{N} = \frac{N_\uparrow - N_\downarrow}{N}, \tag{6.35}$$

which denotes the total spin and valley polarisation of the GS. Because of the N factor in Eq. 6.35, $\widetilde{V}$ always takes values betwen $(0, 1)$, where 1 corresponds to total polarisation SVP ($N = N_{\boldsymbol{K}} = N_\downarrow$ or $N = N_{-\boldsymbol{K}} = N_\uparrow$ for the time-reversed degenerate state) and 0 stands for an IVAF GS (no net valley polarisation $N_{\boldsymbol{K}} = N_\downarrow = N_{-\boldsymbol{K}} = N_\uparrow$) (see section 6.4.3).

Fig. 6.28 shows the values of $\widetilde{V}$ for $N = 2 - 6$ electrons and for the highest allowed $I_{max} = 5$ shells for static screening and varying ω. Each panel in Fig. 6.28 describes a fixed N, while rows in each panel correspond to increasing number of the highest shell I_{max}. White and black labels identify the phases and give schematic spin configurations. Colors encode $\widetilde{V}$: orange depicts SVP phase and dark green stands

Figure 6.28: The nature of the many-body GS for $N = 2 - 6$ electrons with static screening for varied ω (horizontal axis). Colors depict $\widetilde{V}$ (Eq. 6.35): $\widetilde{V} = 1$ for SVP phase (orange) and $\widetilde{V} = 0$ IVAF phase (dark green). Ivory, yellow and light green show intermediate $\widetilde{V}$. Panels (rows) give results for varied N (I_{max}). Inset arrows label phases and give schematic spin configurations. SVP is common for low I_{max} and a IVAF $\rightarrow$ SVP transition is visible for $N = 2, 3, 6$ for $I_{max} = 5$ (and partial for $N = 4$). Changes in features for low ω are linked to shell reordering (see text).

for IVAF GS (yellow, ivory and light green are all intermediate $\widetilde{V}$). Note, that for odd N it is impossible to create an $S_z = 0$ phase, so the IVAF phase for odd N manifests itself with minimal values of $\widetilde{V}$ possible for a given odd N (shown in light green for $N = 3, 5$).

I will now describe the main features of Fig. 6.28. Firstly, an overall high $\widetilde{V}$ for lowest I_{max} and low $\widetilde{V}$ for intermediate I_{max} is apparent. This can be understood as favouring the polarised states for low I_{max} due to all ω corresponding to the strong interaction regime (as explained in section 6.4.3-1.), while, for increasing I_{max}, the correlation effects take over and lower the energy of phases with small $\widetilde{V}$ [73]. E.g. for $N = 2, 3$, including the $I_{max} = 3$ shell adds an allowed level with $L = 0$, which significantly increases the number of configurations with low L, which scatter into unpolarised configurations, and lower their energy. With even higher I_{max}, the strongly correlated ω-dependent trend appears.

Secondly, a dominating feature of the data in Fig. 6.28 involves overall higher

possibility of large $\widetilde{V}$ for small ω. This is especially true for $N = 2, 3, 6$, where a transition appears from IVAF GS for $N = 2, 6$ (and unpolarised state for $N = 3$) to an SVP GS for $N = 2, 3, 6$ [164]. This transition occurs at $\omega_0 \approx 10, 16, 21$ meV respectively. For $N = 4$ a transition to a partially polarised GS occurs (marked with ivory for $I_{max} = 5$), which transitions back to IVAF phase for $\omega < 2.1$ meV. There appears no transition for $N = 5$ (for $I_{max} = 5$).

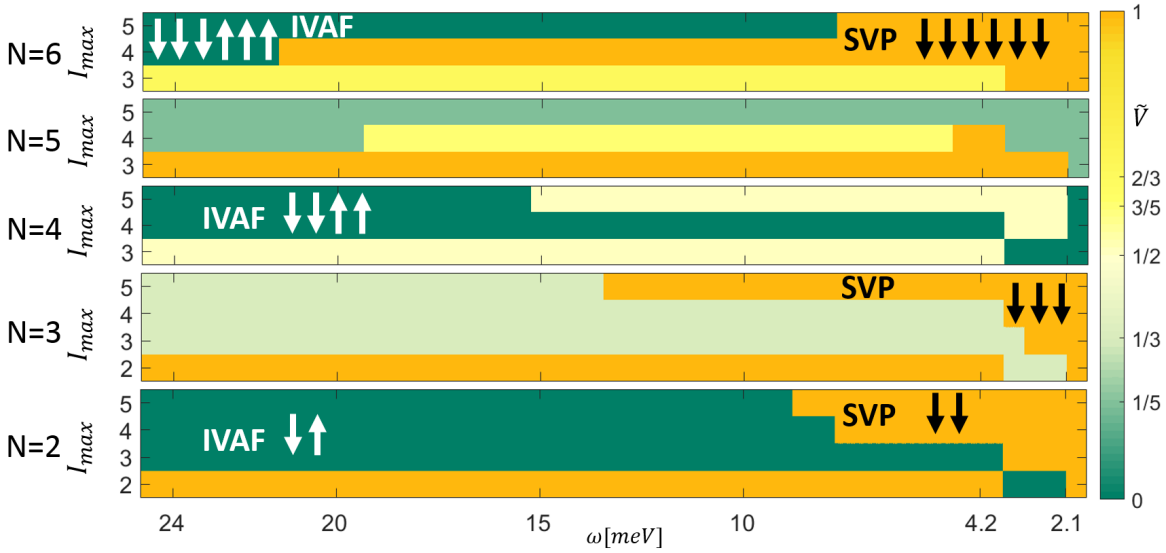

Figure 6.29: The nature of the many-body GS for $N = 2 - 6$ electrons with Keldysh screening for varied ω (horizontal axis). Colors have the same meaning as in Fig. 6.28. IVAF $\rightarrow$ SVP transition for $N = 2, 3, 6, I_{max} = 5$ occurs at lower ω than for static screening.

Thirdly, additional features are visible for $\omega < 4.2$ meV, where the GS phase tendency reverses for some N and I_{max}. This appears because of the labelling convention I took, which assigns I_{max} to the number of the highest SP available shell that is *complete*, i.e. includes the states for both spins. Due to this, there is more SP levels available in the CI calculation than for the same I_{max} for $\omega > 4.2$ meV, because additional incomplete shells are included at lower energies. This is caused by the effect of interpenetrating shells, discussed in section 6.2.3. The changes in $\widetilde{V}$ for $\omega < 4.2$ meV trace the "passing" of shells occuring at $\omega = \Delta_{SO} = 4.2$ meV and $\omega = \Delta_{SO}/2 = 2.1$ meV. For these ω, as more SP levels are available for one spin in each valley, the correlation effects are switched on earlier in I_{max}, which explains the

"jumps" in coloured regions of $\widetilde{V}$.

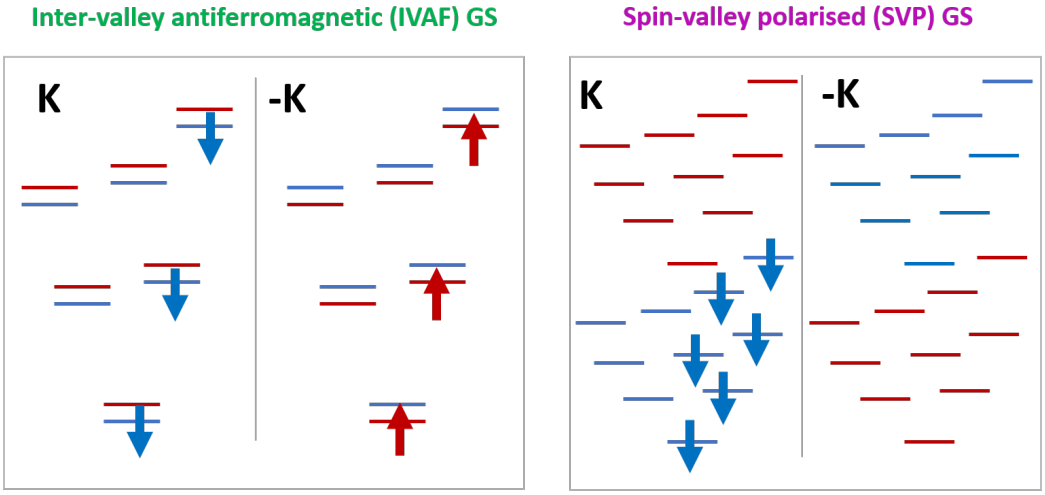

Figure 6.30: (left) IVAF GS and (right) SVP GS for $N = 6$ electrons. Colors denote spins. Electrons occupy higher-energy shells and large-$|L|$ levels.

Let us consider how these results are affected when Keldysh screening is included. Fig. 6.29 shows the GS phases of N electrons for Keldysh-screened interaction, governed with similar physics. The correlation effects induce unpolarised GS for intermediate I_{max}, while polarised states appear for low and high I_{max}. For $N = 2, 6$ a transition from an IVAF (an unpolarised for $N = 3$) to a SVP GS is visible at $\omega_0 \approx 9, 13, 8$ meV respectively. These values are lower than ω_0 was for static sreeening. In particular, the GS phase for $N = 6$ acquires a wide IVAF phase regime for large ω (and $I_{max} = 5$).

Fig. 6.30 shows a schematic picture of the configurations contributing mostly to the GS of $N = 6$ electrons for $I_{max} = 5$ with Keldysh screening. The spin-valley locking is apparent. For high ω the IVAF GS involves $N_{\boldsymbol{K}} = N_{\downarrow} = N_{-\boldsymbol{K}} = N_{\uparrow} = 3$ electrons. This highly correlated state involves occupation of high shells and favours high $|L|$ states, as discussed in section 6.4.3-4., producing a large-total-L GS. For low ω, an SVP phase forms the GS, which populates only one valley with spin-aligned electrons $N = N_{\boldsymbol{K}} = N_{\downarrow} = 6$ (time-reversed partner of $N = N_{-\boldsymbol{K}} = N_{\uparrow}$ is degenerate). The electrons also reach high shells and occupy high $|L|$ states.

6.4.5 Experimental signatures of many-body broken-symmetry states.

This section discusses the possibility of detecting the broken symmetry many-electron GS in experiment.

An important aspect to consider is the stability of the GS phases, which is partly determined by the energy gap between the GS and excited states ΔE_{X-GS}. These gaps impact a transport measurement, by setting the temperature needed to resolve the energy level structure, and they determine their Coulomb diamond signature [75, 169].

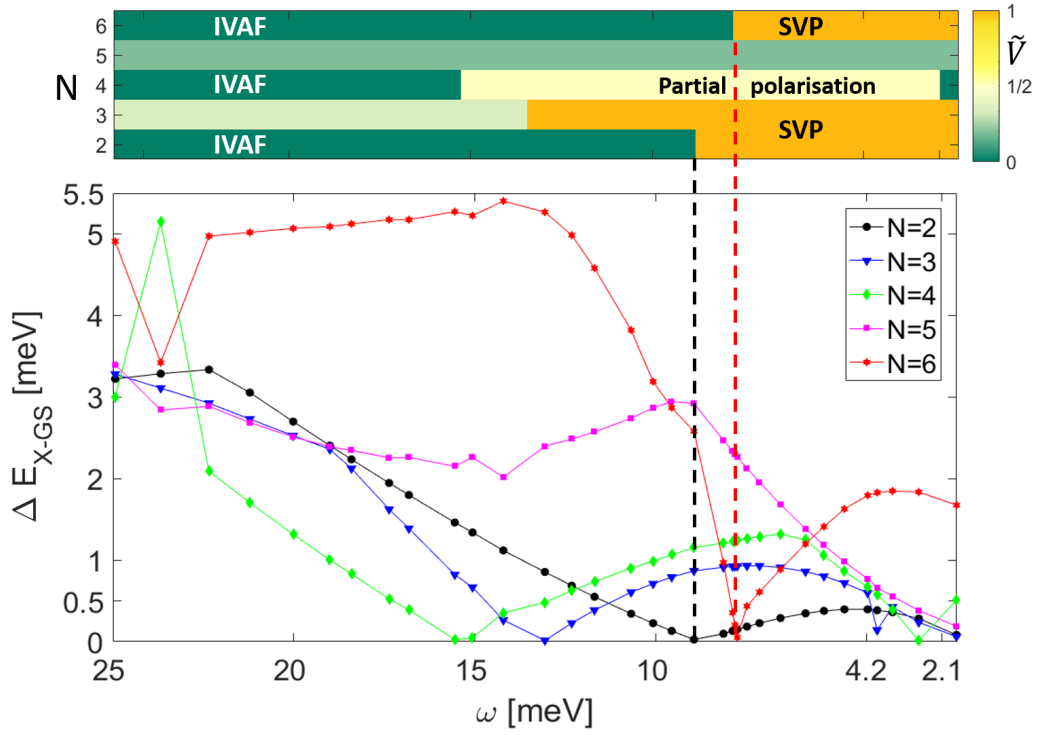

Figure 6.31: (top) GS phases and (bottom) Energy gaps ΔE_{X-GS} for varied N as a function of ω. $\Delta E_{X-GS} = 0$ marks transitions between phases (as illustrated by vertical dashed lines). For $N = 2, 3, 6$ ΔE_{X-GS} vanishes once, and twice (never) for $N = 4$ ($N = 5$). Other smaller dips mark a transition for an excited state.

Fig. 6.31 (bottom) shows the values of ΔE_{X-GS} for $I_{max} = 5$, Keldysh screening, for all N up to $N = 6$ and for varying ω. Values of ω, where $\Delta E_{X-GS} = 0$ mark the transition between phases described in Fig. 6.29 and summarised for I_{max} in the top panel of Fig. 6.31. Transitions for $N = 2, 6$ electrons have been linked between the

panels with vertical dashed lines (black and red respectively) to guide the eye. It is clear that curves for each N exhibit one clear dip each with $\Delta E_{X-GS} = 0$, except for $N = 4$, which exhibits two points of vanishing ΔE_{X-GS} (consistent with Fig. 6.29), which gives the boundary to a partially polarised GS phase.

There are also smaller dips in ΔE_{X-GS} visible, e.g. for $N = 4, 6$ at high ω and for $N = 3$ at low ω, which do not reach $\Delta E_{X-GS} = 0$ and they do not mark a transition in the GS phase. They are however a manifestation of the effect of high SP shells on the many-body GS phases. This is because these small dips correspond to changes in the nature of the excited state phases, which in turn are affected by the spin states order within higher shells, as discussed in section 6.2.3.

Importantly, the gaps shown in Fig. 6.31 are of the order of meV, which could be resolved in a QD transport experiment [75]. The separation of the GS from the excited states is especially promising in this context for $N = 6$, where the transition occurs over a narrow region, and produces a well isolated GS energy level for a wide spectrum of ω within both SVP and IVAF phases [164].

I will now discuss how the two competing GS phases could be distinguished based on the results of a Coulomb and spin blockade spectroscopy experiment. A conductance through an MoS_2 QD can be measured as a function of gate voltage if the QD is connected to metallic leads [75]. The information on the features of the GS can be obtained from the observed relative position and height of the Coulomb blockade conductance peaks, which mark the addition of electron to a QD. The weight of these peaks is proportional to [12, 75, 148, 169, 170]

$$F(\varepsilon, N) = \sum_{p} \left| \langle GS(N+1)| \, d^{\dagger}_{p\sigma} \, |GS(N)\rangle \right|^2 \delta\left(E_{GS(N+1)} - E_{GS(N)} - \varepsilon\right), \qquad (6.36)$$

where $\langle GS(N+1)| \, d^{\dagger}_{p\sigma} \, |GS(N)\rangle$ is the probability of adding an electron to a SP QD state $p\sigma$, in the presence of N electrons occupying the QD.

Fig. 6.32 plots $F(\varepsilon)$ for ω inside two regions dominated by SVP and IVAF phases (for $I_{max} = 5$ and Keldysh screening). Corresponding electron quantum numbers

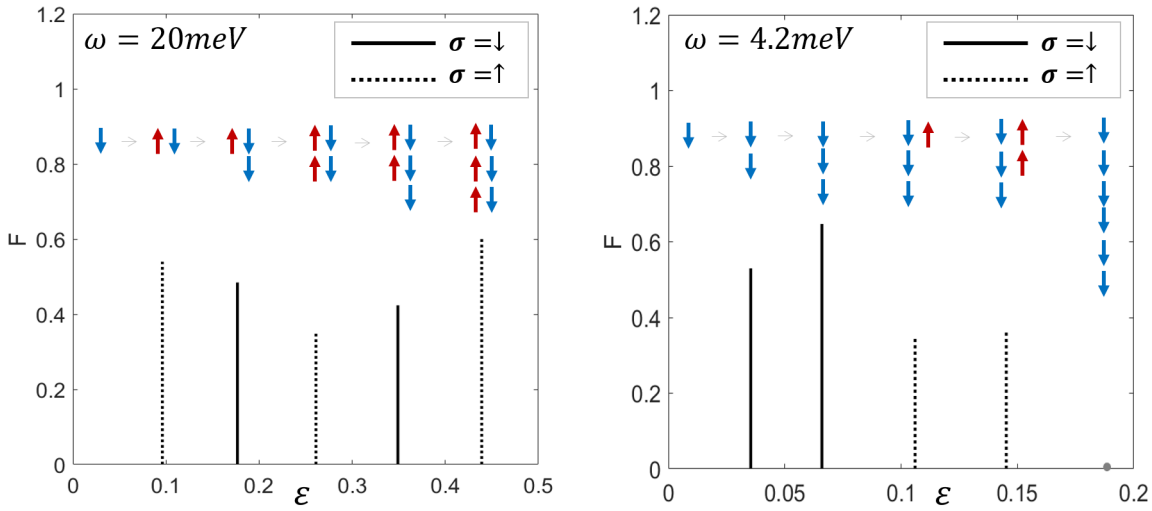

Figure 6.32: Values of $F(\varepsilon)$ (Eq. 6.36) for two ω regimes for $N = 2-6$ electrons. Spin up (down) shown with a dashed (solid) line and red (blue) arrows. As a consequence of the nature of the GS phase, both regimes differ by the spin sequence of peaks. Low ω lacks the last peak (grey dot) due to spin and valley blockade.

are schematically plotted in insets. The valley pseudospin of the initial electron has been fixed (by choosing a specific valley the spin of the electron is determined due to valley-spin locking). Additional electrons are added to a QD, and only a process obeying $\Delta S_z = S_z(N+1) - S_z(N) = \pm 1/2$ and $\Delta N_{\boldsymbol{K}} = \pm 1$ (spin and valley pseudospin conservation) has a nonzero probability. Because the GS phases for low ω in Fig. 6.32 differ by $\Delta S_z > 1/2$ and $\Delta N_{\boldsymbol{K}} > 1$, a transition is forbidden. This is a manifestation of spin and valley blockade and is the reason why a peak is missing for Fig. 6.32 (right).

Also, in a spin-resolved experiment, the peaks will reveal a distinct spin pattern for both phases (spin up and down marked with dashed and solid lines respectively). Left panel of Fig. 6.32 pictures adding electrons of alternating spins, while on the right, spin up electrons can only be added first, followed by only spin up. These signatures could allow for distinguishing the SVP and IVAF GS phases for N electrons in an MoS_2 QD of different ω.

These results suggest that the experimental verification of the discussed nature of the GS for many electrons in MoS_2 QD is likely achievable in transport and could offer further confirmation of the nature of these states.

Chapter 7

Conclusions

In this thesis I have presented results on optical properties and electron-electron interactions in two-dimensional nanostructures of graphene and TMDCs. They offer potential applications in valleytronics - new generation of technology based on the valley pseudospin. Also, honeycomb crystals host new exotic physics, often linked to strong correlations. The results presented in this thesis contribute to the understanding of these materials and identify new effects driven by electron-electron interactions in valley systems.

My results are contained within chapters 3-6. Chapter 3. presents a tight-binding study of hexagonal graphene QDs, which can be analysed with analytically solvable building blocks, significantly reducing the numerical complexity of such problem for large systems. This is an excellent base for exploring many-body effects for experimentally relevant structures within DMRG techniques. This analysis also illuminates the mechanism behind the energy gap formation in graphene QDs, strongly linked to the edge type. The approaches taken in this thesis build on the methods used in this chapter.

Chapter 4. contains a tight-binding theory of MoS_2, derived from ab initio methods. It elucidates the electron tunneling processes in TMDCs and develops the understanding of the physics of d orbitals in honeycomb crystals. Building on this, the origin of the energy band features for TMDCs is thoroughly explained, including the existence of Q-points responsible for band nesting and strong light-matter

interaction. A starting point for studying the valley physics in TMDCs is the massive Dirac fermion model derived in this chapter from the tight-binding Hamiltonian. This minimal but powerful description highlights the role of valley pseudospin and reveals complex behaviour in the presence of electron-electron interactions, as seen in later chapters. The last part of chapter 4. discusses the light-matter interaction of massive Dirac fermions with light, involving valley-dependent optical selection rules. This description is then further developed to include the external magnetic field in chapter 5.

A theory of magnetoexcitons of massive Dirac fermions is presented in chapter 5. The asymmetric Landau level structure for massive Dirac fermions is contrasted with the energy levels of a free electron in external magnetic field. Valley Zeeman splitting and valley polarisation are discussed as a consequence of the asymmetry of the energy structure. As the electron-electron interactions are turned on the valley Zeeman splitting is demonstrated to renormalize with interactions and exhibit oscillations as a function of the valley polarisation. I then present numerical solutions of the Bethe-Salpeter equation for a single magnetoexciton, with all the contributions to the magnetoexciton energies indentified in detail. The cancellation of self-energy and vertex correction has been observed, which leads to small blue shifts of the exciton lines. Finally, I have calculated the magnetoexciton absorption spectrum and observed a splitting of exciton lines for opposite valleys, originating in the non-zero valley polarisation. This chapter demonstrates the computational treatment of a valley polarised system and highlights the complexity of interaction-driven effects for valley-based materials. These concepts are further explored in the final chapter of this thesis.

Chapter 6. gathers the results on single particle energy structure of gated MoS_2 QDs as well as the emerging strongly correlated phases of many electrons in these nanostructures. The first section uses the tight-binding model for bulk MoS_2 in chapter 4. to obtain the eigenstates of a computational box of MoS_2 of up to million atoms treated with periodic boundary conditions. This problem was defined in two separate

bases: atomistic basis and Bloch basis, in order to illuminate the underlying physics. The eigenstates of a box are shown to evolve as a parabolic electrostatic potential is included to define a confining region for a gated QD. The resulting single particle structure for confined electrons is shown to consists of two harmonic oscillator spectra: twofold degenerate derived from K valleys and a sixfold degenerate associated with Q points (vital for TMDCs other than MoS_2). Also, the strong spin orbit coupling in TMDCs as well as a valley-contrasting Berry curvature are shown to play crucial role for the energy spectrum of MoS_2 QDs, as they produce opposite splittings for shells in both valleys. This is linked to the emergence of broken symmetry ground state phases in the final part of this chapter.

The last sections of chapter 6. include results on many-electron behaviour of TMDC QDs. I started with a thorough analysis of scattering Coulomb matrix elements with static and Keldysh screening and identified intravalley and intervalley contributions. I have shown that for two electrons within the first shell with no spin-orbit splitting the ground state is a spin triplet and valley singlet, which matches experimental reports for bilayer graphene QDs. In contrast, in TMDCs QDs with more shells considered, the strong spin-orbit splitting and weak intervalley exchange interaction result in spin-valley locking and produce two competing ground state broken-symmetry phases: spin and valley polarised phase and spin and valley unpolarised but intervalley antiferromagnetic phase. I have demonstrated how these phases emerge in two regimes of shell spacing with a sharp phase transition for two, three and six electrons, and explained the role of correlations in forming of these ground states. Finally, I discussed possibilities for experimental confirmation of these phases by showing large energy gaps separating the ground state from the excited states, which affects operating temperature in experiment. To simulate the results of a transport measurement, I have also calculated a spectral function with different spin signature in both regimes and with absent peaks due to spin-valley blockade effect. These results contribute to the understanding of the interaction-driven phenomena in valley systems and offer valuable insight for creating future valleytronic devices.

Chapter 8

Bibliography

[1] K. S. Novoselov, A. K. Geim, S. V. Morozov, D. Jiang, Y. Zhang, S. V. Dubonos, I. V. Grigorieva, and A. A. Firsov. Electric field effect in atomically thin carbon films. *Science (New York, N.Y.)*, 306(5696):666–669, October 2004.

[2] Yuanbo Zhang, Yan-Wen Tan, Horst L. Stormer, and Philip Kim. Experimental observation of the quantum Hall effect and Berry's phase in graphene. *Nature*, 438(7065):201–204, November 2005.

[3] A. K. Geim and K. S. Novoselov. The rise of graphene | Nature Materials. *Nature Materials*, 2007.

[4] A. Luican, Guohong Li, A. Reina, J. Kong, R. R. Nair, K. S. Novoselov, A. K. Geim, and E. Y. Andrei. Single-Layer Behavior and Its Breakdown in Twisted Graphene Layers. *Physical Review Letters*, 106(12):126802, March 2011. Publisher: American Physical Society.

[5] A. K. Geim and I. V. Grigorieva. Van der Waals heterostructures. *Nature*, 499(7459):419–425, July 2013.

[6] Chih-Pin Lu, Martin Rodriguez-Vega, Guohong Li, Adina Luican-Mayer, Kenji Watanabe, Takashi Taniguchi, Enrico Rossi, and Eva Y. Andrei. Local, global, and nonlinear screening in twisted double-layer graphene. *Proceedings of the*

National Academy of Sciences, 113(24):6623–6628, June 2016. Publisher: National Academy of Sciences Section: Physical Sciences.

[7] Rebeca Ribeiro-Palau, Changjian Zhang, Kenji Watanabe, Takashi Taniguchi, James Hone, and Cory R. Dean. Twistable electronics with dynamically rotatable heterostructures. *Science*, 361(6403):690–693, August 2018.

[8] Chenhao Jin, Emma C. Regan, Aiming Yan, M. Iqbal Bakti Utama, Danqing Wang, Sihan Zhao, Ying Qin, Sijie Yang, Zhiren Zheng, Shenyang Shi, Kenji Watanabe, Takashi Taniguchi, Sefaattin Tongay, Alex Zettl, and Feng Wang. Observation of moiré excitons in WSe2/WS2 heterostructure superlattices. *Nature*, 567(7746):76–80, March 2019.

[9] Jiahao Kang, Wei Cao, Xuejun Xie, Deblina Sarkar, Wei Liu, and Kaustav Banerjee. Graphene and beyond-graphene 2D crystals for next-generation green electronics. page 908305, Baltimore, Maryland, USA, June 2014.

[10] Andres Castellanos-Gomez. Why all the fuss about 2D semiconductors? *Nature Photonics*, 10(4):202–204, April 2016.

[11] Xu Du, Ivan Skachko, Fabian Duerr, Adina Luican, and Eva Y. Andrei. Fractional quantum Hall effect and insulating phase of Dirac electrons in graphene. *Nature*, 462(7270):192–195, November 2009.

[12] A. D. Güçlü, P. Potasz, O. Voznyy, M. Korkusinski, and P. Hawrylak. Magnetism and Correlations in Fractionally Filled Degenerate Shells of Graphene Quantum Dots. *Physical Review Letters*, 103(24):246805, December 2009.

[13] Guohong Li, A. Luican, J. M. B. Lopes dos Santos, A. H. Castro Neto, A. Reina, J. Kong, and E. Y. Andrei. Observation of Van Hove singularities in twisted graphene layers. *Nature Physics*, 6(2):109–113, February 2010.

[14] T. Scrace, Y. Tsai, B. Barman, L. Schweidenback, A. Petrou, G. Kioseoglou, I. Ozfidan, M. Korkusinski, and P. Hawrylak. Magnetoluminescence and valley

polarized state of a two-dimensional electron gas in WS2 monolayers. *Nature Nanotechnology*, 10(7):603–607, July 2015.

[15] John A. McGuire. Growth and optical properties of colloidal graphene quantum dots. *physica status solidi (RRL) - Rapid Research Letters*, 10(1):91–101, January 2016.

[16] Yuan Cao, Valla Fatemi, Ahmet Demir, Shiang Fang, Spencer L. Tomarken, Jason Y. Luo, Javier D. Sanchez-Yamagishi, Kenji Watanabe, Takashi Taniguchi, Efthimios Kaxiras, Ray C. Ashoori, and Pablo Jarillo-Herrero. Correlated insulator behaviour at half-filling in magic-angle graphene superlattices. *Nature*, 556(7699):80–84, April 2018.

[17] Yuan Cao, Valla Fatemi, Shiang Fang, Kenji Watanabe, Takashi Taniguchi, Efthimios Kaxiras, and Pablo Jarillo-Herrero. Unconventional superconductivity in magic-angle graphene superlattices. *Nature*, 556(7699):43–50, April 2018.

[18] Kin Fai Mak, Changgu Lee, James Hone, Jie Shan, and Tony F. Heinz. Atomically Thin mos_2: A New Direct-Gap Semiconductor. *Phys. Rev. Lett.*, 105(13):136805, September 2010.

[19] Eugene S. Kadantsev and Pawel Hawrylak. Electronic structure of a single MoS2 monolayer. *Solid State Communications*, 152(10):909 – 913, 2012.

[20] D. M. Hoffman, P. C. Eklund, R. E. Heinz, P. Hawrylak, and K. R. Subbaswamy. Effect of c-axis dispersion on the optical properties of acceptor-type graphite intercalation compounds. *Physical Review B*, 31(6):3973–3979, March 1985. Publisher: American Physical Society.

[21] A. Rycerz, J. Tworzydlo, and C. W. J. Beenakker. Valley filter and valley valve in graphene. *Nature Physics*, 3(3):172–175, March 2007. arXiv: cond-mat/0608533.

[22] A. H. Castro Neto, F. Guinea, N. M. R. Peres, K. S. Novoselov, and A. K. Geim. The electronic properties of graphene. *Reviews of Modern Physics*, 81(1):109–162, January 2009.

[23] P. R. Wallace. The Band Theory of Graphite. *Phys. Rev.*, 71(9):622–634, May 1947.

[24] K. S Novoselov, A. K. Geim, S. V. Morozov, D. Jiang, M. I. Katsnelson, I. V. Grigorieva, S. V. Dubonos, and A. A. Firsov. Two-dimensional gas of massless Dirac fermions in graphene. *Nature*, 438(7065):197, 2005.

[25] A. King, G. Johnson, D. Engelberg, W. Ludwig, and J. Marrow. Observations of Intergranular Stress Corrosion Cracking in a Grain-Mapped Polycrystal. *Science*, 321(5887):382–385, July 2008.

[26] M.A.H. Vozmediano, M.I. Katsnelson, and F. Guinea. Gauge fields in graphene. *Physics Reports*, 496(4-5):109–148, November 2010.

[27] Sukosin Thongrattanasiri, Frank H. L. Koppens, and F. Javier García de Abajo. Complete Optical Absorption in Periodically Patterned Graphene. *Physical Review Letters*, 108(4):047401, January 2012.

[28] S Y Zhou, G-H Gweon, J Graf, A V Fedorov, C D Spataru, RD Diehl, Y Kopelevich, D-H Lee, Steven G Louie, and A Lanzara. First direct observation of Dirac fermions in graphite. *Nature Physics*, 2(9):595, 2006.

[29] Yi Zhang, Tay-Rong Chang, Bo Zhou, Yong-Tao Cui, Hao Yan, Zhongkai Liu, Felix Schmitt, James Lee, Rob Moore, Yulin Chen, and others. Direct observation of the transition from indirect to direct bandgap in atomically thin epitaxial MoSe2. *Nature nanotechnology*, 9(2):111–115, 2014.

[30] Ting Cao, Gang Wang, Wenpeng Han, Huiqi Ye, Chuanrui Zhu, Junren Shi, Qian Niu, Pingheng Tan, Enge Wang, Baoli Liu, and Ji Feng. Valley-selective circular dichroism of monolayer molybdenum disulphide. *Nature Communications*, 3(1):887, January 2012.

[31] Qing Hua Wang, Kourosh Kalantar-Zadeh, Andras Kis, Jonathan N Coleman, and Michael S Strano. Electronics and optoelectronics of two-dimensional transition metal dichalcogenides. *Nat. Nano.*, 7(11):699–712, 2012.

[32] Hualing Zeng, Junfeng Dai, Wang Yao, Di Xiao, and Xiaodong Cui. Valley polarization in MoS2 monolayers by optical pumping. *Nature Nano.*, 7(8):490–493, 2012.

[33] G. Kioseoglou, A. T. Hanbicki, M. Currie, A. L. Friedman, D. Gunlycke, and B. T. Jonker. Valley polarization and intervalley scattering in monolayer MoS $_2$. *Applied Physics Letters*, 101(22):221907, November 2012.

[34] G. Sallen, L. Bouet, X. Marie, G. Wang, C. R. Zhu, W. P. Han, Y. Lu, P. H. Tan, T. Amand, B. L. Liu, and B. Urbaszek. Robust optical emission polarization in MoS$_2$ monolayers through selective valley excitation. *Phys. Rev. B*, 86(8):081301, August 2012.

[35] Xiaodong Xu, Wang Yao, Di Xiao, and Tony F. Heinz. Spin and pseudospins in layered transition metal dichalcogenides. *Nature Physics*, 10(5):343–350, May 2014.

[36] Di Xiao, Gui-Bin Liu, Wanxiang Feng, Xiaodong Xu, and Wang Yao. Coupled Spin and Valley Physics in Monolayers of mos_2 and Other Group-VI Dichalcogenides. *Phys. Rev. Lett.*, 108(19):196802, May 2012.

[37] Niklas Rohling and Guido Burkard. Universal quantum computing with spin and valley states. *New Journal of Physics*, 14(8):083008, August 2012.

[38] Dimitrie Culcer, A. L. Saraiva, Belita Koiller, Xuedong Hu, and S. Das Sarma. Valley-Based Noise-Resistant Quantum Computation Using Si Quantum Dots. *Physical Review Letters*, 108(12):126804, March 2012.

[39] Niklas Rohling, Maximilian Russ, and Guido Burkard. Hybrid Spin and Valley Quantum Computing with Singlet-Triplet Qubits. *Physical Review Letters*, 113(17):176801, October 2014.

[40] Aaron M Jones, Hongyi Yu, Nirmal J Ghimire, Sanfeng Wu, Grant Aivazian, Jason S Ross, Bo Zhao, Jiaqiang Yan, David G Mandrus, Di Xiao, and others. Optical generation of excitonic valley coherence in monolayer WSe2. *Nat. Nano.*, 8(9):634–638, 2013.

[41] G. Wang, X. Marie, B. L. Liu, T. Amand, C. Robert, F. Cadiz, P. Renucci, and B. Urbaszek. Control of Exciton Valley Coherence in Transition Metal Dichalcogenide Monolayers. *Phys. Rev. Lett.*, 117(18):187401, October 2016.

[42] Di Xiao, Ming-Che Chang, and Qian Niu. Berry phase effects on electronic properties. *Reviews of Modern Physics*, 82(3):1959–2007, July 2010.

[43] Y. D. Chong. Berry's phase and the anomalous velocity of Bloch wavepackets. *Physical Review B*, 81(5), February 2010.

[44] Ajit Srivastava and Ataç Imamoğlu. Signatures of Bloch-Band Geometry on Excitons: Nonhydrogenic Spectra in Transition-Metal Dichalcogenides. *Physical Review Letters*, 115(16), October 2015.

[45] Jianhui Zhou, Wen-Yu Shan, Wang Yao, and Di Xiao. Berry Phase Modification to the Energy Spectrum of Excitons. *Physical Review Letters*, 115(16), October 2015.

[46] Di Xiao, Wang Yao, and Qian Niu. Valley-Contrasting Physics in Graphene: Magnetic Moment and Topological Transport. *Phys. Rev. Lett.*, 99(23):236809, December 2007.

[47] K. F. Mak, K. L. McGill, J. Park, and P. L. McEuen. The valley Hall effect in MoS2 transistors. *Science*, 344(6191):1489–1492, June 2014.

[48] Benjamin T. Zhou, Katsuhisa Taguchi, Yuki Kawaguchi, Yukio Tanaka, and K. T. Law. Spin-orbit coupling induced valley Hall effects in transition-metal dichalcogenides. *Communications Physics*, 2(1):26, December 2019.

[49] Maciej Bieniek, Ludmiła Szulakowska, and Paweł Hawrylak. Band nesting and exciton spectrum in monolayer MoS 2. *Physical Review B*, 101(12):125423, March 2020.

[50] A. Carvalho, R. M. Ribeiro, and A. H. Castro Neto. Band nesting and the optical response of two-dimensional semiconducting transition metal dichalcogenides. *Phys. Rev. B*, 88(11):115205, September 2013.

[51] E. Cappelluti, R. Roldan, J. A. Silva-Guillen, P. Ordejon, and F. Guinea. Tight-binding model and direct-gap/indirect-gap transition in single-layer and multilayer MoS2. *Phys. Rev. B*, 88(7):075409, August 2013.

[52] Gui-Bin Liu, Wen-Yu Shan, Yugui Yao, Wang Yao, and Di Xiao. Three-band tight-binding model for monolayers of group-VIB transition metal dichalcogenides. *Physical Review B*, 88(8):085433, August 2013.

[53] Ferdows Zahid, Lei Liu, Yu Zhu, Jian Wang, and Hong Guo. A generic tight-binding model for monolayer, bilayer and bulk MoS2. *AIP Advances*, 3(5):052111, 2013.

[54] E. Ridolfi, D. Le, T. S. Rahman, E. R. Mucciolo, and C. H. Lewenkopf. A tight-binding model for MoS 2 monolayers. *Journal of Physics: Condensed Matter*, 27(36):365501, 2015.

[55] Shiang Fang, Rodrick Kuate Defo, Sharmila N. Shirodkar, Simon Lieu, Georgios A. Tritsaris, and Efthimios Kaxiras. Ab initio tight-binding Hamiltonian for transition metal dichalcogenides. *Phys. Rev. B*, 92(20):205108, November 2015.

[56] Jose Angel Silva-Guillen, Pablo San-Jose, and Rafael Roldan. Electronic Band Structure of Transition Metal Dichalcogenides from Ab Initio and Slater Koster Tight-Binding Model. *Applied Sciences*, 6(10):284, 2016.

[57] Diana Y. Qiu, Felipe H. da Jornada, and Steven G. Louie. Optical Spectrum of MoS 2 : Many-Body Effects and Diversity of Exciton States. *Physical Review Letters*, 111(21), November 2013.

[58] Alexey Chernikov, Timothy C. Berkelbach, Heather M. Hill, Albert Rigosi, Yilei Li, Ozgur Burak Aslan, David R. Reichman, Mark S. Hybertsen, and Tony F. Heinz. Exciton Binding Energy and Nonhydrogenic Rydberg Series in Monolayer WS 2. *Physical Review Letters*, 113(7):076802, August 2014.

[59] Diana Y. Qiu, Ting Cao, and Steven G. Louie. Nonanalyticity, Valley Quantum Phases, and Lightlike Exciton Dispersion in Monolayer Transition Metal Dichalcogenides: Theory and First-Principles Calculations. *Physical Review Letters*, 115(17), October 2015.

[60] Jonas Gaël Roch, Guillaume Froehlicher, Nadine Leisgang, Peter Makk, Kenji Watanabe, Takashi Taniguchi, and Richard John Warburton. Spin-polarized electrons in monolayer MoS2. *Nature Nanotechnology*, 14(5):432–436, May 2019.

[61] C. Kallin and B. I. Halperin. Excitations from a filled Landau level in the two-dimensional electron gas. *Physical Review B*, 30(10):5655–5668, November 1984.

[62] Félix Rose, M. O. Goerbig, and Frédéric Piéchon. Spin- and valley-dependent magneto-optical properties of MoS 2. *Physical Review B*, 88(12):125438, September 2013.

[63] Tianyi Cai, Shengyuan A. Yang, Xiao Li, Fan Zhang, Junren Shi, Wang Yao, and Qian Niu. Magnetic control of the valley degree of freedom of massive Dirac fermions with application to transition metal dichalcogenides. *Phys. Rev. B*, 88(11):115140, September 2013.

[64] David MacNeill, Colin Heikes, Kin Fai Mak, Zachary Anderson, Andor Kormányos, Viktor Zólyomi, Jiwoong Park, and Daniel C. Ralph. Breaking

of Valley Degeneracy by Magnetic Field in Monolayer mose$_2$. *Phys. Rev. Lett.*, 114(3):037401, January 2015.

[65] Grant Aivazian, Zhirui Gong, Aaron M Jones, Rui-Lin Chu, Jiaqiang Yan, David G Mandrus, Chuanwei Zhang, David Cobden, Wang Yao, and Xiaodong Xu. Magnetic control of valley pseudospin in monolayer WSe2. *Nature Physics*, 11:148–152, 2015.

[66] Zefang Wang, Jie Shan, and Kin Fai Mak. Valley- and spin-polarized Landau levels in monolayer WSe2. *Nature Nanotechnology*, 12(2):144–149, February 2017.

[67] Yilei Li, Jonathan Ludwig, Tony Low, Alexey Chernikov, Xu Cui, Ghidewon Arefe, Young Duck Kim, Arend M. van der Zande, Albert Rigosi, Heather M. Hill, Suk Hyun Kim, James Hone, Zhiqiang Li, Dmitry Smirnov, and Tony F. Heinz. Valley Splitting and Polarization by the Zeeman Effect in Monolayer mose$_2$. *Phys. Rev. Lett.*, 113(26):266804, December 2014.

[68] Ajit Srivastava, Meinrad Sidler, Adrien V Allain, Dominik S Lembke, Andras Kis, and A Imamoğlu. Valley Zeeman effect in elementary optical excitations of monolayer WSe2. *Nature Physics*, 11:141–147, 2015.

[69] Zefang Wang, Kin Fai Mak, and Jie Shan. Strongly Interaction-Enhanced Valley Magnetic Response in Monolayer WSe 2. *Physical Review Letters*, 120(6):066402, February 2018.

[70] Martin V. Gustafsson, Matthew Yankowitz, Carlos Forsythe, Daniel Rhodes, Kenji Watanabe, Takashi Taniguchi, James Hone, Xiaoyang Zhu, and Cory R. Dean. Ambipolar Landau levels and strong band-selective carrier interactions in monolayer WSe2. *Nature Materials*, 17(5):411–415, May 2018.

[71] Riccardo Pisoni, Andor Kormányos, Matthew Brooks, Zijin Lei, Patrick Back, Marius Eich, Hiske Overweg, Yongjin Lee, Peter Rickhaus, Kenji Watanabe, Takashi Taniguchi, Atac Imamoglu, Guido Burkard, Thomas Ihn, and Klaus

Ensslin. Interactions and Magnetotransport through Spin-Valley Coupled Landau Levels in Monolayer MoS 2. *Physical Review Letters*, 121(24):247701, December 2018.

[72] M. Bayer, O. Stern, P. Hawrylak, S. Fafard, and A. Forchel. Hidden symmetries in the energy levels of excitonic 'artificial atoms'. *Nature*, 405(6789):923–926, June 2000.

[73] M. Korkusinski, W. Sheng, and P. Hawrylak. Designing quantum systems in self-assembled quantum dots. *physica status solidi (b)*, 238(2):246–249, July 2003.

[74] S. Raymond, S. Studenikin, A. Sachrajda, Z. Wasilewski, S. J. Cheng, W. Sheng, P. Hawrylak, A. Babinski, M. Potemski, G. Ortner, and M. Bayer. Excitonic Energy Shell Structure of Self-Assembled InGaAs/GaAs Quantum Dots. *Physical Review Letters*, 92(18):187402, May 2004.

[75] M. Ciorga, A. S. Sachrajda, P. Hawrylak, C. Gould, P. Zawadzki, S. Jullian, Y. Feng, and Z. Wasilewski. Addition spectrum of a lateral dot from Coulomb and spin-blockade spectroscopy. *Physical Review B*, 61(24):R16315–R16318, June 2000.

[76] A. Marti, L. Cuadra, and A. Luque. Quantum dot intermediate band solar cell. In *Conference Record of the Twenty-Eighth IEEE Photovoltaic Specialists Conference - 2000 (Cat. No.00CH37036)*, pages 940–943, September 2000. ISSN: 0160-8371.

[77] Stefano Ossicini, Michele Amato, Roberto Guerra, Maurizia Palummo, and Olivia Pulci. Silicon and Germanium Nanostructures for Photovoltaic Applications: Ab-Initio Results. *Nanoscale Research Letters*, 5(10):1637, July 2010.

[78] Xuetao Gan, Ren-Jye Shiue, Yuanda Gao, Inanc Meric, Tony F. Heinz, Kenneth Shepard, James Hone, Solomon Assefa, and Dirk Englund. Chip-integrated

ultrafast graphene photodetector with high responsivity. *Nature Photonics*, 7(11):883–887, November 2013.

[79] Fengjia Fan, Oleksandr Voznyy, Randy P. Sabatini, Kristopher T. Bicanic, Michael M. Adachi, James R. McBride, Kemar R. Reid, Young-Shin Park, Xiyan Li, Ankit Jain, Rafael Quintero-Bermudez, Mayuran Saravanapavanantham, Min Liu, Marek Korkusinski, Pawel Hawrylak, Victor I. Klimov, Sandra J. Rosenthal, Sjoerd Hoogland, and Edward H. Sargent. Continuous-wave lasing in colloidal quantum dot solids enabled by facet-selective epitaxy. *Nature*, 544(7648):75–79, April 2017.

[80] Pieter Geiregat, Dries Van Thourhout, and Zeger Hens. A bright future for colloidal quantum dot lasers. *NPG Asia Materials*, 11(1):41, December 2019.

[81] Luc Robichaud and Jacob J. Krich. Wurtzite InGaN/GaN Quantum Dots for Intermediate Band Solar Cells. In *2019 International Conference on Numerical Simulation of Optoelectronic Devices (NUSOD)*, pages 57–58, July 2019. ISSN: 2158-3242.

[82] José A. Brum and Pawel Hawrylak. Coupled quantum dots as quantum exclusive-OR gate. *Superlattices and Microstructures*, 22(3):431–436, October 1997.

[83] Florian Meier, Jeremy Levy, and Daniel Loss. Quantum Computing with Spin Cluster Qubits. *Physical Review Letters*, 90(4):047901, January 2003.

[84] J. M. Elzerman, R. Hanson, L. H. Willems van Beveren, B. Witkamp, L. M. K. Vandersypen, and L. P. Kouwenhoven. Single-shot read-out of an individual electron spin in a quantum dot. *Nature*, 430(6998):431–435, July 2004.

[85] Björn Trauzettel, Denis V. Bulaev, Daniel V, and Guido Burkard. Spin qubits in graphene quantum dots. *Nature Physics*, 3(3):192–196, March 2007. Number: 3 Publisher: Nature Publishing Group.

[86] Jacob J. Krich and Bertrand I. Halperin. Cubic Dresselhaus Spin-Orbit Coupling in 2D Electron Quantum Dots. *Physical Review Letters*, 98(22):226802, May 2007. Publisher: American Physical Society.

[87] Andrea Morello, Jarryd J. Pla, Floris A. Zwanenburg, Kok W. Chan, Kuan Y. Tan, Hans Huebl, Mikko Möttönen, Christopher D. Nugroho, Changyi Yang, Jessica A. van Donkelaar, Andrew D. C. Alves, David N. Jamieson, Christopher C. Escott, Lloyd C. L. Hollenberg, Robert G. Clark, and Andrew S. Dzurak. Single-shot readout of an electron spin in silicon. *Nature*, 467(7316):687–691, October 2010.

[88] Chang-Yu Hsieh, Yun-Pil Shim, Marek Korkusinski, and Pawel Hawrylak. Physics of lateral triple quantum-dot molecules with controlled electron numbers. *Reports on Progress in Physics*, 75(11):114501, October 2012. Publisher: IOP Publishing.

[89] M. Gullans, J. J. Krich, J. M. Taylor, B. I. Halperin, and M. D. Lukin. Preparation of nonequilibrium nuclear spin states in double quantum dots. *Physical Review B*, 88(3):035309, July 2013. Publisher: American Physical Society.

[90] Andor Kormányos, Viktor Zólyomi, Neil D. Drummond, and Guido Burkard. Spin-Orbit Coupling, Quantum Dots, and Qubits in Monolayer Transition Metal Dichalcogenides. *Physical Review X*, 4(1):011034, March 2014.

[91] Pawel Hawrylak, François Peeters, and Klaus Ensslin. Carbononics – integrating electronics, photonics and spintronics with graphene quantum dots. *physica status solidi (RRL) – Rapid Research Letters*, 10(1):11–12, 2016. _eprint: https://onlinelibrary.wiley.com/doi/pdf/10.1002/pssr.201670707.

[92] Takumi Ito, Tomohiro Otsuka, Takashi Nakajima, Matthieu R. Delbecq, Shinichi Amaha, Jun Yoneda, Kenta Takeda, Akito Noiri, Giles Allison, Arne Ludwig, Andreas D. Wieck, and Seigo Tarucha. Four single-spin Rabi oscil-

lations in a quadruple quantum dot. *Applied Physics Letters*, 113(9):093102, August 2018.

[93] Anderson West, Bas Hensen, Alexis Jouan, Tuomo Tanttu, Chih-Hwan Yang, Alessandro Rossi, M. Fernando Gonzalez-Zalba, Fay Hudson, Andrea Morello, David J. Reilly, and Andrew S. Dzurak. Gate-based single-shot readout of spins in silicon. *Nature Nanotechnology*, 14(5):437–441, May 2019.

[94] T. N. Lin, S. R. M. Santiago, S. P. Caigas, C. T. Yuan, T. Y. Lin, J. L. Shen, and Y. F. Chen. Many-body effects in doped WS2 monolayer quantum disks at room temperature. *npj 2D Materials and Applications*, 3(1):46, December 2019.

[95] Z. Z. Zhang, Kai Chang, and F. M. Peeters. Tuning of energy levels and optical properties of graphene quantum dots. *Physical Review B*, 77(23):235411, June 2008.

[96] Alev Devrim Güçlü, Pawel Potasz, Marek Korkusinski, and Pawel Hawrylak. *Graphene quantum dots*. Springer, 2014.

[97] Isil Ozfidan, Marek Korkusinski, A. Devrim Güçlü, John A. McGuire, and Pawel Hawrylak. Microscopic theory of the optical properties of colloidal graphene quantum dots. *Physical Review B*, 89(8):085310, February 2014.

[98] Isil Ozfidan, Alev Devrim Güçlü, Marek Korkusinski, and Pawel Hawrylak. Theory of optical properties of graphene quantum dots. *physica status solidi (RRL)-Rapid Research Letters*, 10(1):102–110, 2016.

[99] Jeppe V. Lauritsen, Jakob Kibsgaard, Stig Helveg, Henrik Topsøe, Bjerne S. Clausen, Erik Lægsgaard, and Flemming Besenbacher. Size-dependent structure of MoS2 nanocrystals. *Nature Nanotechnology*, 2(1):53–58, January 2007.

[100] G. C. Loh, Ravindra Pandey, Yoke Khin Yap, and Shashi P. Karna. MoS $_2$ Quantum Dot: Effects of Passivation, Additional Layer, and h -BN Substrate

on Its Stability and Electronic Properties. *The Journal of Physical Chemistry C*, 119(3):1565–1574, January 2015.

[101] N. Sabari Arul and V. D. Nithya. Molybdenum disulfide quantum dots: synthesis and applications. *RSC Advances*, 6(70):65670–65682, 2016.

[102] Bo Li, Lan Jiang, Xin Li, Peng Ran, Pei Zuo, Andong Wang, Liangti Qu, Yang Zhao, Zhihua Cheng, and Yongfeng Lu. Preparation of Monolayer MoS2 Quantum Dots using Temporally Shaped Femtosecond Laser Ablation of Bulk MoS2 Targets in Water. *Scientific Reports*, 7(1), December 2017.

[103] J. Güttinger, T. Frey, C. Stampfer, T. Ihn, and K. Ensslin. Spin States in Graphene Quantum Dots. *Physical Review Letters*, 105(11):116801, September 2010.

[104] Ke Wang, Kristiaan De Greve, Luis A. Jauregui, Andrey Sushko, Alexander High, You Zhou, Giovanni Scuri, Takashi Taniguchi, Kenji Watanabe, Mikhail D. Lukin, Hongkun Park, and Philip Kim. Electrical control of charged carriers and excitons in atomically thin materials. *Nature Nanotechnology*, 13(2):128–132, February 2018.

[105] S Bhandari, K Wang, K Watanabe, T Taniguchi, P Kim, and R M Westervelt. Imaging quantum dot formation in MoS $_2$ nanostructures. *Nanotechnology*, 29(42):42LT03, October 2018.

[106] Xiang-Xiang Song, Di Liu, Vahid Mosallanejad, Jie You, Tian-Yi Han, Dian-Teng Chen, Hai-Ou Li, Gang Cao, Ming Xiao, Guang-Can Guo, and Guo-Ping Guo. A gate defined quantum dot on the two-dimensional transition metal dichalcogenide semiconductor WSe $_2$. *Nanoscale*, 7(40):16867–16873, 2015.

[107] M. T. Allen, J. Martin, and A. Yacoby. Gate-defined quantum confinement in suspended bilayer graphene. *Nature Communications*, 3(1):934, January 2012.

[108] C. Volk, S. Fringes, B. Terrés, J. Dauber, S. Engels, S. Trellenkamp, and C. Stampfer. Electronic Excited States in Bilayer Graphene Double Quantum Dots. *Nano Letters*, 11(9):3581–3586, September 2011.

[109] Marius Eich, Riccardo Pisoni, Hiske Overweg, Annika Kurzmann, Yongjin Lee, Peter Rickhaus, Thomas Ihn, Klaus Ensslin, František Herman, Manfred Sigrist, Kenji Watanabe, and Takashi Taniguchi. Spin and Valley States in Gate-Defined Bilayer Graphene Quantum Dots. *Physical Review X*, 8(3):031023, July 2018.

[110] A Kurzmann, M Eich, H Overweg, M Mangold, F Herman, P Rickhaus, R Pisoni, Y Lee, R Garreis, C Tong, K Watanabe, T Taniguchi, K Ensslin, and T Ihn. Excited States in Bilayer Graphene Quantum Dots. *Physical Review Letters*, 123:026803, July 2019.

[111] Riccardo Pisoni, Zijin Lei, Patrick Back, Marius Eich, Hiske Overweg, Yongjin Lee, Kenji Watanabe, Takashi Taniguchi, Thomas Ihn, and Klaus Ensslin. Gate-tunable quantum dot in a high quality single layer MoS2 van der Waals heterostructure. *Applied Physics Letters*, 112(12):123101, March 2018.

[112] Mauro Brotons-Gisbert, Artur Branny, Santosh Kumar, Raphaël Picard, Raphaël Proux, Mason Gray, Kenneth S. Burch, Kenji Watanabe, Takashi Taniguchi, and Brian D. Gerardot. Coulomb blockade in an atomically thin quantum dot coupled to a tunable Fermi reservoir. *Nature Nanotechnology*, 14(5):442–446, May 2019.

[113] Xin Lu, Xiaotong Chen, Sudipta Dubey, Qiang Yao, Weijie Li, Xingzhi Wang, Qihua Xiong, and Ajit Srivastava. Optical initialization of a single spin-valley in charged WSe2 quantum dots. *Nature Nanotechnology*, 14(5):426–431, May 2019.

[114] Zhuo-Zhi Zhang, Xiang-Xiang Song, Gang Luo, Guang-Wei Deng, Vahid Mosallanejad, Takashi Taniguchi, Kenji Watanabe, Hai-Ou Li, Gang Cao, Guang-Can Guo, Franco Nori, and Guo-Ping Guo. Electrotunable artificial molecules based

on van der Waals heterostructures. *Science Advances*, 3(10):e1701699, October 2017.

[115] Gui-Bin Liu, Hongliang Pang, Yugui Yao, and Wang Yao. Intervalley coupling by quantum dot confinement potentials in monolayer transition metal dichalcogenides. *New Journal of Physics*, 16(10):105011, October 2014.

[116] Yue Wu, Qingjun Tong, Gui-Bin Liu, Hongyi Yu, and Wang Yao. Spin-valley qubit in nanostructures of monolayer semiconductors: Optical control and hyperfine interaction. *Physical Review B*, 93(4):045313, January 2016.

[117] A C Dias, Jiyong Fu, L Villegas-Lelovsky, and Fanyao Qu. Robust effective Zeeman energy in monolayer MoS $_2$ quantum dots. *Journal of Physics: Condensed Matter*, 28(37):375803, September 2016.

[118] Matthew Brooks and Guido Burkard. Spin-degenerate regimes for single quantum dots in transition metal dichalcogenide monolayers. *Physical Review B*, 95(24):245411, June 2017.

[119] Fanyao Qu, A. C. Dias, Jiyong Fu, L. Villegas-Lelovsky, and David L. Azevedo. Tunable spin and valley dependent magneto-optical absorption in molybdenum disulfide quantum dots. *Scientific Reports*, 7(1):41044, February 2017.

[120] J. Pawłowski, D. Żebrowski, and S. Bednarek. Valley qubit in a gated MoS 2 monolayer quantum dot. *Physical Review B*, 97(15):155412, April 2018.

[121] G Széchenyi, L Chirolli, and A Pályi. Impurity-assisted electric control of spin-valley qubits in monolayer MoS $_2$. *2D Materials*, 5(3):035004, April 2018.

[122] L Chirolli, E Prada, F Guinea, R Roldán, and P San-Jose. Strain-induced bound states in transition-metal dichalcogenide bubbles. *2D Materials*, 6(2):025010, February 2019.

[123] Tianshu Li and Giulia Galli. Electronic Properties of MoS $_2$ Nanoparticles. *The Journal of Physical Chemistry C*, 111(44):16192–16196, November 2007.

[124] S. Pavlović and F. M. Peeters. Electronic properties of triangular and hexagonal MoS 2 quantum dots. *Physical Review B*, 91(15):155410, April 2015.

[125] Qiao Chen, L. L. Li, and F. M. Peeters. Magnetic field dependence of electronic properties of MoS 2 quantum dots with different edges. *Physical Review B*, 97(8):085437, February 2018.

[126] D. P. Żebrowski, E. Wach, and B. Szafran. Confined states in quantum dots defined within finite flakes of bilayer graphene: Coupling to the edge, ionization threshold, and valley degeneracy. *Physical Review B*, 88(16):165405, October 2013.

[127] S. A. Mikhailov. Quantum-dot lithium in zero magnetic field: Electronic properties, thermodynamics, and Fermi liquid–Wigner solid crossover in the ground state. *Physical Review B*, 65(11):115312, February 2002.

[128] Angelika Knothe and Vladimir Fal'ko. Quartet states in two-electron quantum dots in bilayer graphene. *arXiv:2002.12845 [cond-mat, physics:quant-ph]*, February 2020. arXiv: 2002.12845.

[129] J. C. Slater and G. F. Koster. Simplified LCAO Method for the Periodic Potential Problem. *Physical Review*, 94(6):1498–1524, June 1954.

[130] Douglas Rayner Hartree and W. Hartree. Self-consistent field, with exchange, for beryllium. *Proc. Royal Soc. Lond. A.*, 150(869):9–33, 1935.

[131] A. Szabo and N.S. Ostlund. *Modern Quantum Chemistry: Introduction to Advanced Electronic Structure Theory*. Dover Publications, 1996.

[132] J. Callaway and N. H. March. Density Functional Methods:Theory and Applications. volume 38 of *Solid State Physics*, pages 135 – 221. Academic Press, 1984. ISSN: 0081-1947.

[133] Xavier Gonze, Bernard Amadon, Gabriel Antonius, Frédéric Arnardi, Lucas Baguet, Jean-Michel Beuken, Jordan Bieder, François Bottin, Johann Bouchet,

Eric Bousquet, Nils Brouwer, Fabien Bruneval, Guillaume Brunin, Théo Cavignac, Jean-Baptiste Charraud, Wei Chen, Michel Côté, Stefaan Cottenier, Jules Denier, Grégory Geneste, Philippe Ghosez, Matteo Giantomassi, Yannick Gillet, Olivier Gingras, Donald R. Hamann, Geoffroy Hautier, Xu He, Nicole Helbig, Natalie Holzwarth, Yongchao Jia, François Jollet, William Lafargue-Dit-Hauret, Kurt Lejaeghere, Miguel A.L. Marques, Alexandre Martin, Cyril Martins, Henrique P.C. Miranda, Francesco Naccarato, Kristin Persson, Guido Petretto, Valentin Planes, Yann Pouillon, Sergei Prokhorenko, Fabio Ricci, Gian-Marco Rignanese, Aldo H. Romero, Michael Marcus Schmitt, Marc Torrent, Michiel J. van Setten, Benoit Van Troeye, Matthieu J. Verstraete, Gilles Zérah, and Josef W. Zwanziger. The Abinitproject: Impact, environment and recent developments. *Computer Physics Communications*, 248:107042, March 2020.

[134] Hendrik J. Monkhorst and James D. Pack. Special points for Brillouin-zone integrations. *Physical Review B*, 13(12):5188–5192, June 1976.

[135] John P. Perdew, Matthias Ernzerhof, and Kieron Burke. Rationale for mixing exact exchange with density functional approximations. *The Journal of Chemical Physics*, 105(22):9982–9985, December 1996.

[136] P. E. Blöchl. Projector augmented-wave method. *Physical Review B*, 50(24):17953–17979, December 1994.

[137] Marc Torrent, François Jollet, François Bottin, Gilles Zérah, and Xavier Gonze. Implementation of the projector augmented-wave method in the ABINIT code: Application to the study of iron under pressure. *Computational Materials Science*, 42(2):337–351, April 2008.

[138] M. Zieliński, M. Korkusiński, and P. Hawrylak. Atomistic tight-binding theory of multiexciton complexes in a self-assembled InAs quantum dot. *Physical Review B*, 81(8):085301, February 2010.

[139] E. Anderson, Z. Bai, C. Bischof, J. Demmel, J. Dongarra, J. Du Croz, A. Greenbaum, S. Hammarling, A. Mckenney, and And D. Sorensen. Lapack: A portable linear algebra library for high-performance computers. 1997.

[140] E. Anderson, Z. Bai, and J. Dongarra. Generalized QR factorization and its applications. *Linear Algebra and its Applications*, 162-164:243–271, February 1992.

[141] Eric Polizzi. Density-matrix-based algorithm for solving eigenvalue problems. *Physical Review B*, 79(11):115112, March 2009.

[142] Vicente Hernandez, Jose E. Roman, and Vicente Vidal. SLEPc: A scalable and flexible toolkit for the solution of eigenvalue problems. *ACM Transactions on Mathematical Software (TOMS)*, 31(3):351–362, September 2005.

[143] Gerard L. G. Sleijpen and Henk A. Van der Vorst. A Jacobi-Davidson Iteration Method for Linear Eigenvalue Problems. *SIAM Review*, 42(2):267–293, 2000. Publisher: Society for Industrial and Applied Mathematics.

[144] G. W. Stewart. A Krylov–Schur Algorithm for Large Eigenproblems. *SIAM Journal on Matrix Analysis and Applications*, 23(3):601–614, January 2002.

[145] Leonardo Dagum and Ramesh Menon. OpenMP: an industry standard API for shared-memory programming. *Computational Science & Engineering, IEEE*, 5(1):46–55, 1998. Publisher: IEEE.

[146] Lyndon Clarke, Ian Glendinning, and Rolf Hempel. The MPI Message Passing Interface Standard. In Karsten M. Decker and René M. Rehmann, editors, *Programming Environments for Massively Parallel Distributed Systems*, pages 213–218, Basel, 1994. Birkhäuser Basel.

[147] Pawel Hawrylak. Far infrared absorption by screened D- states in quantum wells in a strong magnetic field. *Solid State Communications*, 88(6):475–479, November 1993.

[148] Pawel Hawrylak and Daniela Pfannkuche. Magnetoluminescence from correlated electrons in quantum dots. *Physical Review Letters*, 70(4):485–488, January 1993.

[149] E. Clementi and D. L. Raimondi. Atomic Screening Constants from SCF Functions. *The Journal of Chemical Physics*, 38(11):2686–2689, June 1963.

[150] E. Clementi, D. L. Raimondi, and W. P. Reinhardt. Atomic Screening Constants from SCF Functions. II. Atoms with 37 to 86 Electrons. *The Journal of Chemical Physics*, 47(4):1300–1307, August 1967.

[151] G Peter Lepage. A new algorithm for adaptive multidimensional integration. *Journal of Computational Physics*, 27(2):192–203, May 1978.

[152] Y Saleem, L Najera Baldo, A Delgado, L Szulakowska, and P Hawrylak. Oscillations of the bandgap with size in armchair and zigzag graphene quantum dots. *Journal of Physics: Condensed Matter*, 31(30):305503, July 2019.

[153] O. Voznyy, A. D. Güçlü, P. Potasz, and P. Hawrylak. Effect of edge reconstruction and passivation on zero-energy states and magnetism in triangular graphene quantum dots with zigzag edges. *Physical Review B*, 83(16):165417, April 2011.

[154] Marlou R. Slot, Thomas S. Gardenier, Peter H. Jacobse, Guido C. P. van Miert, Sander N. Kempkes, Stephan J. M. Zevenhuizen, Cristiane Morais Smith, Daniel Vanmaekelbergh, and Ingmar Swart. Experimental realization and characterization of an electronic Lieb lattice. *Nature Physics*, 13(7):672–676, July 2017.

[155] Steven R. White. Density matrix formulation for quantum renormalization groups. *Physical Review Letters*, 69(19):2863–2866, November 1992.

[156] Maciej Bieniek, Marek Korkusiński, Ludmiła Szulakowska, Paweł Potasz, Isil Ozfidan, and Paweł Hawrylak. Band nesting, massive Dirac fermions, and valley Landé and Zeeman effects in transition metal dichalcogenides: A tight-binding model. *Physical Review B*, 97(8):085153, February 2018.

[157] Kolyo Marinov, Ahmet Avsar, Kenji Watanabe, Takashi Taniguchi, and Andras Kis. Resolving the spin splitting in the conduction band of monolayer MoS2. *Nature Communications*, 8(1):1938, December 2017.

[158] Andor Kormányos, Viktor Zólyomi, Neil D. Drummond, Péter Rakyta, Guido Burkard, and Vladimir I. Fal'ko. Monolayer MoS 2 : Trigonal warping, the γ valley, and spin-orbit coupling effects. *Physical Review B*, 88(4):045416, July 2013.

[159] L. Szulakowska, M. Bieniek, and P. Hawrylak. Electronic structure, magnetoexcitons and valley polarized electron gas in 2D crystals. *Solid-State Electronics*, 155:105–110, May 2019.

[160] L. D. Landau and E. M. Lifshitz. *Quantum Mechanics: Non-relativistic Theory*. Pergamon Press Ltd., Oxford, 1965. Revised second edition. Course of Theoretical Physics, Vol. 3. Translated from the Russian by J. B. Sykes and J. S. Bell.

[161] Andreas V. Stier, Kathleen M. McCreary, Berend T. Jonker, Junichiro Kono, and Scott A. Crooker. Exciton diamagnetic shifts and valley Zeeman effects in monolayer WS2 and MoS2 to 65 Tesla. *Nature Communications*, 7(1):10643, April 2016.

[162] Fengcheng Wu, Fanyao Qu, and A. H. MacDonald. Exciton band structure of monolayer MoS 2. *Physical Review B*, 91(7), February 2015.

[163] Maciej Bieniek, Ludmiła Szulakowska, and Paweł Hawrylak. Effect of valley, spin, and band nesting on the electronic properties of gated quantum dots in a single layer of transition metal dichalcogenides. *Physical Review B*, 101(3):035401, January 2020.

[164] Ludmila Szulakowska, Moritz Cygorek, Maciej Bieniek, and Pawel Hawrylak. Valley and spin polarized broken symmetry states of interacting electrons in

gated MoS$_2$ quantum dots. *arXiv:2005.04467 [cond-mat]*, May 2020. arXiv: 2005.04467.

[165] Pawel Hawrylak. Single-electron capacitance spectroscopy of few-electron artificial atoms in a magnetic field: Theory and experiment. *Physical Review Letters*, 71(20):3347–3350, November 1993.

[166] Pierluigi Cudazzo, Ilya V. Tokatly, and Angel Rubio. Dielectric screening in two-dimensional insulators: Implications for excitonic and impurity states in graphane. *Physical Review B*, 84(8), August 2011.

[167] N S. Rytova. The screened potential of a point charge in a thin film. *Moscow University Physics Bulletin*, 3(3):18, 1967.

[168] LV Keldysh. Coulomb interaction in thin semiconductor and semimetal films. *Soviet Journal of Experimental and Theoretical Physics Letters*, 29:658, 1979.

[169] Y.-P. Shim, F. Delgado, and P. Hawrylak. Tunneling spectroscopy of spin-selective Aharonov-Bohm oscillations in a lateral triple quantum dot molecule. *Physical Review B*, 80(11):115305, September 2009.

[170] A. D. Güçlü, Qing Feng Sun, Hong Guo, and R. Harris. Geometric blockade in a quantum dot: Transport properties by exact diagonalization. *Physical Review B*, 66(19):195327, November 2002.